DESIGN, SYNTHESIS, AND DEVELOPMENT OF SMALL MOLECULE TARGETED BIOCONJUGATES AND INHIBITORS FOR DIAGNOSIS AND THERAPY OF CANCER

Ph.D. Thesis

By

KRATIKA YADAV

MEHTA FAMILY SCHOOL OF BIOSCIENCES AND BIOMEDICAL ENGINEERING
INDIAN INSTITUTE OF TECHNOLOGY INDORE
JULY 2025

DESIGN, SYNTHESIS, AND DEVELOPMENT OF SMALL MOLECULE TARGETED BIOCONJUGATES AND INHIBITORS FOR DIAGNOSIS AND THERAPY OF CANCER

A THESIS

Submitted in partial fulfillment of the
requirements for the award of the degree
of
DOCTOR OF PHILOSOPHY

by

KRATIKA YADAV

MEHTA FAMILY SCHOOL OF BIOSCIENCES AND BIOMEDICAL ENGINEERING
INDIAN INSTITUTE OF TECHNOLOGY INDORE
JULY 2025

INDIAN INSTITUTE OF TECHNOLOGY INDORE

CANDIDATE'S DECLARATION

I hereby certify that the work which is being presented in the thesis entitled **DESIGN, SYNTHESIS, AND DEVELOPMENT OF SMALL MOLECULE TARGETED BIOCONJUGATES AND INHIBITORS FOR DIAGNOSIS AND THERAPY OF CANCER** in the partial fulfillment of the requirements for the award of the degree of **DOCTOR OF PHILOSOPHY** and submitted in **Mehta Family School of Biosciences and Biomedical Engineering, Indian Institute of Technology Indore**, is an authentic record of my own work carried out during the time period from November 2019 to July 2025 under the supervision of Prof Chelvam Venkatesh, (Supervisor) Professor, and Prof Avinash Sonawane, (Co-supervisor), Professor

The matter presented in this thesis has not been submitted by me for the award of any other degree of this or any other institute.

Kratika 30/07/25

Signature of the student with date
(KRATIKA YADAV)

This is to certify that the above statement made by the candidate is correct to the best of my/our knowledge.

Venkatesh. C 30.07.2025

Signature of Thesis Supervisor #1 with date

(Prof. CHELVAM VENKATESH)

30.07.2025

Signature of Thesis Supervisor #2 with date

(Prof. AVINASH SONWANE)

KRATIKA YADAV has successfully given her Ph.D. Oral Examination held on 12/01/2026.

Venkatesh 12.01.2026

Signature of Thesis Supervisor #1 with date

(Prof. CHELVAM VENKATESH)

12.01.2026

Signature of Thesis Supervisor #2 with date

(Prof. AVINASH SONWANE)

ACKNOWLEDGEMENTS

It gives me immense pleasure to acknowledge all the individuals who have helped and supported me over the last five and a half years to complete this thesis. I want to express my deepest gratitude to my supervisor, Prof. Chelvam Venkatesh, for giving me the opportunity to work in such an exciting research area. Without his continuous guidance, support, and motivation, the completion of this thesis research would not have been possible. Through his supervision, I have received many opportunities to learn how to clearly define a research problem, properly document and plan experiments, write and present my work effectively, and translate experimental data into published research work. Beyond the technical aspects, he has continuously emphasized the importance of hard work, discipline, perseverance, and a dedicated work culture in scientific research. His continuous training and constructive feedback have greatly helped me to gain the confidence to excel in any research lab in the future. The skills and work ethics I have developed under his supervision will continue to benefit me throughout my academic and professional career.

I also want to sincerely thank my thesis co-supervisor, Prof. Avinash Sonawane, along with PSPC members Prof. Ganti Murthy and Prof. Sanjay Singh, for their ongoing guidance and valuable suggestions during my yearly progress meetings and throughout my research. I am grateful to the Head of Department and the Department Post-Graduate Committee (DPGC) Convener of the Mehta Family School of Biosciences and Biomedical Engineering for their continuous support in many ways. I also appreciate all faculty members of the Mehta Family School of Biosciences and Biomedical Engineering and the Department of Chemistry for providing access to advanced facilities and equipment, which greatly helped me to produce high-quality data for my research. Additionally, I thank all the support staff from the Mehta Family School of Biosciences and Biomedical Engineering, and the Department of Chemistry, especially Mr. Arif Patel, Mr. Amit Mishra, Mr. Gaurav Singh, Mr. Nilesh Omprakash, Mr. Rameshwar Dohare, Ms. Vinita Kothari, Mr. Shouvik Debnath, and Mr. Manish Kushwaha, for their quick and helpful technical assistance.

My research work has significantly benefited from utilizing various instruments, especially the DST-FIST 500 MHz NMR Facility at the Sophisticated Instrument Centre (SIC). I am deeply grateful to the SIC for providing me with state-of-the-art instrumentation and ancillary equipment for my research. I would like to sincerely acknowledge my appreciation for the

professional support of SIC's technical staff: Dr. Ravinder Kumar, Mr. Ghanashyam A. Bhavsar, and Mr. Kinny Pandey. I also extend my sincere thanks to the academic office staff: Mr. Tapesh Parihar, Mr. Kailash Jamra, Mr. Nitin Parashar, and Mr. Rahul Shrivastav for their continuous help and support.

I am very grateful to the Director, Dean of Academic Affairs (DOAA), and Dean of Student Affairs (DOSA), Indian Institute of Technology, Indore, for providing support and the research facilities within a hostile working environment. I want to express my deepest gratitude to the Indian Institute of Technology Indore for providing me with world-class research facilities, a health centre, and comfortable hostel accommodation. I am also thankful for the platform IIT Indore has offered through various conferences, lectures, and events, which have significantly enriched my Ph.D. journey. I would also like to thank the Ministry of Human Resource Development (MHRD), Department of Higher Education, for financial support.

Further, I am deeply grateful to Dr. Ashok Chandak and Dr. Yogita Shete, Radiation Medicine Centre, BARC, Mumbai, for their guidance and support to carry out my radioactive experiments and *in vivo* studies. I would also like to express my gratitude to the BARC-RMC animal housing centre and staff members for providing excellent facilities and instrumentation to carry out my research.

I want to express my heartfelt gratitude to my senior, Dr. Mena Asha Krishan, for patiently teaching me the procedures and data analysis for various *in vitro* experiments, 3D spheroid studies, solid-phase peptide synthesis, and HPLC purification. Beyond her technical expertise, she has provided insightful feedback, unwavering support and motivation throughout my Ph.D. that helped me to approach every scientific challenge with confidence. Dr. Amit Pandit for performing valuable *in silico* studies for my research work, and Dr. Premansh Dudhe, for his constant support and guidance. I am also grateful to Mr. Lekhnath Sharma, Mr. Saroj Ali, and Mr. Tapash Kalita for teaching me organic synthesis of compounds, NMR and IR data interpretation, valuable input and advice for my thesis, and their prompt cooperation in any work I have requested them.

I cannot thank Dr. Tulika Dixit and Ms. Soumya Shrivastava enough, who stood by me in many ways, supported and motivated me constantly during my highs and lows of my Ph.D. Above all, none of this journey would have been possible without the unwavering love, understanding, and support of my family. It is to them that I owe my deepest gratitude and heartfelt

appreciation. My beloved parents, Mr. Sanjay Kumar Yadav and Mrs. Manju Yadav, for their untiring sacrifices, support, and wise guidance. My dear brother, Mr. Kartik Yadav, has always supported me during my lows with his empathy, motivation, and humour. My loving husband, Mr. Nikhil Singh, whose patience, support, and understanding have been my pillar of strength. My aunt, Mrs. Chitra Puri, for her gentle guidance and wisdom. My cousin, Ms. Khushi Tiwari, her presence and positive energy brought laughter and comfort during my Ph.D journey. Their constant encouragement, motivation, and understanding have been my greatest strength, especially during the challenging final months of my Ph.D. Their presence has been a source of comfort and inspiration throughout both my academic pursuits and life's journey.

KRATIKA YADAV

Dedicated to

almighty god and family

SYNOPSIS

Cancer is one of the primary causes of death, with 20 million new cases and 9.7 million deaths reported in the year 2022 globally. The World Health Organization (WHO) predicted over 35 million new cancer cases to be reported in the year 2035, estimating an increase of 77% from 2022. Among all cancers, prostate cancer (PCa) accounts for 1.46 million new cases and 3.96 lakh deaths worldwide, thus being the second most diagnosed cancer in men. The increase in the number of cases of prostate cancer is mainly due to a lack of diagnostic facilities to detect cancer in the early stages. The conventional diagnostic approaches, like digital rectal exam (DRE) and prostate-specific antigen (PSA) levels in serum, cause physical discomfort and generate false positives, making them less reliable. The non-invasive methods, such as ultrasound, X-ray, magnetic resonance imaging (MRI), and computed tomography (CT), also have disadvantages as they provide only anatomical details, less spatial and contrast resolutions, and fail to differentiate tumours from healthy tissues due to limited sensitivity and specificity. Advancements in imaging modalities and molecular targeting strategies for early diagnostic and intraoperative surgeries are crucial for precise therapy, thereby eliminating the off-target cytotoxicity and improving clinical efficacy. The cargos for these imaging modalities can be attached to a targeting ligand, which can bind with prostate-specific membrane antigen (PSMA) receptor, found to be 1000-fold over-expressed in prostate tumour cells. PSMA, also known as glutamate carboxypeptidase type II (GCP II), causes catalytic hydrolysis of neuropeptide N-acetyl aspartyl glutamate (NAAG) to release glutamate and N-acetyl aspartate. The internal structure of the PSMA receptor comprises an S1′ glutamate recognition pocket, S1 pocket, and two Zn^{2+} ions, along with an irregularly shaped 20 Å tunnel, which forms a primary binding pocket that interacts with the targeting ligand. Therefore, various efforts have been made to design targeting ligands that can bind to the PSMA receptor for the delivery of diagnostic agents and therapeutic cargoes.

Cancer cells show neoplastic characteristics by causing uncontrolled cell proliferation, with each cell passing through four cell cycle phases (G1, S, G2, and M), regulated by checkpoints. These checkpoints work to detect defects and initiate cell repair mechanisms or induce apoptosis to protect cells from further damage. Utilizing this cell cycle machinery, the chemotherapeutic drug development targets microtubule dynamics to induce apoptosis. Microtubules are known to play a crucial role by undergoing polymerization or depolymerization, enabling the separation of

sister chromatids during the M phase of the cell cycle. Disruption in polymerization or depolymerization causes cell cycle arrest, resulting in apoptosis due to failure of chromatid separation. Tubulysins, a class of natural products isolated initially from myxobacteria cultures, have gained significant attention for their potent cytotoxic activity, primarily mediated through the inhibition of microtubule assembly by binding with β-tubulin microfilaments and the induction of apoptosis. This property makes them valuable candidates for anticancer drug development. Among the fourteen naturally occurring tubulysin family of natural products, tubulysin M is one of the most promising anticancer peptides with an IC_{50} of 0.02 nM. However, the availability of Tubulysin M is limited due to its natural scarcity, complex structure with various chiral centres, multistep synthesis, poor yield, and biological instability. Also, most of the drug candidates fail during pre-clinical studies, as a 2D *in vitro* study fails to generate reliable data due to a lack of complexity mimicking the *in vivo* tumour microenvironment.

The objectives of the thesis are to develop novel PSMA-targeted radioactive agent which can aid in the precise and early diagnosis of prostate cancer, studying the effect of amino acid spacers on PSMA targeted bioconjugates, development of a synthetic strategy to synthesize biologically active tubulin inhibitors via solid phase peptide synthesis (SPPS) followed by evaluation of their efficacy in vitro in 2D cell culture model and examination of 3D spheroid model for cytotoxicity studies which can act as a bridge between 2D and *in vivo* studies to reduce the failure of drug candidates during pre-clinical studies.

The thesis consists of the following chapters:

1. General introduction to early diagnosis of prostate cancer, various synthetic routes for the synthesis of tubulysin natural products and their derivatives, and development of a 3D platform that bridges 2D cell culture and *in vivo* studies.
2. Review of work and problem formulation
3. Design and synthesis of small-molecule ligand PSMA-targeted bioconjugate for the diagnosis of prostate cancer.
4. Role of spacers in PSMA-targeted bioconjugates in the diagnosis of prostate cancer using radioactive isotope ^{99m}Tc
5. Design, synthesis, and cytotoxic evaluation of new structurally simplified and highly potent third-generation tubulysin derivatives.

6. 3D Spheroid model development for in vitro cytotoxicity evaluation of tubulin inhibitor: An approach to enhance biomimetic accuracy for clinical research.

1. General introduction to early diagnosis of prostate cancer, various synthetic routes for the synthesis of tubulysin natural products and their derivatives, and development of a 3D platform that bridges 2D cell culture and in vivo studies

This chapter provides general information about cancer and its statistics, along with prostate cancer, which is the second most diagnosed cancer in men, conventional fluorescent imaging techniques, and their drawbacks. This chapter gives detailed insights into prostate-specific membrane antigen and various radioactive isotopes used for the early diagnosis of prostate cancer. It also provides a literature review on various microtubule targeting agents, synthetic strategies developed for the synthesis of biologically active tubulysin natural products, their derivatives, and drawbacks. In addition, various literature methods available to develop 3D spheroid models are discussed in detail, along with their clinical relevance over the 2D cell culture model.

2. Review of work and problem formulation

This chapter, in brief, describes the literature review of various PSMA-targeting ligands and their clinical applications. It also details the chemical synthetic approach developed for the synthesis of tubulysins, natural products. Additionally, it covers the current methods for generating 3D spheroids and their limitations.

3. Design and synthesis of small-molecule ligand PSMA-targeted bioconjugate for the diagnosis of prostate cancer

This chapter describes the design and synthesis of aminoacetamide-based targeting ligands mimicking the NAAG inhibitor that binds to the PSMA receptor. Initially, docking studies were performed with the PSMA protein and the most potent aminoacetamide ligands **1**, **2**, and **3**, with high docking scores, which were subsequently evaluated using the PSMA enzyme inhibition assay for the determination of IC_{50}. The most potent aminoacetamide-based ligand precursor **15a** was further attached to a spacer containing a chelating linker to chelate radioactive isotope, ^{99m}Tc, for an early diagnosis of prostate cancer. The ^{99m}Tc AAPT_PCa radioactive bioconjugate **22** has a binding affinity constant (K_d) in the low nM range of 48 nM with an excellent specificity for the PSMA receptor, as indicated by performing a

competition study with a standard PSMA inhibitor, 2-PMPA (2-phosphonomethylpentanedioic acid).

The *in vivo* studies on tumor-bearing athymic nude mice revealed high selectivity and specificity of the ^{99m}Tc AAPT_PCa radiopharmaceutical **22** in the tumor with minimal uptake in excretory organs such as kidneys and bladder. The biodistribution studies show the highest uptake of 21.5% ID/gm in tumor tissue. These results reveal the potential of PSMA-specific radiopharmaceuticals not only for accurate localization of prostate cancer lesions but also for monitoring therapeutic responses and detection of recurrence post-surgery.

4. **Role of spacers in PSMA-targeted bioconjugates in the diagnosis of prostate cancer using radioactive isotope ^{99m}Tc**

   This chapter describes a series of DUPA (2-[3-(1,3-dicarboxypropyl)-ureido]pentanedioic acid) ligand conjugated PSMA-targeting radioactive bioconjugates synthesized with optimal spacer length to provide maximum binding affinity to the ligand via interaction at the secondary hydrophobic binding pocket in the PSMA protein. The radioactive bioconjugates were designed by varying amino acids. The *in vitro* binding affinity studies show the importance of aromatic amino acids in the spacer of bioconjugates DUPA_Bioconjugate **18** and DUPA_Bioconjugate **19**, which have shown the highest binding affinity constants (K_d) of 21 nM and 27 nM, respectively, in $PSMA^+$ cells. The drastic loss of binding affinity constants from 51 nM to 88 nM was observed when the aromatic amino acids were replaced with aliphatic amino acid such as glycine in DUPA_Bioconjugate **20** to DUPA_Bioconjugate **23**. This strategic design strengthens the use of radioactive isotope ^{99m}Tc, thereby eliminating the drawbacks of conventional fluorescent imaging agents, making it a clinically favourable and cost-effective technique. This modification establishes an important implication of the secondary hydrophobic binding site present in the PSMA protein for the development of PSMA-targeted bioconjugates as radioimaging agents.

5. **Design, synthesis, and cytotoxic evaluation of new structurally simplified and highly potent third-generation tubulysin derivatives**

   This chapter describes the design, synthesis, and development of several new tubulysin derivatives, **14a–l**, with N-terminal and C-terminal modifications. A simple synthesis of valine thiazole and *N*-methyl pipecolic acid fragments was carried out, and the chemically synthesized fragments were coupled using solid-phase peptide synthesis (SPPS) in high

yields. After the successful synthesis and purification of tubulysin derivatives (**14a-l**), *in vitro* cytotoxicity evaluation (IC_{50}) was performed against various cancer cell lines, such as MCF7 (breast cancer), A549 (lung cancer), LNCaP (prostate cancer), A431 (skin cancer), HeLa (cervical cancer), and A375 (melanoma) for an incubation period of 48 h and 24 h. The *in vitro* analysis of these derivatives has shown promising results with IC_{50} = 14 nM for the most potent derivative, **14a**, in comparison to a standard microtubule inhibitor, colchicine, that showed an IC_{50} of 0.31 µM, validating the *in silico* studies of the newly designed tubulysin derivatives. The study also summarizes the effect of structural alterations in C-terminal and N-terminal amino acids on the biological activities. Notably, slight changes at the N-terminal fragment led to a substantial decrease in potency from nM to µM. In contrast, modifications at the C-terminal fragment with aliphatic amino acids had minimal impact on the inhibitor's efficacy. In contrast, the activities were affected moderately by the replacement with aromatic amino acids.

6. **3D Spheroid model development for *in vitro* cytotoxicity evaluation of tubulin inhibitor: An approach to enhance biomimetic accuracy for clinical research**

This chapter explores the cytotoxicity potential of novel tubulysin derivative **15** in both conventional 2D monolayer cell culture and advanced 3D spheroid models. The spheroids were synthesized using the µsphere platform developed in our laboratory and were found to be highly viable. These spheroids were treated with tubulysin derivative **15**, and the cell death was examined by staining with FDA and PI dye. The cytotoxic potential of tubulysin derivative **15** in the 3D model was assessed using two parameters: (1) IC_{50} value, which was obtained using the MTT assay to determine cell viability, and (2) spheroid diameter, indicating the morphological and structural integrity of the spheroid. Tubulysin derivative **15** is effective in a 2D monolayer PC3 model with an IC_{50} of 22 nM but was also found to retain its potency in a complex 3D spheroid model with an IC_{50} of 20 nM.

In contrast, a standard microtubule tubulin inhibitor, colchicine, was found to significantly lose its cytotoxic activity from 277 nM in the 2D model to 0.84 µM in the 3D model, indicating limited penetration and tubulin inhibitory activity. In addition, post-treatment structural analysis of the spheroid with tubulysin derivative **15** shows a reduction in the spheroid diameter and loss of structural compactness, leading to disruption of the spheroid

geometry. The tubulysin derivative **15** has retained cytotoxic activity in the 3D model, making it a promising candidate for *in vivo* validation and clinical translation.

LIST OF PATENTS AND PUBLICATIONS

1. **Yadav K**., Krishnan MA., Venkatesh C. (2022), Curr. Protoc. Chem. Biol. *In Vitro* and *In Vivo* Evaluation of Targeted Fluorescent Imaging Agents for Diagnosis and Resection of Cancer. 2(12), e623-e655. (DOI: 10.1002/cpz1.623).
2. **Yadav K**., Kalita T., Sharma L., Pandit A., Pathak B., Drager G., Kirschning A., Venkatesh C. (2025), Chem. Eur. J. Design, Synthesis and Cytotoxic Evaluation of New Structurally Simplified and Highly Potent Third-Generation Tubulysin Derivatives. 31(46), e01965 . (DOI: 10.1002/chem.202501965).
3. **Yadav K**., Kalita T., Sharma L., Venkatesh C. (2025), Curr. Protoc. Chem. Biol. Design, Synthesis, Development and Biological Evaluation of Third-Generation Tubulin Inhibitors. 5, e70229-e70257. (DOI:10.1002/cpz1.70229).
4. **Yadav K**., Sengupta S., Krishnan MA., Pandit A., Venkatesh C. (2025), Aminoacetamides: A New Class of Small Molecule Inhibitors/Ligands for Prostate Specific Membrane Antigen Expressing ($PSMA^{+)}$ Cancers. (manuscript under submission).
5. **Yadav K**., Venkatesh C. (2025), Role of Spacers in PSMA-Targeted Bioconjugates in The Diagnosis of Prostate Cancer Using Ligand-Targeted Radiopharmaceuticals. (manuscript under preparation).
6. **Yadav K**., Venkatesh C. (2025), 3D Spheroid Model Development for i*n vitro* Cytotoxicity Evaluation of Tubulin Inhibitor: An Approach to Enhance Biomimetic Accuracy for Clinical Research. (manuscript under submission).
7. Venkatesh C., Pandit A., RB Reddy., **Yadav K**., Pathak B., Roy D. (2021), Third Generation Tubulysin Analogues and Process of Preparation thereof. Patent No. US 11,518,786, *USA Patent* (Granted).
8. Venkatesh C., Pandit A., RB Reddy., **Yadav K**., Pathak B. Roy D. (2020), Third Generation Tubulysin Analogues and Process of Preparation thereof. Patent No. 498433, *Indian Patent* (Granted).
9. Dudhe P., Krishnan MA., **Yadav K**., Roy D., Venkatasubbaiah K., Pathak B., Venkatesh C. (2020). Beilstein J. Org. Chem. Synthesis of 1-Indolyl-3,5,8-Substituted γ-Carbolines:

One Pot Metal-Solvent Free Protocol and Biological Evaluation. 17, 1453–1463. (DOI: 10.3762/bjoc.17.101).

10. Pandit A., **Yadav K**., RB Reddy., Sengupta S., Sharma R., Venkatesh C. (2020). J. Mol. Structure. Structure Activity Relationships (SAR) Study to Design and Synthesize New Tubulin Inhibitors with Enhanced Anti-tubulin Activity. 1223, 129-204. (DOI:10.1016/j. molstruc.2020.129204).
11. Krishnan MA., **Yadav K**., Roach P., Venkatesh C. (2021). Biomater. Sci. Targeted Near Infrared Nanoprobes for Early Detection and Surgical Guidance of Prostate Cancer. 9, 2295-2312. (DOI: 10.1039/d0bm01970d).
12. Krishnan MA., **Yadav K**., Roach P., Venkatesh C. (2021). Curr. Protoc. Agarose Micro-Well Platform for Rapid Generation of Homogenous 3D Tumor Spheroids. 1, e199-220. (DOI: 10.1002/cpz1.199).
13. Design, Synthesis and Biological Evaluation of Fused Thieno[3,2-c], Thieno[2,3-c], Benzo[4,5]thieno[3,2-c]pyridine, Benzo[4,5]thieno[2,3-c]pyridine and Thiazolo[4,5-c]pyridine Derivatives for Treatment of Diseased States. Venkatesh C., Sharma L., Kalita T., **Yadav K**, Indian Patent, Application No. 202442108513, Nov. 2024.

TABLE OF CONTENTS

LIST OF FIGURES

LIST OF TABLES

LIST OF SCHEMES

mL, 30 min; 2 × 5 mL, 5 min); (ii) Evaporate TFA;
(iii) Precipitation in ice-cold diethylether.

ACRONYMS

Abbreviations used for amino acids, peptides, derivatives, substituents, reagents, etc., are mainly in accordance with the recommendations of the IUPAC-IUB commission on Biochemical Nomenclature, 1974, Pure and Applied Chemistry, 40, 315-331. The standard three-letter code is used for all amino acids. Additional abbreviations used in this thesis are listed below.

A.U.	Arbitrary unit
A375	Human malignant melanoma cell line
A431	Human epidermoid carcinoma epithelial cells
A549	Adenocarcinomic human alveolar basal epithelial cells
AAPT	Aminoacetamide pentanedioic acid
ADT	Androgen deprivation therapy
Ala	Alanine
AMBA	Aminomethylbenzoic acid
AOC	Aminooctanoic acid
Arg	Arginine
Asn	Asparagine
Asp	Aspartic acid
BOC	tert-Butyloxycarbonyl
BPH	Benign prostatic hyperplasia
$CdCl_3$	Chloroform-d
CDKs	Cyclin-dependent kinases
CLSM	Confocal laser scanning microscopy
CO_2	Carbon dioxide
CPM	Counts per minute
CT	Computed tomography
Cys	Cysteine
d	Doublet
Dap	Diaminopropionic acid
DCM	Dichloromethane
DCNPs	down-conversion nanoparticles
dd	Double doublet
DIPEA	Diisopropylethylamine
D-Mep	Methyl-D-pipecolic acid

DMF	Dimethyl formamide
DRE	Digital rectal examination
DUPA	(2-[3-(1,3-Dicarboxypropyl)ureido] pentanedioic acid)
ECM	Extracellular matrix
ED	Extracellular domain
EDC.HCl	1-Ethyl-3-(3-dimethylaminopropyl)carbodiimide hydrochloride
EDT	Ethane dithiol
EDTA	Ethylenediaminetetraacetic acid
EEO	Low electroendosmosis
equiv	Equivalent
Et_3N	Triethylamine
EtOAc	Ethyl acetate
FDA	Fluoresceine diacetate
Fmoc	9-Fluorenylmethyloxycarbonyl
FOLH 1	Folate hydrolase 1
FTIR	Fourier transform infrared spectroscopy
G1	Gap 1
G2	Gap 2
GCP-II	Glutamate carboxypeptidase
Gln	Glutamine
Glu	Glutamic acid
Gly	Glycine
HATU	Hexafluorophosphate azabenzotriazole tetramethyl uronium
HBA	Hydrogen bond acceptor
HBD	Hydrogen bond donor
HCl	Hydrochloric acid
HEK	Human embryonic kidney
HeLa	Henrietta lacks
Hep	Hepatoma
His	Histidine
HOBt	1-Hydroxybenzotriazole
HPLC	High-performance liquid chromatography

HRMS	High-resolution mass spectrometry
ICG	Indocyanine green
Ile	Isoleucine
IPA	Isopropanol
IR	Infrared
LCMS	Liquid chromatography-mass spectrometry
Leu	Leucine
LNCaP	Lymph node carcinoma of the prostate
Lys	Lysine
M	Mitosis
m.p.	Melting point
MCF7	Michigan cancer foundation-7
mCRPC	Metastatic castration-resistant prostate cancer
MDCK	Madin-darby canine kidney cells
MeOH	Methanol
MFI	Mean fluorescent intensity
MQ	Milli-Q
MRI	Magnetic resonance imaging
MS	Mass spectrometry
MTT	3-(4,5-Dimethylthiazol-2-yl)-2,5-diphenyl-2H-tetrazolium bromide
Na_2SO_4	Sodium sulphate
NAAG	N-acetylaspartylglutamate
NaCl	Sodium chloride
NADH	Nicotinamide adenine dinucleotide
$NAHCO_3$	Sodium bicarbonate
NI	Negatively ionizable
NIR	Near infrared
NMR	Nuclear magnetic resonance
O_2	Oxygen
PC3	Prostate cancer 3
PCa	Prostate cancer
Pd/C	Palladium on carbon
PET	Positron emission tomography

pH	The negative logarithm of hydronium-ion concentration (-log10 [H_3O^+])
Phe	Phenylalanine
PI	Propidium iodide
PMB	Paramethoxybenzyl
PMPA	Phosphonomethyl pentanedioic acid
pRB	Retinoblastoma protein
PSA	Prostate-specific antigen
PSMA	Prostate-specific membrane antigen
PyBOP	Benzotriazol-1-yloxy)tripyrrolidinophosphonium hexafluorophosphate
q	Quartet
QDs	quantum dots
Rf	Retention factor
RP-HPLC	Reverse-phase performance liquid chromatography
RPMI	Roswell park memorial institute
Rt	Retention time
rt	Room temperature
s	Singlet
SD	Standard deviation
Ser	Serine
$SnCl_2$	Stannous chloride
SPECT	Single-photon emission computed tomography
SPPS	Solid phase peptide synthesis
SWNT	Single-walled carbon nanotubes
t	Triplet
Tert	Tertiary
TFA	Trifluoroacetic acid
THF	Tetrahydrofuran
Thr	Threonine
TIPS	Tri-isopropyl silane
TLC	Thin-layer chromatography
TME	Tumor microenvironment

Trt	Trityl
TRUS	Transrectal ultrasound
Tup	Tubuphenylalanine
Tuv	Tubuvaline
Tyr	Tyrosine
UV	Ultraviolet
Val	Valine
Vis	Visible

SYMBOLS/UNIT

α	Alfa
Å	Angstrom
A.U.	Arbitrary Unit
β	Beta
^{64}Cu	Copper-64
°C	Degree Celsius
δ	Delta
ε	Epsilon
^{18}F	Fluorine-18
^{68}Ga	Gallium-68
γ	Gamma
g	Gram
IC_{50}	Half-maximal inhibitory concentration
h	Hour
^{124}I	Iodine-124
keV	Kilo electron volt
µCi	Microcurie
µL	Microliter
µm	Micrometer
µM	Micromolar
mmol	Millimol
mM	Millimolar
mg	Milligram
mL	Milliliter
min	Minute
nm	Nanometer
nM	Nanomolar
π	Pi
pM	Picomolar
^{44}Sc	Scandium-44
^{99m}Tc	Techetium-99

Chapter 1

Introduction

1.1 Cancer and statistics

Cancer is one of the leading causes of death globally, accounting for 20 million new cases and 9.7 million deaths in the year 2022. It has been estimated that in the year 2050, over 35 million new cancer cases will be reported, accounting for an increase of 77% from 2022.[1] The incidence and mortality rate of cancers worldwide (Table 1.1) make it a global burden for the discovery of new and effective diagnostic and therapeutic agents. Despite significant diversification and expansion in treatment strategies, surgery remains the best option for treating solid tumours. For the past 6 decades, conventional approaches, including chemotherapy and immunotherapy, have resulted in a 90% (±5%) failure rate according to government agencies.[2] The rate of recurrence for primary cancers, including ovarian (85%),[3] prostate (48%),[4] lymphoma (75%),[5] and melanoma (87%), has increased.

S.no	Cancer	Incidence cases	Mortality cases
1	Lung	2,480,301	1,817,172
2	Breast	2,308,897	665,684
3	Colorectum	1,926,118	903,859
4	Prostate	1,466,680	396,792
5	Stomach	968,350	659,853

Table 1.1 Incidence and mortality cases for the most prevalent cancer globally in 2022.

In men, prostate cancer is the second most diagnosed cancer and the fifth leading cause of death, accounting for 1.4 million new cases and 396,000 deaths reported globally (Figure 1.1). It is the most frequently diagnosed cancer in 112 countries and the leading cause of cancer death in 48 countries. In India, prostate cancer is the fifth most prevalent diagnosed cancer in men, accounting for 37,948 new cases, rendering

the cumulative risk of developing prostate cancer 1 in every 125 men in the year 2022.[1]

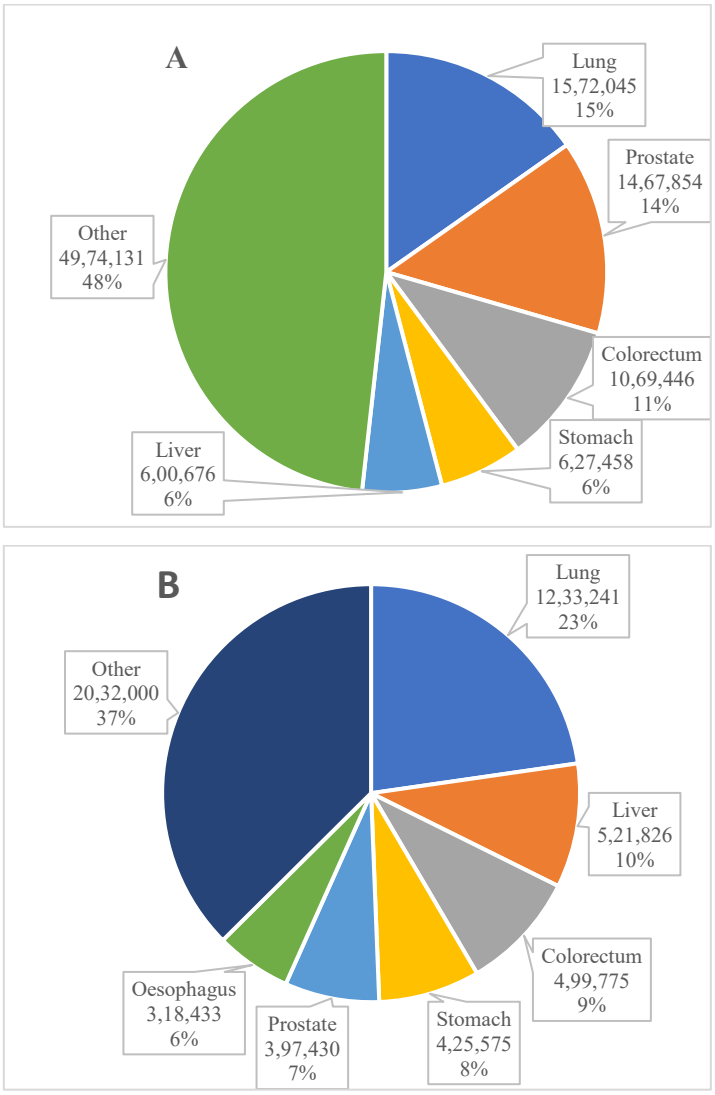

Figure 1.1 Cancer statistics globally in 2022 (A) Incidence cases (B) Mortality cases in men.

1.2 Prostate cancer and the conventional diagnostic approaches

The uncontrollable proliferation in the cells of the prostate gland defines prostate cancer (PCa) based upon its location; it belongs to adenocarcinoma, representing 98% of all PCa.[6] It severely affects a person's life due to physical pain, urine obstruction, erectile dysfunction, weakness, psychological distress, and impairment of social functioning.[7] Advanced PCa tends to metastasize to distant organs, infiltrate tissues, and cause the formation of bone lesions, resulting in muscle wasting and osteoporosis, making it extremely difficult to treat.[8]

Therefore, early detection of this disease is necessary to decrease PCa-related morbidity and mortality. The current diagnosis for early detection relies on a blood test for prostate-specific antigen (PSA) or a prostate biopsy. However, these approaches have faced criticism due to their limitations, such as the inaccuracy of PSA tests in conditions like benign prostatic hypertrophy (BPH) and prostatitis.[9] Detecting later stages of prostate cancer typically involves a painful and costly biopsy. Current diagnostic methods for detecting prostate cancer, including Digital Rectal Examination (DRE), PSA blood tests, and biopsies, often produce inconclusive results, yield false positives, and lack accuracy and sensitivity.[10] Advanced imaging techniques, like transrectal ultrasound combined with magnetic resonance imaging (MRI) and computed tomography (CT) scans, provide better examination, but are costly and not easily accessible for routine screenings. The emergence of castration-resistant prostate cancer (CRPC) and subsequent metastasis, along with limited treatment options, accentuates the urgency for more effective diagnostic tools and treatments. Traditional treatments like surgery, radiation, and androgen-deprivation therapy (ADT) offer limited success, as recurrence is common within 2–3 years, and survival time for CRPC remains 16–18 months.[11]

1.3 Fluorescent imaging

Fluorescent imaging has proven to be an effective, non-invasive, highly sensitive, and real-time imaging method for visualization and differentiation of tumour masses from healthy tissues.[12] This information is helpful for early detection of cancer lesions, diagnosis and staging of cancer, fluorescence-guided surgery, monitoring treatment responses, and detecting any residual tumour mass after surgery.[13] Fluorescence imaging works on the principle of *in situ* excitation and subsequent emission of light from the fluorescent probe. Commonly used fluorescent probes are small organic molecules like cyanine, rhodamine, or BODIPY.[14] However, they are limited by their excitation and emission wavelengths occurring in the UV-Vis range that lies outside the biological transparency window. Furthermore, various

disadvantages include background noise, autofluorescence, and limited penetration depth (1–3 mm). In the UV–Vis wavelength region, various vital organs and endogenous chromophores such as flavins, NADH, and haemoglobin cause autofluorescence, resulting in background noise and interfering with the fluorescence signal from tumour nodules. There is also limited penetration depth encountered in this region due to photon reflections from the tissue surface, scattering of photons due to non-homogeneous tissue surface, photon absorption by various chromophores, and autofluorescence.[15] Efforts focusing on using near-infrared (NIR) fluorescent dyes for early cancer detection and imaging have shown promising results, as the NIR wavelength offers reduced scattering, absorption, and autofluorescence from tissues.[16] The NIR range is typically divided into two windows: NIR-I (650–900 nm) and NIR-II (1000–1700 nm).[17] The NIR-II window has emerged as the next generation fluorescent imaging technology that offers increased deep tissue penetration up to a few cm and reduced background autofluorescence. Current NIR-II fluorophores include single-walled carbon nanotubes (SWNTs), quantum dots (QDs), lanthanide-based down-conversion nanoparticles (DCNPs), and fluorescent dyes.[18] Fluorescent dyes, such as IR-800CW, indocyanine green (ICG), DyLight 680 maleimide, and DyLight 750 maleimide, are in the NIR-I region. These reported NIR–II materials have shown various drawbacks, such as toxicity, photostability, limited excitation and emission wavelength, high cost, low fluorescence quantum efficiency, and longer circulation time.

1.4 Molecular imaging of prostate cancer

Molecular imaging using NIR probes presents a real-time, specific method to visualize target biomarkers overexpressed on cancer tissues. Targeted imaging allows better assessment of different stages of the malignancy, but is most useful for advanced disease states. In 1987, Murphy and Horoszewicz first developed the 7E11-C5 monoclonal antibody (capromab) by immunizing mice with the LNCaP human prostate cancer cell line. This antibody recognizes a novel antigen on

both normal and malignant prostate epithelial cells, but is especially prominent in prostate cancer. The antigen detected was termed prostate-specific membrane antigen (PSMA).[19] Horoszewicz and colleagues suggested that this new antigenic marker could have significant clinical potential for prostate cancer diagnosis and management, using ligands conjugated with various diagnostic and therapeutic cargos (Figure 1.2).

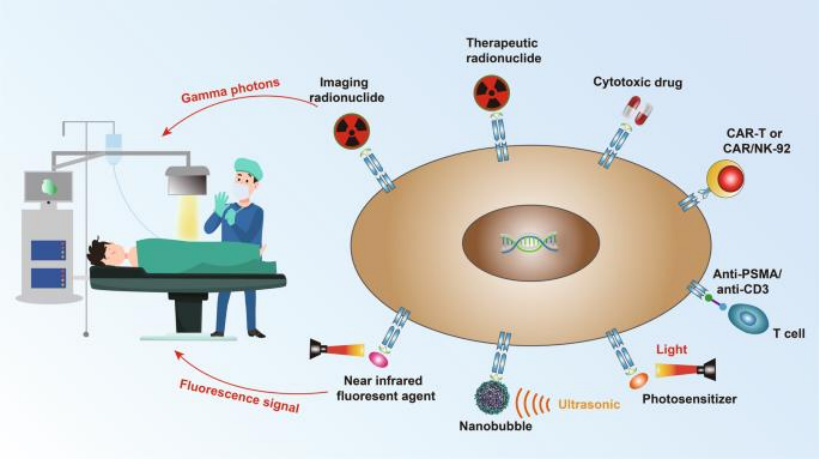

Figure 1.2 PSMA-based imaging and therapy for precise detection and targeted treatment of prostate carcinoma.[20]

1.5 Prostate-specific membrane antigen (PSMA) as a biomarker

Prostate-specific membrane antigen (PSMA) is a popular target as it is a cell membrane protein and overexpressed about 1000-fold in cancerous cells compared to minimal expression in normal tissues such as the small intestine, kidney, salivary gland, and epithelial cells of the prostate gland. PSMA, also known as N-acetyl-aspartyl-glutamate peptidase I (NAAG peptidase I), glutamate carboxypeptidase II (GCPII), or folate hydrolase 1 (FOLH 1), is a type II transmembrane protein consisting of 750 amino acids.[21] It consists of three domains: intercellular, transmembrane, and the enzymatically active extracellular domain (Figure 1.3), which causes catalytic hydrolysis of neuropeptide N-acetyl aspartyl glutamate (NAAG) to release glutamate and N-acetyl aspartate. The internal structure of the PSMA receptor comprises an S1′ glutamate recognition pocket, an S1 pocket, and two Zn^{2+} ions along with an irregularly shaped 20 Å tunnel, which forms a primary binding pocket that interacts with the targeting ligand. The S1′ pocket contains

a glutamate sensor box, which interacts with the glutamate moiety of NAAG, and Glu 424 performs the catalytic hydrolysis (Figure 1.4).[22] In malignancy, PSMA is transferred to the luminal surface of prostatic ducts from the cytoplasm, presenting ligands with a large extracellular domain.[23] PSMA receptor also undergoes clathrin-mediated endocytosis when bound to a targeting moiety.[24] This property has been abundantly exploited to target PSMA by several targeting agents, which include monoclonal antibodies, small molecule ligands, and DNA aptamers.[25] The small molecule ligand inhibitors based on the active site are categorised into (i) glutamate-urea heterodimers, (ii) glutamate-containing phosphoramidates, and (iii) 2-(phosphophenylmethyl) pentanedioic acid. [26] Glutamate-ureido targeted imaging agents, such as PSMA-617 and PSMA-11, have shown extremely promising data in preclinical and clinical trials for prostate cancer.[27] The small molecule radiolabelled ligand ^{177}Lu-PSMA-617 is used in compassionate therapy for end-stage mCRPC patients.[28] Hence, developing a highly efficacious and sensitive PSMA targeting radiopharmaceuticals would address issues currently faced in deep-tissue imaging and surgical guidance.

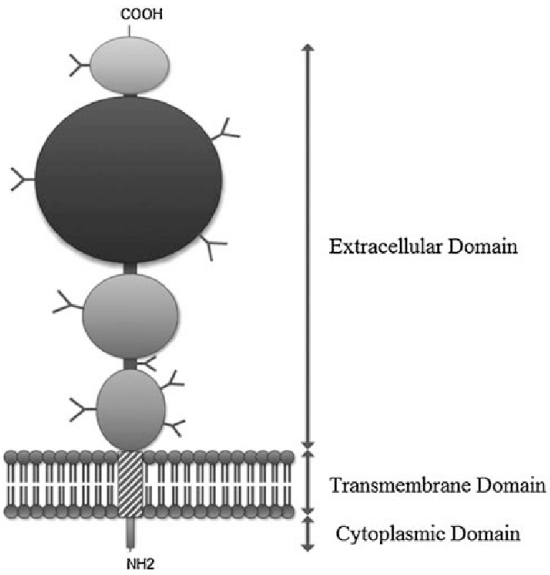

Figure 1.3 Schematic illustration of the PSMA protein.

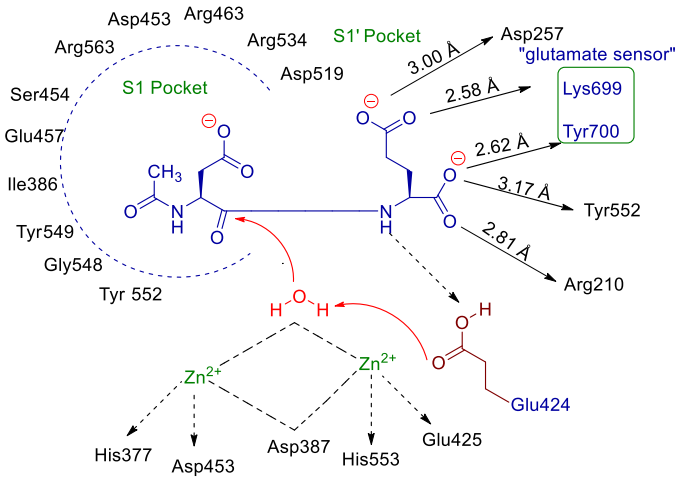

Figure 1.4 PSMA binding site.

1.6 PSMA-based radioactive bioconjugate for diagnosis

The basic structure of the targeted bioconjugate for deep-tissue imaging of cancer is composed of the following components: i) a small molecule homing moiety that binds specifically to cancer cells, ii) a peptidic construct/linker connecting the homing ligand to the diagnostic cargo, and iii) a chelating moiety to tag a radioactive isotope (Figure 1.5). The peptide linker serves a dual role of connecting the PSMA-based targeting ligand and radioactive isotope, interacting with the protein tunnel, and increasing the overall affinity of the bioconjugate with the protein biomarker.

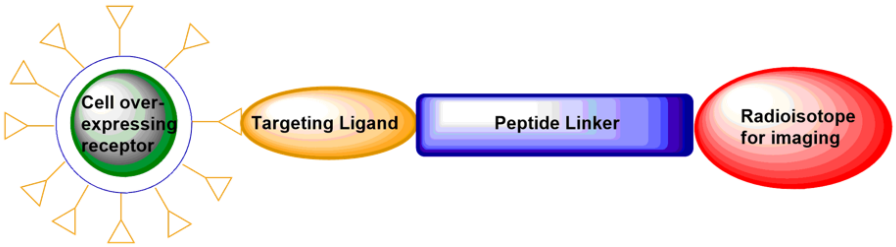

Figure 1.5 Basic structure of PSMA-based radiopharmaceutical.

1.7 Radioactive isotopes for imaging

Radionuclide-based imaging techniques like Positron Emission Tomography (PET) and Single Photon Emission Computed Tomography (SPECT) are the modalities available for tumor imaging. The high sensitivity, non-invasive and real-time monitoring, quantifiability, molecular specificity, and radiotracer flexibility are

significant advantages for widespread application in the diagnosis and treatment of cancer.[29] PET works by the identification of high-energy photon pairs formed during the annihilation of an electron and a positron. The generated photon pairs are detected by a PET scanner, and the computed tomography anatomical data are used to generate a 3D image using PET/CT.[30] PET imaging agents include radioactive isotopes such as ^{18}F, ^{64}Cu, and ^{68}Ga. Clinically, ^{18}F-FDG is widely used for cancer diagnosis but is mainly non-targeted and does not accumulate well in many cancerous tissues, including the prostate. Efforts have been made to develop radiopharmaceuticals by employing ^{68}Ga, attached to a PSMA targeting ligand via a peptidic spacer, offering high sensitivity and specificity for diagnosis, staging, restaging, and therapy evaluation by selectively binding to PSMA overexpressed on prostate cancer cells.[31] SPECT utilises radioactive isotopes that emit a single γ-ray photon for each nuclear de-excitation event for the three-dimensional image construction. The most commonly used radioisotopes are ^{99m}Tc, ^{123}I, and ^{111}In, due to their optimal half-lives, making them convenient for medical use.[32] The ideal characteristics of metastable technitium 99 (^{99m}Tc), such as half-life (6 h, $E\gamma$ = 140 keV), no off-target binding, biological stability, physical and chemical properties, and chelation efficiency, make it suitable for the diagnosis of cancer.[33]

1.8 The cell cycle dysregulation in cancer

Cancer pathogenesis signifies a complex biological process whereby the somatic cell bypasses the normal cell cycling and acquires neoplastic characteristics by malignant transformation from the physiological control growth mechanism.[34] Normal somatic cellular proliferation is under the tight regulation of a cell signaling pathway that performs coordinated growth-promoting and inhibitory signaling, ensuring tissue homeostasis.[35] These signals include cell-cell communication, mitogenic growth factors, extracellular matrix interactions, and intrinsic regulatory checkpoints within the cell cycle machinery. In healthy cells, the cell cycle is regulated by cyclin, cyclin-dependent kinases (CDKs), and CDK inhibitors, collectively called regulatory proteins.[36] The

protein expression and activities of these proteins are controlled by various tumour suppressor genes like BRCA1, BRCA3, p53, and retinoblast protein (pRb), which maintain genomic integrity and cell division.[37] During oncogenesis, the cells undergo dysregulation from regulatory mechanisms due to somatic mutations or epigenetic alterations, resulting in sustained proliferation signals. The epigenetic alteration, such as overexpression of growth factors, activation of receptor tyrosine kinases, mutation in the downstream signaling pathway, or inactivation of tumor suppressor genes, collectively enables the unregulated cell cycle.[38] The cell cycle consists of four distinct phases: the growth 1 (G1), synthesis (S), growth 2 (G2), and mitotic (M) phase. The mitotic phase is further divided into prophase, prometaphase, metaphase, anaphase, and telophase during cell division. In metaphase and anaphase, the α and β tubulin heterodimers undergo polymerization and depolymerization to separate sister chromatids during cell division.[39]

1.9 Microtubules and their targeting agents

The microtubules play a crucial role in cell division; the disruption in their assembly and disassembly critically impairs mitotic spindle function, leading to cell cycle arrest at spindle assembly checkpoints after M phase and triggering apoptosis due to the failure of proper chromatid segregation.[40] Microtubules are dynamic polymers of α- and β-tubulin heterodimers that undergo tightly regulated growth phases (polymerization) and shortening (depolymerization), essential for aligning and separating chromosomes during mitosis.[41] Microtubule targeting agents (MTAs) interfere with this regulation by selectively binding to microtubules and affecting their dynamics. Based on their mode of action, microtubule-targeting agents belong to two categories: microtubule stabilisers and destabilisers.[42] The microtubule-stabilizing agents, including taxanes and epothilone, inhibit the depolymerization of tubulin protein, and the microtubule-destabilizing agents, such as tubulysins, vinca alkaloids, and colchicine, inhibit the polymerization process, thus halting the cell division at metaphase.[43] MTAs are widely

used in therapy due to their potency in inhibiting rapidly proliferating tumor cells by disrupting mitosis.[44] However, their effects on microtubules in normal cells contribute to side effects such as neuropathy and myelosuppression. Newer agents and derivatives aim to increase cancer cell selectivity and reduce toxicity. Structural biology advances revealed multiple drug-binding sites on the tubulin protein, offering avenues to design novel MTAs with improved efficacy and resistance profiles.

1.10 Tubulysin–A microtubule-targeting natural product

Tubulysin has emerged as a promising anticancer agent due to effective intracellular retention and high cytotoxic efficacy. These natural products exhibit cytotoxicity in the low nM range against a broad spectrum of cancer cell lines.[45] Their mechanism of action involves binding at the vinca alkaloid site on β-tubulin, one of the key structural components of the microtubule. By binding to this site, tubulysin inhibits microtubule polymerization, leading to apoptosis due to cytoskeleton collapse.[46] The isolation of tubulysin was first reported by Höfle et al and Reichenbach in 2000 from two strains of Myxobacteria culture broths, *Angiococcus disciformis* and *Archangium gephyra*.[47] Till now, fourteen different tubulysin natural products have been reported, and structural elucidation revealed that they are tetrapeptides with N-methyl-D-pipecolic acid (D-Mep) at the N-terminus, followed by L-isoleucine (L-Ile), tubuvaline (Tuv), and tubuphenylalanine (Tup) or tubutyrosine (Tut) at the C-terminus with a functionalized amide linkage between tubuvaline and isoleucine fragments in a few tubulysin derivatives. Despite their therapeutic potential, the limited natural availability has been a significant challenge.[48] Also, the structural complexity due to the presence of unnatural amino acids and multiple chiral centres results in low overall yield during their total synthesis, causing scalability issues.[49]

1.11 Chemical synthesis of tubulysin

The most active natural tubulysins have a rare tertiary amide N, O-acetyl ester, which makes the central part of the molecule sterically congested and represents a major challenge in the total synthesis of the tubulysins natural products. Chemical synthetic strategies have been reported for the total synthesis of tubulysin natural products and their analogues. Initial efforts began with the synthesis of key structural tubulysin fragments Tuv and Tup by Höfle and Wipf, which are sterically complex amino acid residues present in the tubulysin scaffold. These early fragment syntheses laid a crucial foundation for developing the total syntheses of the parent compounds and their derivatives.[47,50] Building on these, Ellman and co-workers reported the first total synthesis of tubulysin D, one of the most potent members of the tubulysin family of natural products. The synthesis involved 16 steps, with a final target compound obtained in 13% overall yield.[51] In parallel, Wipf and co-workers reported the total asymmetric synthesis of N_{14}-desacetoxytubulysin in 20 steps with 2.1% overall yield, and noted that the N,O-acetal fragment is not essential for inhibitory activity. This natural product was later named as tubulysin M.[52] Also in 2007, Zanda and co-workers reported the total synthesis of tubulysin U and V up to 30% yield by utilizing a diastereoselective multicomponent reaction and stereocontrolled catalysis for the synthesis of unusual amino acids, tubuvaline and tubuphenylaniane.[53] Out of the tubulysin family of natural products, Tubulysin M is one of the most promising candidates, composed of *N*-methyl pipecolic acid, isoleucine, tubuvaline, and tubuphenylalanine fragments for the treatment of solid tumour or multidrug-resistant carcinoma with an IC_{50} in the low nM range of 0.02 nM. In 2016, K.C. Nicolaou and co-workers synthesised various tubulysin analogues with structural modification of all fragments. Their studies suggested retention of the *N*-methyl pipecolic acid fragment for tubulysin activity, as it showed narrow tolerance. The tubuvaline fragment has demonstrated tolerance to aromatic groups, whereas the tubuphenylalanine fragment was not fully explored.[54] However, the clinical development of tubulysins is limited due to the structural

complexity, limited natural supply, robust multistep syntheses and purification, poor yield, lack of scalable synthetic methods, and instability of molecules in biological systems. To improve the scalable synthesis of Tubulysin M, preliminary efforts focused on the synthesis of tubuvaline and tubuphenylalanine fragments, but the robust multistep synthetic routes with low overall yields remain the major challenge. [55,56]

1.12 3D Tumor spheroid model

Clinical candidates in the drug discovery program have to go through the preclinical and clinical phases.[57] In the preclinical phase, novel clinical candidates are initially evaluated *in vitro*, followed by *in vivo* testing to understand the pharmacokinetic, pharmacodynamic, and toxicity profiles.[58] *In vitro* assays mainly rely on a 2D cell culture model that shows a rapid and uncontrolled growth phenotype. However, 2D cell culture-based assays are generally accountable for high drug failures in preclinical trials, as they fail to recapitulate the complex and heterogeneous tumour microenvironment (TME) observed in tumours of *in vivo* models.[59] TME consists of various cancerous and non-cancerous cell types, such as fibroblasts, immune cells, mesenchymal cells, and endothelial cells that play a specific role in the structure and function of the tumour.[60] These limitations can be overcome by the development of 3D cancer spheroids, which are regarded as a promising platform for *in vitro* drug screening. 3D spheroid models mimic the tumour microenvironment and the complexity of tumour biology, and are also an ideal model for screening potential drug candidates.[61] They possess various features like cell-cell interactions, extracellular matrix (ECM) interactions, and hypoxic regions observed in patient solid tumours.[62] These features adequately recapitulate the architecture and tumour pathobiology *in vivo*. 3D Spheroid models are now widely used in drug discovery programmes as an essential addition to 2D culture models before progressing to animal trials. Various methods to generate 3D spheroid models are divided broadly into scaffold-free and scaffold-based methods.[63] Scaffold-free methods, such as hanging drop, liquid drop, micromolding, forced floating, and pellet culture, generate

spheroids without the use of biomaterials. The spheroids generated using scaffold-free methods are non-homogeneous and non-uniform, thus accounting for reproducibility and standardization issues.[64] Scaffold-based methods, such as gel embedding, extrusion-based, and microfluidics, generate 3D spheroids using natural or artificial matrices that allow crosstalking between cells via physical or chemical reactions. The existing methods generate a spheroid that offers various advantages over 2D models, but have their limitations with high cost and complex techniques.[65]

1.13 References

1. Bray F, Laversanne M, Sung H, et al. Global cancer statistics 2022: GLOBOCAN estimates of incidence and mortality worldwide for 36 cancers in 185 countries. *CA Cancer J Clin*. 2024, 74, 229–263. doi:10.3322/caac.21834.

2. Maeda H, Khatami M. Analyses of repeated failures in cancer therapy for solid tumors: Poor tumor-selective drug delivery, low therapeutic efficacy, and unsustainable costs. *Clin Transl Med*. 2018, 7, 1–20. doi:10.1186/s40169-018-0185-6.

3. Corrado G, Salutari V, Palluzzi E, Distefano MG, Scambia G, Ferrandina G. Optimizing treatment in recurrent epithelial ovarian cancer. *Expert Rev Anticancer Ther*. 2017, 17, 1147–1158. doi:10.1080/14737140.2017.1398088.

4. Kurbegovic S, Berg KD, Thomsen FB, et al. The risk of biochemical recurrence for intermediate-risk prostate cancer after radical prostatectomy. *Scand J Urol*. 2017, 51, 450–456. doi:10.1080/21681805.2017.1356369.

5. Chihara D, Fanale MA, Miranda RN, et al. The survival outcome of patients with relapsed/refractory peripheral T-cell lymphoma-not otherwise specified and angioimmunoblastic T-cell lymphoma. *Br J Haematol*. 2017, 176, 750–758. doi:10.1111/bjh.14477.

6. Zhang Y, Shen H, Liao K, et al. Case Report : Prostate adenocarcinoma with mucinous features of normal-level serum psa, atypical imaging, biopsy-negative, and peculiar urethrocystoscopic manifestation. *Front Oncol.* 2020, 10, 1–6. doi:10.3389/fonc.2020.504381.

7. Appleton L, Wyatt D, Perkins E, et al. The impact of prostate cancer on men's everyday life. *Eur J Cancer Care*. 2015, 24, 71–84. doi:10.1111/ecc.12233.

8. Goode EA, Wang N, Munkley J. Prostate cancer bone metastases biology and clinical management. *Oncol Lett*. 2023, 25, 1–18. doi:10.3892/ol.2023.13749.

9. Gudmundsson J, Sigurdsson JK, Stefansdottir L, et al. Genome-wide associations for benign prostatic hyperplasia reveal a genetic correlation with serum levels of PSA. *Nat Commun*. 2018, 9, 1–8. doi:10.1038/s41467-018-06920-9.

10. Krilaviciute A, Becker N, Lakes J, et al. Digital rectal examination is not a useful screening test for prostate cancer. *Eur Urol Oncol*. 2023, 6, 566–573. doi:10.1016/j.euo.2023.09.008.

11. Dutt SS, Gao AC. Molecular mechanisms of castration-resistant prostate cancer progression. *Futur Oncol*. 2009, 5, 1403–1413. doi:10.2217/fon.09.117.

12. Zhao M, Wang R, Li B, et al. Precise in vivo inflammation imaging using in situ responsive cross-linking of glutathione-modified ultra-small NIR-II lanthanide nanoparticles. *Angew Chemie*. 2019, 131, 2072–2076. doi:10.1002/ange.201812878.

13. Cheung S, O'Shea DF. Directed self-assembly of fluorescence responsive nanoparticles and their use for real-time surface and cellular imaging. *Nat Commun*. 2017, 8, 1–12. doi:10.1038/s41467-017-02060-8.

14. Jun J V., Chenoweth DM, Petersson EJ. Rational design of small

molecule fluorescent probes for biological applications. *Org Biomol Chem*. 2020, 18, 5747–5763. doi:10.1039/d0ob01131b.

15. Cao J, Zhu B, Zheng K, et al. Recent progress in NIR-II contrast agent for biological imaging. *Front Bioeng Biotechnol*. 2020, 7, 1–21. doi:10.3389/fbioe.2019.00487.

16. Hong G, Antaris AL, Dai H. Near-infrared fluorophores for biomedical imaging. *Nat Biomed Eng*. 2017, 1, 1–22. doi:10.1038/s41551-016-0010.

17. Zhao J, Zhong D, Zhou S. NIR-I-to-NIR-II Fluorescent nanomaterials for biomedical imaging and cancer therapy. *J Mater Chem B*. 2018, 6, 349–365. doi:10.1039/c7tb02573d.

18. Derks YHW, Löwik DWPM, Sedelaar JPM, et al. PSMA-Targeting agents for radio-and fluorescence-guided prostate cancer surgery. *Theranostics*. 2019, 9, 6824–6839. doi:10.7150/thno.36739.

19. Miyahira AK, Soule HR. The history of prostate-specific membrane antigen as a theranostic target in prostate cancer: The cornerstone role of the prostate cancer foundation. *J Nucl Med*. 2022, 63, 331–338. doi:10.2967/jnumed.121.262997.

20. Wang F, Li Z, Feng X, Yang D, Lin M. Advances in PSMA-targeted therapy for prostate cancer. *Prostate Cancer Prostatic Dis*. 2022, 25, 11–26. doi:10.1038/s41391-021-00394-5.

21. Chang SS. Overview of prostate-specific membrane antigen. *Rev Urol*. 2004, 6, S13–S18.

22. Krishnan MA, Pandit A, Sharma R, Chelvam V. Imaging of prostate cancer: Optimizing affinity to prostate specific membrane antigen by spacer modifications in a tumor spheroid model. *J Biomol Struct Dyn*. 2022, 40, 9909–9930. doi:10.1080/07391102.2021.1936642.

23. Eiber M, Fendler WP, Rowe SP, et al. Prostate-specific

membrane antigen ligands for imaging and therapy. *J Nucl Med*. 2017, 58, 67S–76S. doi:10.2967/jnumed.116.186767.

24. Psimadas D, Valotassiou V, Alexiou S, Tsougos I, Georgoulias P. Radiolabeled mAbs as molecular imaging and/or therapy agents targeting PSMA. *Cancer Invest*. 2018, 36, 118–128. doi:10.1080/07357907.2018.1430816.

25. Wang F, Li Z, Feng X, Yang D, Lin M. Advances in PSMA-targeted therapy for prostate cancer. *Prostate Cancer Prostatic Dis*. 2021, 8, 1–16. doi:10.1038/s41391-021-00394-5.

26. Hillier SM, Maresca KP, Lu G, et al. ^{99m}Tc-Labeled small-molecule inhibitors of prostate-specific membrane antigen for molecular imaging of prostate cancer. *J Nucl Med*. 2013, 54, 1369–1376. doi:10.2967/jnumed.112.116624.

27. Nguyen N, Zimmerman CN, Barrett JA, Eckelman WC. Preclinical evaluation of novel glutamate-urea-lysine analogs that target prostate specific membrane antigen as molecular imaging pharmaceuticals for prostate cancer. *Cancer Res*. 2014, 69, 6932–6940. doi:10.1158/0008-5472.CAN-09-1682.

28. Juzeniene A, Stenberg VY, Bruland ØS, Larsen RH. Preclinical and clinical status of PSMA-targeted alpha therapy for metastatic castration-resistant prostate cancer. *Cancers (Basel)*. 2021, 13, 1–25. doi:10.3390/cancers13040779.

29. Griffeth LK. Use of PET/CT scanning in cancer patients: Technical and practical considerations. *Baylor Univ Med Cent Proc*. 2005, 18, 321–330. doi:10.1080/08998280.2005.11928089.

30. Alavi A, Huang SS. Positron emission tomography in medicine: An overview. *Cancer Imaging*. 2007, 31, 39–44. doi:10.1016/B978-012374212-4.50009-2.

31. Palot Manzil FF, Kaur H, Szabados L. Gallium-68 prostate-

specific membrane antigen positron emission tomography: A practical guide for radiologists and clinicians. *Cureus*. 2022, 14, 22917–22924 doi:10.7759/cureus.22917.

32. Khalil MM, Tremoleda JL, Bayomy TB, Gsell W. Molecular SPECT imaging: An overview. *Int J Mol Imaging*. 2011, 20, 1–15. doi:10.1155/2011/796025.

33. Tachatumvitoon K, Preuksarattanawut C, Tippayamontri T, Khomein P. Tc-99m Labeled PSMA-617 as a potential SPECT radiotracer for prostate cancer diagnostics: Complexation optimization and its in vitro/vivo evaluation. *Bioorganic Med Chem*. 2025, 118, 118058–118061. doi:10.1016/j.bmc.2024.118058.

34. Hanahan D, Weinberg RA. Hallmarks of cancer: The next generation. *Cell*. 2011, 144, 646–674. doi:10.1016/j.cell. 2011.02.013.

35. Saxton RA, Sabatini DM. Erratum: mTOR Signalling in growth, metabolism, and disease. *Cell* 2017, 168, 960–976. doi:10.1016/j.cell.2017.03.035.

36. Pylayeva-Gupta Y, Grabocka E, Bar-Sagi D. RAS Oncogenes: Weaving a tumorigenic web. *Nat Rev Cancer*. 2011, 11, 761–774. doi:10.1038/nrc3106.

37. Kontomanolis EN, Koutras A, Syllaios A, et al. Role of oncogenes and tumor-suppressor genes in carcinogenesis: A review. *Anticancer Res*. 2020, 40, 6009–6015. doi:10.21873/anticanres.14622.

38. Paier CRK, Maranhão SS, Carneiro TR, et al. Natural products as new antimitotic compounds for anticancer drug development. *Clinics*. 2018, 73, 1–11. doi:10.6061/clinics/2018/E813S.

39. Wu Z, Gao L, Ashraf MA, Nan Q. Interaction between actin and microtubules during plant development. *Cytoskeleton*. 2025, 6,

1–9. doi:10.1002/cm.22029.

40. Muroyama A, Lechler T. Microtubule organization, dynamics and functions in differentiated cells. *Dev*. 2017, 144, 3012–3021. doi:10.1242/dev.153171.

41. Risinger AL, Giles FJ, Mooberry SL. Microtubule dynamics as a target in oncology. *Cancer Treat Rev*. 2009, 35, 255–261. doi:10.1016/j.ctrv.2008.11.001.

42. Wang X, Gigant B, Zheng X, Chen Q. Microtubule-targeting agents for cancer treatment: Seven binding sites and three strategies. *MedComm Oncol*. 2023, 2, 12–20. doi:10.1002/mog2.46.

43. Cai J, He M, Wang Y, et al. Discovery of a novel microtubule destabilizing agent targeting the colchicine site based on molecular docking. *Biochem Pharmacol*. 2025, 234, 116804–116816. doi:10.1016/j.bcp.2025.116804.

44. Čermák V, Dostál V, Jelínek M, et al. Microtubule-targeting agents and their impact on cancer treatment. *Eur J Cell Biol*. 2020, 99, 151075–151081 doi:10.1016/j.ejcb.2020.151075.

45. Drača D, Mijatović S, Krajnović T, Kaluđerović GN, Wessjohann LA, Maksimović-Ivanić D. Synthetic tubulysin derivative, tubugi-1, against invasive melanoma cells: The cell death triangle. *Anticancer Res*. 2019, 39, 5403-5415. doi:10.21873/anticanres.13734.

46. Alqarni A, Elnakady YA, Alsadhan L, et al. Prospective mechanism of action of the tubulysin synthetic derivative (TAM 1344) in HCT116 colon cancer cell line. *J King Saud Univ - Sci*. 2023, 35, 102824–102830. doi:10.1016/j.jksus.2023.102824.

47. Sasse F, Steinmetz H, Heil J, Hofle G, Reichenbach H. Tubulysins, new cytostatic peptides from myxobacteria acting on microtubuli. Production, isolation, physico-chemical and

biological properties. *J Antibiot (Tokyo)*. 2000, 53, 879–885. doi:10.7164/antibiotics.53.879.

48. Murray BC, Peterson MT, Fecik RA. Chemistry and biology of tubulysins: Antimitotic tetrapeptides with activity against drug-resistant cancers. *Nat Prod Rep*. 2015, 32, 654–662. doi:10.1039/c4np00036f.

49. Vishwanatha TM, Giepmans B, Goda SK, Dömling A. Tubulysin synthesis featuring stereoselective catalysis and highly convergent multicomponent assembly. *Org Lett*. 2020, 22, 5396–5400. doi:10.1021/acs.orglett.0c01718.

50. Wipf P, Takada T, Rishel MJ. Synthesis of the tubuvaline-tubuphenylalanine (Tuv-Tup) fragment of tubulysin. *Org Lett*. 2004, 6, 4057–4060. doi:10.1021/ol048252i.

51. Peltier HM, McMahon JP, Patterson AW, Ellman JA. The total synthesis of tubulysin D. *J Am Chem Soc*. 2006, 128, 16018–16019. doi:10.1021/ja067177z.

52. Wipf P, Wang Z. Total synthesis of N_{14}-desacetoxytubulysin H. *Org Lett*. 2007, 38, 7–9. doi:10.1002/chin.200735186.

53. Sani M, Fossati G, Huguenot F, Zanda M. Total synthesis of tubulysins U and V. *Angew Chem Int Ed*. 2007, 46, 3526–3529. doi:10.1002/anie.200604557.

54. Nicolaou KC, Yin J, Mandal D, et al. Total synthesis and biological evaluation of natural and designed tubulysins. *J Am Chem Soc*. 2016, 138, 1698–1708. doi:10.1021/jacs.5b12557

55. Reddy RB, Dudhe P, Chauhan P, Sengupta S, Chelvam V. Synthesis of tubuphenylalanine and epi-tubuphenylalanine via regioselective aziridine ring opening with carbon nucleophiles followed by hydroboration-oxidation of 1,1-substituted amino alkenes. *Tetrahedron*. 2018, 74, 6946–6953. doi:10.1016/j.tet.2018.10.024.

56. Reddy RB, M V, Krishnan MA, Chelvam V. Synthesis of tubuvaline (Tuv) fragment of tubulysin via diastereoselective dihydroxylation of homoallylamine. *Synth Commun*. 2021, 51, 797–809. doi:10.1080/00397911.2020.1855355.

57. Paul SM, Mytelka DS, Dunwiddie CT, et al. How to improve RD productivity: The pharmaceutical industry's grand challenge. *Nat Rev Drug Discov*. 2010, 9, 203–214. doi:10.1038/nrd3078.

58. Issa NT, Wathieu H, Ojo A, Byers SW, Dakshanamurthy S. Drug Metabolism in Preclinical Drug Development: A survey of the discovery process, toxicology, and computational tools. *Curr Drug Metab*. 2017, 18, 556–565. doi:10.2174/1389200218666170316093301.

59. Saglam-Metiner P, Gulce-Iz S, Biray-Avci C. Bioengineering-inspired three-dimensional culture systems: Organoids to create tumor microenvironment. *Gene*. 2019, 686, 203–212. doi:10.1016/j.gene.2018.11.058.

60. Sant S, Johnston PA. The production of 3D tumor spheroids for cancer drug discovery. *Drug Discov Today Technol*. 2017, 23, 27–36. doi:10.1016/j.ddtec.2017.03.002.

61. Pound P, Ritskes-Hoitinga M. Is it possible to overcome issues of external validity in preclinical animal research? Why most animal models are bound to fail. *J Transl Med*. 2018, 16, 1–8. doi:10.1186/s12967-018-1678-1.

62. Li J, Zhou Y, Chen W, et al. A novel 3D in vitro tumor model based on silk fibroin/chitosan scaffolds to mimic the tumor microenvironment. *ACS Appl Mater Interfaces*. 2018, 10, 36641–36651. doi:10.1021/acsami.8b10679.

63. Barbosa MAG, Xavier CPR, Pereira RF, Petrikaitė V, Vasconcelos MH. 3D Cell culture models as recapitulators of the tumor microenvironment for the screening of anticancer drugs. *Cancers (Basel)*. 2022, 14, 1–30. doi:10.3390/cancers14010190.

64. Zanoni M, Piccinini F, Arienti C, et al. 3D Tumor spheroid models for in vitro therapeutic screening: A systematic approach to enhance the biological relevance of data obtained. *Sci Rep*. 2016, 6, 1–11. doi:10.1038/srep19103.

65. Salinas-Vera YM, Valdés J, Pérez-Navarro Y, et al. Three-dimensional 3D culture models in gynecological and breast cancer research. *Front Oncol*. 2022, 12, 1–13. doi:10.3389/fonc.2022.826113.

Chapter 2

Review of past work and problem formulation

2.1 Prostate-specific membrane antigen

Prostate-specific membrane antigen (PSMA) is a type II transmembrane glycoprotein highly expressed on the surface of prostate cancer cells, particularly in advanced and metastatic stages, but its expression in normal tissues is limited.[1] Due to its elevated and specific expression, PSMA has become a well-validated target for prostate cancer (PCa) imaging and therapy.[2] Over the past two decades, significant progress has been made in the development of PSMA-targeted ligands for diagnostic and therapeutic applications.

2.1.1 PSMA-Based ligand development

Advancements in the field of PCa have revealed that the PSMA targeting ligands or inhibitors attached to various diagnostics and therapeutics cargoes via peptidic spacers hold promise for radio and optical imaging in cancer diagnosis and treatment. PSMA receptor exhibits the property of clathrin-mediated endocytosis after binding with the targeting moiety.[3] This property has led to the development of several PSMA targeting agents, including monoclonal antibodies, small molecule ligands, and DNA aptamers.[4] Several small-molecule inhibitors for PSMA with documented nanomolar binding affinities, such as 2-[3-(1,3-dicarboxypropyl)ureido] pentanedioic acid (DUPA), have shown promising results during clinical studies.[5] Glutamate-ureido targeted imaging agents, such as PSMA-617 and PSMA-11, have shown promising results in preclinical and clinical trials for prostate cancer.[6] In recent years, promising results were found for radio-labelled peptides with beta emitters, leading to the FDA approval of ^{177}Lu-PSMA-617 and [^{177}Lu]Lu-DOTA-TATE as compassionate therapeutic agents for the treatment of end-stage metastatic castration resistant prostate cancer (mCRPC).[7,8] The alpha-emitter peptides, such as [^{225}Ac]Ac-PSMA-617, are limited in their clinical use as they have low availability due to complex production, limited precursor material, handling difficulties

because of the long decay chain, and challenging transportation, resulting in gamma emitters being an alternative and promising source for diagnosis.[9] The gamma emitter-based radioactive bioconjugate was designed using the DUPA ligand attached with peptidic spacers to ^{99m}Tc, showing promising results during an *in vitro* binding affinity study with a K_d of 14 nM. Additionally, *in vivo* studies revealed a %ID/g of 11.3,[10] supporting the development of a PSMA-targeting ligand linked via peptidic spacer to ^{99m}Tc. Furthermore, the recent identification of a third hydrophobic binding pocket suggests that incorporating aromatic moieties in the peptidic spacer could enhance binding affinity.

2.2 Tubulysin

Microtubule assembly, composed of tubulin proteins, is an essential target for anticancer drugs. Inhibition of microtubule formation by targeting the tubulin protein induces apoptosis, leading to cell death. Tubulysin M, with an IC_{50} of 0.02 nM against cancer cells, has emerged as a promising drug candidate to treat multidrug-resistant and aggressive tumors. The high potency of the tubulin inhibitors to kill cancer cells made them a first choice in developing targeted drug delivery systems. However, the clinical development is hampered due to scarce natural supply, structural complexity, off-site toxicity, and instability of antibody drug conjugates in the blood serum. In one of the human clinical trials of a natural tubulin inhibitor for anticancer therapy, the drug failed to elicit the expected anticancer activity in the human body due to probable degradation in the blood serum by proteases. Various synthetic strategies have been developed to address the complexity of tubulysin molecules. Initial efforts focused on synthesizing key fragments such as Tuv and Tup, as reported by Höfle and Wipf.[11,12] Ellman and co-workers achieved the first total synthesis of tubulysin D in 20 steps with a 13% overall yield.[13] Later, Wipf and co-workers completed a 20-step asymmetric total synthesis of N_{14}-desacetoxytubulysin (tubulysin M) with a 2.1% overall yield, demonstrating that the N,O-acetal fragment is not essential for activity.[14] In 2016, K.C. Nicolaou and co-workers reported that the *N*-methyl

pipecolic acid fragment is crucial for tubulysin activity due to its narrow tolerance, while the tubuvaline fragment can accommodate aromatic substitutions; the tubuphenylalanine fragment, however, remained less explored, but clinical development was limited due to structural complexity.[15] Our research group developed efficient synthetic routes for the tubuvaline and tubuphenylalanine fragments, to enable scalable synthesis and improve pharmacokinetic profiles, facilitating further analogue development; however, robust synthesis remains the major challenge.[16,17] To address this issue, systemic modification of the tubulysin fragment was carried out, and a novel third-generation tubulysin derivative was developed, named Tub_01, without tubuvaline and tubuphenylalanine fragments. The simplified tubulysin framework enables single-step purification, significantly enhancing its practicality for large-scale production and potential therapeutic application.

2.3 3D Spheroid model

Drug development is an expensive and time-consuming process regulated at each stage. The increased attrition rate of 90% during the preclinical and clinical stages affects productivity and cost collectively, adversely affecting the drug discovery programme.[18] This primary failure of drugs is attributed to the reliance on a 2D monolayer cell culture model during early preclinical studies to test the efficacy of novel compounds. This 2D monolayer cell model has significant drawbacks, such as a planar structure resulting in homogeneous drug distribution and the absence of CO_2, O_2, and a nutrient gradient. In the past few years, to address this issue, 3D models have gained attention for their ability to mimic the tumour microenvironment closely, thus bridging the gap between 2D monolayer cell models and *in vitro* studies.[19] The 3D models offer cell population differentiation, cell-cell interaction, cell-matrix interaction, drug diffusion gradient, CO_2, O_2, and nutrient gradient, thereby mimicking complex tumour architecture present *in vivo.* These 3D spheroid models can be generated using techniques like hanging drop, spinner flask, pellet culture, microfluidics, and gel embedding.[20] The existing methods are associated with multiple

drawbacks, like non-homogeneous and non-uniform spheroid formation, thus accounting for reproducibility and standardization issues. Moreover, the generation of uniform spheroids is often related to complex techniques and high cost. In our laboratory, we have developed the microsphere platform to generate uniform spheroids with the desired diameter in a few days at low cost. [21]

2.4 References

1. Miyahira AK, Soule HR. The history of prostate-specific membrane antigen as a theranostic target in prostate cancer: The cornerstone role of the prostate cancer foundation. *J Nucl Med*. 2022, 63, 331–338. doi:10.2967/JNUMED.121.262997.

2. Eiber M, Fendler WP, Rowe SP. Prostate-specific membrane antigen ligands for imaging and therapy. *J Nucl Med*. 2017, 58, 67S–76S. doi:10.2967/jnumed.116.186767.

3. Neale JH, Yamamoto T. N-Acetylaspartylglutamate (NAAG) and glutamate carboxypeptidase II: An abundant peptide neurotransmitter-enzyme system with multiple clinical applications. *Prog Neurobiol*. 2020, 184, 101722–101731. doi:10.1016/j.pneurobio.2019.101722.

4. Wang F, Li Z, Feng X, Yang D, Lin M. Advances in PSMA-targeted therapy for prostate cancer. *Prostate Cancer Prostatic Dis*. 2022, 25, 11–26. doi:10.1038/s41391-021-00394-5.

5. Kularatne SA, Wang K, Santhapuram HKR, Low PS. Prostate-specific membrane antigen targeted imaging and therapy of prostate cancer using a PSMA inhibitor as a homing ligand. *Mol Pharm*. 2009, 6, 780–789. doi:10.1021/mp900069d.

6. Kopka K, Benešová M, Bařinka C, Haberkorn U, Babich J. Glu-ureido-based inhibitors of prostate-specific membrane antigen: Lessons learned during the development of a novel class of low-molecular-weight theranostic radiotracers. *J Nucl Med*. 2017, 58, 17–26. doi:10.2967/jnumed.116.186775.

7. Bodei L, Herrmann K, Schöder H, Scott AM, Lewis JS. Radiotheranostics in oncology: Current challenges and emerging opportunities. *Nat Rev Clin Oncol*. 2022, 19, 534–550. doi:10.1038/s41571-022-00652-y.

8. Rasul S, Hacker M, Kretschmer-Chott E, et al. Clinical outcome of standardized ^{177}Lu-PSMA-617 therapy in metastatic prostate cancer patients receiving 7400 MBq every 4 weeks. *Eur J Nucl Med Mol Imaging*. 2020, 47, 713–720. doi:10.1007/s00259-019-04584-1.

9. Santos JF, Braz MT, Raposinho P, et al. Synthesis and preclinical evaluation of PSMA-targeted ^{111}In-radioconjugates containing a mitochondria-tropic triphenylphosphonium carrier. *Mol Pharm*. 2024, 21, 216–233. doi:10.1021/acs.molpharmaceut.3c00787.

10. Kularatne SA, Zhou Z, Yang J, Post CB, Low PS. Design, synthesis, and preclinical evaluation of prostate-specific membrane antigen-targeted (99m)Tc-radioimaging agents. *Mol Pharm*. 2009, 6, 790–800. doi:10.1021/mp9000712.

11. Sasse F, Steinmetz H, Heil J, Hofle G, Reichenbach H. Tubulysins, new cytostatic peptides from myxobacteria acting on microtubuli. Production, isolation, physico-chemical and biological properties. *J Antibiot (Tokyo)*. 2000, 53, 879–885. doi:10.7164/antibiotics.53.879.

12. Wipf P, Takada T, Rishel MJ. Synthesis of the tubuvaline-tubuphenylalanine (Tuv-Tup) fragment of tubulysin. *Org Lett*. 2004, 6, 4057–4060. doi:10.1021/ol048252i.

13. Peltier HM, McMahon JP, Patterson AW, Ellman JA. The total synthesis of tubulysin D. *J Am Chem Soc*. 2006, 128, 16018–16019. doi:10.1021/ja067177z.

14. Wipf P, Wang Z. Total Synthesis of N_{14}-Desacetoxytubulysin H. *ChemInform*. 2007, 38, 7–9. doi:10.1002/chin. 00735186.

15. Nicolaou KC, Yin J, Mandal D, et al. Total synthesis and biological evaluation of natural and designed tubulysins. *J Am Chem Soc*. 2016, 138, 1698–1708. doi:10.1021/jacs.5b12557.

16. Reddy RB, Dudhe P, Chauhan P, Sengupta S, Chelvam V. Synthesis of tubuphenylalanine and epi-tubuphenylalanine via regioselective aziridine ring opening with carbon nucleophiles followed by hydroboration-oxidation of 1,1-substituted amino alkenes. *Tetrahedron*. 2018, 74, 6946–6953. doi:10.1016/j.tet.2018.10.024.

17. Reddy RB, Vijay M, Krishnan MA, Chelvam V. Synthesis of tubuvaline (Tuv) fragment of tubulysin via diastereoselective dihydroxylation of homoallylamine. *Synth Commun*. 2021, 51, 797–809. doi:10.1080/00397911.2020.1855355.

18. Matthews H, Hanison J, Nirmalan N. "Omics"-informed drug and biomarker discovery: Opportunities, challenges and future perspectives. *Proteomes*. 2016, 4, 1–12. doi:10.3390/proteomes4030028.

19. Adjei I, Blanka S, Ugariogu SN, Matthews H, Hanison J, Nirmalan N. Modulation of the tumor microenvironment for cancer treatment: A biomaterials approach. *Int J Pharmacogn Chinese Med*. 2020, 4, 1–8. doi:10.3390/jfb6010081.

20. Salinas-Vera YM, Valdés J, Pérez-Navarro Y. Three-dimensional 3D culture models in gynaecological and breast cancer research. *Front Oncol*. 2022, 12, 1–13. doi:10.3389/fonc.2022.826113.

21. Krishnan MA, Chelvam V. Developing μsphereplatform using a commercial hairbrush: An agarose 3D culture platform for deep-tissue imaging of prostate cancer. *ACS Appl Bio Mater*. 2021, 4, 4254–4270. doi:10.1021/acsabm.1c00086.

Chapter 3

Design and synthesis of small-molecule ligand PSMA-targeted bioconjugate for the diagnosis of prostate cancer

3.1 Introduction

Prostate cancer (PCa) remains a significant challenge, accounting for 1.46 million new cases and 3.96 lakh deaths worldwide in the year 2022, making it the second most diagnosed cancer in men globally.[1] The current diagnosis of PCa often detects malignancy only after metastasis has occurred, resulting in delayed diagnosis. The widely used prostate-specific antigen (PSA) level[2] and digital rectal examination (DRE)[3] often results in limited specificity due to false positives, as elevated PSA levels are also related to non-cancerous clinical conditions like benign prostatic hyperplasia (BPH).[4] Apart from poor diagnosis, the current therapeutic modalities, like androgen deprivation therapy (ADT) and chemotherapy, have resulted in major drawbacks, causing therapeutic resistance and ultimately resulting in increased chances of tumour recurrence.[5] The use of radiation therapy and fluorescent image-guided surgery has shown significant improvement in mortality, particularly in patients with localized low or intermediate-stage tumours (Gleason score <7).[6] However, these approaches rely on the use of precise tumour visualization and targeted delivery agents to ensure accurate and effective treatment. Advancements in imaging modalities and molecular targeting strategies for intraoperative surgeries are crucial for early diagnosis and precise therapy, thereby eliminating off-target cytotoxicity and improving clinical efficacy.

The recent development of various radiopharmaceuticals using radionuclides (^{18}F, ^{64}Cu, ^{68}Ga, ^{99m}Tc, ^{111}In, and ^{11}C) for diagnosis has overcome the drawbacks of fluorescent imaging agents that were proven to be ineffective due to their excitation and emission wavelengths lying outside the biological transparency window, resulting in high

background noise, autofluorescence, and limited penetration depth.[7] However, the development of radiopharmaceutical agents majorly depends upon the correct radionuclide selection based on various factors such as half-life, permeability, effective chelation methodology, and off-target binding. However, technetium-99 (^{99m}Tc) and Gallium-68 (^{68}Ga) are favourable due to precise half-life, availability, biological stability, no nonspecific interaction in a biological system, ease of elimination, and chelation efficiency of 99.99%, resulting in low dosage administration to the patient, thereby reducing overall treatment cost.[8,9] These radionuclides are further attached to targeting agents via a peptidic linker for precise tumour visualization.

Prostate Specific Membrane Antigen (PSMA) is found to be 1000-fold over-expressed in PCa cells as compared to normal tissue, thus making it a promising biomarker.[10] Once bound to the targeting moiety, it can undergo clathrin-mediated endocytosis. This property has led to the development of various PSMA-targeted agents, including monoclonal antibodies, small-molecule ligands, and DNA aptamers.[11] PSMA, also known as *N*-acetyl-aspartyl-glutamate (NAAG) peptidase I, consists of three domains: outer, transmembrane, and the enzymatically active, largest domain that causes hydrolysis of γ-glutamyl derivatives of folic acid to release glutamate and liberation of *N*-acetyl aspartate and glutamate after proteolysis of neuropeptide NAAG.[12] This active site prediction resulted in the initial development of 2-(phosphonomethyl)pentanedioic acid (2-PMPA), an inhibitor of PSMA by Jackson et al. in 1996,[13] causing an extensive structural activity relationship study that resulted in the development of a new class of inhibitors, majorly belonging to three categories: urea, thiols, and phosphonates.[14] Among the three, glutamate-urea homodimer and glutamate-urea heterodimer are the most preferred classes for PSMA due to their sub-nanomolar binding affinity and impressive results *in vivo* with different radioisotopes.[15] The internal structure of the PSMA receptor comprises an S1′ glutamate recognition pocket, an S1 pocket, and two Zn^{2+} ions, along with an irregularly shaped 20 Å tunnel, which

forms a primary binding pocket that interacts with the targeting ligand.[16] Glutamate-ureido targeted imaging agents, such as PSMA-617 and PSMA-11, have shown auspicious data in preclinical and clinical trials for prostate cancer.[17] The small molecule radiolabelled ligand ^{177}Lu-PSMA-617 is being used in therapy for end-stage metastatic castration-resistant prostate cancer (mCRPC) patients.[18] Hence, developing a highly efficacious and sensitive PSMA targeting radioactive bioconjugate would address issues currently being faced in deep-tissue imaging and surgical guidance. The recent discovery of the remote hydrophobic pocket in the PSMA cavity, composed of β sheets, allows binding of a distantly placed aromatic moiety inside the PSMA cavity.[19] Exploration of the cavity suggested the introduction of a structural spacer that provides optimal length between the aromatic moiety and the targeting ligand for stable interaction with the hydrophobic pocket.[20] Based on this concept, we have designed a *tert*-butyl-protected aminoacetamide ligand consisting of a glutamic acid residue that binds in the S1′ glutamate recognition pocket of the PSMA receptor, and the remaining part of the inhibitor interacts with the S1 pocket. Introduction of one methylene carbon unit after the amide group resulted in new hydrogen bonding interactions with the glutamic acid side chain residue in the binding pocket of PSMA. Based on this observation, a small library of glutamate-based ligands containing an aminoacetamide moiety was designed. The most potent aminoacetamide-based ligand precursor **15a** was further attached to a spacer comprising a chelating linker to chelate radioactive isotope, ^{99m}Tc, for an early diagnosis of prostate cancer. Aromatic amino acids, which interact with the hydrophobic pocket, were introduced in the peptidic spacer to increase the stability of the bioconjugate in the PSMA pocket and are essential for increasing the binding affinity of the ligand. Moreover, to optimally place the aromatic moiety for interactions with the hydrophobic pocket, a long aliphatic carbon chain was incorporated into the spacer to appropriately separate the targeting ligand and aromatic moiety. *In vitro* binding affinity of the radioactive bioconjugate in the LNCaP cell line,

in the presence of 2-PMPA for competitive inhibition, revealed binding of the bioconjugate with high affinity in the $PSMA^+$ LNCaP cell line, with a K_d value in the low nM concentration.

3.2 Results and discussion

Active site prediction of the PSMA receptor facilitated the development of a novel class of urea-based PSMA targeting ligands that mimic their natural substrate. We designed a new PSMA-targeting ligand consisting of a glutamic acid moiety that interacts with the PSMA receptor at the S1′ pocket. The interactions of the newly designed inhibitors (Figure 3.1) at the PSMA active site were evaluated by molecular docking studies. The docking study of aminoacetamide ligand **1** shows the highest docking score of 13.96, followed by ligands **3** (13.63) and **2** (12.51), compared to JB7, the docking score of which is 16.38 (Table 3.1). Ligand **1,** with 9/7 hydrogen bonds at S1′/S1, shows a similar kind of interaction that was shown by JB7 with the amino acids Arg 210, Asn 257, Lys 699, Tyr 552, Tyr 700, and Glu 424 at the S1′ pocket of the PSMA receptor, suggesting its effective binding at the S1′ pocket. With the insertion of an extra methylene carbon, new interactions were observed with amino acid residues Arg 210, Glu 424, Arg 534, and Arg 536 (Table 3.2). The interaction between the carbonyl oxygen of ligand **1** and Tyr552 may be responsible for the higher binding affinity compared to other ligands, due to its position near the Zn atom, which accounts for the catalytic activity of PSMA. Ligand **3**, with 10/4 hydrogen bonds at S1'/S1, shows interactions with Arg 210, Asn 257, Lys 699, Tyr 552, and Glu 424, like interactions shown by JB7. Likewise, ligand **2**, with 7/6 hydrogen bonds at S1'/S1, shows interactions with Arg 210, Lys 699, Tyr 552, Tyr 700, and Glu 424, like interactions shown by JB7 (Table 3.2). Ligands **2** and **3** were found to be less potent compared to ligand **1**, as a smaller number of hydrogen bonding interactions were observed compared to ligand **1**. In ligand **3**, interactions with Tyr 700 and Arg 536; and for ligand **2**, interactions with Asn 257 of the S1′ pocket were absent, whereas these interactions were observed with ligand **1** and JB7.

Table 3.1 Docking scores of aminoacetamide ligands **1**–**10** and JB7.

Aminoacetamide Ligands	Docking Scores	Rank
JB7	16.38	1
1	13.96	2
3	13.63	3
2	12.51	4
6	12.01	5
9	11.99	6
8	11.45	7
4	11.35	8
7	10.94	9
10	10.79	10
5	10.67	11

Table 3.2 Hydrogen bonding interactions of aminoacetamide ligands **1–10** and JB7 with GCPII protein, with the bond distance of interaction represented in Å.

Site	Amino acid residue	JB7 H-bonding interaction with GCPII in Å from PDB 4NGM	JB7 post or re-docking interactions with GCPII in Å	H-bonding interactions of ligands 1-10 with GCPII protein in Å									
				1	3	2	6	9	8	4	7	10	5
' Site of GCPII (Hydrophilic pocket)	Arg 210	2.8	2.3	2.72 2.05	1.89 2.47	1.87	1.74 2.41	2.03	2.12	2.34	2.18	2.03	1.86 2.49
	Asn 257	2.89	2.03	1.90	1.94 2.40		1.89 2.70	1.92	2.72 1.91	2.32 2.73	2.00 2.41	1.78	1.93
	Lys 699	2.7	2.47, 2.06	1.83	1.87 2.52	2.08	1.98	2.59 1.79		2.25, 2.55		1.88	1.9
	Tyr 552	2.63	2.65	1.72	1.89	2.66 1.79	2.33 2.54	2.64	2.27	1.7	2.35	2.45	2.16
	Tyr 700	2.53	1.8	2.73		1.84	2.2		2.32 2.06	2.27		2.69	2.72
	Glu 424	3.01		2.06 2.03	2.04 1.85	2.79 1.85	2.67 2.23	2.41 2.01	2.1	1.91			
	Glu 425			2.01	2.13		2		2.55	2.55			2.13 2.74 2.44
Site of GCPII (Hydrophobic che)	Gly 518	3.04 3.05	1.88	2.4	2.15				1.76	2.44 1.85	1.94	1.9	
	Asn 519	2.98	2.16	2.10	2.47 2.07		1.99	1.81	2.04	2.28	2.08		
	Arg 534	2.84	2.03	1.91 1.92	2.09		2.21	2.03	2.03	1.83 2.06	2.04	2.53	
	Arg 536	2.99 3.0	2.32 , 1.99, 1.96	2.21 2.21					2.68 2.57 1.90			2.61 2.08 2.31	
	Asp 453			2.51		2.57							
	Asp 387					2.56 2.72					2.37		
	Ser 454					2.29					1.72 2.30 1.89		
	Tyr 549					2.34		1.8			2		
	Ser 517					2.03		2.23		2.05			
	Arg 463								2.4				
Total number of hydrogen bonds at S1'/S1		**6/6**	**6/6**	**9/7**	**10/4**	**7/6**	**11/2**	**7/4**	**8/7**	**9/6**	**4/8**	**5/5**	**9/0**

3.2.1 Chemical synthesis of carboxyester-protected aminoacetamide precursors 14a–j

The protected aminoacetamide precursors **14a**–**j** were chemically synthesized as shown in scheme 3.1. Initially, nucleophilic substitution reactions were carried out between the salts of benzyl-protected glutamic acid **11a**–**c** and α-chloroacetyl chloride in the presence of sodium bicarbonate ($NaHCO_3$) at 0 °C for 1.5 h in a biphasic DCM/H_2O solvent system to afford the intermediates **12a**–**c** in 94–96% yields. In the next step, intermediates **12a**–**c** were reacted with the di-*tert*-butyl protected glutamic acid salts **13a**–**j**, utilizing potassium iodide (KI) as an activating agent and potassium carbonate (K_2CO_3) as base in dry THF under reflux conditions for 12 h to synthesize the precursors **14a**–**j** via substitution of chlorine in the chloroacetyl group. The most potent aminoacetamide ligands **1**–**3** were then synthesized as shown in scheme 3.2. In the first step, the debenzylation reaction on **14a**–**c** was carried out using palladium on carbon (Pd/C) (30 mol%), in the presence of H_2 gas in MeOH for 48 h to afford **15a**–**c** in 72–78% yields. In the final step, the tris(*tert*-butylcarboxy) group was deprotected under acidic conditions using a mixture of trifluoroacetic acid (TFA) and CH_2Cl_2 (DCM) (1:1) at room temperature to afford the inhibitors **1**–**3** in 95–98% yields. The synthesized ligands **1**–**3** were then biologically evaluated for binding with PSMA protein using a fluorescent-based enzyme inhibition assay to determine half-inhibitory concentration (IC_{50}).

3.2.2 *In vitro* GCPII inhibition assay

After the successful synthesis of PSMA or glutamate carboxypeptidase (GCPII) inhibitors **1**–**3**, *in vitro* evaluation of the top-ranking aminoacetamide-based inhibitors **1**–**3** was performed using the PSMA protein isolated from $PSMA^+$ LNCaP cancer cell line. Briefly, the membrane portion of the PSMA enzyme was extracted from the $PSMA^+$ LNCaP cell line by following a reported protocol.[21] The isolated PSMA enzyme was incubated with various concentrations of the inhibitors **1–3** in the presence of a competitive inhibitor, *N*-acetylaspartylglutamate (NAAG). The amount of glutamic acid released by the hydrolysis of

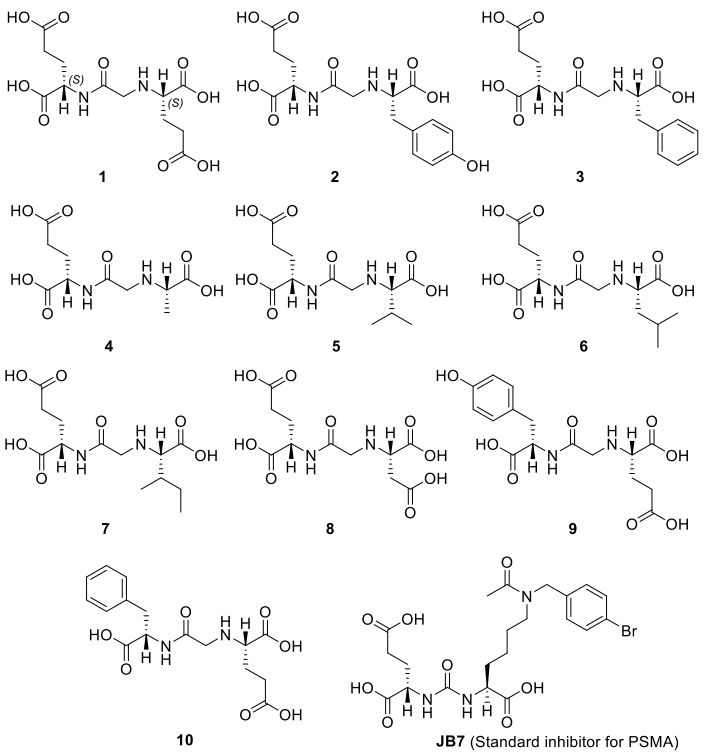

Figure 3.1 Structure of newly designed aminoacetamide inhibitors **1**–**10** and JB7.

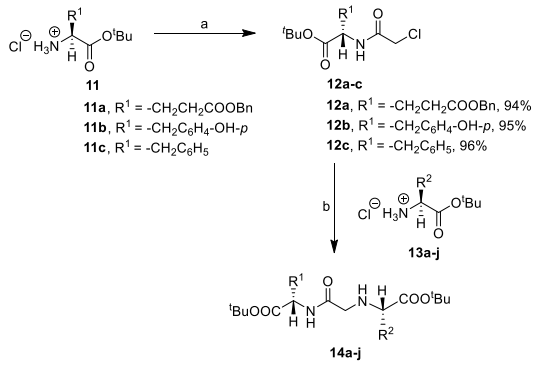

14a, R^1 = -CH_2CH_2COOBn; R^2 = -$CH_2CH_2COO^tBu$, 80%
14b, R^1 = -CH_2CH_2COOBn; R^2 = -$CH_2C_6H_4$-OH-*p*, 75%
14c, R^1 = -CH_2CH_2COOBn; R^2 = -$CH_2C_6H_5$, 70%
14d, R^1 = -CH_2CH_2COOBn; R^2 = -CH_3, 72%
14e, R^1 = -CH_2CH_2COOBn; R^2 = -$CH(CH_3)_2$, 75%
14f, R^1 = -CH_2CH_2COOBn; R^2= -$CH_2CH(CH_3)_2$, 82%
14g, R^1 = -CH_2CH_2COOBn; R^2 = -$CH(CH_3)CH_2CH_3$, 86%
14h, R^1 = -CH_2CH_2COOBn; R^2 = -CH_2O^tBu, 85%
14i, R^1 = -$CH_2C_6H_4$-OH-*p*; R^2 = -$CH_2CH_2COO^tBu$, 85%
14j, R^1 = -$CH_2C_6H_5$; R^2= -$CH_2CH_2COO^tBu$, 80%

Scheme 3.1 Synthesis of aminoacetamide precursors **14a**–**j**. Reagents and conditions: (a) α-Chloroacetyl chloride, $NaHCO_3$, DCM/H_2O, 0 °C to rt, 1.5 h; (b) KI, K_2CO_3, dry THF, reflux, 12 h.

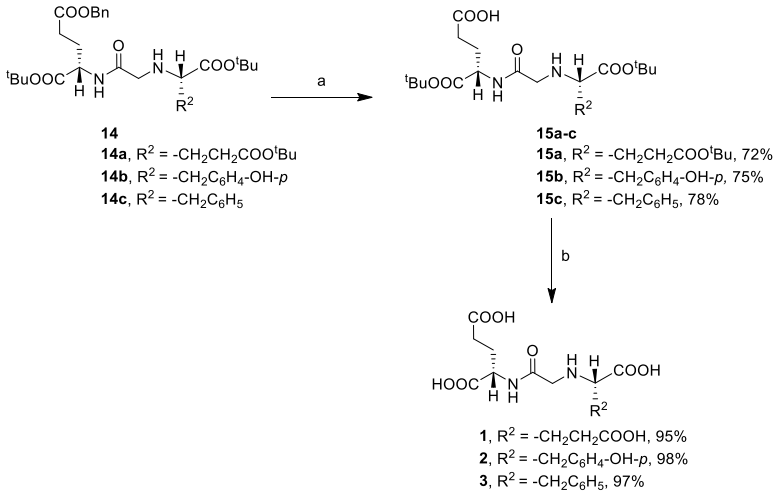

Scheme 3.2 Synthesis of ligands/inhibitors **1**, **2**, and **3**. Reagents and conditions: (a) Pd/C (30 mol%), H_2 (1 atm.), MeOH, rt, 48 h; (b) CF_3COOH:CH_2Cl_2 (1:1), rt, 2 h.

NAAG was measured by incubating a working solution of Amplex Red reagent for 30 min at 37 °C. The fluorescence emission intensity from the oxidation product of Amplex Red reagent, resorufin, is measured at 590 nm by excitation at 530 nm. A plot of fluorescence intensity vs. log [Inhibitors **1**–**3**] is drawn to determine the experimental half-maximal inhibitory concentration (IC_{50}) for the inhibitors **1-3**. Simultaneously, the GCPII enzyme inhibition assay was also performed with a standard PSMA inhibitor, 2-(phosphonomethyl)pentanedioic acid (PMPA), whose IC_{50} is reported to be 0.28 nM, and experimentally, we have observed a value of IC_{50} = 0.40 nM, validating our assay for inhibition of GCPII with the new GCPII inhibitors **1**–**3** (Figure 3.2).

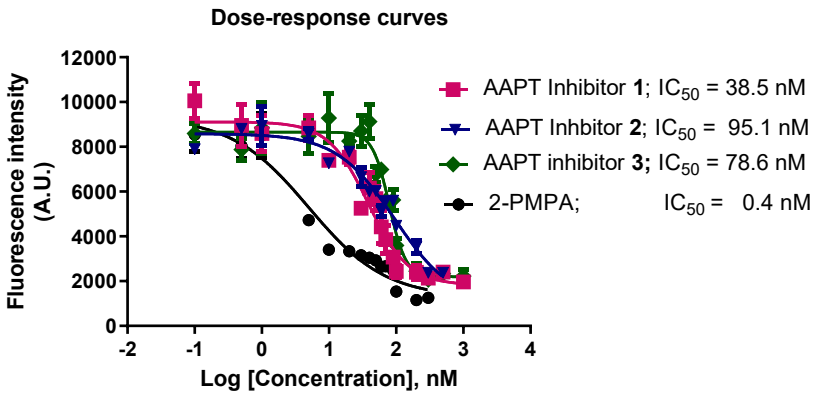

Figure 3.2 Dose-response curves of aminoacetamide inhibitor **1** (IC_{50} = 38.5 nM), inhibitor **2** (IC_{50} = 95.1 nM), inhibitor **3** (IC_{50} = 78.6 nM), and 2-PMPA (IC_{50} = 0.4 nM) from PSMA or GCPII enzyme inhibition assay, ± S.D. (n = 3).

3.2.3 Synthesis of radioactive [^{99m}Tc] AAPT_PCa bioconjugate 22

Crystal structure analysis of PSMA has shown a 20 Å-long narrow tunnel, forming a hydrophobic pocket, suggesting the incorporation of suitable hydrophobic amino acids in the peptidic spacer may enhance the binding affinity of the bioconjugate at the primary hydrophobic binding site. The α- and α'-carboxylic acids of glutamic acid-based aminoacetamide pentanedioic acid (AAPT) derivative **1** interact with Arg 210 and Arg 534 amino acid residues, and the carbonyl oxygen coordinates with the catalytic zinc ions of PSMA. The free γ'-carboxylic acid of **15a** was further utilised as a bioconjugate handle to attach the chelating core via a peptidic spacer. The peptidic spacer was designed to have amino acids such as cysteine, aspartic acid, and diamino propionic acid coupled to form the chelation core, which provides high affinity and stability for ^{99m}Tc, a metastable radioisotope of ^{99m}Tc. The aromatic amino acid, phenylalanine, was introduced to bind at the primary binding hydrophobic pockets of the PSMA receptor, thereby providing higher affinity to the bioconjugate. 8-Aminocaprylic acid, an amino acid containing a long carbon chain, is utilized to provide adequate distance between the targeting ligand and aromatic amino acids present in the peptidic spacer.

The solid-phase peptide synthesis (SPPS) of AAPT_PCa bioconjugate was carried out as shown in scheme 3.3, using H-Cys(Trt)-2-Cl Trt resin **16**. The free NH_2 group of the resin was coupled with Fmoc-Asp(O^{t}Bu)-OH using PyBOP, DIPEA, and DMF for 6 h to obtain dipeptide **17**. The Fmoc deprotection was performed using 20% piperidine in DMF for 30 min, followed by coupling with 1,2-diaminopropionic acid (DAP) to obtain tripeptide **18**. The tripeptide **18** was then attached sequentially with two phenylalanine moieties, followed by Fmoc-8-aminocaprylic

acid in a similar manner to provide **20,** and finally, the targeting ligand **1** was attached to the growing peptide chain. The final bioconjugate was cleaved from the resin using a cleavage cocktail solution to obtain AAPT_PCa bioconjugate **21**, which was purified using reverse-phase high-performance liquid chromatography (RP-HPLC) and further chelated with ^{99m}Tc as shown in scheme 3.4.

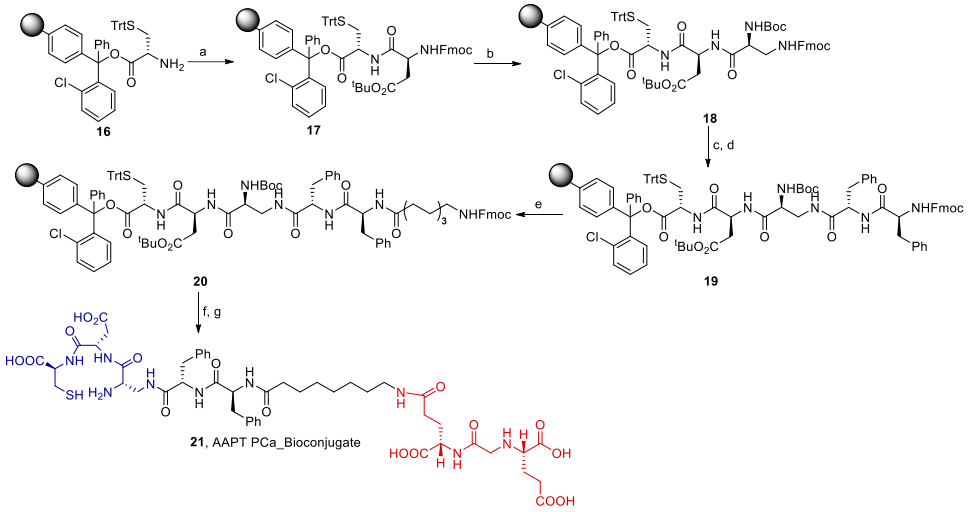

Scheme 3.3 Synthesis of AAPT_PCa bioconjugate **21** using SPPS: Reagents and conditions: (a) Fmoc-Asp(O^{t}Bu)-OH, PyBOP, DIPEA, DMF, 6 h; (b) (i) 20% Piperidine in DMF, rt, 30 min; (ii) Fmoc-diaminopropionic (DAP) acid, PyBOP, DIPEA, DMF, 6 h; (c) (i) 20% Piperidine in DMF, rt, 30 min; (ii) Fmoc-Phe-OH, PyBOP, DIPEA, DMF, 6 h; (d) (i) 20% Piperidine in DMF, rt, 30 min; (ii) Fmoc-Phe-OH, PyBOP, DIPEA, DMF, 6 h; (e) (i) 20% Piperidine in DMF, rt, 30 min; (ii) Fmoc-8-aminocaprylic acid-OH, PyBOP, DIPEA, DMF, 6 h; (f) (i) 20% Piperidine in DMF, rt, 30 min; (ii) **15a**, PyBOP, DIPEA, DMF, 6 h; (g) (i) TFA/H_2O/TIPS/EDT (92.5:2.5:2.5:2.5) (1 × 5 mL, 30 min; 2 × 2.5 mL, 15 min); (ii) Evaporate TFA; (iii) Precipitate in ice cold diethyl ether.

For efficient labelling of ^{99m}Tc, a cold kit was prepared by using a lyophilized mixture of AAPT-spacer-Dap-Asp-Cys, stannous chloride (to reduce ^{99m}Tc-pertechnetate), and sodium (*R*)-D-glucoheptonate (to stabilize the Sn(II) and ^{99m}Tc(IV) intermediates). After the addition of sodium pertechnetate ^{99m}Tc ($Na^{99m}TcO_4$), complexation of the

radiotracer was achieved by boiling the solution for 18 min in a boiling water bath, followed by cooling to room temperature. The desired [^{99m}Tc] AAPT_PCa bioconjugate **22**, obtained with high specific radioactivity (purity >98%), was then used for both *in vitro* and *in vivo* studies.

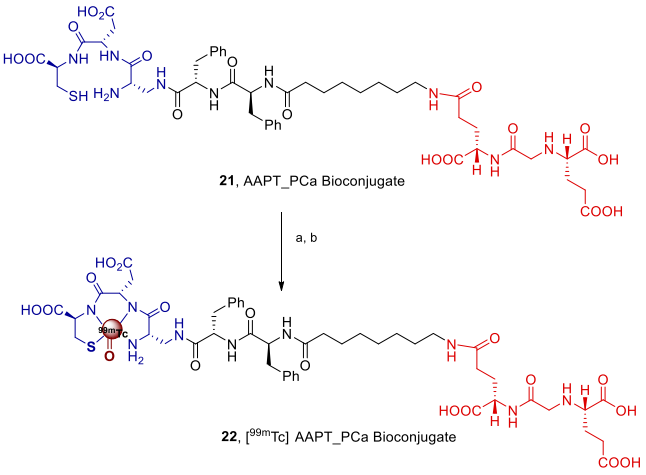

Scheme 3.4 Synthesis of [^{99m}Tc] AAPT_PCa bioconjugate **22**. Reagents and conditions: (a) $SnCl_2$, α-D-glucoheptonate, $Na^{99m}TcO_4$; (b) Boil in water bath for 18 min.

3.2.4 Cell viability studies

The cytotoxicity of AAPT_PCa bioconjugate **21** on various non-cancerous cell lines, such as Macrophage (RAW264.7), Human Embryonic Kidney (HEK293), Madin-Darby Canine Kidney (MDCK), and Hepatoma (HepG2), was assessed using the methylthiazolyldiphenyl-tetrazolium bromide (MTT) assay. The cells were incubated with various concentrations of AAPT_PCa bioconjugate **21** (10 pM, 100 pM, 1 nM, 10 nM, 100 nM, 1 µM, 10 µM) for an incubation period of 24 h and 48 h. The results, as shown in figure 3.3, demonstrate that even at higher concentrations and longer incubation periods, the IC_{50} values remain in the high micromolar (µM) range, varying from 103.21 µM to 124.10 µM for 48 h, and 139.19 µM to 185.25 µM for 24 h. These outcomes validate the non-toxic nature of the AAPT_PCa bioconjugate **21** and indicate its potential safety for preclinical use, with cell viability exceeding 98%.

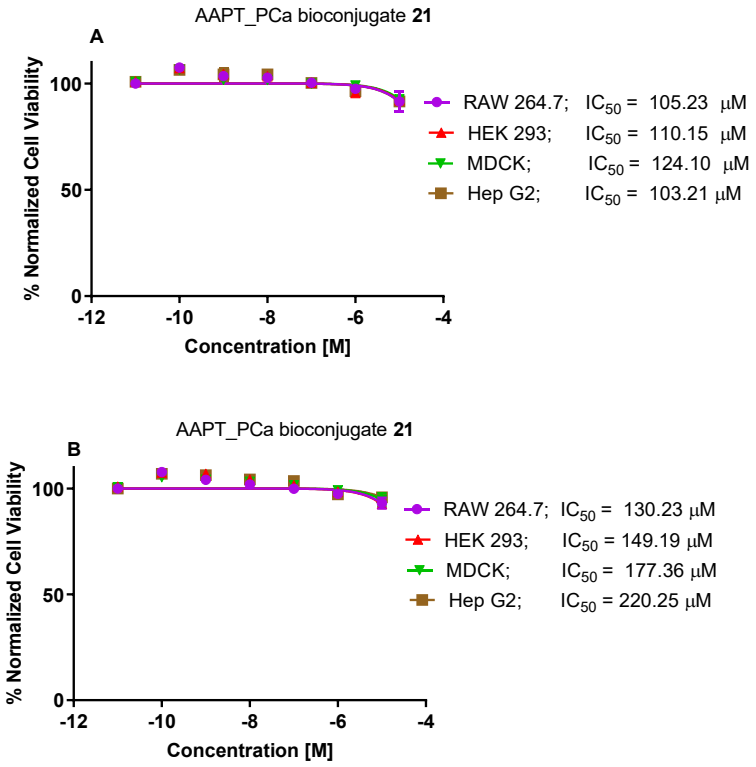

Figure 3.3 Dose response curves of **21** in RAW264.7, HEK293, MDCK, and HepG2 cell lines for incubation period of (A) 48 h and (B) 24 h. Data are expressed in triplicate as mean ± S.D. (n = 3).

3.2.5 Binding affinity study of [^{99m}Tc] AAPT_PCa bioconjugate 22

The ability of [^{99m}Tc] AAPT_PCa bioconjugate **22** to bind with the PSMA receptors was evaluated by incubating PSMA$^+$ LNCaP cells with increasing concentrations of [^{99m}Tc] AAPT_PCa bioconjugate **22** (10, 20, 30, 40, 50, 75, 100, 125, 300, 750, 1215 nM). A hyperbolic curve with a dissociation constant (K_d) of 48.13 nM was obtained for the [^{99m}Tc] AAPT_PCa radioactive bioconjugate **22** with an excellent specificity for PSMA receptor, as indicated by the competition study with a standard PSMA inhibitor, 2-PMPA (2-phosphonomethylpentanedioic acid) (Figure 3.4). The level of bound radioactivity was assessed by γ-counting. As shown in figure 3.4, [^{99m}Tc] AAPT_PCa bioconjugate **22** associated with PSMA$^+$ cells with an apparent K_d of 48 nM (shown in red) in a manner that was quantitatively inhibited by a 100-fold molar excess of 2-PMPA (shown in black). The result confirms that the radiotracer **22**

binds with high specificity to PCa cells overexpressing the PSMA receptor.

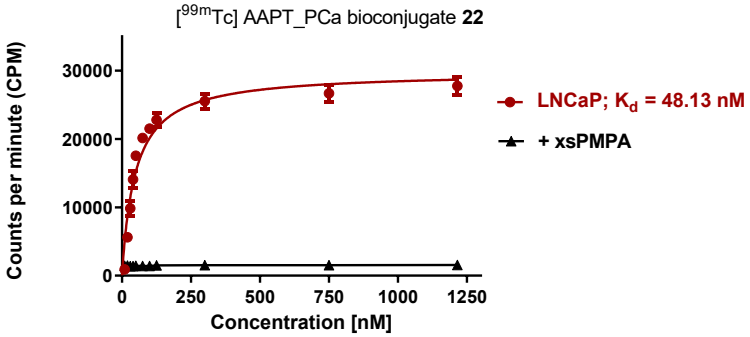

Figure 3.4 Binding affinity constant (K_d = 48.13 nM) measurement and specificity of [^{99m}Tc] AAPT_PCa bioconjugate **22** in PSMA$^+$ LNCaP cell line; Error bars represent ± S.D. (n = 3).

3.2.6 Tumor model, imaging, and biodistribution studies

Radio imaging and biodistribution studies were performed using athymic *nu/nu* mice bearing PSMA$^+$ LNCaP tumor to assess the specificity of [^{99m}Tc] AAPT_PCa bioconjugate **22** *in vivo*. The athymic *nu/nu* mouse was subcutaneously injected with PSMA$^+$ LNCaP cells (7 x 10^6). After the tumor had grown to the desired size, the mouse was intravenously injected with [^{99m}Tc] AAPT_PCa bioconjugate **22** (67 nM, 180 μCi), and the distribution of radiolabelled bioconjugate was evaluated after 1 h and 4 h post-injection (p.i.). The tumor-bearing athymic nude mouse revealed high selectivity and specificity of the ^{99m}Tc AAPT_PCa radiopharmaceutical **22** in the PSMA$^+$ tumor with minimal uptake in excretory organs such as kidneys and bladder, adequate clearance from circulation within 1 h post-injection (Figure 3.5). The mouse was sacrificed, organs were harvested, weighed, and activity was quantified using a gamma counter for biodistribution studies. The biodistribution studies show the highest uptake of 21.5% ID/g in the tumor tissue, as shown in figure 3.6 and table 3.3. All other vital organs displayed the %ID/g of less than 1% resulting in an excellent tumour to tissue ratio. Interestingly, the radiolabelled bioconjugate showed no nonspecific tissue binding and was also

effectively cleared from circulation, with a high tumor to tissue ratio observed from blood, suggesting low serum protein binding and adequate clearance.

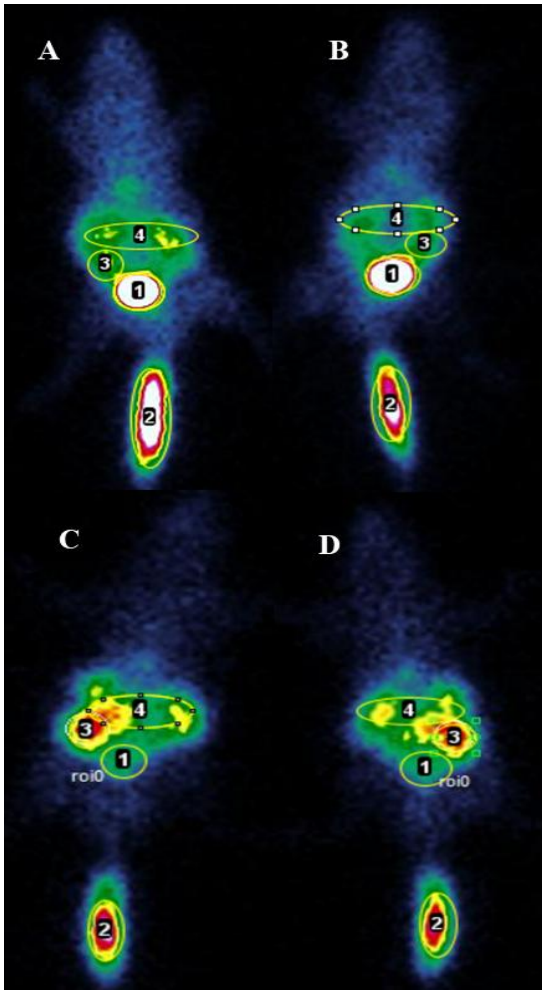

Figure 3.5 Radioimaging of athymic nu/nu mouse bearing $PSMA^{+}$ LNCaP tumor with intravenously injected [^{99m}Tc] AAPT_PCa bioconjugate **22** (67 nM, 180 μCi) after 1 h (A) anterior sides, (B) posterior sides, and 4 h (C) anterior (D) posterior sides. The organs and tissues are labelled as (1) bladder, (2) injection site, (3) tumor, and (4) kidneys.

Table 3.3 Accumulation of [^{99m}Tc] AAPT_PCa bioconjugate **22** expressed in %ID/g and tumor to tissue ratio in various vital organs and PSMA^{+} LNCaP tumor.

Organs	%ID/g[a]	Tumor:Tissue
Brain	0.26	82
Heart	0.39	55
Lung	0.38	57
Stomach	0.16	139
Liver	0.22	97
Pancreas	0.29	73
Intestine	0.34	64
Bladder	2.70	8
Kidney	4.88	4
Spleen	0.19	115
Blood	0.33	66
Bone (femur)	0.39	55
Muscle (femoris)	0.25	86
Skin	0.21	102
Tumor	21.55	1

[a](% ID/g) = Percentage injected dose per gram of wet tissue.

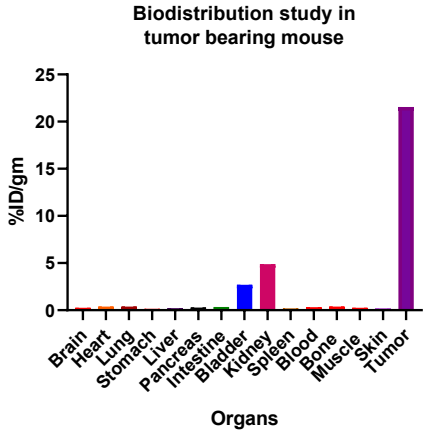

Figure 3.6 Biodistribution studies of [^{99m}Tc] AAPT_PCa bioconjugate **22** in athymic *nu/nu* mouse bearing PSMA^{+} LNCaP tumor xenograft.

3.2.7 Biodistribution studies in athymic *nu/nu* healthy male mice

The biodistribution profile of the [^{99m}Tc] AAPT_PCa bioconjugate **22** was evaluated in athymic *nu/nu* healthy male mice at 1 h, 2 h, and 4 h

p.i. to assess its *in vivo* clearance kinetics and organ-specific retention. As shown in figure 3.8, 1 h p.i., the accumulation was observed in excretory organs like the kidneys and bladder, and rapid clearance from the circulatory system, without any non-specific protein binding. A significant reduction in renal radioactivity was observed 2 h p.i., demonstrating decreased renal retention and no reabsorption in the proximal tubules, with effective elimination through urine via the urinary bladder. Minimal radioactivity was seen 4 h p.i. in the bladder due to urinary accumulation, aligning with the normal physiological excretion rate. The mice were sacrificed, and organs were harvested, weighed, and radioactivity was quantified using a gamma counter for biodistribution studies. Figure 3.7 shows the %injected dose/gram (%ID/g) in vital organs at 1 h, 2 h, and 4 h p.i.. The data demonstrate rapid clearance of the [^{99m}Tc] AAPT_PCa bioconjugate **22** from the circulatory system and non-targeted vital organs such as the brain, heart, lung, stomach, liver, and pancreas. It also shows efficient renal elimination and minimal off-target retention.

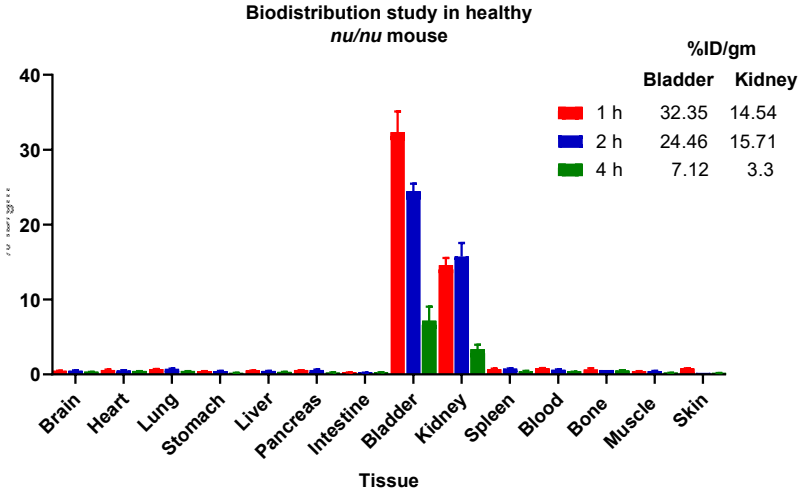

Figure 3.7 Biodistribution studies of [^{99m}Tc] AAPT_PCa bioconjugate **22** in athymic *nu/nu* healthy mice. Data are expressed in triplicate as mean ± S.D. (n = 3).

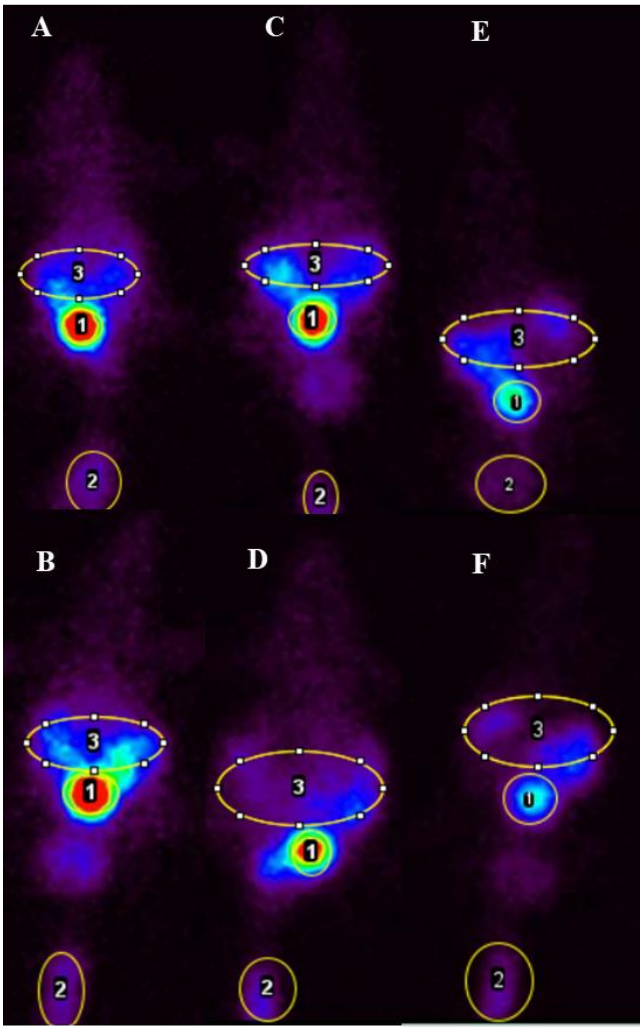

Figure 3.8 Radioimaging of athymic *nu/nu* healthy mice intravenously injected with [^{99m}Tc] AAPT_PCa bioconjugate **22** (67 nM, 180 μCi) after 1 h (A) anterior sides (B) posterior sides, 2 h (C) anterior sides (D) posterior sides, and 4 h (E) anterior sides (F) posterior sides. The organs and tissues are labelled as (1) bladder, (2) site of injection, and (3) kidneys.

3.3 Conclusion

In conclusion, a novel and effective PSMA-targeted radioactive bioconjugate was successfully developed for an early diagnosis of prostate cancer. The radioactive bioconjugate **22** exhibited high binding affinity in the low nM range of 48 nM with an excellent specificity for the PSMA receptor, as indicated by the *in vitro* binding affinity study along with 2-PMPA. The *in vivo* studies further revealed high selectivity

and specificity with %ID/g of 21.5%, which is significantly higher than the currently existing DUPA-based bioconjugate that shows %ID/g of 11.2.[22] These results indicate the potential of PSMA-specific radiopharmaceuticals not only for accurate localization of prostate cancer lesions but also for monitoring therapeutic responses, detecting recurrence post-surgery, and guiding patient selection for PSMA-targeted radionuclide therapy, making it a promising clinical candidate for early and sensitive detection of small tumour masses, enhancing the visual contrast between malignant and non-malignant tissue.

3.4 Experimental section

3.4.1 General method and materials

Chlorotrityl resins, coupling reagents, Fmoc-protected amino acids, chemicals, and solvents used for chemical synthesis of targeting ligand and solid-phase peptide synthesis (SPPS) were purchased from Sigma Aldrich, Iris Biotech GmbH, TCI, Merck, Spectrochem, and Expressolv. Dry solvents were prepared using standard drying agents and procedures. All reactions were performed in oven-dried glasswares. The moisture-sensitive reactions were performed under an inert atmosphere, and a glass syringe was used to transfer the solution. Reaction progress was monitored by thin-layer chromatography (TLC) using TLC plates (60 F254) and visualized under a UV chamber. The compounds **12a–c**, **14a–j**, and **15a** were purified by column chromatography using 230–400 mesh size silica gel as the stationary phase and distilled hexane and ethyl acetate as eluents. The AAPT_PCa bioconjugate **21** was synthesized using a peptide vessel (Chemglass) following the standard orthogonal peptide coupling methodology. The ^{1}H and ^{13}C NMR spectra were recorded using a Bruker AV 500 MHz NMR spectrometer with TMS as an internal standard. The ^{1}H NMR signals were reported in ppm with reference to residual $CDCl_3$ (7.26 ppm), DMSO-d_6 (2.50 ppm), MeOH-d_4 (3.31 ppm), and multiplicities were reported as s = singlet, d = doublet, t = triplet, q = quartet, m = multiplet or unresolved, and brs = broad singlet, with coupling constants in Hz. $CDCl_3$ and DMSO-d_6 were used as solvents for recording the NMR spectra. AAPT_PCa

bioconjugate **21** was obtained as a salt of TFA. Mass spectra were recorded on a Bruker Micro TOF-Q II instrument using positive mode electrospray ionization methods. The AAPT_PCa bioconjugate **21** was purified using an RP-PFP column (XSelect CSH Prep Fluorophenyl 5 μm OBD, 19 mm × 150 mm) in a Buchi Reveleris High Performance Preparative Chromatography instrument. The AAPT_PCa bioconjugate **22** purity was analysed using a Dionex HPLC-Ultimate 3000.

3.4.2 Docking method

During a drug discovery program, molecular docking studies are employed to predict the probable interactions between the designed ligands or inhibitors with target proteins or receptors. In this study, the structure of glutamate carboxypeptidase II (GCPII), also known as prostate-specific membrane antigen (PSMA), complexed with the urea-based inhibitor JB7 (PDB ID: 4NGM), was obtained from the Protein Data Bank to serve as a reference model. The newly designed aminoacetamide-derived PSMA inhibitors (**1–10**) were then subjected to docking simulations using the Surflex-Dock module implemented within the Sybyl X2.1.1 software. This approach enabled a detailed investigation of the binding interactions between the novel inhibitors and the GCPII/PSMA receptor, facilitating the rational design and optimization of more effective candidate compounds

3.4.3 General procedure for synthesis of α-chloroacetamide intermediates 12a–c

In a single-neck round-bottom flask (25 mL), α-amino *tert*-butyl ester **11a–c** (1.00 mmol) and sodium bicarbonate ($NaHCO_3$) (0.267 g, 3.18 mmol) were dissolved in a mixture of dichloromethane (1.5 mL) and water (0.15 mL), and the reaction mixture was cooled to 0 °C. α-Chloroacetyl chloride (0.18 mL, 2.27 mmol) was added dropwise over a period of 2 min at 0 °C. The reaction mixture was allowed to warm to room temperature slowly with stirring for another 1.5 h. After the completion of the reaction, as monitored by TLC, the reaction mixture was diluted with CH_2Cl_2 (1 × 5 mL) and water (1 × 5 mL). The aqueous

layer was further extracted with CH_2Cl_2 (2 × 5 mL). The combined organic layer was then collected, washed with saturated sodium bicarbonate solution (2 × 20 mL), dried over anhydrous Na_2SO_4, filtered, concentrated, and the crude reaction mixture was purified through silica gel (neutral, 100–200 mesh) column chromatography using 20% EtOAc in hexane as eluent.

3.4.3.1 (*S*)-5-Benzyl 1-*tert*-butyl 2-(2-chloroacetamido)pentanedioate (12a)

Yellowish gummy liquid (yield = 60%); R_f = 0.56 (EtOAc:hexane = 1:4); IR (CH_2Cl_2): 3322 (N–H), 3032, 2975 (=C–H), 2928 (C–H), 1729 (C=O), 1652 (N–H), 1537 (C=C), 1454 (C–H), 1166 (C–O), 750, 699 (=C–H) cm^{-1}; ^1H NMR (400 MHz, $CDCl_3$): δ 7.37–7.31 (m, 5H), 7.05 (d, J = 7.28 Hz, 1H), 5.13, 5.10 (AB quartet, J = 13.28 Hz, 2H), 4.49 (ddd, J = 7.28, 5.24, 5.14 Hz, 1H), 3.83 (s, 2H), 2.49–2.38 (m, 2H), 2.27–2.20 (m, 1H), 2.07–1.99 (m, 1H), 1.46 (s, 9H); ^{13}C NMR (100 MHz, $CDCl_3$): δ 172.5, 170.3, 165.8, 135.6, 128.6, 128.3, 128.2, 83.0, 66.6, 52.8, 30.1, 28.6, 27.9, 27.3; HRMS (ESI) m/z $[M+Na]^+$ calcd. for $C_{15}H_{20}ClNO_3$, 364.0519, found, 364.0522.

3.4.3.2 (*S*)-*tert*-Butyl-2-(2-chloroacetamido)-3-(4-hydroxyphenyl) propanoate (12b)

Colourless gummy liquid (yield = 70%); R_f = 0.4 (EtOAc:hexane = 1:4); IR (CH_2Cl_2): 3341 (O–H), 3275 (N–H), 2979 (=C–H), 2933 (C–H), 1733 (C=O), 1657 (N–H), 1518(C=C), 1456 (C–H), 1155 (C–O), 750, 698 (=C–H) cm^{-1}; ^1H NMR (400 MHz, $CDCl_3$): δ 7.03 (d, J = 8.44 Hz, 2H), 6.93 (d, J = 7.32 Hz, 1H), 6.73 (d, J = 8.44 Hz, 2H), 5.96 (brs, 1H), 4.71–4.63 (m, 1H), 3.85, 3.81 (AB quartet, J = 13.80 Hz, 2H), 3.09–2.96 (m, 2H), 1.43 (s, 9H); ^{13}C NMR (100 MHz, $CDCl_3$): δ 170.1, 165.3, 155.2, 130.6, 127.2, 115.4, 82.9, 54.3, 37.1, 28.7, 27.9; HRMS (ESI) m/z $[M+Na]^+$ calcd. for $C_{15}H_{20}ClNO_4$, 336.0979, found, 336.0987.

3.4.3.3 (*S*)-*tert*-Butyl 2-(2-chloroacetamido)-3-phenylpropanoate (12c)

Colourless gummy liquid (yield = 65%); R_f = 0.52 (EtOAc:hexane = 1:4); IR (CH_2Cl_2): 3298 (N–H), 2979 (=C–H), 2933 (C–H), 1734 (C=O), 1657 (N–H), 1528 (C=C), 1456 (C–H), 1155 (C–O), 740 (=C–H) cm^{-1}; ^1H NMR (400 MHz, $CDCl_3$): δ 7.31–7.26 (m, 3H), 7.17–7.15 (m, 2H), 6.89 (d, J = 6.52 Hz, 1H), 4.72 (ddd, J = 6.52, 6.0, 4.52 Hz, 1H), 3.87, 3.83 (AB quartet, J = 13.80 Hz, 2H), 3.12 (d, J = 6.04 Hz, 2H), 1.42 (s, 9H); ^{13}C NMR (100 MHz, $CDCl_3$): δ 169.9, 164.9, 135.7, 129.5, 128.4, 127.1, 82.8, 54.1, 37.9, 28.8, 27.9; HRMS (ESI) m/z $[M+Na]^+$ $C_{15}H_{20}ClNO_3$, 320.1029, found, 320.1034.

3.4.4 General procedure for synthesis of carboxy ester-protected aminaoacetamide precursors 14a–j

Chloroacetamide intermediates **12a–c** (1.00 mmol), α-amino *tert*-butyl esters **13a–j** (1 mmol), potassium carbonate (597 mg, 4.32 mmol), and potassium iodide (262 mg, 1.58 mmol) were suspended in an oven-dried 25 mL round-bottom flask, and the reaction vessel was flushed with nitrogen gas. Dry tetrahydrofuran (2 mL) was then added to the reaction mixture, and the round-bottom flask was fitted with a Liebig condenser. After flushing the system with nitrogen gas, the reaction mixture was allowed to reflux overnight in a silicon oil bath at 90 °C. The reaction mixture was then cooled to room temperature, and the progress of the reaction was monitored by thin-layer chromatography (TLC). The reaction mixture was filtered through a coarse frit glass Buchner filtering funnel, and the residue was thoroughly washed with ether (2 × 15 mL). The filtrate was evaporated under reduced pressure, and the crude reaction mixture was purified through silica gel (neutral, 230–400 mesh) column chromatography using 25-35% EtOAc in hexane as eluent.

3.4.4.1 (*S*)-5-Benzyl-1-*tert*-butyl-2-(2-(((*S*)-1,5-di-*tert*-butoxy-1,5-dioxopentan-2-yl)amino)acetamido)pentanedioate (14a)

Yellowish gummy liquid (yield = 75%); R_f = 0.3 (EtOAc:hexane = 1:2), IR (CH_2Cl_2): 3349 (N–H), 2978 (=C–H), 2928 (C–H), 1729 (C=O), 1682 (N–H), 1517(C=C), 1456 (C–H), 1155 (C–O), 750, 699 (=C–H) cm^{-1}; ^1H NMR (400 MHz, $CDCl_3$): δ 7.70 (d, J = 8.4 Hz, 1H), 7.40–7.26

(m, 5H), 5.10 (s, 2H), 4.52 (ddd, *J* = 7.99, 5.66, 4.76, 1H), 3.39 (d, *J* = 17.2 Hz, 1H), 3.13–3.05 (m, 1H), 3.00 (d, *J* = 17.2 Hz, 1H), 2.48–2.32 (m, 4H), 2.28–2.18 (m, 1H), 2.04–1.91 (m, 3H), 1.87–1.75 (m, 1H), 1.45 (s, 9H), 1.44 (s, 9H), 1.42 (s, 9H); ^{13}C NMR (100 MHz, $CDCl_3$): δ 173.7, 172.6, 171.3, 170.7, 135.9, 128.6, 128.3, 82.2, 81.9, 80.5, 66.4, 61.9, 51.7, 51.0, 32.4, 30.5, 28.7, 28.1, 28.0, 27.6; HRMS (ESI) m/z $[M+Na]^+$ calcd. for $C_{31}H_{48}N_2O_9$, 615.3252, found, 615.3308.

3.4.4.2 (*S*)-5-Benzyl-1-*tert*-butyl-2-(2-(((*S*)-1-(*tert*-butoxy)-3-(4-hydroxyphenyl)-1-oxopropan-2-yl)amino)acetamido)pentanedioate (14b)

Gummy liquid (yield = 75%); R_f = 0.25 (EtOAc:hexane = 1:2); IR (CH_2Cl_2): 3321 (O–H), 3279 (N–H), 3067, 2979 (=C–H), 2929, 2851 (C–H), 1731 (C=O), 1650 (N–H), 1537, 1517 (C=C), 1448 (C–H), 1154 (C–O), 750, 699 (=C–H) cm^{-1}; ^{1}H NMR (400 MHz, $CDCl_3$): δ 7.40–7.32 (m, 5H), 7.07 (d, *J* = 7.52 Hz, 3H), 6.70 (d, *J* = 7.52 Hz, 2H), 5.15, 5.10 (AB quartet, *J* = 12.28 Hz, 2H), 4.31–4.26 (m, 1H), 3.36 (d, *J* = 17.56 Hz, 1H), 3.33–3.25 (m, 1H), 3.00 (d, *J* = 17.56 Hz, 1H), 2.93 (dd, *J* = 13.8, 4.52 Hz, 1H), 2.68 (dd, *J* = 12.80, 9.28 Hz, 1H), 2.40–2.21 (m, 2H), 2.10–1.95 (m, 1H), 1.87–1.58 (m, 2H), 1.44 (s, 9H), 1.41 (s, 9H); ^{13}C NMR (100 MHz, $CDCl_3$): δ 173.4, 172.4, 171.3, 170.6, 137.2, 135.8, 129.6, 128.6, 128.4, 128.3, 126.7, 82.1, 81.8, 66.4, 63.2, 51.5, 50.6, 39.9, 30.5, 28.0, 27.9, 27.3; HRMS (ESI) m/z $[M+H]^+$ calcd. for $C_{31}H_{42}N_2O_8$, 571.3014, found, 571.3007.

3.4.4.3 (*S*)-5-Benzyl-1-*tert*-butyl-2-(2-(((*S*)-1-(*tert*-butoxy)-1-oxo-3-phenylpropan-2-yl)amino)acetamido)pentanedioate (14c)

White solid (yield = 70%); R_f = 0.35 (EtOAc:hexane = 1:2); IR (CH_2Cl_2): 3326 (N–H), 2979 (=C–H), 2929 (C–H), 1723 (C=O), 1668 (N–H), 1520 (C=C), 1455 (C–H), 1154 (C–O), 735, 698 (=C–H) cm^{-1}; ^{1}H NMR (400 MHz, $CDCl_3$): δ 7.40–7.34 (m, 5H), 7.28–7.20 (m, 5H), 5.13, 5.09 (AB quartet, *J* = 14.04 Hz, 2H), 4.45–4.35 (m, 1H), 3.41–3.34 (m, 2H), 3.07–2.84 (m, 3H), 2.43–2.24 (m, 2H), 2.18–2.06 (m, 1H), 2.04–1.85 (m, 1H), 1.82–1.70 (m, 1H), 1.46 (s, 9H), 1.37 (s, 9H), 1.25–1.21 (m, 1H); ^{13}C NMR (100 MHz, $CDCl_3$): δ 173.7, 172.9, 171.9,

170.4, 155.0, 135.7, 130.6, 128.9, 128.6, 128.4, 128.3, 115.7, 82.1, 81.8, 66.6, 63.5, 51.7, 50.5, 38.9, 30.6, 28.0, 27.9, 26.9; HRMS (ESI) m/z $[M+Na]^+$ calcd. for $C_{31}H_{42}N_2O_7$, 577.2884, found, 577.2888.

3.4.4.4 (*S*)-5-Benzyl-1-*tert*-butyl-2-(2-(((*S*)-1-(*tert*-butoxy)-1-oxopropan-2-yl)amino) acetamido)pentanedioate (14d)

White solid (yield = 72%); R_f = 0.32 (EtOAc:hexane = 1:2); IR (CH_2Cl_2): 3338 (N–H), 2974 (=C–H), 2927 (C–H), 1730 (C=O), 1666 (N–H), 1523 (C=C), 1455 (C–H), 1152, 1064 (C–O), 734, 697 (=C–H) cm^{-1}; ^1H NMR (400 MHz, $CDCl_3$): δ 7.77 (d, J = 8.52 Hz, 1H), 7.36–-7.30 (m, 5H), 5.12, 5.08 (AB quartet, J = 13.04 Hz, 2H), 4.53 (ddd, J = 8.52, 5.78, 5.0 Hz, 1H), 3.37 (d, J = 17.32 Hz, 1H), 3.16 (q, J = 7.04 Hz, 1H), 3.04 (d, J = 17.32 Hz, 1H), 2.52–2.32 (m, 2H), 2.27–2.15 (m, 1H), 2.04–1.92 (m, 1H), 1.45 (s, 9H), 1.44 (s, 9H), 1.28 (d, J = 7.04 Hz, 3H), 1.24 (brs, 1H); ^{13}C NMR (100 MHz, $CDCl_3$): δ 174.5, 172.6, 171.4, 170.8, 135.8, 128.6, 128.3, 128.2, 82.3, 81.5, 66.5, 57.5, 51.6, 50.8, 30.4, 28.0, 27.9, 27.8, 19.3; HRMS (ESI) m/z $[M+Na]^+$ calcd for $C_{25}H_{38}N_2O_7$, 501.2571, found, 501.2572.

3.4.4.5 (*S*)-5-Benzyl-1-*tert*-butyl-2-(2-(((*S*)-1-(*tert*-butoxy)-3-methyl-1-oxobutan-2-yl)amino)acetamido)pentanedioate (14e)

Yellowish gummy liquid (yield = 75%); R_f = 0.36 (EtOAc:hexane = 1:2); IR (CH_2Cl_2): 3363 (N–H), 2975 (=C–H), 2933 (C–H), 1733 (C=O), 1681 (N–H), 1513 (C=C), 1457 (C–H), 1157 (C–O), 746, 699 (=C–H) cm^{-1}; ^1H NMR (400 MHz, $CDCl_3$): δ 7.73 (d, J = 8.28 Hz, 1H), 7.38–7.32 (m, 5H), 5.12, 5.08 (AB quartet, J = 12.56 Hz, 2H), 4.51 (ddd, J = 8.28, 5.66, 5.24, 1H), 3.40 (d, J = 17.32 Hz, 1H), 2.98–2.93 (m, 2H), 2.51–2.33 (m, 2H), 2.25–2.15 (m, 1H), 2.05–1.93 (m, 1H), 1.44 (s, 18H), 1.30–1.13 (m, 2H), 0.97–0.86 (m, 6H); ^{13}C NMR (100 MHz, $CDCl_3$): δ 173.9, 172.6, 171.6, 170.7, 135.9, 128.6, *128.4, 82.3, 81.6, 68.0, 66.5, 51.8, 51.3, 31.6, 30.5, 28.2, 28.1, 27.9, 19.5, 18.4 (*higher intensity signal); HRMS (ESI) m/z $[M+Na]^+$ calcd. for $C_{27}H_{42}N_2O_7$, 529.2884, found, 529.2882.

3.4.4.6 (*S*)-5-Benzyl-1-*tert*-butyl-2-(2-(((*S*)-1-(*tert*-butoxy)-4-methyl-1-oxopentan-2-yl)amino)acetamido)pentanedioate (14f)

Yellowish liquid (yield = 82%); R_f = 0.4 (EtOAc:hexane = 1:2); IR (CH_2Cl_2): 3354 (N–H), 2959 (=C–H), 2934 (C–H), 1734 (C=O), 1681 (N–H), 1511 (C=C), 1456 (C–H), 1155, 1081 (C–O), 749, 699 (=C–H) cm^{-1}; ^1H NMR (400 MHz, $CDCl_3$): δ 7.74 (d, J = 8.28 Hz, 1H), 7.40–7.30 (m, 5H), 5.11, 5.08 (ABquartet, J = 12.80 Hz, 2H), 4.51 (ddd, J = 8.28, 5.40, 5.28, 1H), 3.37 (d, J = 17.32 Hz, 1H), 3.09 (t, J = 7.0 Hz, 1H), 2.99 (d, J = 17.32 Hz, 1H), 2.51–2.32 (m, 2H), 2.26–2.15 (m, 1H), 2.04–1.92 (m, 1H), 1.83–1.71 (m, 3H), 1.44 (s, 9H), 1.43 (s, 9H) 1.29–1.22 (m, 1H), 0.92 (d, J = 6.52 Hz, 3H), 0.90 (d, J = 6.52 Hz, 3H); ^{13}C NMR (100 MHz, $CDCl_3$): δ 174.7, 172.5, 171.4, 170.6, 135.8, 128.6, 128.3, 128.2, 82.2, 81.5, 66.4, 60.9, 51.7, 50.8, 42.9, 30.4, 28.1, 27.9, 27.8, 24.9, 22.6, 22.5; HRMS (ESI) m/z $[M+Na]^+$ calcd. for $C_{28}H_{44}N_2O_7$, 521.3221, found, 521.3222.

3.4.4.7 (2*S*)-5-Benzyl-1-*tert*-butyl-2-(2-(((2*S*)-1-(*tert*-butoxy)-3-methyl-1-oxopentan-2-yl)amino)acetamido)pentanedioate (14g)

Yellowish solid (yield = 86%); R_f = 0.34 (EtOAc:hexane = 1:2); IR (CH_2Cl_2): 3347(N–H), 2977 (=C–H), 2933 (C–H), 1727 (C=O), 1668 (N–H), 1515 (C=C), 1458 (C–H), 1153 (C–O), 734, 698 (=C–H) cm^{-1}; ^1H NMR (400 MHz, $CDCl_3$): δ 7.72 (d, J = 8.52 Hz, 1H), 7.42–7.27 (m, 5H), 5.11, 5.08 (AB quartet, J = 12.52 Hz, 2H), 4.51 (ddd, J = 8.52, 5.38, 5.24, 1H), 3.40 (d, J = 17.32 Hz, 1H), 2.95 (d, 1H, J = 17.32 Hz), 2.86 (d, J = 5.76 Hz, 1H), 2.51–2.32 (m, 2H), 2.26–2.14 (m, 1H), 2.04–1.87 (m, 4H), 1.44 (s, 18H), 1.28–1.23 (m, 1H), 0.99 (d, J = 6.80 Hz, 3H), 0.95 (d, J = 7.04 Hz, 3H); ^{13}C NMR (100 MHz, $CDCl_3$): δ 173.6, 172.6, 171.5, 170.6, 135.8, 128.6, 128.3, 128.2, 82.2, 81.5, 66.8, 66.5, 51.7, 51.3, 38.5, 30.4, 28.2, 27.9, 27.8, 25.5, 15.7, 11.7; HRMS (ESI) m/z $[M+Na]^+$ calcd. for $C_{28}H_{44}N_2O_7$, 521.3221, found, 521.3223.

3.4.4.8 (*S*)-5-Benzyl-1-*tert*-butyl-2-(2-(((*S*)-1,4-di-*tert*-butoxy-1,4-dioxobutan-2-yl)amino)acetamido)pentanedioate (14h)

Yellowish liquid (yield = 85%); R_f = 0.32 (EtOAc:hexane = 1:2); IR (CH_2Cl_2): 3327 (N–H), 2975 (=C–H), 2926 (C–H), 1723 (C=O), 1672 (N–H), 1519 (C=C), 1456 (C–H), 1149 (C–O), 750, 698 (=C–H) cm^{-1}; ^{1}H NMR (400 MHz, $CDCl_3$): δ 8.00 (d, J = 8.52 Hz, 1H), 7.40–7.27 (m, 5H), 5.11, 5.08 (AB quartet, J = 12.80 Hz, 2H), 4.50 (ddd, J = 8.52, 6.14, 4.76 Hz, 1H), 3.48–3.40 (m, 2H), 3.18–3.14 (d, J = 17.32 Hz, 1H), 2.66 (dd, J = 16.7, 4.24, Hz, 1H), 2.57–2.37 (m, 3H), 2.30–2.17 (m, 1H), 2.10–1.96 (m, 1H), 1.44 (s, 9H), 1.43 (s, 9H), 1.41(s, 9H), 1.27–1.24 (m, 1H); ^{13}C NMR (100 MHz, $CDCl_3$): δ 172.6, 172.5, 171.6, 170.7, 170.4, 135.9, 128.5, 128.3, 128.2, 82.0, 81.9, 81.5, 66.4, 58.1, 51.8, 50.9, 38.8, 30.6, 28.1, *27.9, 27.2 (*higher intensity signal); HRMS (ESI) m/z $[M+Na]^+$ calcd. for $C_{30}H_{46}N_2O_9$, 578.3203, found, 579.3275.

3.4.4.9 (*S*)-Di-*tert*-butyl-2-(2-(((*S*)-1-(*tert*-butoxy)-3-(4-hydroxy phenyl) -1-oxopropan-2-yl)amino) -2-oxoethyl)amino) pentane dioate (14i)

White solid (yield = 85%); R_f = 0.25 (EtOAc:hexane = 1:2); IR (CH_2Cl_2): 3349 (O–H), 3275 (N–H), 2979 (=C–H), 2933 (C–H), 1730 (C=O), 1660 (N–H), 1517(C=C), 1456 (C–H), 1155 (C–O), 753 (=C–H) cm^{-1}; ^{1}H NMR (400 MHz, $CDCl_3$): δ 7.57 (d, J = 8.44 Hz, 1H), 7.01 (d, J = 8.08 Hz, 2H), 6.72 (d, J = 8.08 Hz, 2H), 4.75–4.65 (m, 1H), 3.35 (d, J = 16.88 Hz, 1H), 3.10–2.90 (m, 4H), 2.37–2.20 (m, 2H), 1.90–1.67 (m, 2H), 1.43 (s, 18H), 1.42 (s, 9H), 1.27–1.22 (m, 1H); ^{13}C NMR (100 MHz, $CDCl_3$): δ 173.6, 172.8, 171.2, 170.6, 155.3, 130.4, 127.7, 115.7, 82.1, 81.9, 80.8, 61.6, 53.3, 50.8, 37.2, 32.3, 28.7, 28.7, 28.09, 28.06, 28.0; HRMS (ESI) m/z $[M+Na]^+$ calcd. for $C_{28}H_{44}N_2O_8$, 559.2990, found, 559.2983.

3.4.4.10 (*S*)-Di-*tert*-butyl-2-((2-(((*S*)-1-(*tert*-butoxy)-1-oxo-3-phenyl propan-2-yl)amino)-2-oxoethyl)amino)pentanedioate (14j)

White solid (yield = 80%); R_f = 0.30 (EtOAc:hexane = 1:2); IR (CH_2Cl_2): 3350 (N–H), 2979 (=C–H), 2933 (C–H), 1732 (C=O), 1682

(N–H), 1518 (C=C), 1456 (C–H), 1155, 1080 (C–O), 741 (=C–H) cm^{-1}; ^1H NMR (400 MHz, $CDCl_3$): δ 7.54 (d, J = 8.44 Hz, 1H), 7.30–7.15 (m, 5H), 4.80–4.65 (m, 1H), 3.36 (d, J = 17.24 Hz, 1H), 3.15–3.07 (m, 2H), 3.07–3.01 (m, 1H), 2.98 (d, J = 17.24 Hz, 1H), 2.35–2.17 (m, 2H), 1.92–1.83 (m, 1H), 1.78–1.67 (m, 2H), 1.44 (s, 9H), 1.43 (s, 9H), 1.39 (s, 9H); ^{13}C NMR (100 MHz, $CDCl_3$): δ 173.7, 172.5, 170.8, 170.5, 136.5, 129.4, 128.4, 126.9, 82.0, 81.8, 80.4, 61.6, 53.2, 50.9, 37.9, 32.3, 28.6, 28.1, 28.0, 27.9; HRMS (ESI) m/z $[M+H]^+$ calcd. for $C_{28}H_{44}N_2O_7$, 521.3221, found, 521.3226.

3.4.5 General procedure for the deprotection of 14a–c

In a double-neck round-bottom flask (25 mL), a hydrogen-filled bladder was fitted to one neck of the round-bottom flask through a borosilicate glass heavy-wall glass stop cock adapter. **14a–c** (1.0 mmol) was added to the round-bottom flask and dissolved in dichloromethane (5 mL). 10% Pd/C (134 mg, 0.126 mmol) was added slowly to the mixture, and the reaction mixture was sealed using a rubber septum. The residual air in the reaction vessel was expunged through a syringe needle inserted through the rubber septum that is connected to a filtration pump through a silicone tube for 2 minutes or until the solution starts bubbling. The reaction mixture is now filled with hydrogen gas from the bladder via a stop cock and allowed to stir at room temperature for 48 h. After the completion of the reaction, as monitored by TLC, the reaction mixture was filtered through a celite pad (sintered glass filter was half-filled with celite powder) and washed with ethyl acetate (3 × 20 mL) using a suction pump. The ethyl acetate layer was concentrated under reduced pressure, and the crude product was purified through column chromatography using 100% ethyl acetate to obtain pure **15a–c**.

3.4.5.1 (*S*)-5-(*Tert*-butoxy)-4-(2-(((*S*)-1,5-di-*tert*-butoxy-1,5-dioxo-pentan-2-yl)amino)acetamido)-5-oxopentanoic acid (15a)

Colourless gummy liquid (yield = 60%); R_f = 0.58 (EtOAc:hexane = 1:1); IR (CH_2Cl_2): 3350 (N–H), 2979 (=C–H), 2933 (C–H), 1732 (C=O), 1682 (N–H), 1518 (C=C), 1456 (C–H), 1155, 1080 (C–O), 741

(=C–H) cm^{-1}; ^1H NMR (400 MHz, $CDCl_3$): δ 7.81 (d, J = 8.44 Hz, 1H), 4.50 (ddd, J = 7.79, 6.06, 4.76 Hz, 1H), 3.43 (d, J = 16.84 Hz, 1H), 3.15–3.07 (m, 1H), 3.04 (d, J = 16.84 Hz, 1H), 2.45–2.35 (m, 4H), 2.27–2.15 (m, 1H), 2.05–2.15 (m, 1H), 2.05–1.92 (m, 2H), 1.90–1.80 (m, 1H), 1.46 (s, 9H), 1.45 (s, 9H), 1.43 (s, 9H), 1.13–1.07 (brs, 1H); ^{13}C NMR (100 MHz, $CDCl_3$): δ 175.9, 173.7, 172.9, 171.8, 170.6, 82.3, 82.0, 80.8, 61.7, 51.9, 50.8, 32.3, 30.5, 28.6, 28.1, 27.9, 27.6; HRMS (ESI) m/z M+H]$^+$ calcd for $C_{24}H_{42}N_2O_9$, 503.2963, found, 503.2927.

3.4.6 Procedure for the deprotection of tris(*tert*-butylcarboxylic ester) in 15a–c to afford inhibitors 1–3

In a single-neck round-bottom flask (50 mL), tris(*tert*-butylcarboxylic ester) **15a–c** (1.0 mmol) were dissolved in DCM (2 mL). A mixture of trifluoroacetic acid (2.5 mL) and DCM (2.5 mL) (1:1) was added to the reaction mixture at room temperature and stirred for 2 h. After the completion of the reaction, as monitored by TLC, trifluoroacetic acid and DCM were evaporated under reduced pressure. The products **1–3** were precipitated by the addition of ice-cold diethyl ether (5 mL). The precipitates were again washed with diethyl ether (3 × 5 mL) to remove any excess trifluoroacetic acid and other non-polar impurities. The products **1–3** were purified using Buchi Reveleris preparative high-performance liquid chromatography using an RP-PFP column (XSelect CSH Prep Fluorophenyl 5 µm OBD, 19 mm × 150 mm). The purified inhibitors **1–3** were utilized for the NAALADase or PSMA enzyme inhibition assay to determine the IC_{50}.

3.4.7 Preparative HPLC method

The purification of ligands **1–3** was performed using a Buchi Reveleris Preparative HPLC System. Crude ligand (20 mg) was dissolved in a 1:1 ratio of CH_3CN:H_2O (1 mL) and injected into the sample injector for elution using RP-PFP (Reverse Phase PentafluoroPhenyl) preparative column (XSelect CSH Prep Fluorophenyl 5 µm OBD, 19 mm × 150 mm). A flow rate of 10 mL/min (mobile phase, A = 0.1% trifluoroacetic acid in H_2O and B = acetonitrile) was maintained throughout the run,

and the mobile phase gradient was gradually increased from 1% B (v/v) to 50% B (v/v) over 40 min. The mobile phase gradient was increased to 80% B (v/v) in the next 15 min, and the chromatogram was recorded at λ = 200–254 nm as well as by an ELSD detector. Pure fractions of **1–3** were collected using an automatic fraction collector, acetonitrile was evaporated under reduced pressure and lyophilised to afford pure ligands **1–3**. The pure ligands were further used for the GCPII enzyme inhibition assay.

3.4.8 General procedure of solid-phase peptide synthesis

3.4.8.1 Resin swelling

The resins used in solid-phase peptide synthesis were first swollen with DCM (5 mL) for 30 minutes by bubbling nitrogen gas through the beads in the peptide vessel. After draining DCM, the beads were swollen with DMF (3 × 5 mL), repeating the process for 15 minutes.

3.4.8.2 General procedure for the Kaiser test

Kaiser test kit preparation reagents

a) Dissolve 500 mg of ninhydrin in 10 mL of ethanol
b) Dissolve 80 g of phenol in 20 mL of ethanol
c) Dilute 2 mL of 0.001M solution of potassium cyanide (KCN) to 100 mL with pyridine

Add two drops of each of the above solutions to a few dried resin beads in a glass test tube and heat at 110 °C in a sea sand bath for 2–3 minutes. The freshly prepared Kaiser test kit can be stored at room temperature for 6 months without decomposition. The appearance of dark blue colour signifies the presence of free amine groups in the resin beads, indicating the deprotection of the Fmoc group. In contrast, the colourless beads signify the absence of the amine group, indicating the completion of the coupling reaction. The test was performed after coupling of each amino acid, as well as after the deprotection of the Fmoc group at each step.

3.4.8.3 General procedure for Fmoc deprotection

The Fmoc group of the N-terminus of the growing peptide chain was deprotected using 20% piperidine in DMF (10 mL) by bubbling nitrogen gas through the resin beads for 10 minutes in each step of Fmoc deprotection. The procedure was repeated three times (1 × 4 mL; 2 × 3 mL) to ensure the complete deprotection of the Fmoc group.

3.4.8.4 General procedure for peptide cleavage from resin beads

The peptide was cleaved from the resin beads using 10 mL of cleavage cocktail (a mixture of 9.25 mL trifluoroacetic acid, 0.25 mL triisopropylsilane (TIPS), 0.25 mL ethane dithiol (EDT) and 0.25 mL water) by bubbling nitrogen gas. First, 5 mL of the cocktail was added to the resin, and nitrogen gas was bubbled for 30 minutes, followed by the addition of the remaining cocktail solution (2 × 2.5 mL), with nitrogen gas bubbling for 5 minutes each time. The cocktail solution was evaporated under reduced pressure from the mother liquor after peptide cleavage, and the concentrated solution was precipitated in ice-cold diethyl ether. The precipitate was then dried using nitrogen gas, and the obtained crude product was further purified using HPLC.

3.4.8.5 Procedure for solid-phase peptide synthesis of AAPT_PCa bioconjugate 21

H-Cys-2-ClTrt resin (0.200 g, 0.148 mmol) was swollen in CH_2Cl_2 (5 mL) for 30 minutes by bubbling nitrogen, and after draining CH_2Cl_2, the resin was swollen again in DMF (5 mL × 3) for 15 minutes each. Fmoc-Asp(O^tBu)-OH (118 mg, 0.296 mmol), PyBOP (154 mg, 0.296 mmol), and DIPEA (0.25 mL, 1.48 mmol) were dissolved in DMF (0.5 mL) in a 2 mL glass vial, mixed thoroughly using a Pasteur pipette, transferred to the peptide vessel containing resin beads and the coupling reaction was carried out for 6 h by bubbling a stream of nitrogen gas through the resin beads in the peptide vessel. The resin beads were then washed with DMF (3 × 5 mL), followed by isopropanol (3 × 5 mL) for 10 min each. The solvent was drained using a filtration pump, and the beads were dried until freely flowing by bubbling N_2 gas through the peptide vessel.

The amide coupling was confirmed by performing the Kaiser test. Next, the FmocNH protecting group was cleaved by the addition of 20% piperidine in DMF (1 × 4 mL; 2 × 3 mL) for 10 min each to the resin beads. The resin beads were then washed with DMF (3 × 5 mL), followed by isopropanol (3 × 5 mL). The solvent was drained using a suction pump, and the beads were dried until freely flowing by bubbling N_2 gas through the resin beads in the peptide vessel. The formation of free amine was confirmed by performing the Kaiser test. Consecutively, Boc-Dap(Fmoc)-OH (137 mg, 0.296 mmol), Fmoc-Phe-OH (114 mg, 0.296 mmol), Fmoc-Phe-OH (114 mg, 0.296 mmol), and Fmoc-8-Aoc-OH (112 mg, 0.296 mmol) were coupled in sequence to the growing peptide chain, as mentioned before. After deprotection of the NHFmoc group from the last amino acid Fmoc-8-Aoc-OH, targeting ligand precursor **15a** (148 mg, 0.296 mmol), PyBOP (154 mg, 0.296 mmol), and DIPEA (0.25 mL, 1.48 mmol) were dissolved in DMF (0.5 mL) in a 2 mL glass vial, mixed thoroughly using a Pasteur pipette, transferred to the peptide vessel containing resin beads and the coupling reaction was continued for 6 h. The resin beads were then washed with DMF (3 × 5 mL), followed by isopropanol (3 × 5 mL). The solvent was drained using a suction pump, and the beads were dried by bubbling N_2 gas through the resin beads in the peptide vessel until free-flowing. The coupling was confirmed by performing the Kaiser test. A mixture of 9.25 mL trifluoroacetic acid (TFA), 0.25 mL ethane dithiol (EDT), 0.25 mL triisopropylsilane (TIPS), and 0.25 mL H_2O was prepared in a 15 mL centrifuge tube, and 5 mL of this cocktail solution was added to the resin beads. Nitrogen gas was bubbled through the solution for 30 minutes. The cocktail solution with cleaved ligand targeted AAPT_PCa bioconjugate **21** in the peptide vessel was collected into a round-bottom flask (25 mL). The resin beads were treated again with the remaining cocktail solution (2 × 2.5 mL) for 15 minutes each, and the mother liquor was collected in the same round-bottom flask (25 mL). The pooled cocktail mixture with cleaved peptide AAPT_PCa bioconjugate **21** was transferred to a 15 mL centrifuge tube, fitted with a needle-pierced

septum, and concentrated under reduced pressure to obtain a viscous liquid. Ice-cold ether (5 mL) was added to the concentrated, viscous mixture to precipitate AAPT_PCa bioconjugate **21** as a white solid, and the solid was washed with ice-cold ether (3 × 5 mL). The crude bioconjugate **21** was purified by RP-HPLC using a pentafluorophenyl preparative column (5 μm, 10 mm × 150 mm) [λ = 254 nm; solvent gradient 0% B to 95% B in 24 min; A = 10 mM NH_4OAc buffer, pH = 5; B = acetonitrile (ACN)]. Acetonitrile was removed under reduced pressure from HPLC fractions, and the pure fractions were freeze-dried to yield AAPT_PCa bioconjugate **21**.

3.4.9 HPLC purification

The purification of crude AAPT_PCa bioconjugate **21** was performed using a Buchi Reveleris Prep RP-HPLC System. Crude AAPT_PCa bioconjugate 21 was dissolved in a mixture of CH_3CN:H_2O (1:1, 1 mL) and injected into the sample injector for elution using RP-PFP (Reverse Phase PentafluoroPhenyl) preparative column (XSelect CSH Prep Fluorophenyl 5 μm; 19 × 150 mm). A flow rate of 10 mL/min (mobile phase, A = 10 mM NH_4OAc buffer, pH = 5; B = acetonitrile (ACN)) is maintained throughout the run, and the mobile phase gradient was gradually changed from 0% B (v/v) to 95% B (v/v) over 24 min. The gradient of the mobile phase was further increased to 100% B (v/v) in another 2 min. The chromatograms were recorded at λ = 240, 254, and 280 nm for crude AAPT_PCa bioconjugate **21**. Pure fractions of AAPT_PCa bioconjugate **21** were collected using an automatic fraction collector, the organic solvent was evaporated under reduced pressure using a rotary evaporator, and the aqueous solution was lyophilized for 48 h to yield AAPT_PCa bioconjugate **21**. White solid (yield = 68%); retention time (t_R)= 11.1 min; HRMS (ESI) m/z $[[M + CH_2] + H]^+$ calcd for $C_{48}H_{67}N_9O_{17}S$, 1088.4605, found, 1088.4651.

3.4.10 Procedure for non-radioactive kit preparation of AAPT_PCa bioconjugate 21

A solution of stannous chloride dihydrate (0.80 mg, 0.003 mmol) in 0.2 M hydrochloric acid (0.8 mL) was added to a solution of sodium-α-D-glucoheptonate dihydrate (800 mg, 2.815 mmol) in nitrogen-purged water of AAPT_PCa bioconjugate **21** (0.001 mmol) was then added to the reaction mixture while continuously purging with nitrogen. The pH of the solution was adjusted to 6.8 using 0.1 N sodium hydroxide solution. After pH adjustment, nitrogen-purged water was added to bring the total volume to 10 mL. The solution was dispensed in 5 mL vials (1 mL/vial) under a nitrogen atmosphere and lyophilized for 48 h. The vials were then sealed under a nitrogen atmosphere to yield the non-radioactive kits, which were stored at –20 °C until further use.

3.4.11 Procedure for chelation of radioisotope ^{99m}Tc with AAPT_PCa bioconjugate 21

In the cold kit vial, containing AAPT_PCa bioconjugate **21**, a solution of sodium pertechnetate ^{99m}Tc (1 mL, 15 mCi) was added. The vial was kept in boiling water for 18 min, resulting in the formation of [^{99m}Tc]AAPT_PCa radiotracer **22**, that was cooled to room temperature before use.

3.4.12 Cell lines and culture

Lymph Node Carcinoma of the Prostate (LNCaP) (CRL-1740) and Prostate Carcinoma (PC3) (CRL-1435) cancer cell lines were procured from ATCC. Macrophage (RAW264.7), Human Embryonic Kidney cell line (HEK293), Madin-Darby Canine Kidney cells (MDCK), and Hepatoma (HepG2) cell lines were procured from the National Centre for Cell Sciences (NCCS), Pune, India. The cell lines were grown in T-75 Flask (Tarson, 950040) containing sterile filtered RPMI 1640 medium (Thermo Fisher, 11875093) or F12K medium (Thermo Fisher, 21127022) supplemented with fetal bovine serum (Thermo Fisher, 1027016), 100 mM of sodium pyruvate (Thermo Fisher, 11360070), non-essential amino acid (Thermo Fisher, 11140050), and 1% penicillin

streptomycin (Thermo Fisher, 15140122), at 37 °C and 5% CO_2 to form a monolayer until 60% confluency. The cells were then trypsinized using 0.25% trypsin-EDTA (Thermo Fisher, 15050065), collected, and centrifuged at 800 rpm for 5 min. The cell pellet was resuspended in a fresh medium and then utilized for the *in vitro* and *in vivo* studies. For *in vitro* competition studies, cells were preincubated with 100-fold excess of 2-PMPA (Sigma-Aldrich, SML 1612) for 1 h before treatment with the test article. The subcutaneous tumor implantation was performed using LNCaP cells (7×10^6) in 100 µL of RPMI 1640 medium and Matrigel (BD Biosciences, 354234).

3.4.13 PSMA or GCPII enzyme inhibition assay

The half-maximal inhibitory concentrations (IC_{50}) of newly synthesized PSMA or GCPII inhibitors **1–3** (AAPT ligands) were determined by fluorescent-based enzyme inhibition assay, using the Amplex Glutamate kit, which was procured from Invitrogen, and a working solution of Amplex Red reagent (5 mL, 100 µM) was prepared. The membrane portion of the PSMA enzyme was extracted from the $PSMA^+$ LNCaP cell line by following a reported protocol. Briefly, LNCaP cells (1×10^6) were harvested in HEPES buffer (1 mL) and lyzed twice using a probe sonicator for 30 sec. The lysate was ultracentrifuged at 100,000 × g for 30 min; the supernatant was discarded, and the cell pellet was homogenized by the addition of HEPES buffer (1 mL) and used for the PSMA enzyme inhibition assay. The isolated enzyme (100 µL, 8.3027 ng) was incubated with various concentrations (1, 5, 10, 25, 50, 75, 90, 100, 200, 300, 500 and 1000 nM) of the inhibitors **1–3** (100 µL) in the presence of *N*-acetylaspartylglutamate (NAAG) (50 µL, 30 nM) for 60 min. The amount of glutamic acid released by the NAAG hydrolysis was quantified by incubating a working solution of Amplex Red reagent (50 µL, 100 µM) for 30 min at 37 °C. The fluorescence emission after the oxidation of Amplex Red reagent was measured by using a Synergy H1 multimode plate reader (BioTek Instruments, Inc., Winooski, VT, USA). The excitation wavelength was fixed at 530 nm, and the fluorescence emission was measured at 590 nm. The dose v/s response

inhibition curve was obtained using a semi-log plot of fluorescence intensity vs concentration of inhibitors **1–3** to provide experimental IC_{50} values and compared with a known standard GCPII inhibitor, PMPA, by following a similar procedure. The data analysis was performed using GraphPad Prism, version 7.04.

3.4.14 Cell viability study of AAPT_PCa bioconjugate 21

The cytotoxicity studies of AAPT_PCa bioconjugate **21** on various healthy cell lines were performed using the MTT assay. In a T-75 flask, Macrophage (RAW264.7), Human Embryonic Kidney (HEK293), Madin-Darby Canine Kidney (MDCK), and Hepatoma (Hep G2) cell lines were grown to 60–70% confluency. The cells were gently dissociated using 0.25% trypsin (1 mL) for 3 minutes, followed by the addition of fresh RPMI 1640 medium (2 mL). The cells were collected using a micropipette (1 mL) and centrifuged at 700 rpm for 3 minutes at room temperature to obtain the cell pellet. The cell pellet was resuspended in a fresh medium (1 mL), and the cell suspension (10 µL) was counted using a haemocytometer. Approximately 5000 cells/well were seeded on a 96-well plate and allowed to form a monolayer until they reached 60% confluency for 24 h at 37 °C and 5% CO_2. The cells were treated with various concentrations of AAPT_PCa bioconjugate **21** (10 pM, 100 pM, 1 nM, 10 nM, 100 nM, 1 µM, 10 µM) and incubated for 24 h and 48 h at 37 °C and 5% CO_2. After incubation, the spent medium was discarded, and cells were gently washed with 1X PBS buffer (1 × 0.5 mL). The cells were then incubated with MTT dye (0.5 mg/mL, 0.05 mL) for 4 h at 37 °C and 5% CO_2. After incubation, MTT dye was removed, and DMSO (0.1 mL) was added to each well to dissolve the blue color formazan crystals. The absorbance from each well, proportional to the live cells, was quantified using a Synergy H4 multi-plate reader at a wavelength of 570 nm. Dose vs Response curves were obtained from a plot of log[concentration] vs normalized response curves, and IC_{50} values were calculated using GraphPad Prism, version 7.04.

3.4.15 Binding affinity studies of [^{99m}Tc] AAPT_PCa bioconjugate 22

$PSMA^+$ LNCaP cells were cultured in a T-75 flask for 48 h until 80% confluency for binding affinity evaluation of [^{99m}Tc]AAPT_PCa bioconjugate **22**. The LNCaP cells were gently dissociated using 0.25% trypsin (1 mL) for 3 minutes, followed by the addition of fresh RPMI 1640 medium (2 mL). The cells were collected using a micropipette (1 mL) and centrifuged at 700 rpm for 3 minutes at room temperature to obtain the cell pellet. The cell pellet was resuspended in a fresh medium (1 mL), and the cell suspension (10 µL) was counted using a haemocytometer. Approximately, 1.2×10^5 cells were suspended in a fresh RPMI 1640 medium (100 µL) in Eppendorf tubes (2 mL) and treated with increasing concentrations of [^{99m}Tc] AAPT_PCa bioconjugate **22** (10, 20, 30, 40, 50, 75, 100, 125, 300, 750, 1215 nM) prepared in RPMI 1640 medium (400 µL) in triplicates and incubated in a CO_2 incubator for 1 h. For competition experiments, cells were preincubated with 2-PMPA (500 µL) (100-fold excess of 1215 nM) for 1 h before treatment with the test articles, [^{99m}Tc] AAPT_PCa bioconjugate **22**. After incubation for an hour with 2-PMPA, cells were centrifuged to form cell pellets, and the excess PMPA with the spent medium was discarded. The cell pellets were resuspended in a fresh medium (100 µL) and the PSMA receptor blocked cells were then treated with increasing concentrations of [^{99m}Tc]AAPT_PCa bioconjugate **22** (10, 20, 30, 40, 50, 75, 100, 125, 300, 750, 1215 nM) prepared in RPMI 1640 medium (400 µL) in triplicates and incubated in a CO_2 incubator for 1 h. The treated cells were washed with an ice-cold buffer (2 × 500 µL) (84 mg EDTA and 1 mL of 25 mM HEPES buffer in 50 mL 1X DPBS) and centrifuged. The cell pellets, free of unbound [^{99m}Tc] AAPT_PCa bioconjugate **22**, were resuspended in an ice-cold buffer (500 µL) to evaluate cell-bound radioactivity using a gamma counter. The dissociation constant (Kd) was calculated using GraphPad Prism 7.04.

3.4.16 Animals

All animal handling and experiments were carried out in accordance with the Indian Animal Ethical Committee (IAEC) guidelines at the BARC-RMC animal housing facility. The athymic male *nu/nu* mice, 3 to 4 weeks old and weighing between 15 to 20 g, were procured from GV Safety Assessment Platform Pvt. Ltd / Envigo RMS LLC (Inotiv). The animals were housed in a standard animal housing facility for a week before carrying out experiments. After tumor implantation, the mice were kept in a standard animal housing laboratory facility with sterile food and autoclaved water to prevent infection. The cages were weekly changed and cleaned to avoid cross-infection among the mice. Mice were injected with dihydrotestosterone (100 µg/mouse) to facilitate the tumor growth. For radioimaging studies, the mice were anesthetised with ketamine (10 µL/mouse), and after completion of radioimaging, they were sacrificed using CO_2 asphyxiation.

3.4.17 Subcutaneous tumor model development

Athymic male *nu/nu* mice, aged between 3 to 4 weeks, were subcutaneously injected with LNCaP cells (7×10^6) in 100 µL of RPMI 1640 medium and Matrigel (1:1 ratio) in the right hip region. Dihydrotestosterone (100 µg/mouse) was injected at the site of tumor implantation weekly up to four weeks to facilitate tumor growth. Tumor growth was carefully monitored weekly using a vernier calliper. Once the tumor volume size reached between 400–500 mm^3, typically 4 weeks p.i., the mice were used for *in vivo* studies.

3.4.18 Imaging and biodistribution in $PSMA^+$ LNCaP tumor model

After 4 weeks, once the tumor reached between 400–500 mm^3, the mouse was injected with [^{99m}Tc] AAPT_PCa bioconjugate (67 nmol, 150 µCi) via lateral tail vein in sterile saline (100 µL). SPECT-CT (Optima CT 540.Tandem_Discovery_670_Pro) imaging was performed 1 h and 4 h p.i. The mouse was anaesthetized using ketamine (10 µL/mouse), and images were acquired from both the anterior and posterior sides. After 4 h, the mouse was sacrificed via CO_2 asphyxiation

and carefully dissected to harvest vital organs (brain, heart, lung, stomach, liver, pancreas, intestine, bladder, kidney, spleen, blood, bone, muscle, skin) and tumor tissue. The organs and tumor tissue were placed into a pre-weighed gamma counter tube and weighed precisely using an analytical balance. Radioactivity in each organ and tumor tissue was measured using a gamma counter. The counts per minute (CPM) values were decay corrected and expressed as %Injected dose/g. Tumour-to-organ uptake ratios were subsequently determined to assess the specificity and selectivity of the bioconjugate for prostate tumor tissue.

3.4.19 Imaging and biodistribution in healthy mice

Four-week-old healthy athymic *nu/nu* male mice (n = 3) were taken and injected with [^{99m}Tc] AAPT_PCa bioconjugate **22** (67 nmol, 150 µCi) via lateral tail vein. SPECT-CT imaging was performed 1 h, 2 h, and 4 h p.i.. Mice were anesthetized using a ketamine solution (10 µL/mouse), and images were acquired from both the anterior and posterior sides. At each time point, mice were sacrificed via CO_2 asphyxiation and carefully dissected to harvest vital organs (brain, heart, lung, stomach, liver, pancreas, intestine, bladder, kidney, spleen, blood, bone, muscle, skin). The organs were placed into a pre-weighed gamma counter tube and weighed precisely using an analytical balance. Radioactivity in each organ was measured using a gamma counter. The counts per minute (CPM) values were decay corrected and expressed as the % Injected dose/g was calculated for each organ.

3.4.20 Copies of ^{1}H, ^{13}C NMR, and HRMS spectra

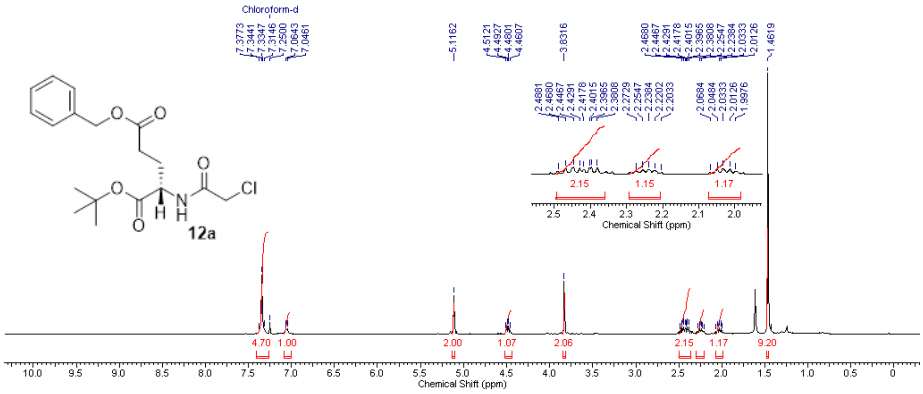

Figure 3.9 ^{1}H NMR spectrum (400 MHz, $CDCl_3$) of **12a**.

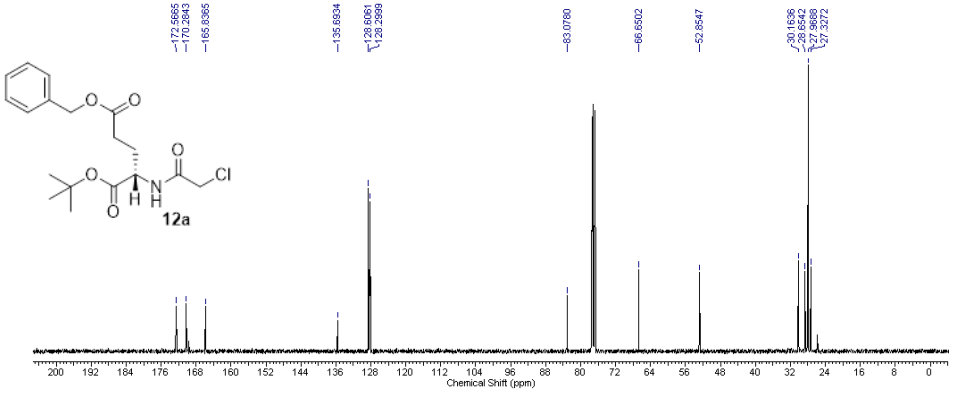

Figure 3.10 ^{13}C NMR spectrum (100 MHz, $CDCl_3$) of **12a**.

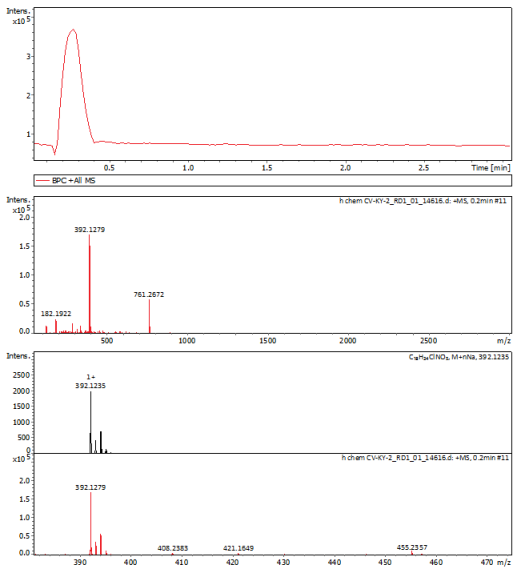

Figure 3.11 HRMS of **12a**.

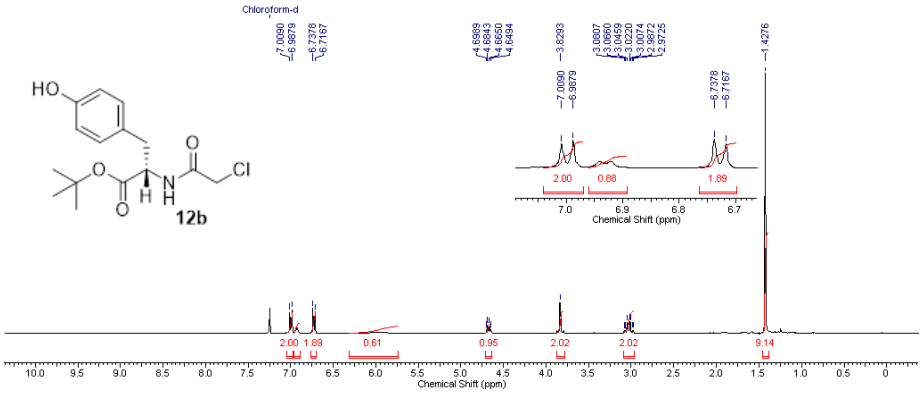

Figure 3.12 ^{1}H NMR spectrum (400 MHz, $CDCl_3$) of **12b**.

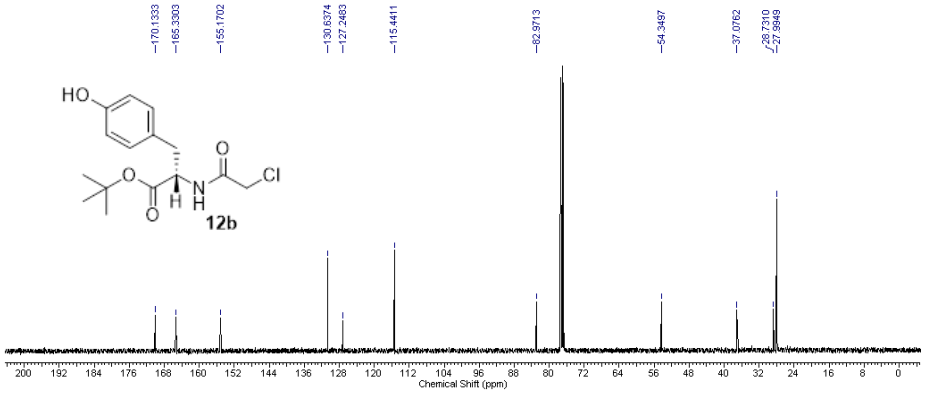

Figure 3.13 ^{13}C NMR spectrum (100 MHz, $CDCl_3$) of **12b**.

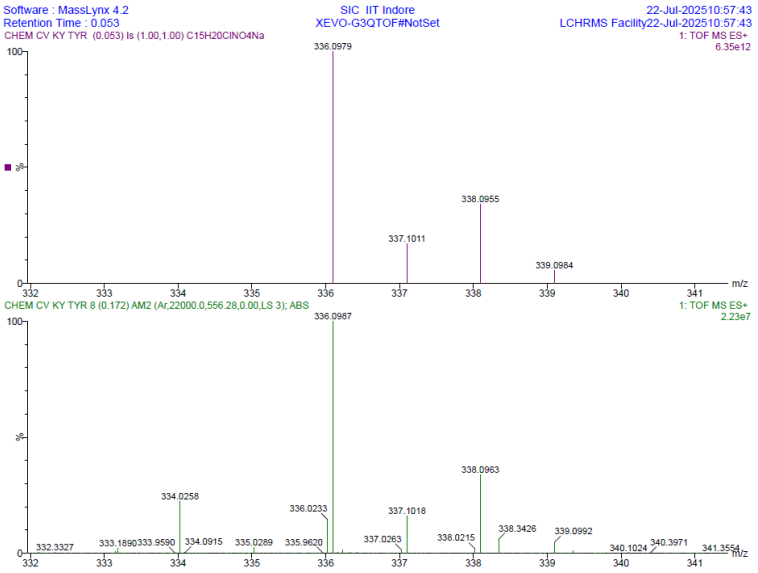

Figure 3.14 HRMS of **12b**.

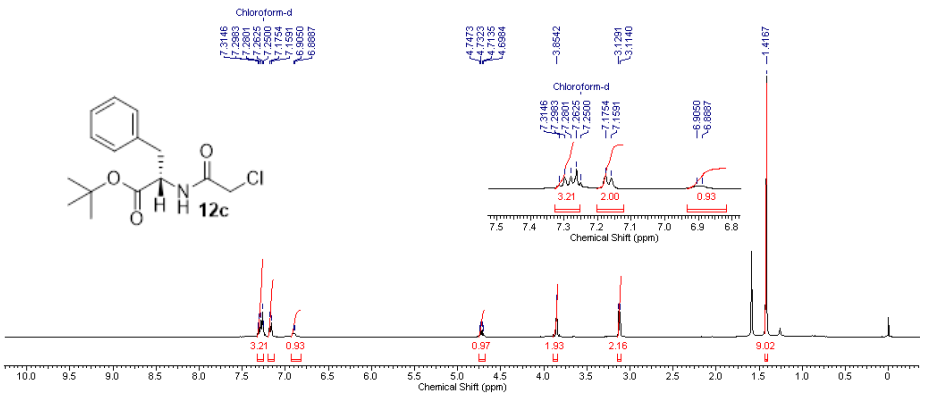

Figure 3.15 ^{1}H NMR spectrum (400 MHz, $CDCl_3$) of **12c**.

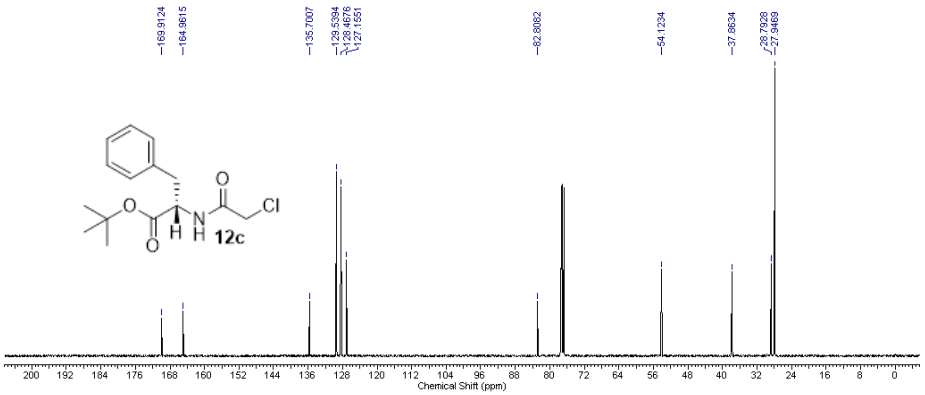

Figure 3.16 ^{13}C NMR spectrum (100 MHz, $CDCl_3$) of **12c**.

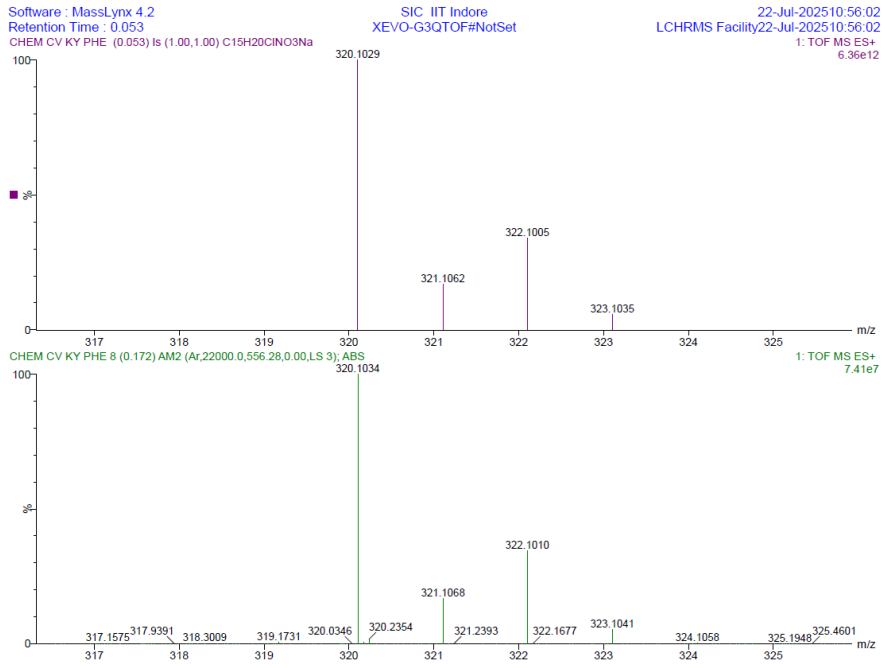

Figure 3.17 HRMS of **12c**.

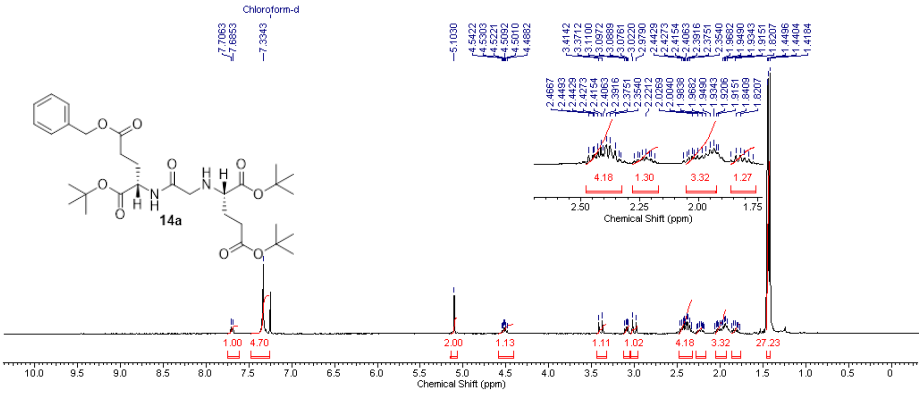

Figure 3.18 ^{1}H NMR spectrum (400 MHz, $CDCl_3$) of **14a**.

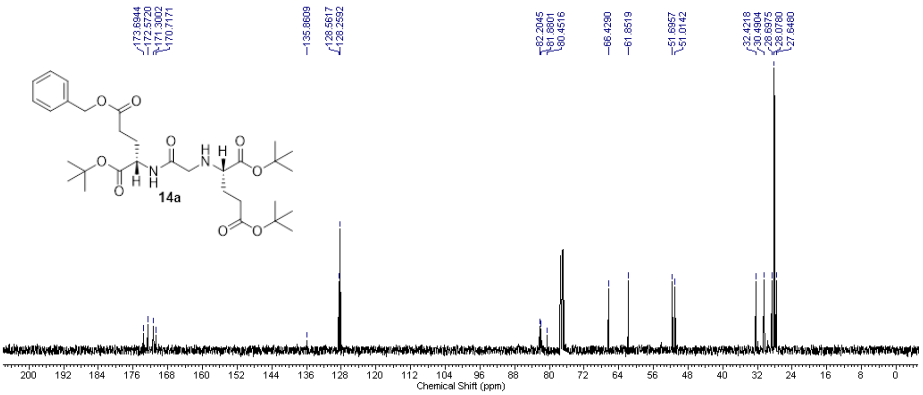

Figure 3.19 ^{13}C NMR spectrum (100 MHz, $CDCl_3$) of **14a**.

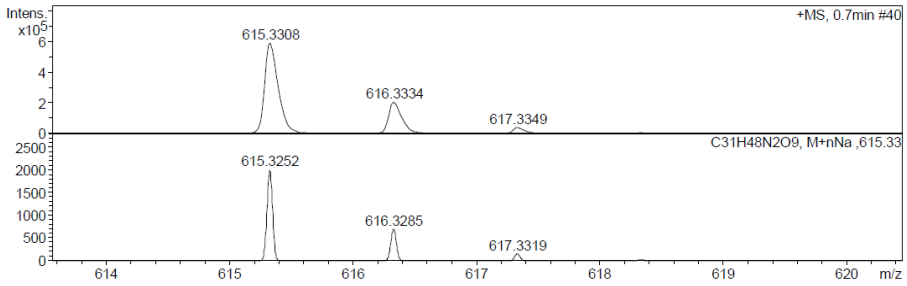

Figure 3.20 HRMS of **14a**.

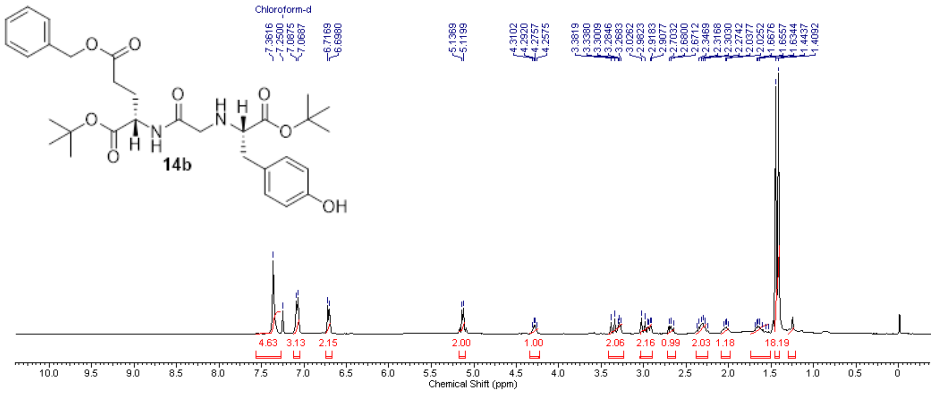

Figure 3.21 ^{1}H NMR spectrum (400 MHz, $CDCl_3$) of **14b**.

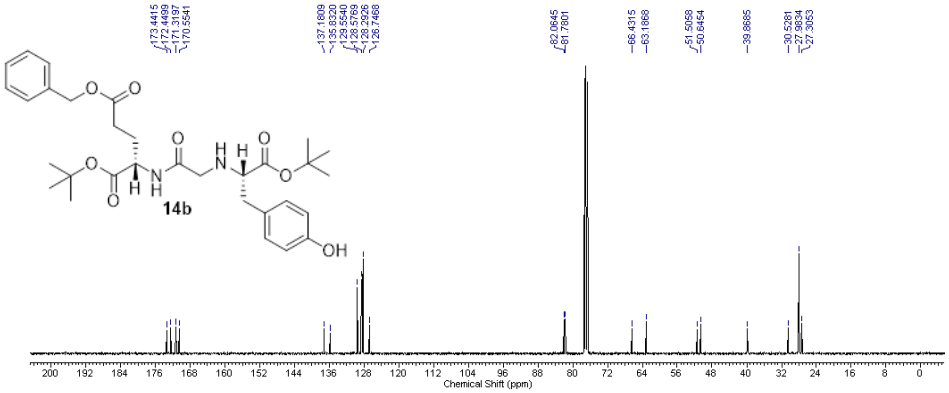

Figure 3.22 ^{13}C NMR spectrum (100 MHz, $CDCl_3$) of **14b**.

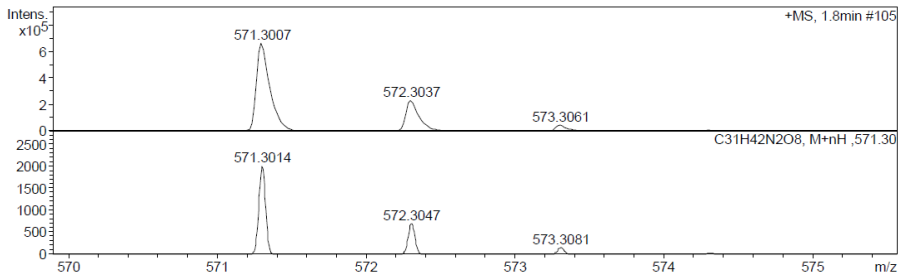

Figure 3.23 HRMS of **14b**.

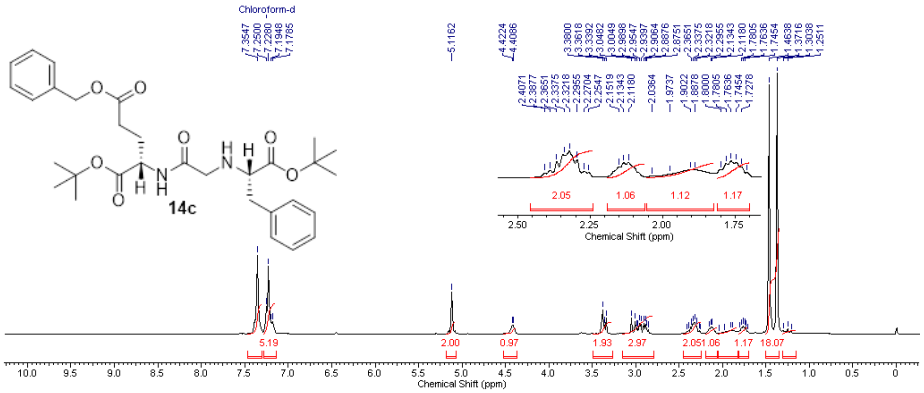

Figure 3.24 ^{1}H NMR spectrum (400 MHz, $CDCl_3$) of **14c**.

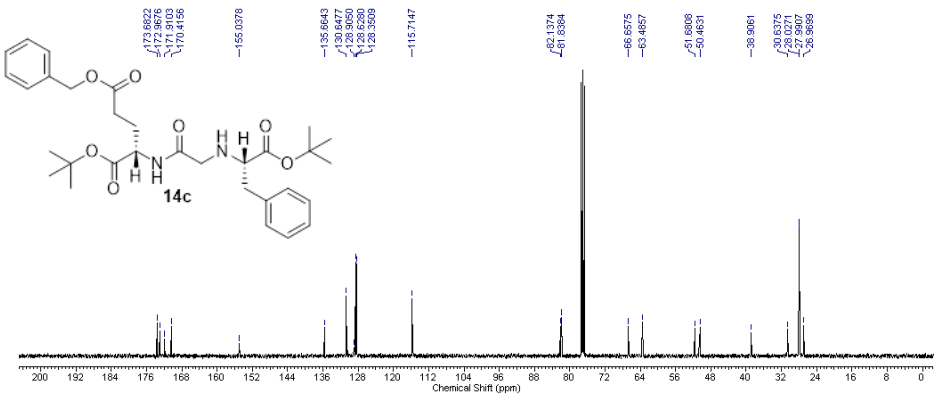

Figure 3.25 ^{13}C NMR spectrum (100 MHz, $CDCl_3$) of **14c**.

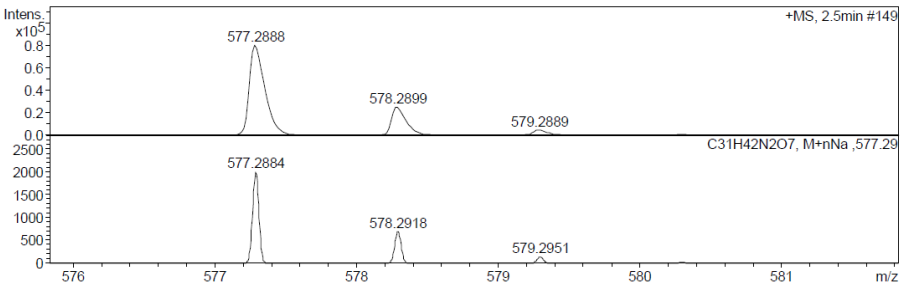

Figure 3.26 HRMS of **14c**.

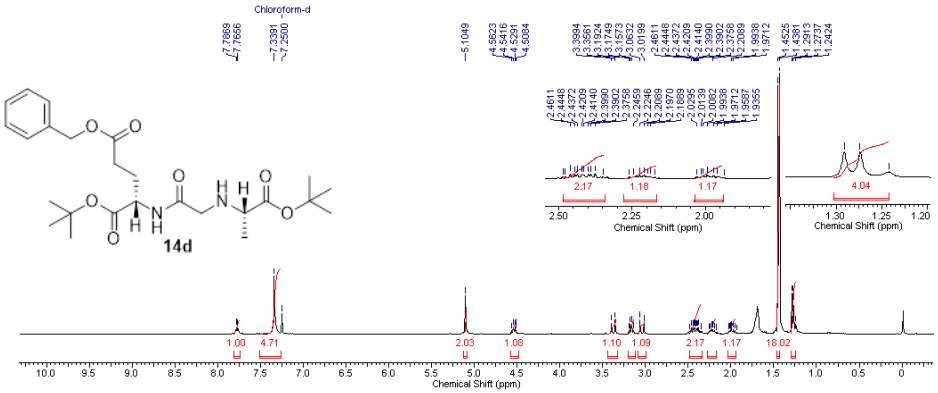

Figure 3.27 ^{1}H NMR spectrum (400 MHz, $CDCl_3$) of **14d**.

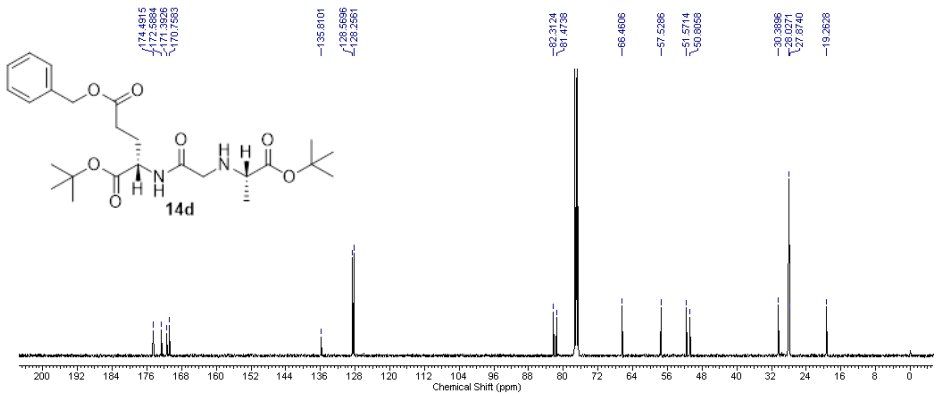

Figure 3.28 ^{13}C NMR spectrum (100 MHz, $CDCl_3$) of **14d**.

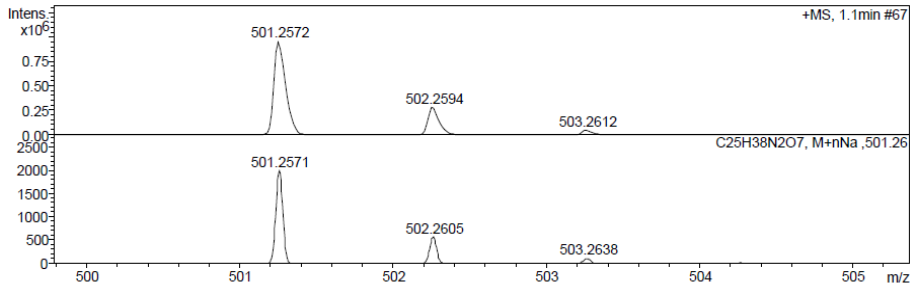

Figure 3.29 HRMS of **14d**.

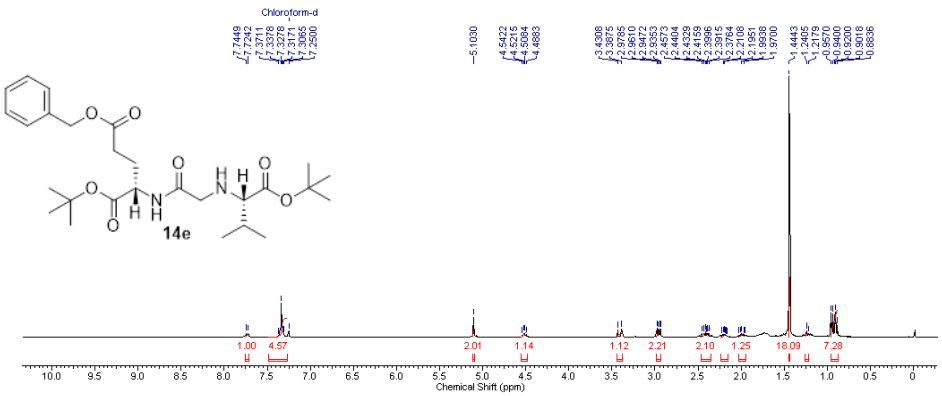

Figure 3.30 ^{1}H NMR spectrum (400 MHz, $CDCl_3$) of **14e**.

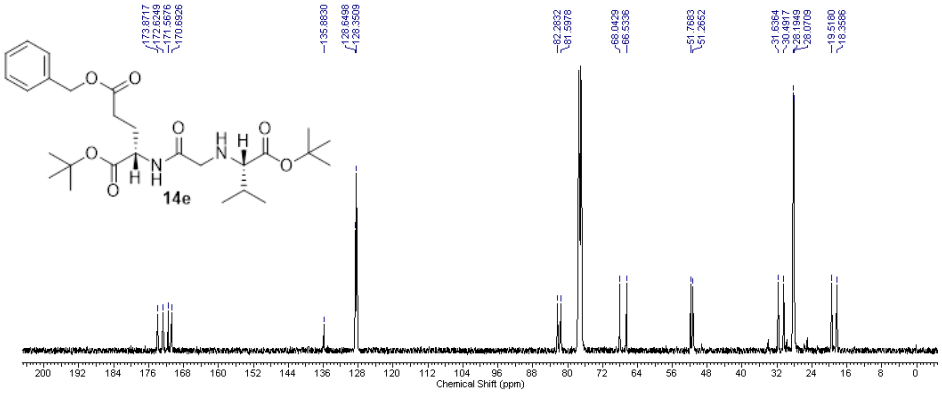

Figure 3.31 ^{13}C NMR spectrum (100 MHz, $CDCl_3$) of **14e**.

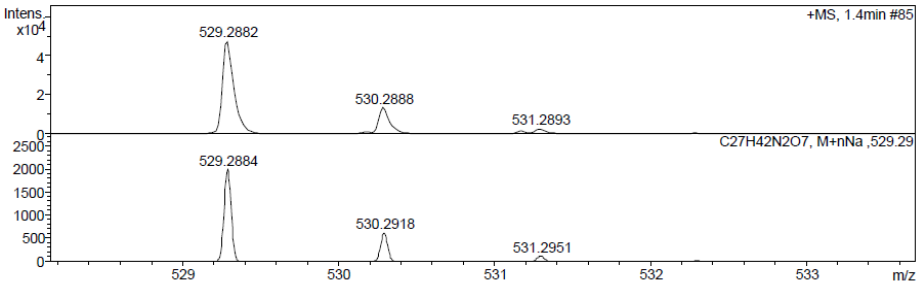

Figure 3.32 HRMS of **14e**.

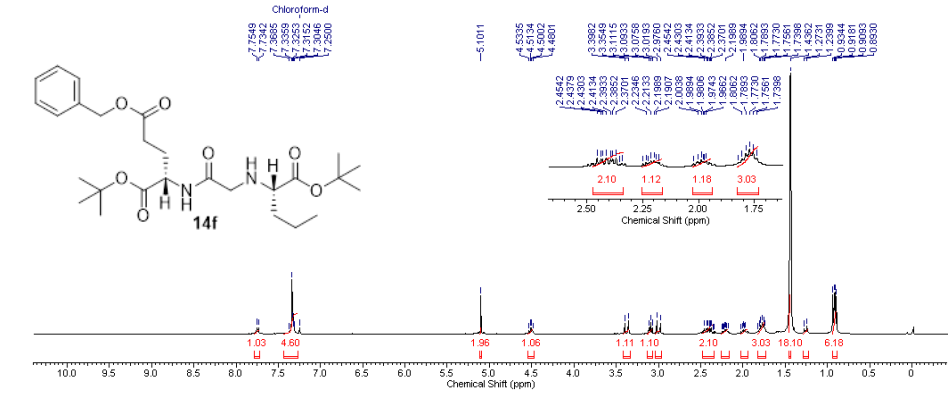

Figure 3.33 ^{1}H NMR spectrum (400 MHz, $CDCl_3$) of **14f**.

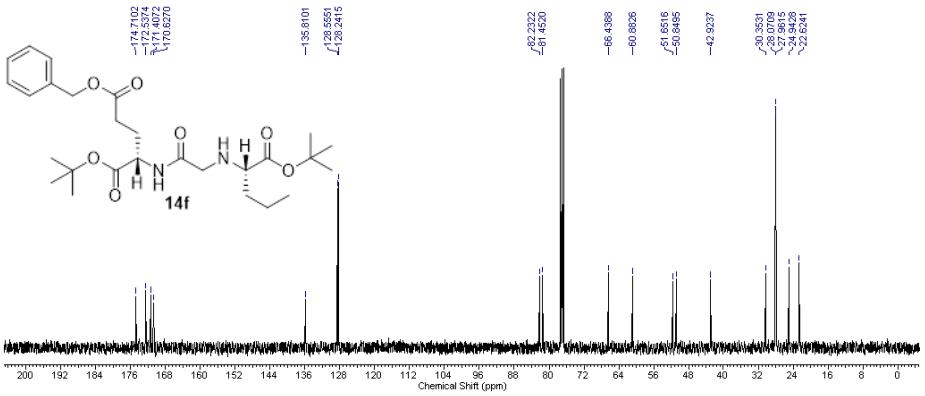

Figure 3.34 ^{13}C NMR spectrum (100 MHz, $CDCl_3$) of **14f**.

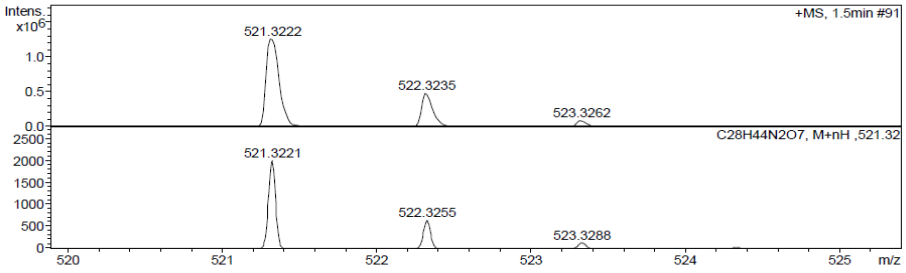

Figure 3.35 HRMS of **14f**.

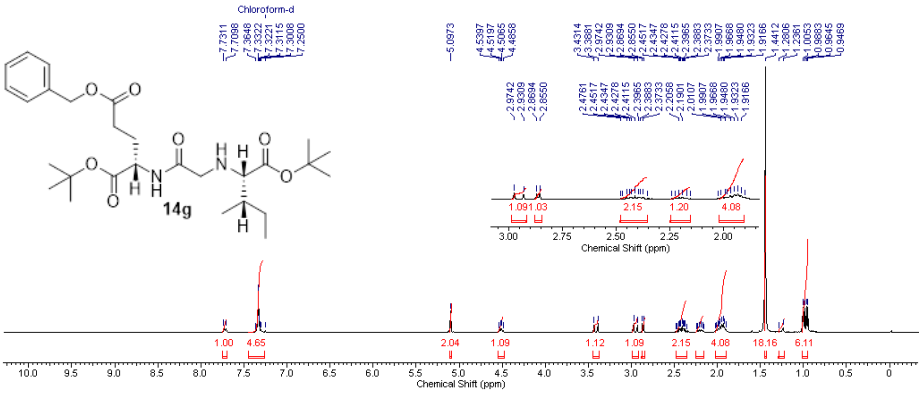

Figure 3.36 ^{1}H NMR spectrum (400 MHz, $CDCl_3$) of **14g**.

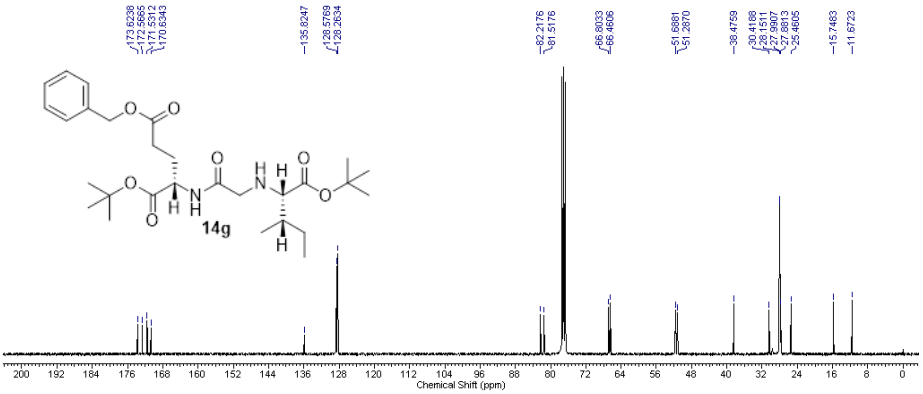

Figure 3.37 ^{13}C NMR spectrum (100 MHz, $CDCl_3$) of **14g**.

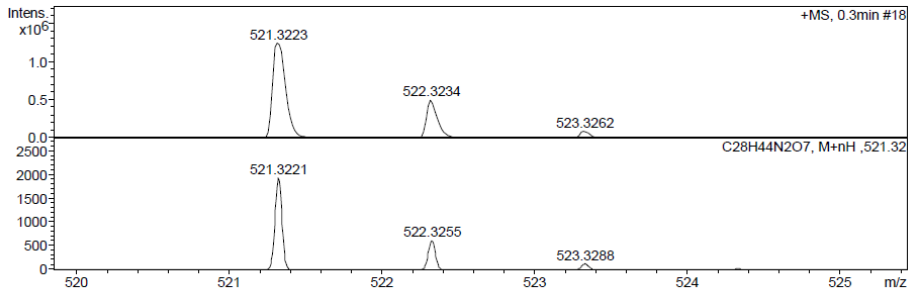

Figure 3.38 HRMS of **14g**.

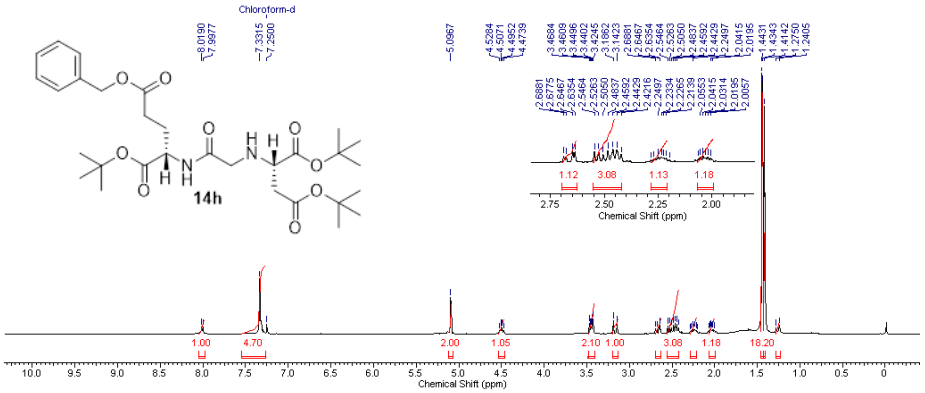

Figure 3.39 ^{1}H NMR spectrum (400 MHz, $CDCl_3$) of **14h**.

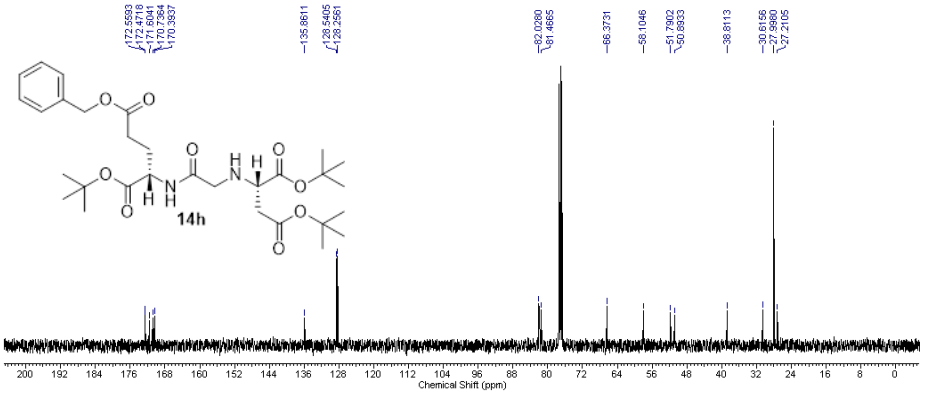

Figure 3.40 ^{13}C NMR spectrum (100 MHz, $CDCl_3$) of **14h**.

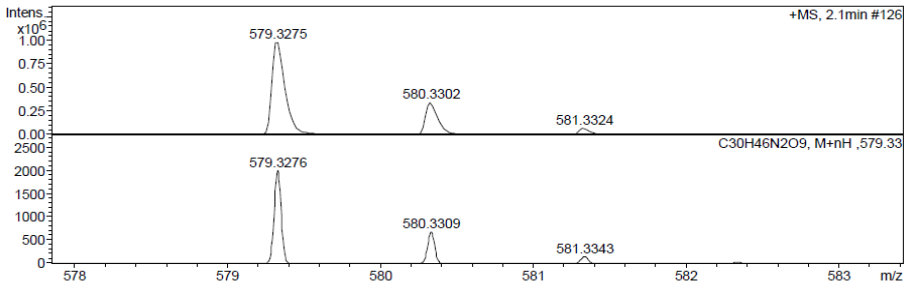

Figure 3.41 HRMS of **14h**.

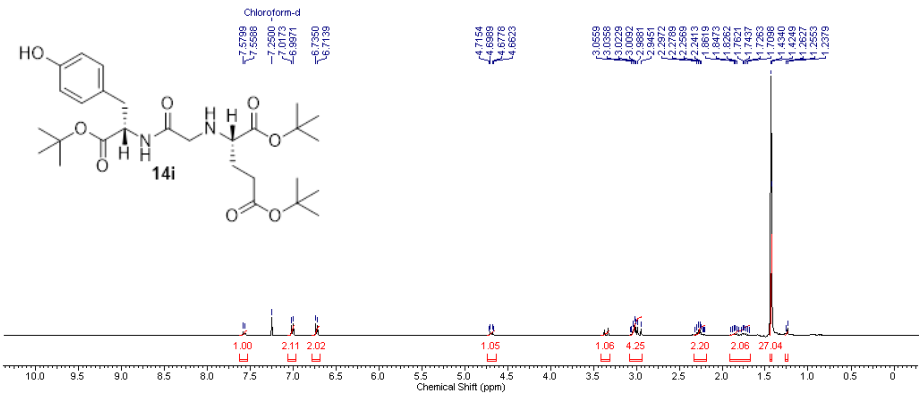

Figure 3.42 ^{1}H NMR spectrum (400 MHz, $CDCl_3$) of **14i**.

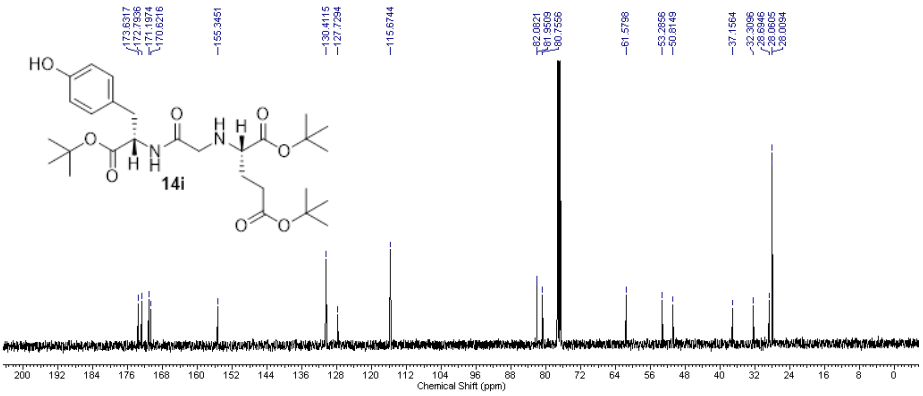

Figure 3.43 ^{13}C NMR spectrum (100 MHz, $CDCl_3$) of **14i**.

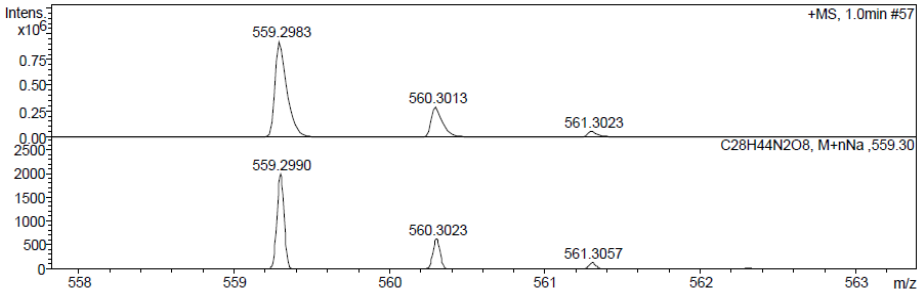

Figure 3.44 HRMS of **14i**.

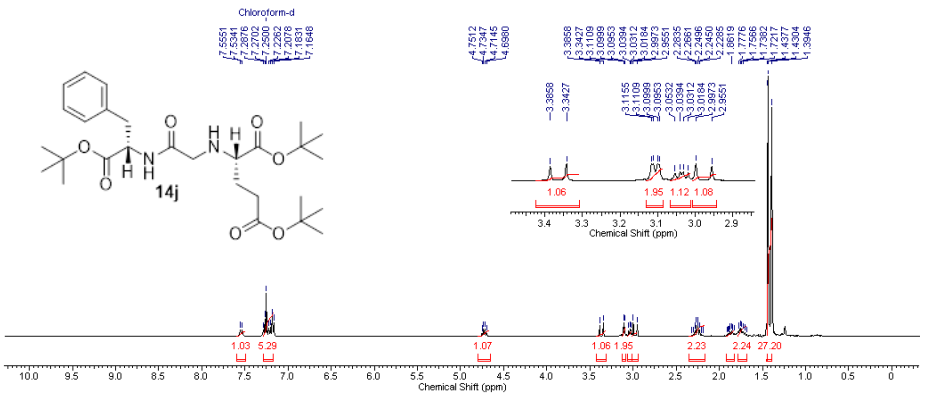

Figure 3.45 ^{1}H NMR spectrum (400 MHz, $CDCl_3$) of **14j**.

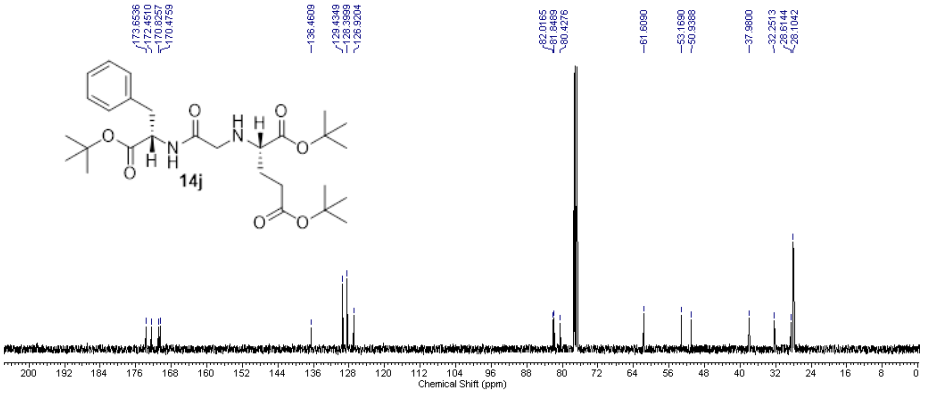

Figure 3.46 ^{13}C NMR spectrum (100 MHz, $CDCl_3$) of **14j**.

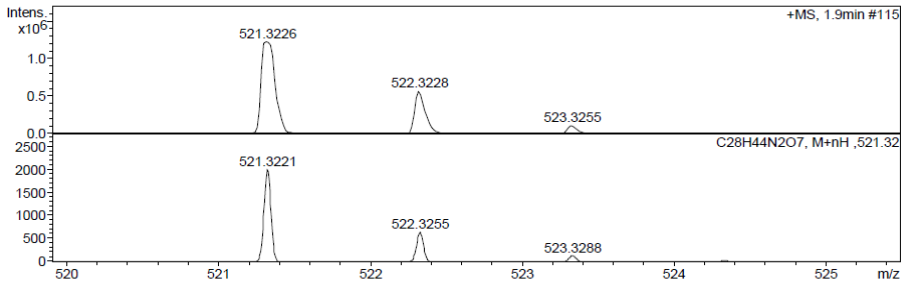

Figure 3.47 HRMS of **14j**.

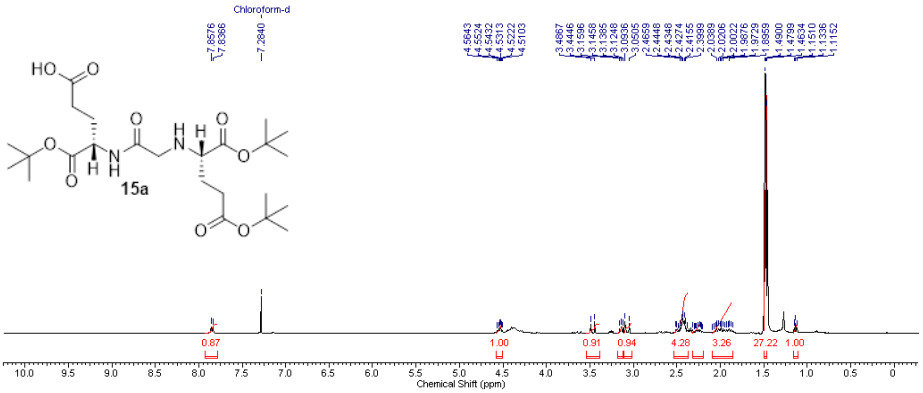

Figure 3.48 ^{1}H NMR spectrum (400 MHz, $CDCl_3$) of **15a**.

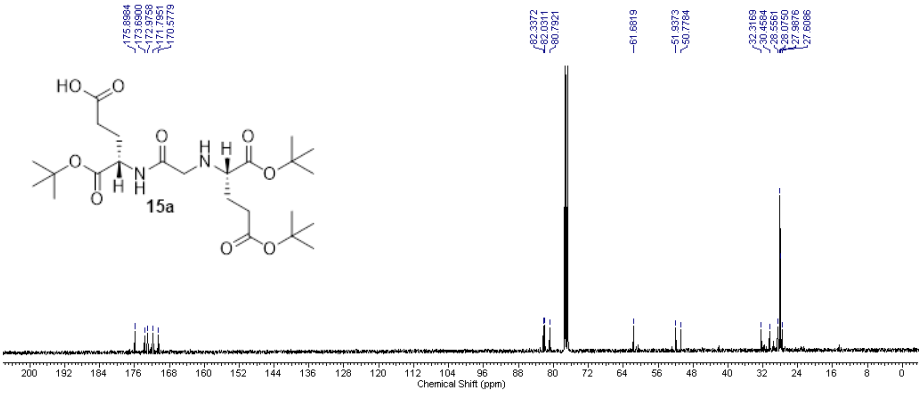

Figure 3.49 ^{13}C NMR spectrum (100 MHz, $CDCl_3$) of **15a**.

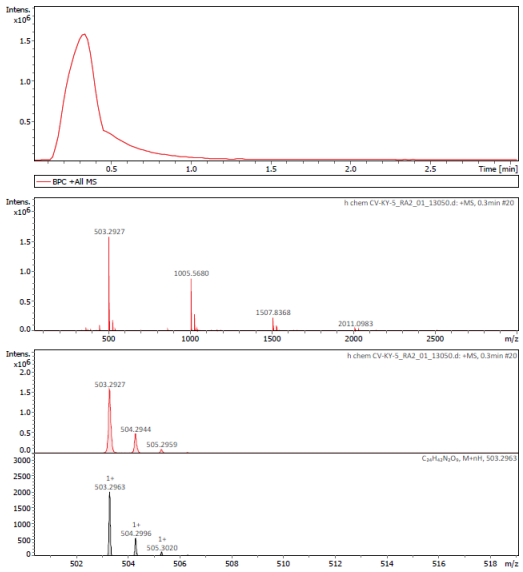

Figure 3.50 HRMS of **15a**.

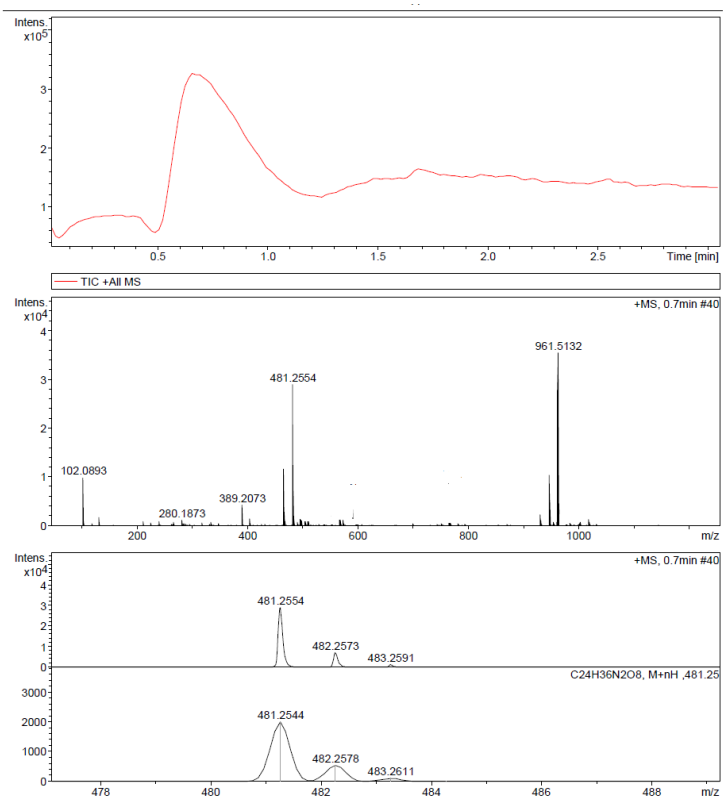

Figure 3.51 HRMS of **15b**.

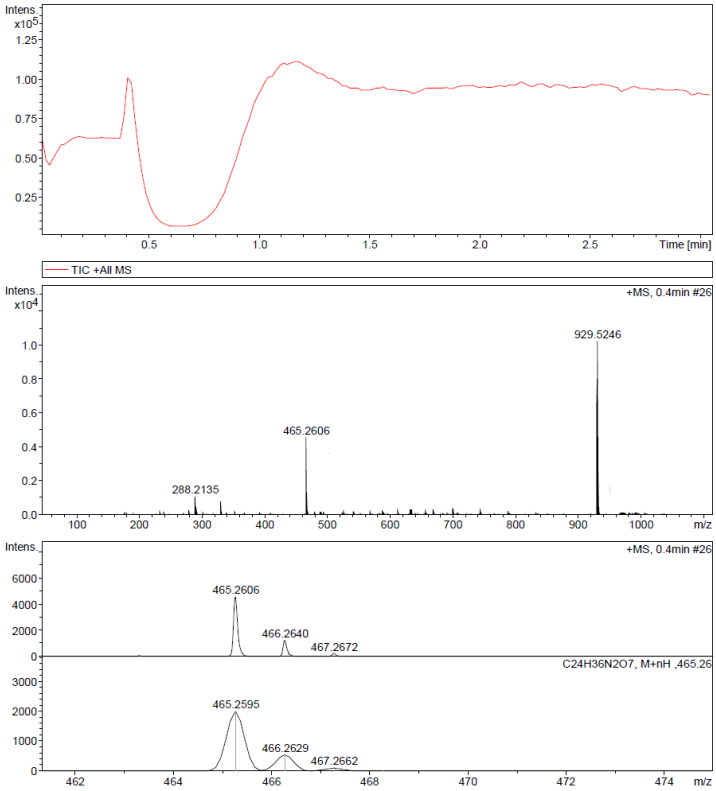

Figure 3.52 HRMS of **15c**.

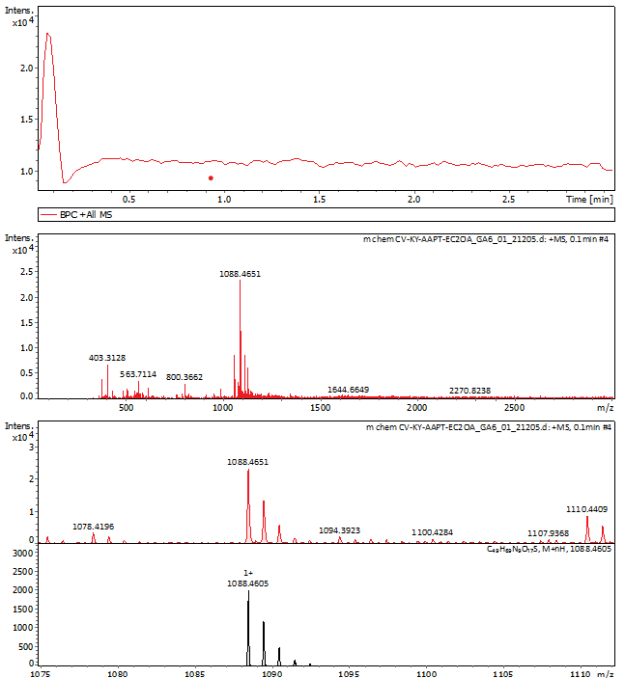

Figure 3.53 HRMS of **22**.

3.5 References

1. Bray F, Laversanne M, Sung H, et al. Global cancer statistics 2022: GLOBOCAN estimates of incidence and mortality worldwide for 36 cancers in 185 countries. *CA Cancer J Clin*. 2024, 74, 229–263. doi:10.3322/caac.21834.

2. Sundaresan VM, Smani S, Rajwa P, et al. Prostate-specific antigen screening for prostate cancer: Diagnostic performance, clinical thresholds, and strategies for refinement. *Urol Oncol Semin Orig Investig*. 2024, 43, 41–48. doi:10.1016/j.urolonc.2024.06.003.

3. Krilaviciute A, Becker N, Lakes J, et al. Digital rectal examination is not a useful screening test for prostate cancer. *Eur Urol Oncol*. 2023, 6, 566–573. doi:10.1016/j.euo.2023.09.008.

4. Gudmundsson J, Sigurdsson JK, Stefansdottir L, et al. Genome-wide associations for benign prostatic hyperplasia reveal a genetic correlation with serum levels of PSA. *Nat Commun*. 2018, 9, 1–8. doi:10.1038/s41467-018-06920-9.

5. Bagrodia A, DiBlasio C, Wake R, Derweesh I. Adverse effects of androgen deprivation therapy in prostate cancer: Current management issues. *Indian J Urol*. 2009, 25, 169–176. doi:10.4103/0970-1591.52907.

6. Abdollah F, Sun M, Schmitges J, et al. Cancer-specific and other-cause mortality after radical prostatectomy versus observation in patients with prostate cancer: Competing-risks analysis of a large North American population-based cohort. *Eur Urol*. 2011, 60, 920–930. doi:10.1016/j.eururo.2011.06.039.

7. Mohtavinejad N, Shafiee Ardestani M, Khalaj A, et al. Application of radiolabeled peptides in tumor imaging and therapy. *Life Sci*. 2020, 258, 118206–118214. doi:10.1016/j.lfs.2020.118206.

8. Banerjee SR, Pullambhatla M, Byun Y, et al. ^{68}Ga-Labeled

inhibitors of prostate-specific membrane antigen (PSMA) for imaging prostate cancer. *J Med Chem*. 2010, 53, 5333–5341. doi:10.1021/jm100623e.

9. Hillier SM, Maresca KP, Lu G, et al. ^{99m}Tc-Labeled small-molecule inhibitors of prostate-specific membrane antigen for molecular imaging of prostate cancer. *J Nucl Med*. 2013, 54, 1369–1376. doi:10.2967/jnumed.112.116624.

10. Maes J, Gesquière S, De Spiegeleer A, Maes A, Van de Wiele C. Prostate-specific membrane antigen biology and pathophysiology in prostate carcinoma, an update: Potential implications for targeted imaging and therapy. *Int J Mol Sci*. 2024, 25, 9755–9761. doi:10.3390/ijms25179755.

11. Wang F, Li Z, Feng X, Yang D, Lin M. Advances in PSMA-targeted therapy for prostate cancer. *Prostate Cancer Prostatic Dis*. 2022, 25, 11–26. doi:10.1038/s41391-021-00394-5.

12. Neale JH, Yamamoto T. N-acetylaspartylglutamate (NAAG) and glutamate carboxypeptidase II: An abundant peptide neurotransmitter-enzyme system with multiple clinical applications. *Prog Neurobiol*. 2020, 184, 101722–101731. doi:10.1016/j.pneurobio.2019.101722.

13. Jackson PF, Cole DC, Slusher BS, et al. Design, synthesis, and biological activity of a potent inhibitor of the neuropeptidase N-acetylated α-linked acidic dipeptidase. *J Med Chem*. 1996, 39, 619–622. doi:10.1021/jm950801q.

14. Gourni E, Henriksen G, Gamez P, Caballero AB. Metal-based PSMA radioligands. *Molecules*. 2017, 22, 1–34. doi:10.3390/molecules22040523.

15. Sengupta S, Pandit A, Krishnan MA, Sharma R, Kularatne SA, Chelvam V. Design, synthesis, and biological evaluation of novel thiourea derivatives as small molecule inhibitors for prostate specific membrane antigen. *Bioorg Chem*. 2025, 155, 108130–

108148. doi:10.1016/j.bioorg.2025.108130.

16. Murce E, Beekman S, Spaan E, et al. Preclinical evaluation of a PSMA-targeting homodimer with an optimized linker for imaging of prostate cancer. *Molecules*. 2023, 28, 4022–4032. doi:10.3390/molecules28104022.

17. Kopka K, Benešová M, Bařinka C, Haberkorn U, Babich J. Glu-ureido-based inhibitors of prostate-specific membrane antigen: Lessons learned during the development of a novel class of low-molecular-weight theranostic radiotracers. *J Nucl Med*. 2017, 58, 17–26. doi:10.2967/jnumed.116.186775.

18. Juzeniene A, Stenberg VY, Bruland ØS, Larsen RH. Preclinical and clinical status of PSMA-targeted alpha therapy for metastatic castration-resistant prostate cancer. *Cancers (Basel)*. 2021, 13, 1–25. doi:10.3390/cancers13040779.

19. Krishnan MA, Yadav K, Roach P, Chelvam V. A targeted near-infrared nanoprobe for deep-tissue penetration and imaging of prostate cancer. *Biomater Sci*. 2021, 9, 2295–2312. doi:10.1039/d0bm01970d.

20. Krishnan MA, Pandit A, Sharma R, Chelvam V. Imaging of prostate cancer: Optimizing affinity to prostate specific membrane antigen by spacer modifications in a tumor spheroid model. *J Biomol Struct Dyn*. 2022, 4, 9909–9930. doi:10.1080/07391102.2021.1936642.

21. Kozikowski AP, Zhang J, Nan F, et al. Synthesis of urea-based inhibitors as active site probes of glutamate carboxypeptidase II: Efficacy as analgesic agents. *J Med Chem*. 2004, 47, 1729–1738. doi:10.1021/jm0306226.

22. Kularatne SA, Zhou Z, Yang J, Post CB, Low PS. Design, synthesis, and preclinical evaluation of prostate-specific membrane antigen targeted (99m)Tc-radioimaging agents. *Mol Pharm*. 2009, 6, 790–800. doi:10.1021/mp9000712.

Chapter 4

Role of spacers in PSMA-targeted bioconjugates in the diagnosis of prostate cancer using radioactive isotope ^{99m}Tc

4.1 Introduction

Prostate cancer (PCa) remains a significant challenge, accounting for 1.46 million new cases and 3.96 lakh deaths worldwide in the year 2022, making it the second most diagnosed cancer in men globally.[1] The infiltrative nature of tumour cells makes it challenging to differentiate between healthy and tumour masses, causing incomplete removal of cancerous tissue at margins or removal of healthy tissues.[2] Current approaches employing magnetic resonance imaging (MRI), ultrasound, X-ray and computed tomography (CT) have disadvantages such as: (i) low spatial and contrast resolutions, (ii) provides only anatomical details (iii) lack of functional or physiological details (iv) inability to differentiate necrotic tumours from fibrous tissues, and (v) limited sensitivity and signal specificity leading to recurrence of cancer.[3] Fluorescent imaging has proven to be an effective, non-invasive, highly sensitive, and real-time method for visualising and differentiating tumour masses from healthy tissues.[4] Fluorescence imaging works on the principle of the fluorescent probe's in situ excitation and light emission. Small molecule dyes such as cyanine, rhodamine, or BODIPY are commonly used as fluorescent probes.[5,6] However, they are limited by their excitation and emission wavelengths occurring in the UV-Vis range that lies outside the biological transparency window. Apart from that, these fluorophores also have other disadvantages, including background noise, autofluorescence, and limited penetration depth (1–3 mm). In the visible wavelength region, various vital organs and endogenous chromophores such as flavins, NADH, and haemoglobin, cause autofluorescence, resulting in background noise and interference with the fluorescence signals from tumour nodules.[7] There is also limited penetration depth encountered in this region due to i) photon

reflections from the tissue surface, scattering of photons due to non-homogeneous tissue surface, photon absorption by various chromophores, and autofluorescence.[8] Recently, the development of radioisotope-based diagnostic agents has gained attention due to their low cost, availability, and favourable biological and chemical properties.[9] Clinical imaging using positron emission tomography (PET) based radionuclides ^{18}F, ^{68}Ga, ^{64}Cu, ^{11}C, ^{124}I, and ^{44}Sc has gained widespread clinical acceptance.[10] This discovery paved the way for different diagnostic techniques, including single-photon emission computed tomography (SPECT), which uses radioactive isotopes to visualise organ structure and metabolic activities of various tissues.[11] Radioisotopes offer various advantages over conventional imaging agents.[12] Their chemical property allows their chelation into specific molecules, providing detailed information about their function and potential abnormalities. Technetium-99m (^{99m}Tc) remains one of the most widely used radioactive isotopes, particularly in single photon emission computed tomography (SPECT), due to its physical attributes such as a half-life of 6.02 h and gamma photon emission at 140 keV. Chemically, it enables efficient and stable chelation using a chelating moiety (EC-20), thereby reducing overall costs and allowing non-invasive imaging. This recent advancement in diagnostic techniques has led to the development of various PSMA-targeted radioimaging agents that are currently being clinically developed and pursued for the detection of PCa.[13,14]

The imaging agents can be attached to a targeting ligand that can bind with prostate-specific membrane antigen (PSMA) receptor, which is 1000-fold overexpressed in prostate tumour cells.[15] The internal structure of the PSMA receptor comprises an S1′ glutamate recognition pocket, an S1 pocket, and two Zn^{2+} ions along with an irregularly shaped 20 Å tunnel, which forms a primary binding pocket that interacts with the targeting ligand.[16] Small-molecule PSMA targeting ligands make promising clinical candidates due to rapid clearance from circulation, leading to low background noise post-injection. 3-[(1,3-

dicarboxypropyl)-ureido]pentanedioic acid (DUPA), a member of glutamate-ureido compounds, exhibits high binding affinity for PSMA (K_d = 14 nM).[17] The recent discovery of the secondary binding hydrophobic pocket,[18] located within the PSMA cavity and composed of β sheets, has affinity towards the distantly placed aromatic moiety inside the PSMA cavity. Exploration of the hydrophobic cavity suggested that the introduction of a structural spacer allows optimal length between the aromatic moiety and the targeting ligand for stable interaction with the hydrophobic pocket.[19]

4.2 Results and discussion

The effect of various aromatic substitutions on the binding affinity of the DUPA (2-[3-(1,3-dicarboxypropyl)-ureido] pentanedioic acid) ligand is explored by synthesizing PSMA-targeting radioactive bioconjugates with optimal spacer length to provide maximum binding affinity to the ligand via interaction at the secondary hydrophobic binding pocket in the PSMA protein. Due to various drawbacks and limitations of the fluorescent imaging agents, the radioactive isotope ^{99m}Tc was used. The bioconjugates were designed with an EC-20 chelation moiety formed from the coupling of cysteine, aspartic acid, and 1,2-diaminopropionic acid. Further, aspartic acid was added to increase the polarity and distantly place the EC-20 from the ligand. The systematic arrangement and replacement of aromatic amino acid moieties, such as phenylalanine and aminomethyl benzoic acid, were carried out with aliphatic amino acid such as glycine to determine the impact of aromatic moiety arrangement on the biological activity.

The synthesis of the DUPA targeting ligand is shown in scheme 4.1. The commercially available glutamic acid di-*tert*-butyl ester salt **1** was reacted with triphosgene to yield an intermediate **2**, which, upon further reaction with the salt of γ-benzylated glutamic *tert*-butyl ester **3**, affords DUPA precursor **4** in high yield. The carboxybenzyl group of DUPA precursor **4** was deprotected using catalytic hydrogenolysis in the presence of activated palladium-carbon and hydrogen gas to afford

tris(*t*-butylcarboxyester) protected DUPA targeting ligand **5** with a free γ-carboxylic acid group.

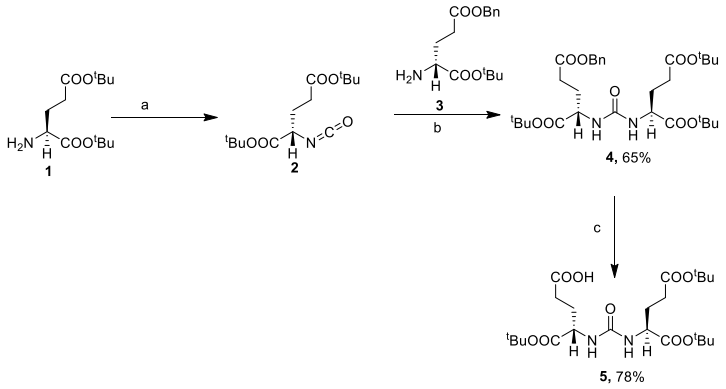

Scheme 4.1 Reagents and conditions: (a) Triphosgene, Et_3N, CH_2Cl_2, −50 °C, 1.5 h, then rt, 1.5 h; (b) Et_3N, CH_2Cl_2, rt, overnight; (c) Pd/C (10 mol% %), H_2 (1 atm), MeOH, rt, 24 h.

The γ-carboxylic acid group of **5** has been used as a handle to attach the polypeptide chain of the bioconjugate. The solid-phase peptide synthesis (SPPS) of DUPA_Bioconjugates **12**–**17** was carried out as shown in scheme 4.2, using H-Cys(Trt)-2-Cl Trt resin **6**. The free NH_2 group of the resin was coupled with Fmoc-Asp(O^{t}Bu)-OH using PyBOP, DIPEA, and DMF for 6 h to obtain dipeptide **7**. The Fmoc deprotection was carried out using 20% piperidine in DMF for 30 min, followed by coupling with 1,2-diaminopropionic acid to obtain tripeptide **8**. The tripeptide **8** was then attached sequentially with two aspartic acid moieties to obtain pentapeptide **9**. The pentapeptide **9** was then coupled with combinations of three amino acids for the synthesis of the bioconjugates **12**–**17**; specifically, for bioconjugate **12** pentapeptide **9** was coupled with 4-aminomethylbenzoic acid (AMBA) and two units of phenylalanine; bioconjugate **13** (phenylalanine, 4-aminomethylbenzoic acid and phenylalanine); bioconjugate **14** (two units of phenylalanine and glycine); bioconjugate **15** (4- aminomethyl benzoic acid and two units of glycine); biconjugate **16** (phenylalanine and two units of glycine), and bioconjugate **17** (three units of glycine) to yield the corresponding peptides **10**. The polypeptides **10** were then coupled with Fmoc-8-aminocaprylic acid to provide **11**, and finally, the

targeting ligand **5** was attached to the growing peptide chain. The bioconjugates were cleaved from the resin using a cleavage cocktail solution to obtain DUPA_Bioconjugates **12**–**17**, which were purified using RP-HPLC and chelated with ^{99m}Tc to obtain ligand-conjugated PSMA-targeting [^{99m}Tc] chelated radioactive bioconjugates **18**–**23** as shown in scheme 4.3. For efficient labelling of ^{99m}Tc, the cold kit was prepared by using a lyophilised mixture of AAPT-spacer-Dap-Asp-Cys, stannous chloride to reduce ^{99m}Tc-pertechnetate, and sodium *R*-D-glucoheptonate to stabilise the Sn(II) and ^{99m}Tc(IV) intermediates. After adding Na^{99m}TcO$_4$, complexation of the radiotracer was achieved by boiling the solution for 18 min in a boiling water bath and then cooling to room temperature. The desired [^{99m}Tc] DUPA_Bioconjugates **18**–**23**, obtained with high specific radioactivity (purity >98%), were further used for *in vitro* studies.

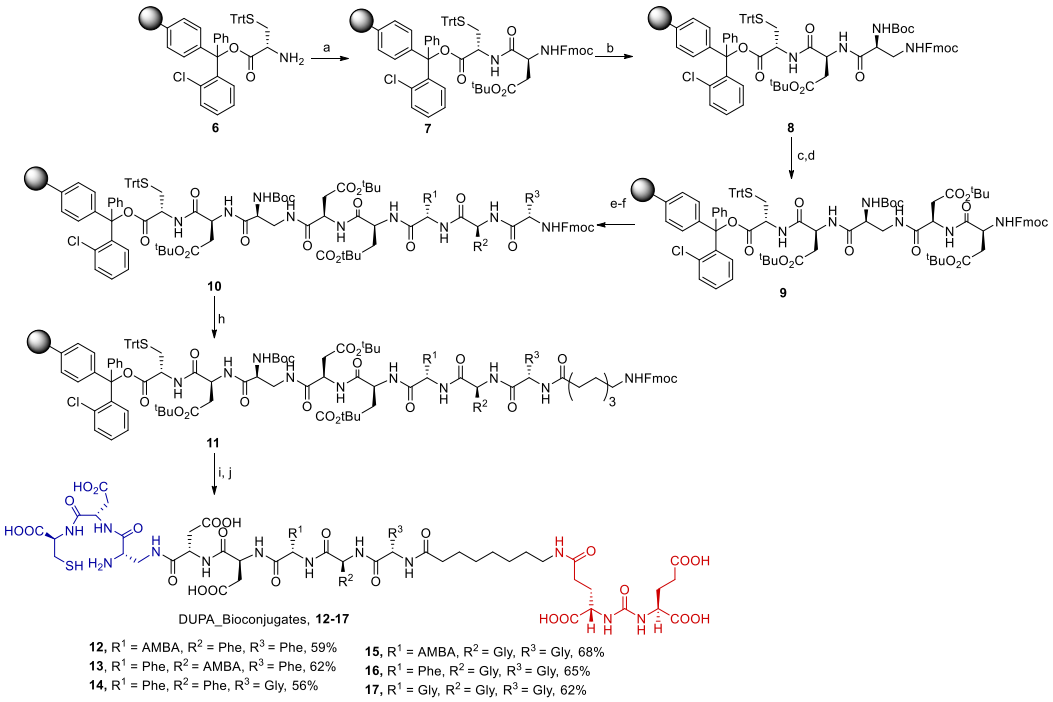

Scheme 4.2 Synthesis of DUPA_Bioconjugates **12**–**17** using SPPS: Reagents and conditions: (a) Fmoc-Asp(O^{t}Bu)-OH, PyBOP, DIPEA, DMF, 6 h; (b) (i) 20% Piperidine in DMF, rt, 30 min; (ii) Fmoc-diamino propionic (DAP) acid, PyBOP, DIPEA, DMF, 6 h; (c) (i) 20% Piperidine in DMF, rt, 30 min; (ii) Fmoc- Asp(O^{t}Bu)-OH, PyBOP, DIPEA, DMF, 6 h; (d) (i) 20% Piperidine in DMF, rt, 30 min; (ii) Fmoc- Asp(O^{t}Bu)-

OH, PyBOP, DIPEA, DMF, 6 h; (e) (i) 20% Piperidine in DMF, rt, 30 min; (ii) Fmoc-R^1-OH, PyBOP, DIPEA, DMF, 6 h; (f) (i) 20% Piperidine in DMF, rt, 30 min; (ii) Fmoc-R^2-OH, PyBOP, DIPEA, DMF, 6 h; (g) (i) 20% Piperidine in DMF, rt, 30 min; (ii) Fmoc-R^3-OH, PyBOP, DIPEA, DMF, 6 h; (h) (i) 20% Piperidine in DMF, rt, 30 min; (ii) Fmoc-8-Aoc-OH, PyBOP, DIPEA, DMF, 6 h; (i) (i) 20% Piperidine in DMF, rt, 30 min; (ii) **5**, PyBOP, DIPEA, DMF, 6 h; (j) (i) TFA/H_2O/TIPS/EDT (92.5:2.5:2.5:2.5) (1 × 5 mL, 30 min; 2 × 2.5 mL, 15 min); (ii) Evaporate TFA; (iii) Precipitate in ice cold diethyl ether.

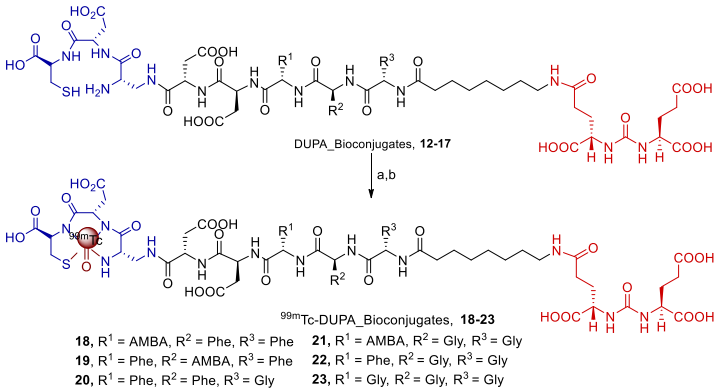

Scheme 4.3 Synthesis of [^{99m}Tc] DUPA_Bioconjugates **18–23.** Reagents and conditions: (a) $SnCl_2$, α-D-glucoheptonate, $Na^{99m}TcO_4$, (b) Boil in water bath for 18 min.

4.2.1 Cell viability studies

The cytotoxicity of DUPA_Bioconjugates **12–17** on various non-cancerous cell lines, such as macrophage (RAW264.7), human embryonic kidney cell line (HEK293), Madin-Darby canine kidney cells (MDCK), and Hepatoma cell line (Hep G2) were performed using methylthiazolydiphenyl-tetrazolium bromide (MTT) assay. The cells were incubated with various concentrations of bioconjugates (10 μM–10 pM) for an incubation periods of 24 h and 48 h. The results, as shown in figure 4.1, demonstrate that even at higher concentrations and longer incubation periods, the IC_{50} values remain in the high micromolar (μM) range, varying from 71 μM to 160 μM for 48 h and 89 μM to 263 μM for 24 h. These outcomes validate the non-toxic nature of

DUPA_Bioconjugates **12**–**17** and indicate their potential safety for preclinical use, with cell viability exceeding 98%.

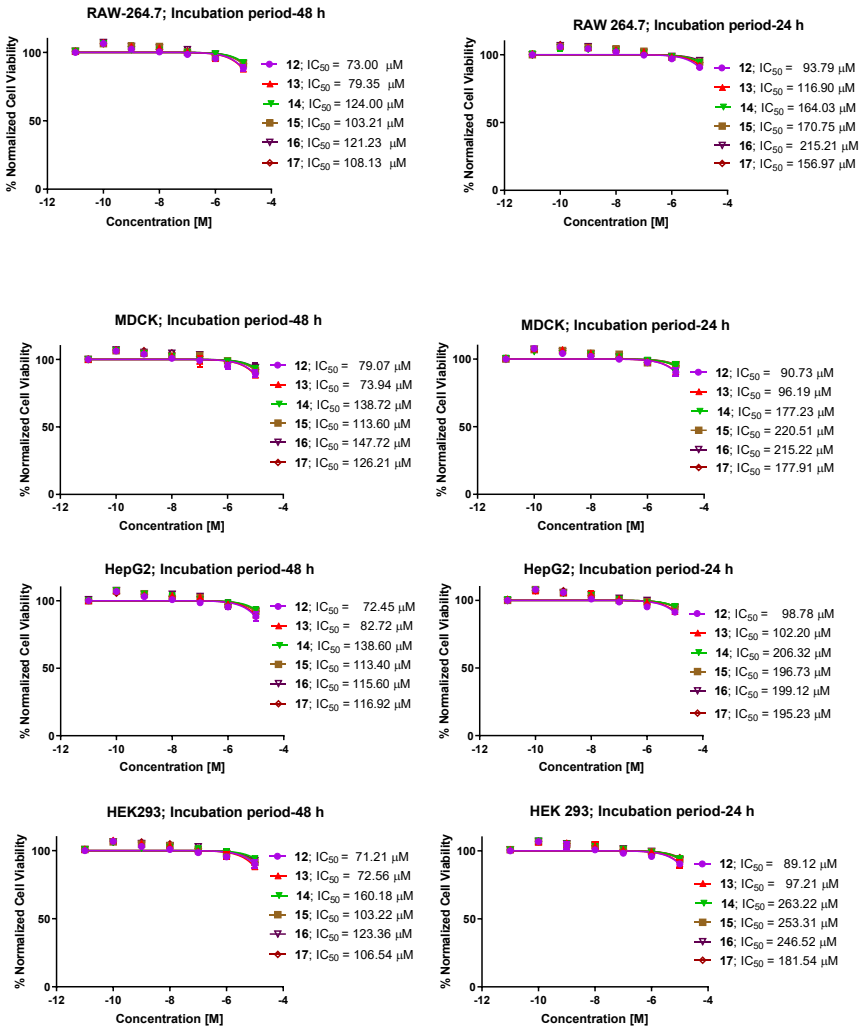

Figure 4.1 Cytotoxicity studies of **12**–**17** in RAW 264.7, MDCK, HepG2, and HEK 293 cell lines for 48 h and 24 h incubation periods. Data are expressed in triplicate as mean ± S.D. (n=3).

4.2.2 Binding affinity studies

The ability of the bioconjugates [^{99m}Tc] DUPA_Bioconjugates **18**–**23** to bind with the PSMA receptors was evaluated by incubating PSMA^{+} LNCaP cells with increasing concentrations of [^{99m}Tc] DUPA_Bioconjugates **18**–**23** (10, 20, 30, 40, 50, 75, 100, 125, 300, 750, 1215 nM). A hyperbolic curve with a dissociation constant (K_d) ranging from 28–88 nM for bioconjugates **18**–**23**, respectively, (Figure 4.2), were obtained. The low nanomolar K_d values of bioconjugates **18** and **19**, containing aromatic amino acids (**18**, 4-aminomethylbenzoic acid

and two units of phenylalanine; **19**, phenylalanine, 4-aminomethylbenzoic acid and phenylalanine), signify the strong and specific binding with PSMA receptor, as indicated by performing a competition study with a standard PSMA inhibitor, 2-PMPA (2-phosphonomethylpentanedioic acid). The significant reduction of binding affinity constants from 51 nM to 88 nM was observed when the aromatic amino acids were replaced with aliphatic amino acid such as glycine in DUPA_Bioconjugates **20** to **23**. The results validate the effect of hydrophobicity and π-π-stacking interaction of aromatic amino acid residues in the secondary binding pocket of PSMA (Figure 4.3).

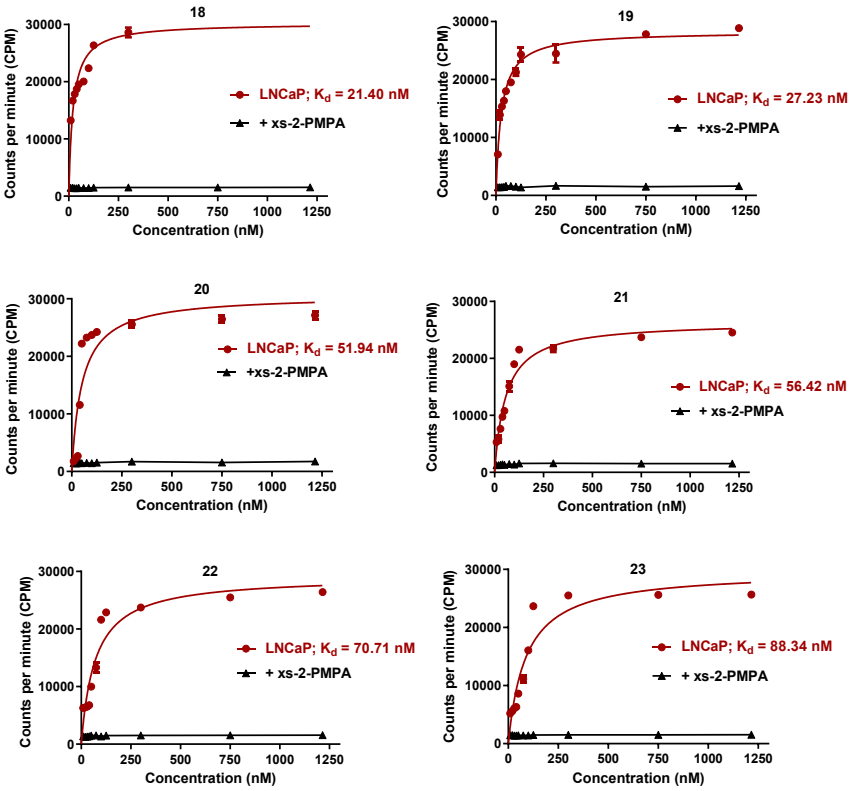

Figure 4.2 Binding affinity constant of [^{99m}Tc] DUPA_Bioconjugates **18**–**23**, in PSMA^{+} LNCaP cell line; Error bars represent S.D. (n=3).

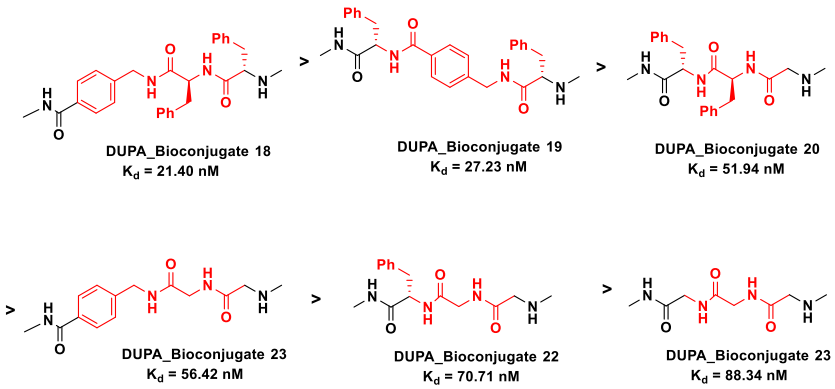

Figure 4.3 A decrease in binding affinity constants of PSMA-targeted DUPA_Bioconjugates **18**–**23** due to replacing aromatic amino acids with a glycine moiety.

4.3 Conclusion

In this chapter, a series of DUPA (2-[3-(1,3-dicarboxypropyl)-ureido]pentanedioic acid) ligand conjugated PSMA-targeting radioactive bioconjugates were synthesized with optimal spacer length to provide maximum binding affinity to the ligand with interaction at the secondary hydrophobic binding pocket present in the PSMA protein. The radioactive bioconjugates were designed by utilising aromatic amino acids such as phenylalanine and aminomethyl benzoic acid, facilitating π-π stacking and hydrophobic interactions with the PSMA amino acid residues, while maintaining the spacer length via 8-aminocaprylic acid and aspartic acid. The *in vitro* binding affinity studies of **18** and **19** have shown the highest binding affinity constants (K_d) of 21 nM and 27 nM, respectively, in $PSMA^+$ LNCaP cells. The significant reduction of binding affinity constants from 51 nM to 88 nM was observed when the aromatic amino acids were replaced with aliphatic amino acid such as glycine in **20**–**23** bioconjugates. This strategic design strengthens the use of radioactive isotope ^{99m}Tc, thereby eliminating the drawbacks of conventional fluorescent imaging agents, making it a clinically favourable and cost-effective technique. This modification establishes an essential implication of the secondary hydrophobic binding site present in the PSMA protein for the development of PSMA-targeted bioconjugates as radioimaging agents.

4.4 Experimental section

4.4.1 General methods and materials

Chlorotrityl resins, Fmoc-protected amino acids, coupling reagents, and solvents used for chemical synthesis of fragments and solid-phase peptide synthesis (SPPS) were procured from Iris Biotech GmbH, Sigma Aldrich, Merck, Spectrochem, TCI, and Expressolv. Dry solvents were prepared using appropriate drying agents and standard procedures. All reactions were carried out in oven-dried glasswares. Moisture-sensitive reactions were performed under a nitrogen atmosphere, and all solutions were transferred via a glass syringe. The progress of the reaction was monitored by thin-layer chromatography (TLC) using silica gel 60 F254 TLC plates and visualized under a UV chamber. The intermediates **4** and **5** were purified by column chromatography using 230–400 mesh size silica gel as the stationary phase with distilled hexane and ethyl acetate as eluents. DUPA targeted bioconjugates **12**–**17** were synthesized using a peptide vessel (Chemglass) following the standard orthogonal peptide coupling methodology. The ^{1}H and ^{13}C NMR spectra were recorded using a Bruker AV 500 MHz NMR spectrometer with TMS as an internal standard. The ^{1}H NMR signals were reported in ppm with reference to residual $CDCl_3$ (7.26 ppm), DMSO-d_6 (2.50 ppm), MeOH-d_4 (3.31 ppm), and multiplicities were reported as s = singlet, d = doublet, t = triplet, q = quartet, m = multiplet or unresolved, and brs = broad singlet, with coupling constants in Hz. $CDCl_3$ and DMSO-d_6 were used as solvents for recording the NMR spectra. DUPA targeted bioconjugates **12**–**17** were obtained as a salt of TFA. Mass spectra were recorded on a Bruker Micro TOF-Q II instrument using positive mode electrospray ionization methods. The DUPA targeted bioconjugates **12**–**17** were purified using an RP-PFP column (XSelect CSH Prep Fluorophenyl 5 µm OBD, 19 mm × 150 mm) in a Buchi Reveleris High Performance Preparative Chromatography instrument. DUPA-targeted bioconjugates **12**–**17** purity was analysed using a Dionex HPLC-Ultimate 3000 Analytical HPLC instrument. The purified bioconjugates were chelated with ^{99m}Tc.

4.4.2 Procedure for synthesis (*S*)-5-benzyl 1-*tert*-butyl 2-(3-((*S*)-1,5-di-*tert*-butoxy-1,5-dioxopentan-2-yl)ureido)pentanedioate (4)

In a double-neck round-bottom flask (50 mL), triphosgene (0.200 g, 0.682 mmol) was dissolved in dry DCM (5 mL), and the solution was cooled to −50 °C. Bis(*tert*-butyl)-L-glutamate.HCl **1** (0.605 g, 2.04 mmol) and triethylamine (2.07 mL, 20.47 mmol) were dissolved in 5 mL of dry DCM, and was added dropwise to the reaction mixture at −50 °C. The reaction mixture was stirred continuously for 1.5 h at –50 °C and then further stirred for 1.5 h at room temperature to generate isocyanate intermediate **2**. After that, a solution of L-glutamic-γ-benzyl-α-*tert*-butyl.HCl **3** (0.675 g, 2.04 mmol) and triethylamine (2.07 mL, 20.47 mmol) in DCM (2 mL) was added to the reaction mixture and stirred overnight at room temperature. After the completion of the reaction, as monitored by TLC, the reaction mixture was diluted with ethyl acetate (1 × 20 mL) and quenched with chilled brine (1 × 10 mL). The aqueous layer was further extracted with EtOAc (3 × 10 mL). The organic layer was dried over anhydrous Na_2SO_4, filtered, and the solvent was evaporated under reduced pressure to afford a crude reaction mixture, which was purified through silica gel (neutral, 100–200 mesh) column chromatography using 25% ethyl acetate and hexane as eluent to obtain purified benzyl tris(*tert*-butylcarboxy) protected DUPA precursor **4**. Yellowish gummy liquid (yield = 82%, 1.23 g), R_f = 0.29 (EtOAc: hexane = 1:3); ^{1}H NMR (400 MHz, $CDCl_3$): δ 7.33 (m, 5H), 5.10–5.04 (m, 4H), 4.38–4.28 (m, 2H), 2.51–2.37 (m, 2H), 2.32–2.23 (m, 2H), 2.20–2.12 (m, 1H), 2.09–2.00 (m, 1H), 1.96–1.81 (m, 2H), 1.44 (s, 9H), 1.43 (s, 9H), 1.41 (s, 9H); ^{13}C NMR (100 MHz, $CDCl_3$): δ 172.9, 172.5, 172.0, 171.9, 156.8, 135.8, 128.5, 128.2, 82.1, 82.0, 80.5, 66.4, 53.1, 53.0, 31.5, 30.3, 28.4, 28.3, 28.1, 28.0; HRMS (ESI) m/z $[M+Na]^+$ calcd. for $C_{30}H_{46}N_2O_9$, 601.3096, found, 601.3092.

4.4.3 Procedure for debenzylation of benzyl tris(*tert*-butylcarboxy) protected DUPA precursor (4) to give (*S*)-5-(*tert*-butoxy)-4-(3-((*S*)-1,5-di-*tert*-butoxy-1,5-dioxopentan-2-yl)ureido)-5-oxopentanoic acid (5)

In a double-neck round-bottom flask (25 mL), a hydrogen-filled bladder was fitted to one neck of the round-bottom flask through a borosilicate glass heavy-wall glass stop cock adapter. DUPA precursor **4** (1 g 1.73 mmol) was added to the 50 mL two-neck round-bottom flask and dissolved in dichloromethane (10 mL). 10% Pd/C (0.160 g, 10 mol%) was added slowly to the mixture, and the reaction mixture was sealed using a rubber septum. The residual air in the reaction vessel was expunged through a syringe needle inserted through the rubber septum connected to a filtration pump through a silicone tube for 2 minutes or until the solution bubbles. The reaction mixture is now filled with hydrogen gas from the bladder via a stop cock and allowed to stir at room temperature for 48 h. After the completion of the reaction, as monitored by TLC, the reaction mixture was filtered through a celite pad (sintered glass filter was half-filled with celite powder) and washed with ethyl acetate (3 × 20 mL) using a suction pump. The ethyl acetate layer was concentrated under reduced pressure, and the crude product was purified through column chromatography using 100% ethyl acetate to obtain pure DUPA targeting ligand **5** for further peptide coupling during SPPS. Colorless viscous liquid solidified on standing (yield = 81%, 678 mg), R_f = 0.48 (EtOAc: hexane = 1:1); ^{1}H NMR (400 MHz, $CDCl_3$): δ 5.01 (d, J = 7.76 Hz, 2H), 4.32 (ddd, J = 5.0, 5.26, 7.76 Hz, 2H), 2.37–2.21 (m, 4H), 2.10–2.01 (m, 2H), 1.89–1.80 (m, 2H), 1.45 (s, 9H), 1.42 (s, 18H); ^{13}C NMR (100 MHz, $CDCl_3$): δ 176.1, 173.1, 172.5, 171.9, 157.8, 82.5, 82.1, 80.6, 53.3, 53.0, 31.5, 30.3, 28.4, 28.1, 28.0, 27.9, 27.8; HRMS (ESI) m/z $[M+Na]^+$ calcd. for $C_{23}H_{40}N_2O_9$, 511.2626, found, 511.2640.

4.4.4 General procedure of solid-phase peptide synthesis

4.4.4.1 Resin swelling

The resins used in solid-phase peptide synthesis were first swollen with DCM (5 mL) for 30 minutes by bubbling nitrogen gas through the beads in the peptide vessel. After draining DCM, the beads were swollen with DMF (3 × 5 mL), repeating the process for 15 minutes.

4.4.4.2 General procedure for the Kaiser test

Kaiser test kit preparation reagents

a) Dissolve 500 mg of ninhydrin in 10 mL of ethanol.
b) Dissolve 80 g of phenol in 20 mL of ethanol.
c) Dilute 2 mL of 0.001M solution of KCN to 100 mL with pyridine.

Add two drops of the above solutions to a few dried resin beads in a glass test tube and heat at 110 °C in a sea sand bath for 2-3 minutes. The freshly prepared Kaiser test kit can be stored at room temperature for 6 months without decomposition. The appearance of dark blue color signifies the presence of free amine groups in the resin beads, indicating the deprotection of the Fmoc group. In contrast, the colourless beads signify the absence of the amine group, marking the completion of the coupling reaction. The test was performed after coupling each amino acid, as well as after the deprotection of the Fmoc group at each step.

4.4.4.3 General procedure for Fmoc deprotection

The Fmoc group of the N-terminus of the growing peptide chain was deprotected using 20% piperidine in DMF (10 mL) by bubbling nitrogen gas through the resin beads for 10 minutes in each step of Fmoc deprotection. The procedure was repeated three times (1 × 4 mL; 2 × 3 mL) to ensure the complete deprotection of the Fmoc group.

4.4.4.4 General procedure for peptide cleavage from resin beads

The peptide was cleaved from the resin beads using 10 mL of cleavage cocktail (a mixture of 9.5 mL trifluoroacetic acid, 0.25 mL triisopropylsilane, and 0.25 mL water) by bubbling nitrogen gas. First, 5 mL of the cocktail was added to the resin, and nitrogen gas was

bubbled for 30 minutes, followed by the addition of the remaining cocktail solution (2 × 2.5 mL), with nitrogen bubbling for 5 minutes each time. The cocktail solution was evaporated under reduced pressure from the mother liquor after peptide cleavage, and the concentrated solution was precipitated in ice-cold diethyl ether. The precipitate was then dried using nitrogen gas, and the obtained crude product was further purified using HPLC.

4.4.4.5 Procedure for solid-phase peptide synthesis of DUPA bioconjugates (12–17)

H-Cys-2-ClTrt resin (0.200 g, 0.148 mmol) was swollen in CH_2Cl_2 (5 mL) for 15 min by bubbling nitrogen, and after draining CH_2Cl_2, the resin beads were swollen again with DMF (5 mL) for 15 min. The solvent was drained using a filtration pump, and the beads were dried until freely flowing. Fmoc-Asp(O^{t}Bu)-OH (118 mg, 0.296 mmol), PyBOP (154 mg, 0.296 mmol), and DIPEA (0.25 mL, 1.48 mmol) were dissolved in DMF (0.5 mL) in a 2 mL glass vial, mixed thoroughly using a Pasteur pipette, added to the peptide vessel containing resin beads and the coupling reaction was carried out for 6 h by bubbling a stream of nitrogen gas through the resin beads in the peptide vessel. The resin beads were washed with DMF (3 × 5 mL), followed by isopropanol (3 × 5 mL) for 10 min each. The solvent was drained using a filtration pump, and the beads were dried until freely flowing by bubbling N_2 gas through the peptide vessel. The amide coupling was confirmed by performing the Kaiser test. Next, the FmocNH protecting group was cleaved by addition of 20% piperidine in DMF (1 × 4 mL; 2 × 3 mL) for 10 min each to the resin beads. The resin beads were washed with DMF (3 × 5 mL) and isopropanol (3 × 5 mL). The solvent was drained using a filtration pump, and the beads were dried until freely flowing by bubbling N_2 gas through the resin beads in the peptide vessel. The formation of free amine was confirmed by performing the Kaiser test. Consecutively, Boc-Dap(Fmoc)-OH (137 mg, 0.296 mmol), Fmoc-Asp(O^{t}Bu)-OH (118 mg, 0.296 mmol), and Fmoc-Asp(O^{t}Bu)-OH (118 mg, 0.296 mmol), were coupled in sequence to the growing peptide chain, as mentioned before. The amino acids were then sequentially

varied for the preparation of bioconjugates **12** [Fmoc-4-Abz-OH (110 mg, 0.296 mmol), Fmoc-Phe-OH (114 mg, 0.296 mmol), and Fmoc-Phe-OH (114 mg, 0.296 mmol)]; **13** [Fmoc-Phe-OH (114 mg, 0.296 mmol), Fmoc-4-Abz-OH (110 mg, 0.296 mmol), and Fmoc-Phe-OH (114 mg, 0.296 mmol)]; **14** [Fmoc-Phe-OH (114 mg, 0.296 mmol), Fmoc-Phe-OH (114 mg, 0.296 mmol), and Fmoc-Gly-OH (88 mg, 0.296 mmol)]; **15** [Fmoc-4-Abz-OH (110 mg, 0.296 mmol), Fmoc-Gly-OH (88 mg, 0.296 mmol), and Fmoc-Gly-OH (88 mg, 0.296 mmol)]; **16** [Phe-OH (114 mg, 0.296 mmol), Fmoc-Gly-OH (88 mg, 0.296 mmol) and Fmoc-Gly-OH (88 mg, 0.296 mmol)]; **17** [Fmoc-Gly-OH (88 mg, 0.296 mmol), Fmoc-Gly-OH (88 mg, 0.296 mmol), Fmoc-Gly-OH (88 mg, 0.296 mmol)], and finally Fmoc-8-Aoc-OH (112 mg, 0.296 mmol) was coupled to the growing peptide chains to complete the synthesis. After deprotection of the NHFmoc group from the last amino acid, Fmoc-8-Aoc-OH, the targeting ligand **5** (144 mg, 0.296 mmol), PyBOP (154 mg, 0.296 mmol), and DIPEA (0.25 mL, 1.48 mmol) dissolved in DMF (0.5 mL) in a 2 mL glass vial, mixed thoroughly using a Pasteur pipette, was added to the peptide vessel containing resin beads and the coupling reaction was continued for 6 h. The resin beads were washed with DMF (3 × 5 mL), followed by isopropanol (3 × 5 mL). The solvent was drained using a suction pump, and the beads were dried until freely flowing by bubbling N_2 gas through the resin beads in the peptide. The coupling was confirmed by performing the Kaiser test. A mixture of 9.25 mL trifluoroacetic acid (TFA), 0.25 mL ethane dithiol, 0.25 mL triisopropylsilane (TIPS), and 0.25 mL H_2O was prepared in a 15 mL centrifuge tube, and 5 mL of this cleavage cocktail solution was added to the resin beads. Nitrogen gas was bubbled through the solution for 30 minutes. The cocktail solution with cleaved ligand targeted cysteine bioconjugates **12**–**17** in the peptide vessel were collected into a round-bottom flask (25 mL). The resin beads were treated again with the remaining cocktail solution (2 × 2.5 mL) for 15 minutes each, and the mother liquor was collected in the same round-bottom flask (25 mL). The pooled cocktail mixture with cleaved peptide bioconjugates **12**–**17** were transferred to a 15 mL centrifuge tube, fitted with a needle-pierced

septum, and concentrated under reduced pressure to obtain a viscous liquid. Ice-cold ether (5 mL) was added to the concentrated, viscous mixture to precipitate ligand-targeted bioconjugates **12**–**17** as white solids, and the solids were washed with ice-cold ether (3 × 5 mL).

The crude bioconjugates **12**–**17** were purified by RP-HPLC using a pentafluorophenyl preparative column (5 µm, 10 mm × 150 mm), and the pure fractions were freeze-dried to yield ligand-targeted cysteine chelating bioconjugates **12**–**17**.

4.4.5 HPLC purification

The crude bioconjugates **12**–**17** were purified using a Buchi Reveleris Prep RP-HPLC System. Crude bioconjugates **12−17** were dissolved in a mixture of CH_3CN:H_2O (1:1, 1 mL) and injected into the sample injector for elution using RP-PFP (Reverse Phase PentafluoroPhenyl) preparative column (XSelect CSH Prep Fluorophenyl 5 µm; 19 × 150 mm). A flow rate of 10 mL/min (mobile phase, A = 10 mM NH_4OAc buffer, pH = 5; B = acetonitrile (ACN)) is maintained throughout the run, and the mobile phase gradient was gradually changed from 0% B (v/v) to 95% B (v/v) over 24 min. The mobile phase gradient was further increased to 100% B (v/v) in another 2 min. The chromatograms were recorded at λ = 240, 254, and 280 nm for bioconjugates **12**–**17,** respectively. Pure fractions of crude bioconjugates **12**–**17** were collected using an automatic fraction collector. The organic solvent was evaporated under reduced pressure using a rotary evaporator, and the aqueous solution was lyophilized for 48 h to yield pure bioconjugates **12**–**17**.

DUPA_Bioconjugate **12**, White solid (yield = 59%, retention time (t_R)= 11.2 min, HRMS (ESI) m/z $[M+H]^+$ calcd. for ($C_{63}H_{82}N_{12}O_{24}S$):1423.5358; found: 1423.5231

DUPA_Bioconjugate **13**, White solid (yield = 62%, retention time (t_R)= 11.3 min, HRMS (ESI) m/z $[M+H]^+$ calcd. for ($C_{63}H_{82}N_{12}O_{24}S$):1423.5358; found: 1423.5270

DUPA_Bioconjugate **14**, White solid (yield = 56%, retention time (t_R)= 12.1 min, HRMS (ESI) m/z $[M+H]^+$ calcd. for ($C_{57}H_{78}N_{12}O_{24}S$):1347.5045; found: 1347.4082

DUPA_Bioconjugate **15**, White solid (yield = 68%, retention time (t_R)= 12.5 min, HRMS (ESI) m/z $[M+H]^+$ calcd. for ($C_{49}H_{70}N_{12}O_{24}S$):1243.4419; found: 1242.3538

DUPA_Bioconjugate **16**, White solid (yield = 65%, retention time (t_R)= 13.1 min, HRMS (ESI) m/z $[M+H]^+$ calcd. for ($C_{50}H_{72}N_{12}O_{24}S$):1257.4576; found: 1257.4215

DUPA_Bioconjugate **17**, White solid (yield = 62%, retention time (t_R)= 15.2 min, HRMS (ESI) m/z $[M+H]^+$ calcd. for ($C_{43}H_{66}N_{12}O_{24}S$):1167.4106; found: 1167.4021

4.4.6 Procedure for non-radioactive kit preparation of chelating bioconjugates 18–23

A solution of stannous chloride dihydrate (0.80 mg, 0.003 mmol) in 0.2 M hydrochloric acid (0.8 mL) was added to a solution of sodium-α-D-glucoheptonate dihydrate (800 mg, 2.815 mmol) in nitrogen-purged water. Chelating bioconjugates **18**–**23** (0.001 mmol) were then added to the reaction mixture while continuous nitrogen purging. The pH of the solution was adjusted to 6.8 using 0.1 N sodium hydroxide solution. After the pH adjustment, nitrogen-purged water was added to bring the total volume to 10 mL. The solution was then dispensed in 5 mL vials (1 mL/vial) under a nitrogen atmosphere and lyophilized for 48 h. The vials were then sealed under a nitrogen atmosphere to yield the non-radioactive kits, which were stored at –20 °C until further use.

4.4.7 Procedure for chelation of radioisotope ^{99m}Tc with bioconjugates 12–17

In the cold kit vial containing bioconjugates **12**–**17**, a solution of sodium pertechnate ^{99m}Tc (1 mL, 15 mCi) was added, and the vials were kept in boiling water for 18 min, rendering ^{99m}Tc chelated bioconjugates **18**–**23** that were cooled to room temperature before use.

4.4.8 Cell lines and culture

LNCaP (CRL-1740) and PC3 (CRL-1435) cancer cell lines were procured from ATCC. Macrophage (RAW264.7), Human Embryonic Kidney cell line (HEK293), Madin-Darby Canine Kidney cells (MDCK), and Hepatoma cell line (Hep G2) were procured from the National Centre for Cell Sciences (NCCS), Pune, India. The cell lines were grown in T-75 Flask (Tarson, 950040) containing sterile filtered RPMI 1640 medium (Thermo Fisher, 11875093) or F12K medium (Thermo Fisher, 21127022) supplemented with fetal bovine serum (Thermo Fisher, 1027016), 100 mM of sodium pyruvate (Thermo Fisher, 11360070), non-essential amino acid (Thermo Fisher, 11140050), and 1% penicillin streptomycin (Thermo Fisher, 15140122) at 37 °C and 5% CO_2 to form a monolayer until 60% confluency. The cells were then trypsinized using 0.25% trypsin-EDTA (Thermo Fisher, 15050065), collected, and centrifuged at 800 rpm for 5 min. The cell pellet was resuspended in fresh medium and then used for cell viability and binding affinity assays. For competition *in vitro* studies, cells were preincubated with 2-PMPA (Sigma-Aldrich, SML 1612) for 1 h before treatment with the test articles. The subcutaneous tumor implantation was performed using LNCaP cells (7×10^6) in 100 µL of RPMI 1640 media and Matrigel (BD Biosciences, 354234).

4.4.9 Cell viability studies of bioconjugates 12–17

The cytotoxicity studies of bioconjugates **12**–**17** on various healthy cell lines were performed using the MTT assay. In a T-75 flask, Macrophage (RAW264.7), Human Embryonic Kidney (HEK293), Madin-Darby Canine Kidney (MDCK), and Hepatoma (Hep G2) cell lines were grown to 60–70% confluency. The cells were gently dissociated using 0.25% trypsin (1 mL) for 3 minutes, followed by the addition of fresh RPMI 1640 medium (2 mL). The cells were collected using a micropipette (1 mL) and centrifuged at 700 rpm for 3 minutes at room temperature to obtain the cell pellet. The cell pellet was resuspended in a fresh medium (1 mL), and the cell suspension (10 µL) was counted using a haemocytometer. Approximately 5000 cells/well were seeded on a 96-

well plate and allowed to form a monolayer until they reached 60% confluency for 24 h at 37 °C and 5% CO_2. The cells were then treated with various concentrations of bioconjugates (10 pM, 100 pM, 1 nM, 10 nM, 100 nM, 1 μM, 10 μM) prepared in RPMI 1640 medium (200 μL) in triplicate and incubated for 24 h and 48 h at 37 °C and 5% CO_2. After incubation, the spent medium was discarded, and cells were gently washed with 1X PBS buffer (1 × 0.5 mL). The cells were then incubated with MTT dye (0.5 mg/mL, 0.05 mL) for 4 h at 37 °C and 5% CO_2. After incubation, MTT dye was removed, and DMSO (0.1 mL) was added to each well to dissolve the blue color formazan crystals. The absorbance from each well, proportional to the live cells, was quantified using a Synergy H4 multi-plate reader at a wavelength of 570 nm. Dose vs Response curves were obtained from a plot of log[concentration] vs normalized response curves, and IC_{50} values were calculated using GraphPad Prism, version 7.04.

4.4.10 Binding affinity studies of ^{99m}Tc chelated bioconjugates 18–23

$PSMA^+$ LNCaP cells were cultured in a T-75 flask for 48 h until 80% confluency for binding affinity evaluation of DUPA ligand targeted ^{99m}Tc chelated bioconjugates **18**–**23**. The LNCaP cells were gently dissociated using 0.25% trypsin (1 mL) for 3 minutes, followed by the addition of fresh RPMI 1640 medium (2 mL). The cells were collected using a micropipette (1 mL) and centrifuged at 700 rpm for 3 minutes at room temperature to obtain the cell pellet. The cell pellet was resuspended in a fresh medium (1 mL), and the cell suspension (10 μL) was counted using a hemocytometer. Approximately, 1.2×10^5 cells were suspended in a fresh RPMI 1640 medium (100 μL) in Eppendorf tubes (2 mL) and treated with increasing concentrations of ^{99m}Tc bioconjugates **18**–**23** (10, 20, 30, 40, 50, 75, 100, 125, 300, 750, 1215 nM) prepared in RPMI 1640 medium (400 μL) in triplicates and incubated in a CO_2 incubator for 1 h. For competition experiments, cells were preincubated with 2-PMPA (500 μL) (100-fold excess of 1215 nM) for 1 h before treatment with the test articles, ^{99m}Tc bioconjugates **18**–

23. After incubation for an hour with 2-PMPA, cells were centrifuged to the cell pellets, and the excess PMPA with the spent medium was discarded. The cell pellets were resuspended in a fresh medium (100 µL) and the PSMA receptor blocked cells were then treated with increasing concentrations of ^{99m}Tc bioconjugates **18**–**23** (10, 20, 30, 40, 50, 75, 100, 125, 300, 750, 1215 nM) prepared in RPMI 1640 medium (400 µL) in triplicates and incubated in a CO_2 incubator for 1 h. The treated cells were washed with an ice-cold buffer (2 × 500 µL) (84 mg EDTA and 1 mL of 25 mM HEPES buffer in 50 mL 1X DPBS) and centrifuged. The cell pellets, free of unbound ^{99m}Tc bioconjugates **18**–**23**, were resuspended in an ice-cold buffer (500 µL) to evaluate cell-bound radioactivity using a gamma counter. The dissociation constant K_d was calculated using GraphPad Prism 7.04.

4.4.11 Copies of ^{1}H, ^{13}C NMR, and HRMS spectra

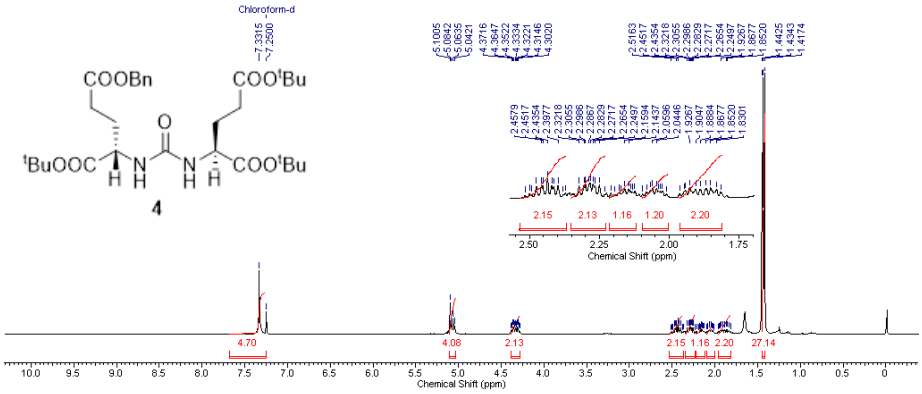

Figure 4.4 ^{1}H NMR spectrum (400 MHz, $CDCl_3$) of **4**.

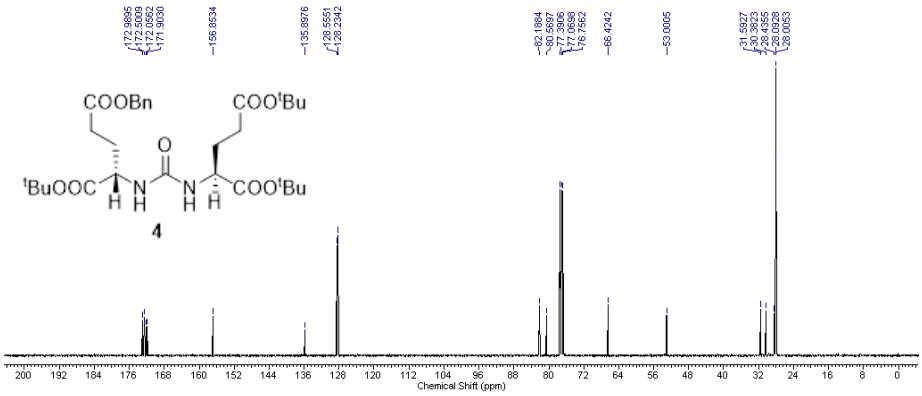

Figure 4.5 ^{13}C NMR spectrum (100 MHz, $CDCl_3$) of **4**.

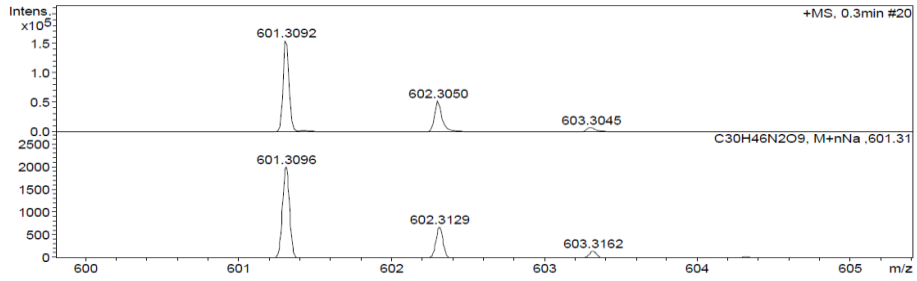

Figure 4.6 HRMS of **4**.

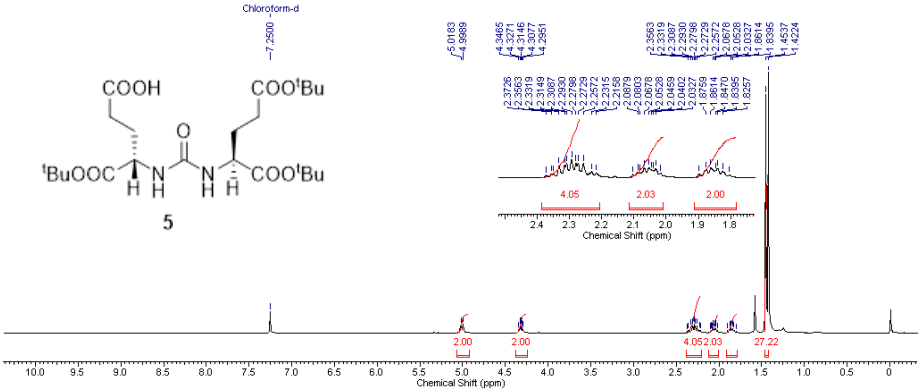

Figure 4.7 ^{1}H NMR spectrum (400 MHz, $CDCl_3$) of **5**.

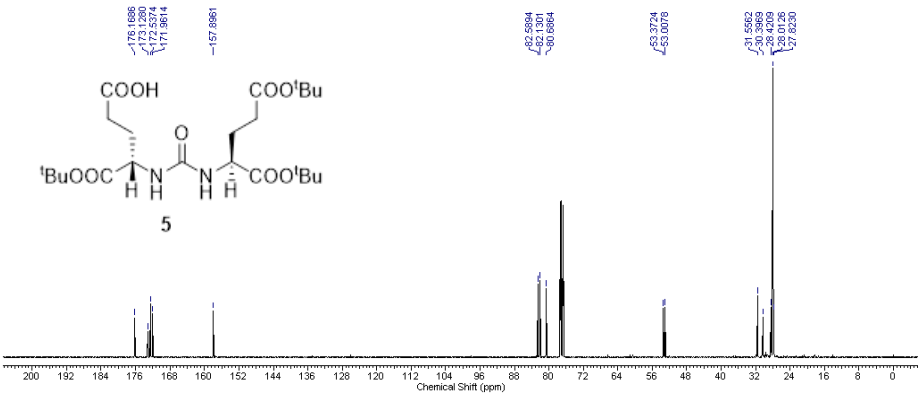

Figure 4.8 ^{13}C NMR spectrum (100 MHz, $CDCl_3$) of **5**.

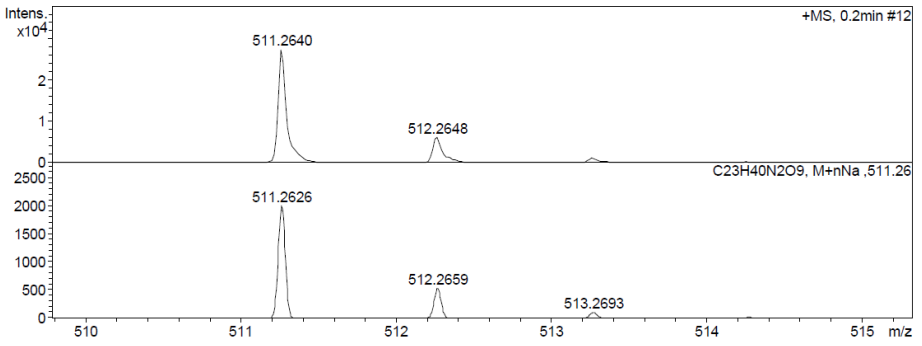

Figure 4.9 HRMS of **5**.

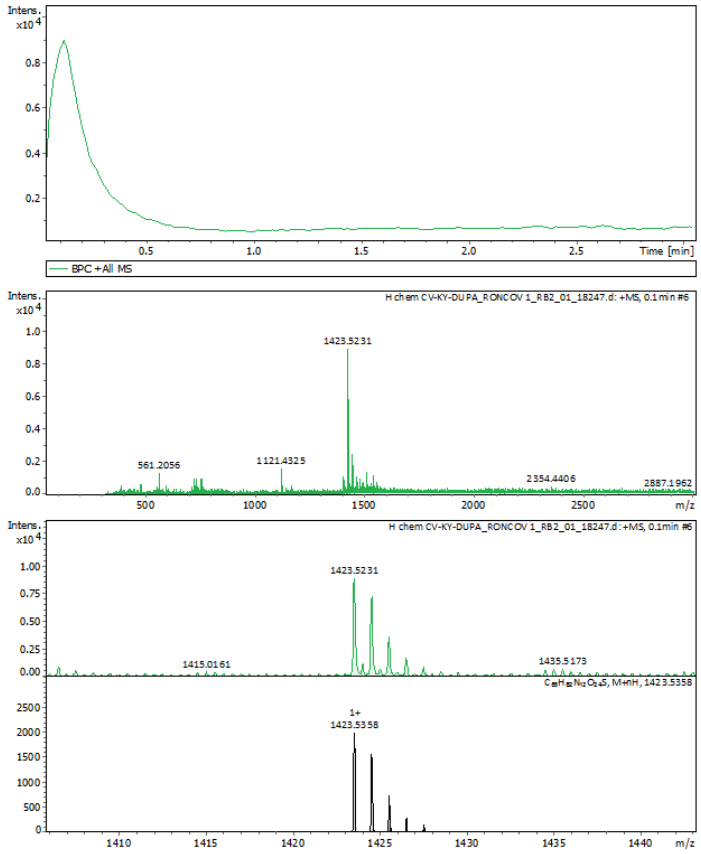

Figure 4.10 HRMS data of **12**.

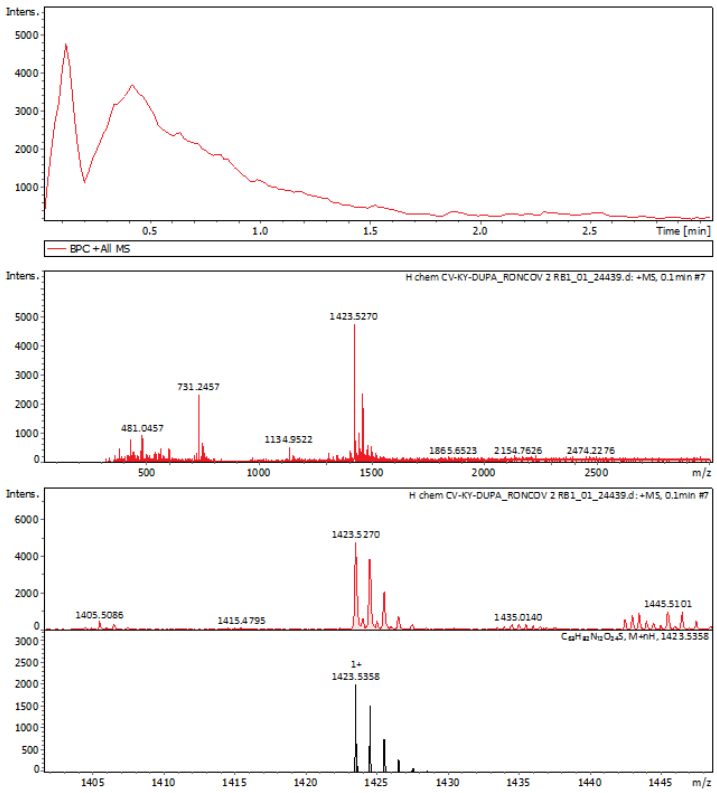

Figure 4.11 HRMS data of **13**.

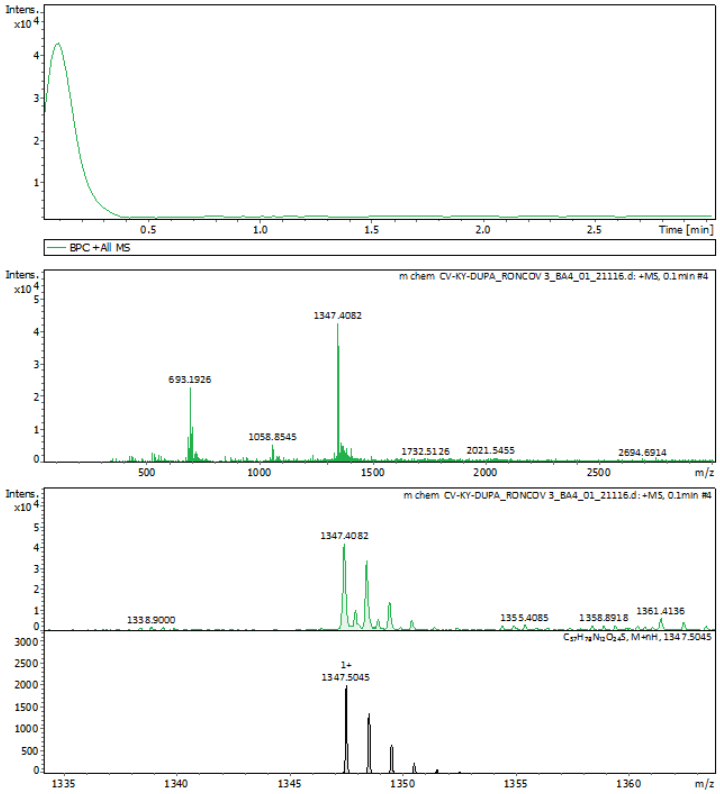

Figure 4.12 HRMS data of **14**.

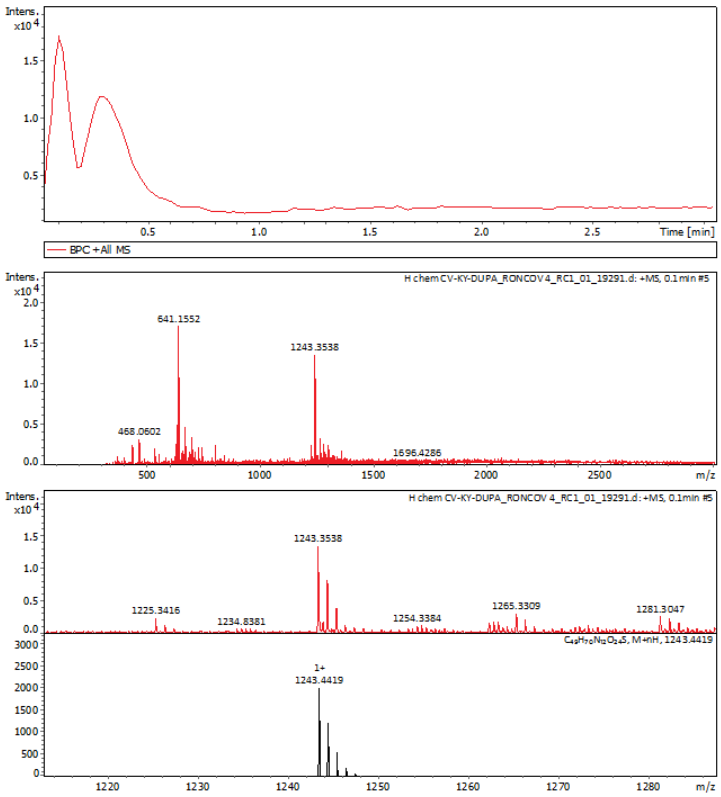

Figure 4.13 HRMS data of **15**.

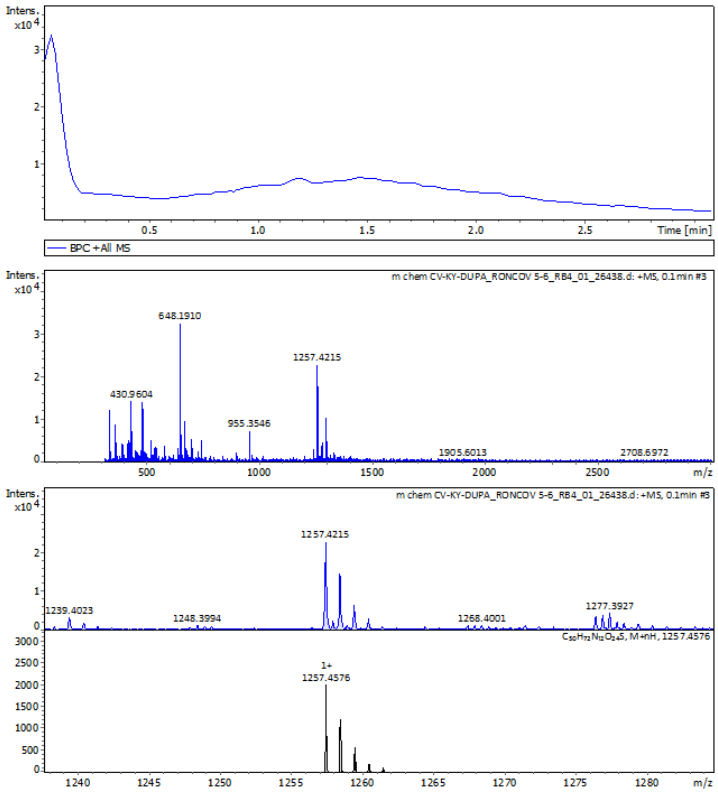

Figure 4.14 HRMS data of **16**.

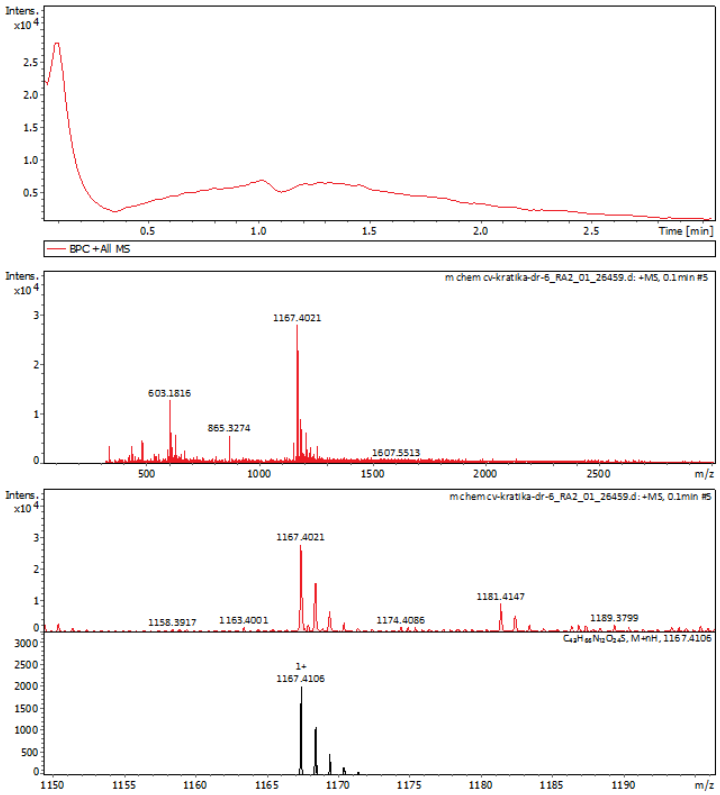

Figure 4.15 HRMS data of **17**.

4.5 References

1. Bray F, Laversanne M, Sung H, et al. Global cancer statistics 2022: GLOBOCAN estimates of incidence and mortality worldwide for 36 cancers in 185 countries. *CA Cancer J Clin*. 2024, 74, 229–263. doi:10.3322/caac.21834.

2. Olson MT, Ly Q P, Mohs AM. Fluorescence guidance in surgical oncology: Challenges, opportunities, and translation. *Mol Imaging Biol*. 2019, 176, 200–218. doi:10.1007/s11307-018-1239-2.

3. Wang P, Fan Y, Lu L, et al. NIR-II Nanoprobes in vivo assembly to improve image-guided surgery for metastatic ovarian cancer. *Nat Commun*. 2018, 9, 1–10. doi:10.1038/s41467-018-05113-8.

4. Zhao M, Wang R, Li B, et al. Precise in vivo inflammation imaging using in situ responsive cross-linking of glutathione-modified ultra-small NIR-II lanthanide nanoparticles. *Angew Chemie*. 2019, 131, 2072–2076. doi:10.1002/ange.201812878.

5. Askari Rizvi SF, Zhang H. Emerging trends of receptor-mediated tumor targeting peptides: A review with perspective from molecular imaging modalities. *Eur J Med Chem*. 2021, 221, 113538–113555. doi:10.1016/j.ejmech.2021.113538.

6. Jun JV, Chenoweth DM, Petersson EJ. Rational design of small molecule fluorescent probes for biological applications. *Org Biomol Chem*. 2020, 18, 5747–5763. doi:10.1039/d0ob01131b.

7. Hong G, Dai H. In vivo fluorescence imaging in the second near-infrared window using carbon nanotubes. *Methods Mol Biol*. 2016, 1444, 167–181. doi:10.1007/978-1-4939-3721-9_15.

8. Cao J, Zhu B, Zheng K, et al. Recent progress in NIR-II contrast agent for biological imaging. *Front Bioeng Biotechnol*. 2020, 7, 1–21. doi:10.3389/fbioe.2019.00487.

9. Mohtavinejad N, Shafiee AM, Khalaj A. Application of

radiolabeled peptides in tumor imaging and therapy. *Life Sci*. 2020, 258, 118206–118212. doi:10.1016/j.lfs.2020.118206.

10. Banerjee SR, Pullambhatla M, Byun Y, et al. ^{68}Ga-labeled inhibitors of prostate-specific membrane antigen (PSMA) for imaging prostate cancer. *J Med Chem*. 2010, 53, 5333–5341. doi:10.1021/jm100623e.

11. Abubakr A, Othman AI, Ewedah TM. The applications of radioisotopes in modern medicine: A review of diagnostic, therapeutic, and research advancements. *ERU Res J*. 2024, 4, 1680–1694. doi:10.21608/erurj.2024.294087.1157.

12. Fassbender ME. Guest edited collection: Radioisotopes and radiochemistry in health science. *Sci Rep*. 2020, 10, 14–16. doi:10.1038/s41598-019-56278-1.

13. Hillier SM, Maresca KP, Lu G, et al. ^{99m}Tc-Labeled small-molecule inhibitors of prostate-specific membrane antigen for molecular imaging of prostate cancer. *J Nucl Med*. 2013, 54, 1369–1376. doi:10.2967/jnumed.112.116624.

14. Sengupta S, Pandit A, Krishnan MA, Sharma R, Kularatne SA, Chelvam V. Design, synthesis, and biological evaluation of novel thiourea derivatives as small molecule inhibitors for prostate specific membrane antigen. *Bioorg Chem*. 2025, 155, 108130–10848. doi:10.1016/j.bioorg.2025.108130.

15. Kularatne SA, Zhou Z, Yang J, Post CB, Low PS. Design, synthesis, and preclinical evaluation of prostate-specific membrane antigen targeted ^{99m}Tc-radioimaging agents. *Mol Pharm*. 2009, 6, 790–800. doi:10.1021/mp9000712.

16. Krishnan MA, Yadav K, Roach P, Chelvam V. A targeted near-infrared nanoprobe for deep-tissue penetration and imaging of prostate cancer. *Biomater Sci*. 2021, 9, 2295–2312. doi:10.1039/d0bm01970d.

17. Kularatne SA, Zhou Z, Yang J, Post CB, Low PS. Design, synthesis, and preclinical evaluation of prostate-specific membrane antigen targeted (^{99m})Tc-radioimaging agents. *Mol Pharm*. 2009, 6, 790–800. doi:10.1021/mp9000712.

18. Zhang AX, Murelli RP, Barinka C, et al. A Remote arene-binding site on prostate specific membrane antigen revealed by antibody-recruiting small molecules. J Am Chem Soc. 2010, 132, 12711-12716. doi:10.1021/ja104591m

19. Krishnan MA, Pandit A, Sharma R, Chelvam V. Imaging of prostate cancer: Optimizing affinity to prostate specific membrane antigen by spacer modifications in a tumor spheroid model. *J Biomol Struct Dyn*. 2022, 40, 9909–9930. doi:10.1080/07391102.2021.1936642.

Chapter 5

Design, synthesis, and cytotoxic evaluation of new structurally simplified and highly potent third-generation tubulysin derivatives

5.1 Introduction

Cancer remains a leading cause of death globally, with 20 million new cases and 9.7 million deaths as reported in 2022.[1] Therefore, there is an urgent need for innovative treatments to reduce cancer incidence and mortality worldwide. The cancer cells display neoplastic characteristics by passing through four distinct cell cycle phases, due to checkpoint failure, impairing defect detection, repair mechanisms, or apoptosis induction.[2,3] Current chemotherapeutic drug development targets microtubule dynamics using targeted antibody-drug conjugates (ADCs)[4] or validated proteins in tumor cells, immune cells, stromal cells, and the extracellular matrix to induce apoptosis.[5] Microtubules play a crucial role during the M phase of the cell cycle.[6] Disruption in microtubule assembly and disassembly triggers apoptosis due to failure in chromatid separation. Based on their mode of action, the microtubule targeting agents can be classified into two categories: one that stabilizes the microtubules and binds to the taxanes binding site (taxanes and epothilones),[7, 8] and the other which destabilizes the microtubules by binding to the vinca and colchicine domain of αβ tubulin heterodimer (vinca alkaloids and colchicine).[9] The long-term use of the microtubule targeting agents has been associated with multidrug resistance and poor solubility, requiring higher doses. Therefore, there is a need for the development of new tubulin inhibitors that can address a few of the preclinical requirements, such as systemic toxicities and poor bioavailability.[10] In 2000, Reichenbach and Höfle et al. reported the isolation of tubulysins, natural tetrapeptides from myxobacterial culture, found to have antitumor activity in the low nM range. The cytotoxic properties of tubulysins are due to the strong binding interaction

between tubulysin and its binding site, near the vinca domain of β-tubulin. As a result, they inhibit the polymerization of microtubules, leading to cytoskeleton collapse and induction of apoptosis.[11]

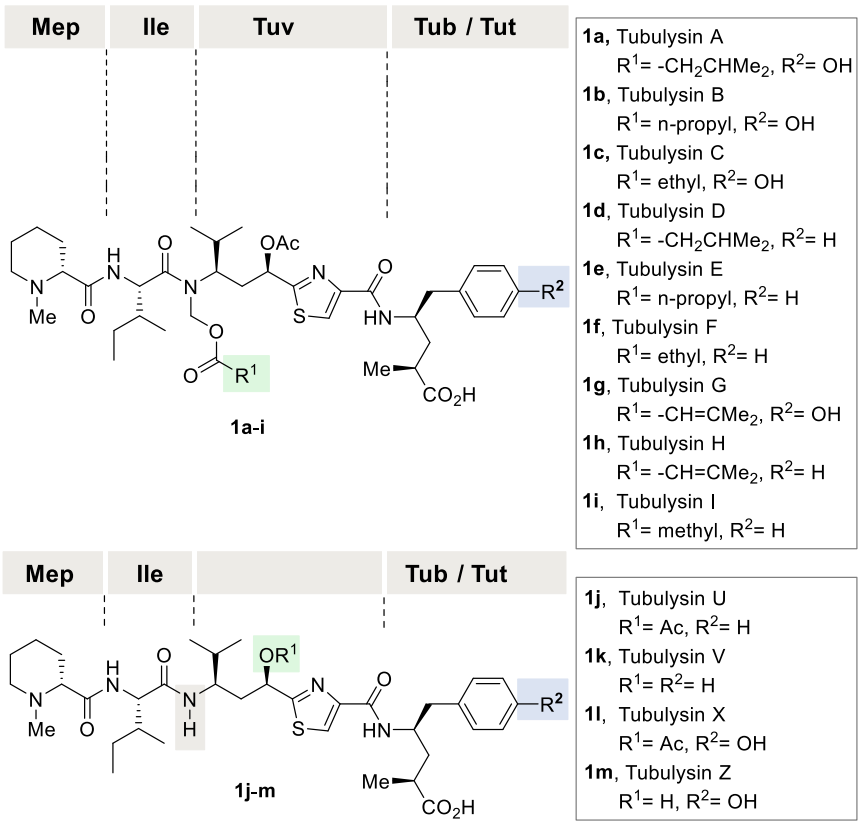

Figure 5.1 Structures of naturally occurring tubulysin derivatives A-I (**1a**–**i**), and tubulysin U, V, X, and Z (**1j**–**m**); (Mep = *N*-methyl-D-pipecolic acid, Ile = isoleucine, Tuv = tubuvaline, Tub = tubuphenylalanine, Tut = tubutyrosine).

Up to date, 14 naturally occurring tubulysin derivatives (A-I, U, V, X, and Z, **1a**–**m**) have been reported (Figure 5.1). These tetrapeptides are composed of *N*-methyl-D-pipecolic acid (D-Mep) at the N-terminus, followed by tubuvaline (Tuv), L-isoleucine (L-Ile), and tubuphenylalanine (Tup) or tubutyrosine (Tut) located at the C-terminus.[12] Unique structural features comprise a tertiary amide N, an O-acetyl ester as part of the central thiazole bearing amino acid, and a γ-amino acid unit, called tubuphenylalanine (Tup) or tubutyrosine (Tut), respectively, at the C-terminus. Therefore, tubulysin poses synthetic challenges hampering large-scale approaches.

Despite their therapeutic potential, the limited biotechnological availability has been regarded as another hurdle for profiling tubulysin as an antitumor drug. So far, synthetic efforts were directed as part of total synthesis programs, and here, the unusual amino acids were the first targets.[13, 14] Ellmann and co-workers disclosed the first total synthesis of tubulysin D in 13% yield.[15] This was followed by the total synthesis of N_{14}-desacetoxy analogue of tubulysin H by Wipf et al. in 2.1% yield.[16] This derivative was given the name Tub M and served as the starting point for the first medicinal chemistry program. In 2016, Nicolau and coworkers reported the synthesis and biological evaluation of a tubulysin library with structural modifications in all the units of the tetrapeptide.[17] From these studies, it was concluded that *N*-methyl pipecolic acid is essential for tubulysin activity. The tubuphenylalanine fragment was not fully explored, and for the tubuvaline unit, structural tolerance with respect to the aromatic system. Tubulysin M **1n** turned out to be one of the most promising candidates for the treatment of solid tumours or multidrug-resistant carcinoma with an IC_{50} value in the low nM range of 0.02 nM (Figure 5.2, top). Recently, we reported convenient syntheses of tubuvaline (Tuv) and tubuphenylalanine (Tub) from our laboratory.[18,19] However, the structural complexity along with the hurdle to prepare larger amounts, the limited supply, and issues concerning its stability in biological environments have hampered clinical development so far. A systematic modifications of the tubulysin fragments were carried out to address the existing shortcomings, and a novel third-generation tubulysin derivative was developed as an illustration, namely Tub_01, without the tubuvaline and tubuphenylalanine fragments. The initial molecular docking studies demonstrated that the interactions of the newly designed tubulysin derivative (Tub_01) with the tubulin protein were similar to those of the natural product, Tubulysin M.[20] In this chapter, we disclose the first solid-phase peptide synthesis (SPPS) and biological evaluation of a new class of third-generation tubulin inhibitors based on the tubulysin derivative **14a**.

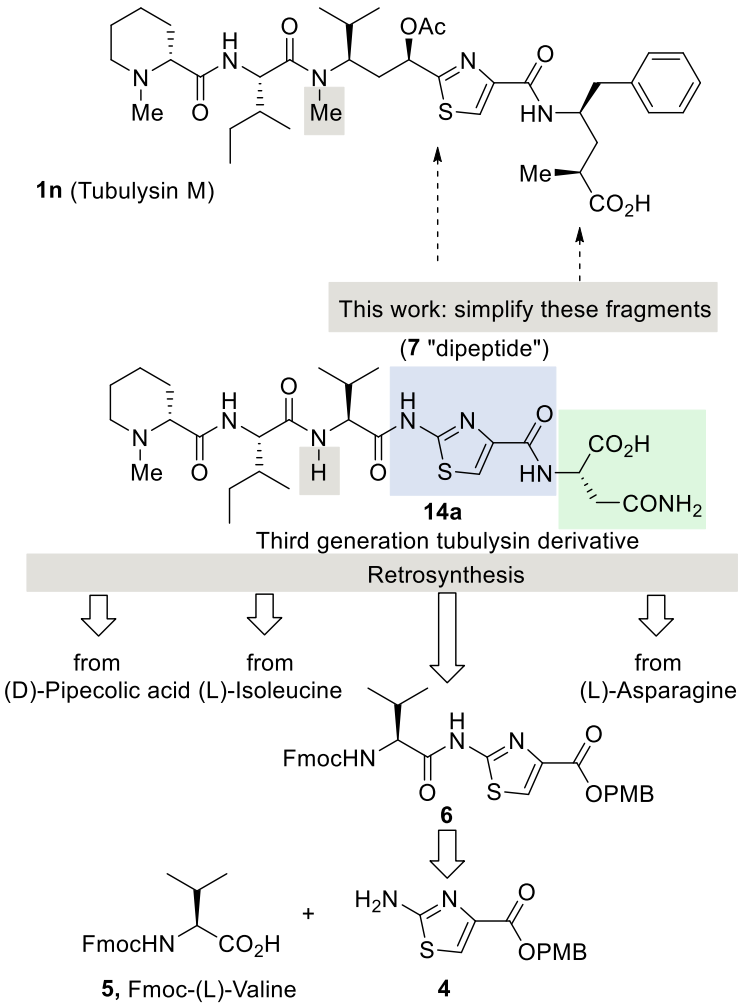

Figure 5.2 Top: Structure of tubulysin M **1n** with simplified tertiary amide *N*-methyl-Tuv, central: Structural changes and simplifications pursued in this work; structure of **14a**, and bottom: Retrosynthetic analysis of **14a**.

Compared to the natural tubulysins **1**, it is substantially simplified in the tubuvaline (Tuv) and the tubuphenylalanine (Tup) units in that a) Tuv is exchanged by valine and an aminothiazole amino acid, which provides a central dipeptide element, and b) Tub is simplified instead by using asparagine (Figure 5.2, central). Support for these substantial structural changes was gained from initial molecular docking studies between the newly designed derivative **14a** and the tubulysin binding site of the tubulin protein. These revealed similar interactions as reported for natural tubulysin M **1n**.[21] Extensive *in silico* molecular docking studies provided strong support for the suggested design of the new tubulysin

derivatives, and these calculations are detailed in the results and discussion section. Our new design challenges the proposed key role of the two complex amino acids, Tuv and Tup, for biological activity. The design of the valine-thiazole dipeptide is based on the rationale to combine the hydrophobic valine with the electron-rich thiazole ring via an amide moiety. The heterocycle stabilizes interactions through π-stacking and provides resistance towards enzymatic degradation. Finally, the asparagine unit at the C-terminus provides improved water solubility.

As these proposed structural simplifications are enormous, we planned to develop a solid-phase synthetic approach with minimum need for purification. The retrosynthetic analysis is straightforward and is summarized in figure 5.2 (bottom). (D)-*N*-Methyl pipecolic acid, (L)-iosleucine, Fmoc-protected (L)-valine, and (L)-asparagine are readily available building blocks. At the same time, the aminothiazole was utilized as p-methoxybenzyl ester **4** and was planned to be first coupled with Fmoc-protected (L)-valine. Thus, three single amino acids and the dipeptide **7** serve as four building blocks. Once the solid phase peptide synthesis towards tubulysin **14a** has been established, we plan to extend the protocol to generate a tubulysin library with tubulysin derivative **14a** as the lead structure. Specifically, the central new dipeptide unit would stay fixed while variations were planned to be installed at the C- and N-termini.

5.2 Results and discussion

The initial docking studies of the tubulysin derivatives in the active site cavity between the interface of tubulin monomers β (B-chain) and α (C-chain) showed the interacting amino acid residues similar to those of tubulysin M. The Asp 179 B, Tyr 224 B, Val 177 B, and Leu 248 C amino acid residues of the B and C-chains in the tubulin protein interact quite well with tubulysin derivatives **14a**–**l**. These results motivated us to synthesise the designed tubulin inhibitors based on *in silico* data. Retrosynthetically, we dissected the target tubulysin **14a** into four building blocks suited to be employed for solid phase synthesis:

protected (L)-asparagine, Fmoc-protected (L)-isoleucine, (D)-*N*-methylpipecolic acid **9**, and dipeptide **7**. The synthesis of dipeptide **7** was achieved through a simple three-step process, using 2-aminothiazole-4-carboxylic acid **2** (Scheme 5.1). In the first step, a nucleophilic substitution reaction was performed by the reaction of 2-aminothiazole-4-carboxylic acid with 4-methoxybenzyl chloride (PMBCl) **3**, in the polar aprotic solvent, dry DMF, in the presence of sodium carbonate (Na_2CO_3) as a base, to afford 4-methoxybenzyl 2-aminothiazole-4-carboxylate **4** in 56% yield. The free amine group in **4** was subsequently coupled with Fmoc-protected valine **5**, via the formation of an amide bond, to obtain dipeptide **6** in 75% yield. The coupling reaction was carried out using 1-ethyl-3-(3-dimethylaminopropyl)carbodiimide hydrochloride (EDC·HCl) as the coupling agent in the presence of 1-hydroxybenzotriazole (HOBt) as an additive to prevent racemization in dry DCM. Finally, in the third step, the acid-labile 4-methoxybenzyl (PMB) protecting group in **6** was selectively deprotected using a 10% trifluoroacetic acid (TFA) solution in DCM, resulting in the formation of a building block, Fmoc-Val-thiazole-OH **7** in 98% yield (Scheme 5.1). Additionally, *N*-methyl pipecolic acid **9** was chemically synthesized from pipecolic acid (Scheme 5.2). Pipecolic acid **8** was first reacted with formaldehyde in methanol to form an iminium salt, which, on in situ reductive amination using 10% palladium on activated carbon (Pd/C) under a hydrogen atmosphere, led to the formation of *N*-methyl-D-pipecolic acid (D-Mep) **9** in 98% yield. The synthesized fragments were then coupled via SPPS to obtain the tubulysin derivatives **14a**–**l** (Schemes 5.3 and 5.4). The chlorotrityl resin **10** has been employed as a polymeric support that was already capped with asparagine **10a**, which was trityl-protected at the amide group. From there, we straightforwardly prepared tubulysin derivative **14a** in 70% yield via intermediates **11**, **12**, and **13** after cleavage from the resin and a final HPLC purification step (Scheme 5.3). The synthesis is based on standard orthogonal peptide chemistry using Fmoc solid-phase peptide synthesis.

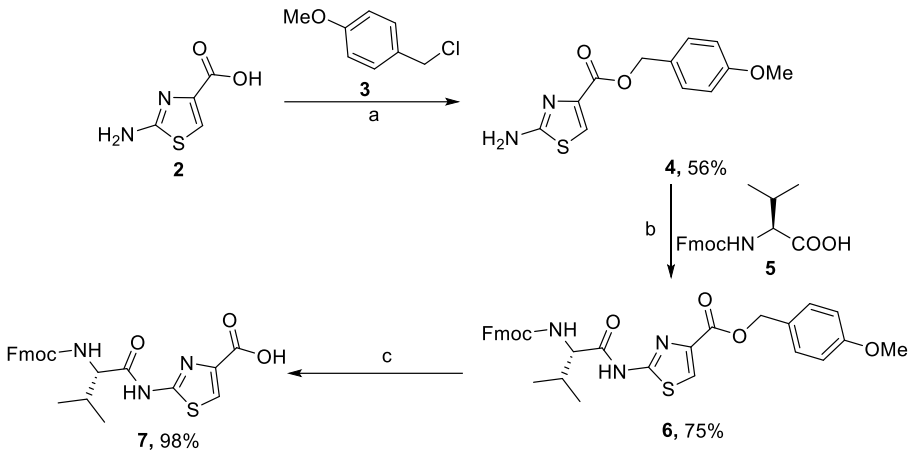

Scheme 5.1 Synthesis of Fmoc valine thiazole dipeptide **7**. Reagents and conditions:(a) Na_2CO_3, DMF, rt, 16 h; (b) EDC.HCl, HOBt, DCM, rt, 16 h; (c) 10% TFA in DCM, rt, 1.5 h.

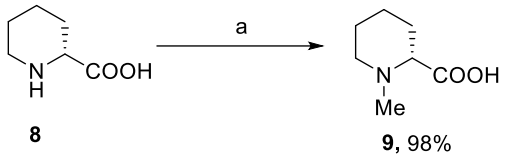

Scheme 5.2 Synthesis of *N*-methyl pipecolic acid **9**. Reagents and conditions: (a) Formaldehyde (37% in water), 10 mol% Pd/C, H_2 (1 atm), MeOH, rt, 24 h.

Once we had established the solid-phase synthesis, we prepared tubulysin derivatives **14b**–**l** based on this protocol. Specifically, we exchanged asparagine by (L)-Glu (**14b**), (L)-Glu-Gly (**14c**), (L)-Asp (**14d**), (L)-Asp-Gly (**14e**), (L)-Phe-Gly (**14f**) and (L)-Tyr-Gly (**14g**) without changing the N-terminus (Figure 5.3, labelled in blue). For the second series of tubulysin derivatives, asparagine has been retained at the C-terminus while *N*-methylpipecolic acid was replaced with (L)-His (**14h**), *trans*-4-(aminomethyl) cyclohexanecarboxylic acid (**14i**), hydrido (**14j**), (L)-phenylalanine (**14k**), and 2-napthylalanine (**14l**) (Figure 5.3, labelled in green). The solid-phase synthesis of the tubulysin derivatives **14h**–**l** (Scheme 5.3) has been initiated with the same asparagine-capped chlorotrityl resin **10** that was already employed for the preparation of tubulysin derivative **14a**.

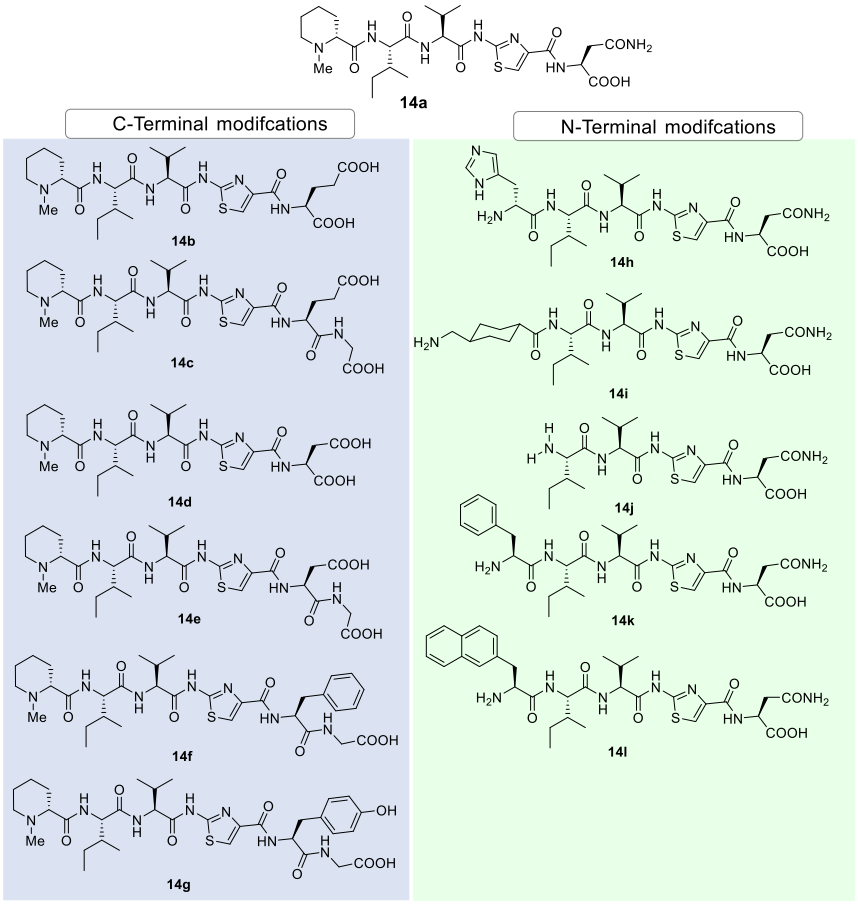

Figure 5.3 Structures of new tubulysin derivatives **14a**–**l** prepared according to the solid phase protocol developed for **14a** (Schemes 5.3 and 5.4).

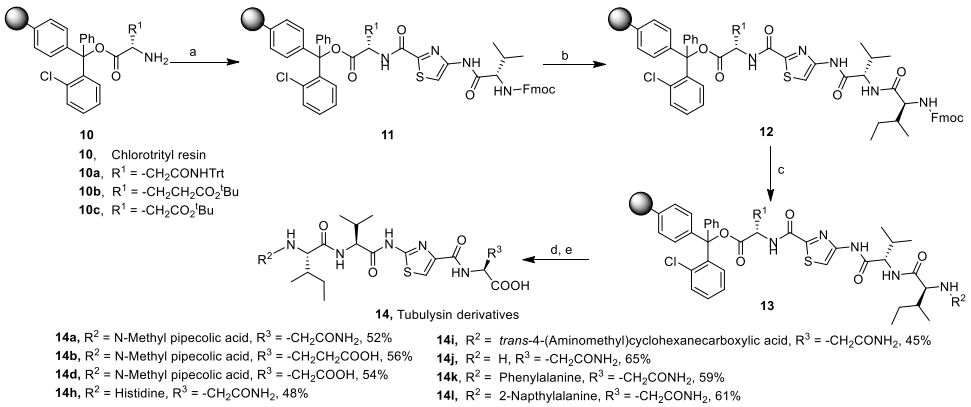

Scheme 5.3 Synthesis of tubulysin derivatives **14a**, **14b**, **14d**, **14h**–**l**. Reagents and conditions: (a) Dipeptide **7**, PyBOP, DIPEA, DMF, 6 h; (b) (i) 20% Piperidine in DMF, rt, 30 min; (ii) Fmoc-Ile-OH, PyBOP, DIPEA, DMF, 6 h; (c) (i) 20% Piperidine in DMF, rt, 30 min; (ii) Fmoc-R^2-OH or R^2, PyBOP, DIPEA, DMF, 6 h; **14a**, **14b**, **14d:** (d) (i)

TFA/TIPS/H_2O (9.5:0.25:0.25) (1 × 5 mL, 30 min; 2 × 5 mL, 5 min); (ii) evaporate TFA; (iii) precipitate in ice-cold diethylether; **14h**–**l:** (e) (i) 20% Piperidine in DMF, rt, 30 min; (ii) TFA/TIPS/H_2O (9.5:0.25:0.25) (1 × 5 mL, 30 min; 2 × 5 mL, 5 min); (iii) Evaporate TFA; (iv) Precipitate in ice-cold diethyl ether.

The starting point had to be altered for accessing **14b**–**g** in that a resin had to be used capped with (L)-Glu (for **14b**) in which the δ-carboxylic acid was protected as trityl ester, Gly (for **14c** and **14e**–**g**) and (L)-Asp also protected as trityl ester (**14d**). For tubulysin derivatives **14c** and **14e**–**g**, an additional amino acid was incorporated first before the dipeptide unit **7** was coupled (Scheme 5.4). These included (L)-Glu (leading to **14c**), (L)-Asp (leading to **14e**), (L)-Phe (leading to **14f**), and (L)-Tyr (leading to **14g**).

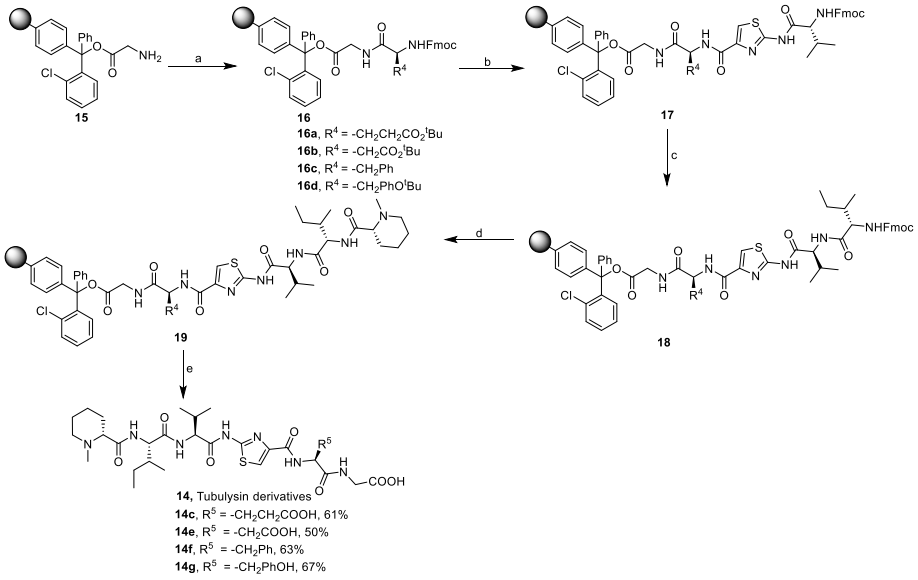

Scheme 5.4 Synthesis of tubulysin derivatives **14c**, **14e**–**g**. Reagents and conditions: (a) Fmoc-R^4-OH, PyBOP, DIPEA, DMF, 6 h; (b) (i) 20% Piperidine in DMF, rt, 30 min; (ii) Fmoc-Val-thiazole-OH, PyBOP, DIPEA, DMF, 6 h; (c) (i) 20% Piperidine in DMF, rt, 30 min; (ii) Fmoc-Ile-OH, PyBOP, DIPEA, DMF, 6 h; (d) (i) 20% Piperidine in DMF, rt, 30 min; (ii) **9**, PyBOP, DIPEA, DMF, 6 h; (e) (i) TFA/TIPS/H_2O (9.25:0.25:0.25), (1 × 5 mL, 30 min; 2 × 5 mL, 5 min); (ii) Evaporate TFA; (iii) Precipitate in ice-cold diethyl ether.

.*In vitro* cytotoxic studies were conducted for tubulysin derivatives, **14a**–**l**, to determine the half-maximal inhibitory concentration (IC_{50}) against different human cancer cell lines for an incubation period of 24 h and 48 h (Figure 5.4). Cell lines MCF7 (breast cancer), A549 (lung cancer), LNCaP (Prostate cancer), A431 (skin cancer), HeLa (cervical cancer), and A375 (melanoma) were chosen as shown in tables 5.1 and 5.2.

Table 5.1 *In vitro* cytotoxicity analysis of new tubulysin derivatives **14a**–**l** in various cancer cell lines: Breast cancer (MCF7), adenocarcinoma alveolar basal epithelial (A549), epidermoid carcinoma (A431), malignant melanoma (A375), cervical carcinoma (HeLa), prostate carcinoma (LNCaP) for an incubation period of 48 h. Inhibitory concentrations, IC_{50}, are given in nM and are compared with colchicine as a standard. Data are expressed as mean ±S.D. (n=3).

Human Cancer Cell Lines (IC_{50} in nM for 48 h)						
Tubulysin Derivative	**LNCaP**	**HeLa**	**MCF7**	**A549**	**A375**	**A431**
14a	14.29	18.86	17.45	19.87	20.60	16.66
14b	26.80	11.97	16.57	18.11	21.92	13.11
14c	25.67	27.13	22.54	16.90	27.36	23.37
14d	53.33	30.99	52.50	50.55	53.85	54.51
14e	46.92	34.41	49.23	36.45	38.09	51.47
14f	115.21	82.94	129.70	117.21	111.82	130.32
14g	226.79	214.55	125.09	144.90	210.41	131.58
14h	>500	474.20	>500	>500	221.23	312.50
14i	333.01	>500	>500	>500	335.85	>500
14j	371.12	>500	>500	224.50	481.22	>500
14k	141.23	313.21	173.12	463.71	141.92	268.80
14l	460.23	>500	>500	>500	>500	>500
Colchicine	317.66	349.51	227.01	242.66	395.41	266.55

Table 5.2 *In vitro* cytotoxicity analysis of new tubulysin derivatives **14a**–**l** in various cancer cell lines: Breast cancer (MCF7), adenocarcinoma alveolar basal epithelial (A549), epidermoid carcinoma (A431), malignant melanoma (A375), cervical carcinoma (HeLa), prostate carcinoma (LNCaP) for an incubation period of 24 h. Inhibitory concentrations, IC_{50}, are given in nM and are compared with colchicine as a standard. Data are expressed as mean ±S.D. (n=3).

Human Cancer Cell Lines (IC_{50} in nM for 24 h)						
Tubulysin Derivative	**LNCaP**	**HeLa**	**MCF7**	**A549**	**A375**	**A431**
14a	83.29	109.41	97.17	89.61	127.56	82.30
14b	117.61	212.75	96.26	80.85	195.21	164.81
14c	138.93	139.83	100.13	136.42	113.31	165.42
14d	169.90	109.41	122.32	207.81	133.42	91.07
14e	>500	369.32	433.21	48.03	396.81	198.81
14f	>500	>500	>500	>500	>500	>500
14g	>500	>500	>500	>500	>500	>500
14h	>500	>500	>500	>500	>500	>500
14i	>500	>500	>500	>500	>500	>500
14j	>500	>500	>500	>500	>500	>500
14k	>500	>500	>500	>500	>500	>500
14l	>500	>500	>500	>500	>500	>500
Colchicine	>500	>500	>500	>500	>500	>500

It has been found that replacing the C-terminal amino acid asparagine with various amino acids such as aspartic acid, glutamic acid, and glycine did not result in any significant loss of activity, indicating an effective tolerance of the amino acids at the C-terminus. Over an incubation period of 48 h and 24 h, the IC_{50} values are found to be in the range of 13.11 nM to 50.55 nM, and 80.65 nM to 0.52 µM against various cancer cell lines, respectively. These cytotoxicities are particularly significant in light of the corresponding IC_{50} values for colchicine (227.01 nM to 395.41 nM for 48h and 1.14 µM to 2.19 µM for 24 h). The observation with respect to the C-terminus cannot be generalised entirely, as the pentapeptides **14f** and **14g**, with the aromatic amino acids phenylalanine and tyrosine, respectively, lead to a significant reduction in biological activity, considering that the natural tubulysins carry aromatic residues in this area. Concerning the N-terminus, it is evident that small structural changes by replacing *N*-methylpipecolic acid (tubulysin derivatives **14h**–**l**) lead to a significant loss of activity from nM down to the µM range.

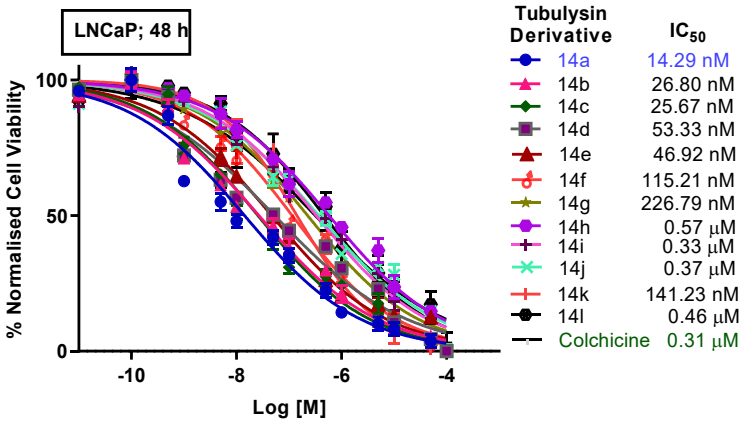
LNCaP; 48 h
% Normalised Cell Viability
100
50
0
-10
-8
-6
-4
Log [M]
Tubulysin Derivative
IC50
14a 14.29 nM
14b 26.80 nM
14c 25.67 nM
14d 53.33 nM
14e 46.92 nM
14f 115.21 nM
14g 226.79 nM
14h 0.57 µM
14i 0.33 µM
14j 0.37 µM
14k 141.23 nM
14l 0.46 µM
Colchicine 0.31 µM

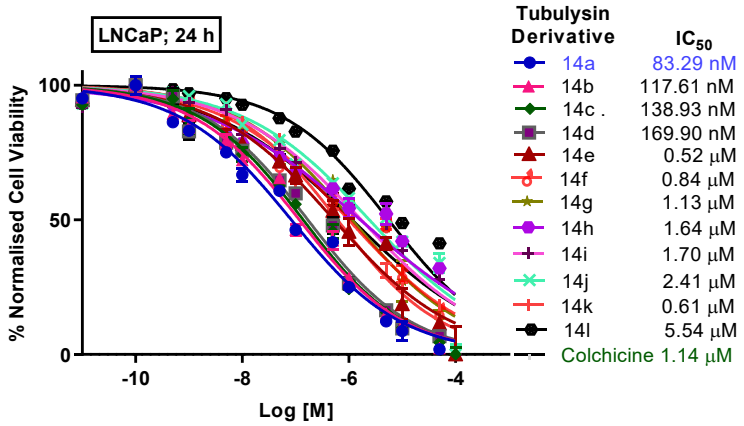
LNCaP; 24 h
% Normalised Cell Viability
100
50
0
-10
-8
-6
-4
Log [M]
Tubulysin Derivative
IC50
14a 83.29 nM
14b 117.61 nM
14c . 138.93 nM
14d 169.90 nM
14e 0.52 µM
14f 0.84 µM
14g 1.13 µM
14h 1.64 µM
14i 1.70 µM
14j 2.41 µM
14k 0.61 µM
14l 5.54 µM
Colchicine 1.14 µM

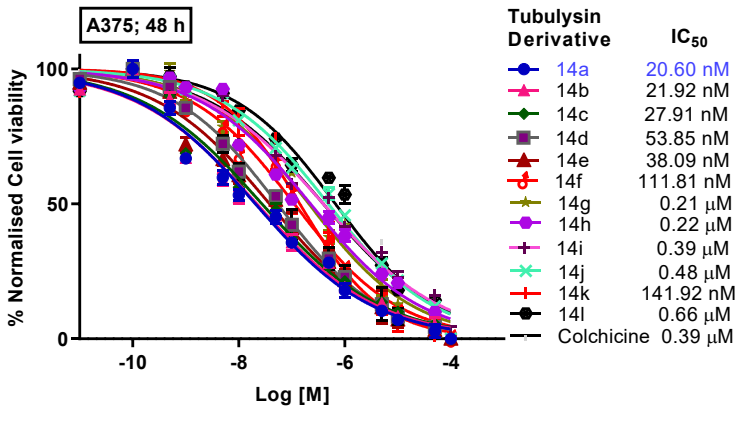
A375; 48 h
% Normalised Cell viability
100
50
0
-10
-8
-6
-4
Log [M]
Tubulysin Derivative
IC50
14a 20.60 nM
14b 21.92 nM
14c 27.91 nM
14d 53.85 nM
14e 38.09 nM
14f 111.81 nM
14g 0.21 µM
14h 0.22 µM
14i 0.39 µM
14j 0.48 µM
14k 141.92 nM
14l 0.66 µM
Colchicine 0.39 µM

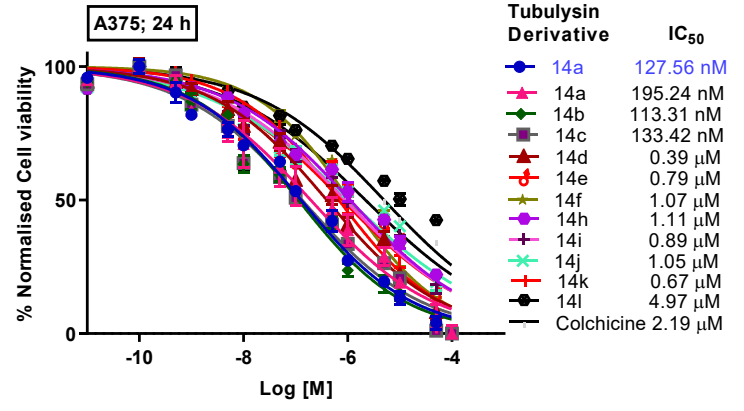
A375; 24 h
% Normalised Cell viability
100
50
0
-10
-8
-6
-4
Log [M]
Tubulysin Derivative
IC50
14a 127.56 nM
14a 195.24 nM
14b 113.31 nM
14c 133.42 nM
14d 0.39 µM
14e 0.79 µM
14f 1.07 µM
14h 1.11 µM
14i 0.89 µM
14j 1.05 µM
14k 0.67 µM
14l 4.97 µM
Colchicine 2.19 µM

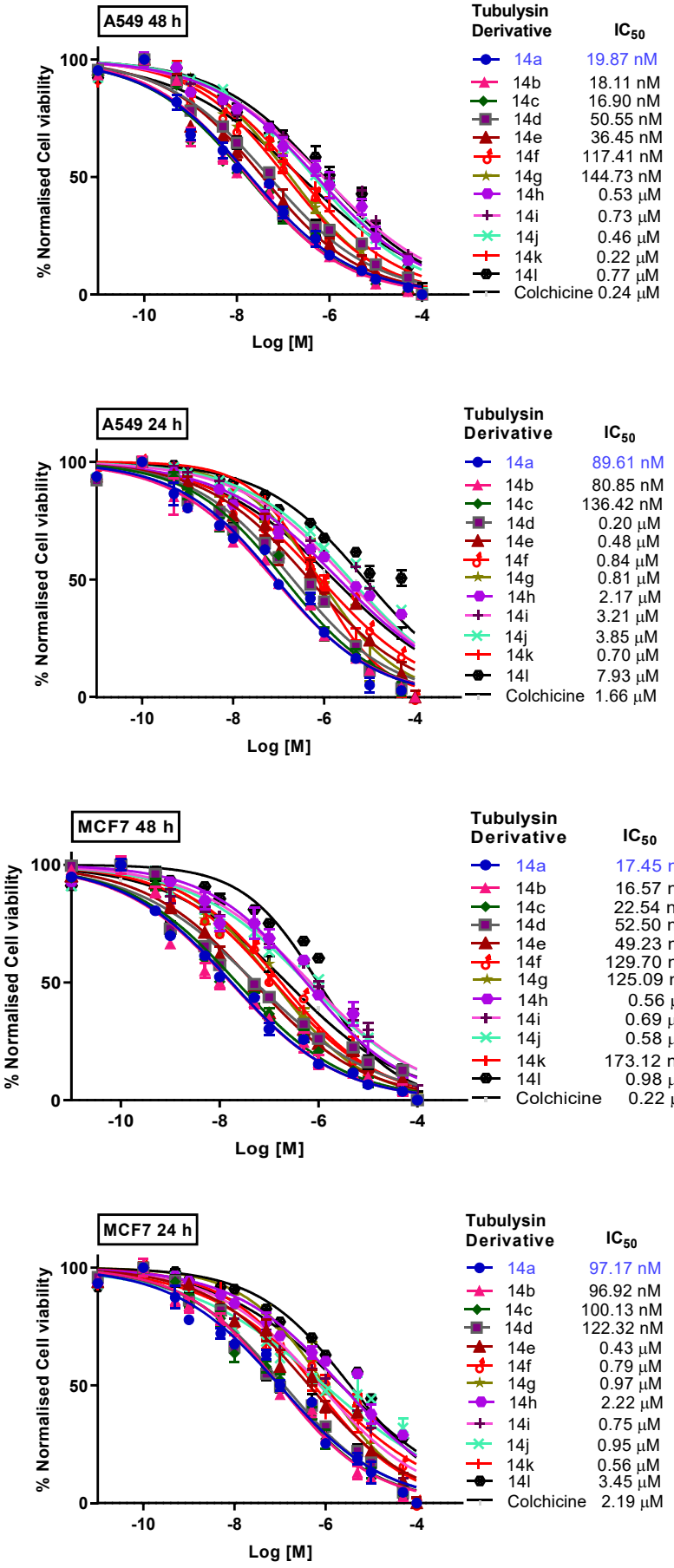
A549 48 h
% Normalised Cell viability
Log [M]
Tubulysin Derivative
IC50
14a 19.87 nM
14b 18.11 nM
14c 16.90 nM
14d 50.55 nM
14e 36.45 nM
14f 117.41 nM
14g 144.73 nM
14h 0.53 µM
14i 0.73 µM
14j 0.46 µM
14k 0.22 µM
14l 0.77 µM
Colchicine 0.24 µM
A549 24 h
% Normalised Cell viability
Log [M]
Tubulysin Derivative
IC50
14a 89.61 nM
14b 80.85 nM
14c 136.42 nM
14d 0.20 µM
14e 0.48 µM
14f 0.84 µM
14g 0.81 µM
14h 2.17 µM
14i 3.21 µM
14j 3.85 µM
14k 0.70 µM
14l 7.93 µM
Colchicine 1.66 µM
MCF7 48 h
% Normalised Cell viability
Log [M]
Tubulysin Derivative
IC50
14a 17.45 nM
14b 16.57 nM
14c 22.54 nM
14d 52.50 nM
14e 49.23 nM
14f 129.70 nM
14g 125.09 nM
14h 0.56 µM
14i 0.69 µM
14j 0.58 µM
14k 173.12 nM
14l 0.98 µM
Colchicine 0.22 µM
MCF7 24 h
% Normalised Cell viability
Log [M]
Tubulysin Derivative
IC50
14a 97.17 nM
14b 96.92 nM
14c 100.13 nM
14d 122.32 nM
14e 0.43 µM
14f 0.79 µM
14g 0.97 µM
14h 2.22 µM
14i 0.75 µM
14j 0.95 µM
14k 0.56 µM
14l 3.45 µM
Colchicine 2.19 µM

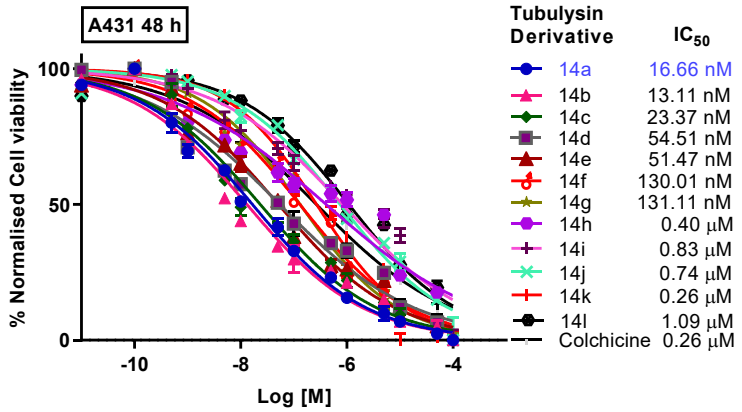
A431 48 h
% Normalised Cell viability
100
50
0
-10
-8
-6
-4
Log [M]
Tubulysin Derivative
IC50
14a 16.66 nM
14b 13.11 nM
14c 23.37 nM
14d 54.51 nM
14e 51.47 nM
14f 130.01 nM
14g 131.11 nM
14h 0.40 µM
14i 0.83 µM
14j 0.74 µM
14k 0.26 µM
14l 1.09 µM
Colchicine 0.26 µM

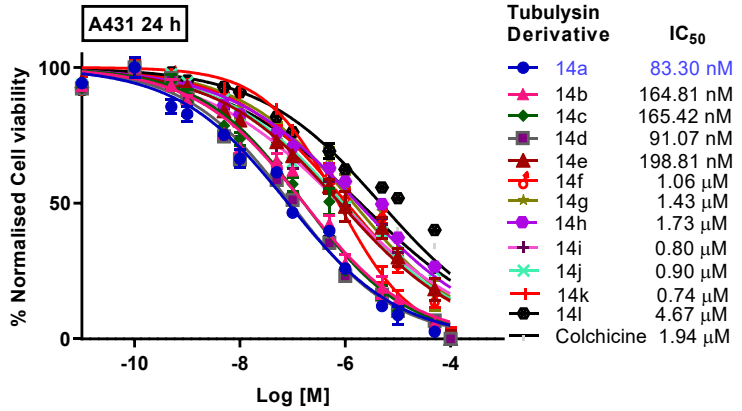
A431 24 h
% Normalised Cell viability
100
50
0
-10
-8
-6
-4
Log [M]
Tubulysin Derivative
IC50
14a 83.30 nM
14b 164.81 nM
14c 165.42 nM
14d 91.07 nM
14e 198.81 nM
14f 1.06 µM
14g 1.43 µM
14h 1.73 µM
14i 0.80 µM
14j 0.90 µM
14k 0.74 µM
14l 4.67 µM
Colchicine 1.94 µM

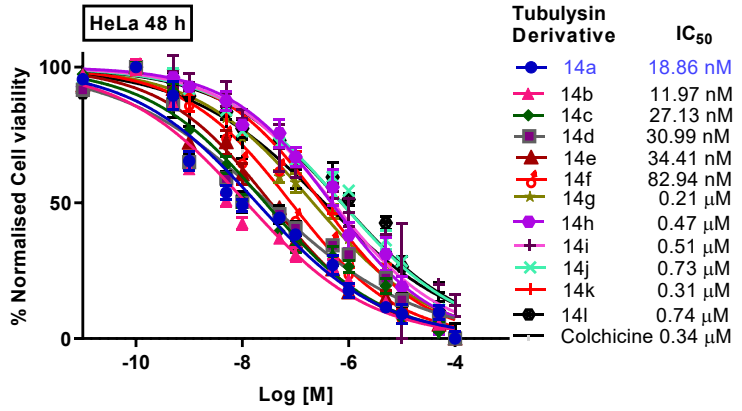
HeLa 48 h
% Normalised Cell viability
100
50
0
-10
-8
-6
-4
Log [M]
Tubulysin Derivative
IC50
14a 18.86 nM
14b 11.97 nM
14c 27.13 nM
14d 30.99 nM
14e 34.41 nM
14f 82.94 nM
14g 0.21 µM
14h 0.47 µM
14i 0.51 µM
14j 0.73 µM
14k 0.31 µM
14l 0.74 µM
Colchicine 0.34 µM

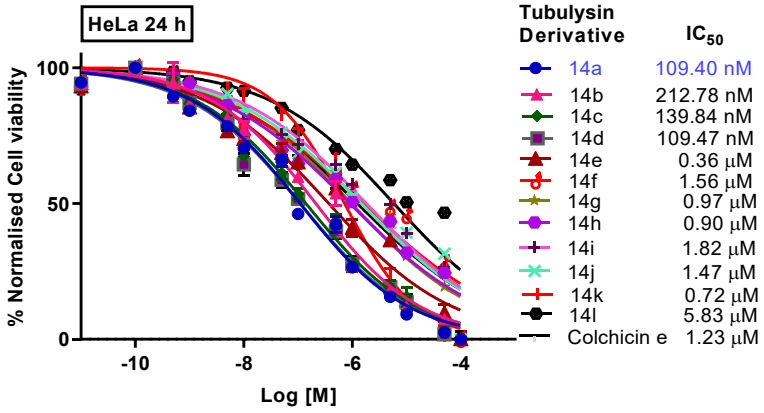
HeLa 24 h
% Normalised Cell viability
100
50
0
-10
-8
-6
-4
Log [M]
Tubulysin Derivative
IC50
14a 109.40 nM
14b 212.78 nM
14c 139.84 nM
14d 109.47 nM
14e 0.36 µM
14f 1.56 µM
14g 0.97 µM
14h 0.90 µM
14i 1.82 µM
14j 1.47 µM
14k 0.72 µM
14l 5.83 µM
Colchicin e 1.23 µM

Figure 5.4 IC_{50} studies of tubulysin derivatives **14a**–**l** in various human cancer cell lines for an incubation period of 48 h and 24 h, along with colchicine as a standard. Data are expressed as mean ±S.D. (n=3).

5.2.1 Molecular docking of the third generation of tubulysin derivatives 14a-l

5.2.2 Validation

In the current computational work, the tubulin protein and the synthesized third-generation tubulysin derivatives binding pattern were analyzed by molecular docking studies and pharmacophore analysis. The reliability of the applied docking protocol was first validated using re-docking of a co-crystallized inhibitor **55Q**.

5.2.3 Validation of the docking protocol

The molecular docking protocol should be validated to ensure the accuracy of the generated results. The validation of the protocol was performed by re-docking of the co-crystallized inhibitor tubulysin M (**55Q**) and correlating its docked orientation with the native orientation through visual analysis. The correlation is statistically represented as root mean square deviation (RMSD) scores. An online tool was employed for RMSD (E.W. Bell, Y. Zhang. DockRMSD: an Open-Source Tool for Atom Mapping and RMSD calculation of Symmetric Molecules through Graph Isomorphism. Journal of Cheminformatics, 11:40 (2019)), which was found to be in the acceptable range (2.91 Å). The superimposed orientation of the native and docked pose of the **55Q** inhibitor is depicted in figure 5.5.

Following the validated protocol, molecular docking studies of inhibitors **14a**–**l** were performed. The molecular docking score is represented as “S”, which depicts the predicted binding affinity of a ligand to a target protein, and its unit is kcal/mol. The S is calculated in the final refinement method, which was induced fit, and the scoring function used was Generalised-Born Volume Integral/Weighted Surface Area dG (GBVI/WSA dG). It estimates the free energy of binding between a ligand and a receptor, considering the desolvation effects, van der Waals interactions, electrostatics, and solvation energy into account.

A more negative value closer to –9 kcal/mol in the "S" score represents strong binding interactions. The S scores of all the inhibitors are depicted in table 5.3. The co-crystallized inhibitor 55Q scored highest, –9.143 kcal/mol. The synthesized inhibitors **14a**, **14b**, **14c**, **14d**, **14e**, **14f,** and **14k** with potent anticancer activity (IC_{50} < 200 nM) scored in the range of –9.03 kcal/mol to –8.50 kcal/mol. The less potent inhibitors **14g**, **14h**, **14i**, **14j**, and **14l** (IC_{50} in the range of 200–600 nM) scored low in the docking study in the range of –8.82 to –7.20 kcal/mol, and the least active inhibitor **14h** scored –8.14 kcal/mol. This validates the correlation between the experimental anticancer activity and computationally predicted scores.

Further, the binding pose of all the inhibitors **14a**–**l** was compared with the co-crystallized inhibitor tubulysin M, and the superimposed orientation of inhibitors **14a**–**l** is shown in figure 5.6. All the inhibitors were docked in the active site cavity between the interface of tubulin monomers β (B-chain) and α (C-chain), showing the interacting amino acid residues similar to tubulysin M. The protein-inhibitor interactions counted from molecular docking studies were analyzed and depicted in table 5.3, and the details of amino acid-inhibitor interactions are reported in tables 5.4 and 5.5.

Table 5.3. Comparison of the total number of interacting amino acids and docking scores, along with experimental IC_{50} studies of the third generation of tubulysin inhibitors in LNCaP cells.

Inhibitor	Total number of interacting amino acids	Total number of interactions	PI	NI	HBA	HBD	H	IC_{50} in nM (LNCaP cells/48 h incubation)	Docking Score "S" in kcal/mol
Tubulysin M	12	16	1	1	5	1	8	**NA**	–9.14
14a	12	14	1	1	3	1	8	14.29	–8.94
14c	11	14	1	1	3	2	7	25.67	–8.96
14b	12	16	1	1	5	2	7	26.80	–9.01

14e	8	11	1	1	3	1	5	46.92	–8.70
14d	14	15	1	1	3	2	8	53.33	–8.50
14f	9	11	1	0	2	2	6	115.21	–8.91
14k	13	13	1	0	0	3	9	141.23	–9.03
14g	11	13	1	1	3	1	7	226.79	–8.26
14i	9	10	1	0	2	1	6	333.01	–8.49
14l	9	12	1	1	4	1	5	460.23	–8.82
14j	11	11	0	1	5	1	4	371.12	–7.20
14h	9	10	1	0	1	1	7	>500	–8.14

PI- Positively ionizable, NI- Negatively ionizable, HBA- Hydrogen bond acceptor, HBD-Hydrogen bond donor, H-Hydrophobic interaction

The interaction of native co-crystallized pose of tubulysin M was reported with 12 amino acid residues of the active site of tubulin protein through 16 total number of interactions that include positive ionizable (1), negative ionizable (1), hydrogen bonding (H-bond acceptor-5, H-bond donor-1), and hydrophobic (8) interactions. In a comparative study, the synthesized potent inhibitors with IC_{50} < 30 nM (**14a**, **14b**, and **14c**) were found to interact with 12, 12 and 11 amino acid residues of the active site of tubulin protein via 14, 16, and 14 total interactions, respectively, like that of tubulysin M interactions where hydrophobic interactions (8, 7 and 7) dominates. Additionally, the most potent inhibitors **14a**, **14b**, and **14c** show a minimum of 3 hydrogen bond acceptors, a hydrogen bond donor, a strong positive and a negative ionic type of interactions with tubulin amino acid residues, which were in close alignment with the standard inhibitor.

The next potent inhibitors **14d**–**f, 14g**, and **14k** with 30 nM< IC_{50} <250 nM were found to interact with 8-14 amino acid residues through 11-15 total interactions as mentioned in table 5.4. The least potent inhibitors **14h**, **14i**, **14j**, and **14l**, with IC_{50}>250 nM, were found to have interactions with 9-11 tubulin amino acid residues through 10-12 total number of interactions, accounting for the observed experimental cytotoxicity studies as shown in table 5.4.

Further, the correlation between the structural features and anticancer activity of tubulysin derivatives can be established by analysing critical amino acid residues which are involved in the inhibitory activity and comparing them with a standard inhibitor, tubulysin M. Table 5.3 includes the list of amino acid residues of active site of tubulin protein and its type of interactions with tubulin inhibitors **14a**–**l**. The interactions of amino acid residues, which are reported for co-crystallized inhibitor (Tubulysin M), are critical, and in the molecular docking study, the newly designed inhibitors should interact at the protein active site with similar amino acid residues. Figures 5.7-5.19 depict the hydrogen bond and ionic interactions of inhibitors **14a**–**l** with the amino acid residues of the tubulin active binding site.

In the case of PDB ID 4ZOL, tubulysin M was found to exhibit a strong positive ionizable (PI) ionic interaction with Asp 179 B amino acid residue (Figure 5.7). In the molecular docking studies, the N-terminal amino acid of the synthesized inhibitors **14a**–**l** were found to orient and interact with Asp 179 B amino acid residue, except inhibitors **14j** and **14k**. Asp 179 B is a negatively charged amino acid with a carboxylate group, and the inhibitor's structural analysis suggests that tubulysin M, **14a**–**g**, have an *N*-methylpiperidine ring with pKa ~9.8, which gets protonated at physiological pH. This protonation promotes a stable and strong interaction between the *N*-methylpiperidine moiety of **14a**–**g** and Asp 179 B amino acid residue (Figures 5.8-5.14). This could be a probable reason for **14a**–**g** being the top 8 inhibitors having low IC_{50} values (14–226 nM) during cytotoxicity analysis. But inhibitor **14k**, where the *N*-methylpipecolic acid moiety was replaced by phenylalanine, showed higher potency (IC_{50} = 141 nM) due to the presence of two hydrophobic interactions of the phenyl ring with Ile 332 C and Ala 333 C tubulin amino acid residue along with a PI interaction of amino group of phenyl alanine amino acid (Figure 5.18).

The inhibitors where N-terminus amino acids were modified led to less potent inhibitors (Figures 5.15-5.17 and 5.19), like in the case of **14h**, **14i**, **14j,** and **14l** (IC_{50} = 333–500 nM). Even though **14g**, **14h**, and **14k**

exhibit PI interaction with tubulin amino acid residue Asp 179 B (Figures 5.15-5.16 and Figure 5.19), the cationic functionality in these inhibitors is derived from primary amines, which are less basic compared to the *N*-methylpiperidine ring, a tertiary amine present in the inhibitors **14a**–**g**. Reduced basicity of primary amino groups present in the N-terminal amino acids of **14h**, **14i**, **14j**, and **14l** may be one of the reasons for their weak potency and high IC_{50} values due to weak binding affinity with the tubulin protein.

Moreover, in the case of **14h**, the *N*-methylpipecolic acid moiety was replaced with an electron-rich imidazole ring, which may be repelled by negatively charged tubulin amino acid residue Asp 179 B (Figure 5.15). Similarly, in the case of **14l**, the *N*-methylpipecolic acid moiety was replaced with a more bulky naphthylalanine amino acid, leading to severe steric hindrance and a change in the orientation of **14l** (Figure 5.19). From the *in silico* docking studies, it is suggested that the introduction of aromatic bulkiness at the N-terminus of inhibitors would be detrimental for anti-tubulin activity.

At the C-terminus, tubulysin M was reported to have a negatively ionizable (NI) interaction with the positively charged tubulin active site amino acid residue Arg 278 B (Figure 5.7). This interaction was also observed in the most potent inhibitors **14a**-**14e** (Figures 5.8-5.12) and less potent inhibitors **14g**, **14j**, **14l** (Figure 5.14, Figure 5.15, and Figure 5.19) out of the 12 inhibitors examined in the current study. Thus, an *in silico* study suggests the importance of negative ionizable functionality at the C-terminus of tubulysin derivatives to furnish the required ionic interactions with the amino acid residue Arg 278 B. During the computational study, it was also observed that the tubulin protein active site pocket was larger, where the C-terminus of tubulysin derivatives can form better interactions as compared to the smaller N-terminus active binding site. Therefore, one can explore further modifications at the C-terminus with bulkier H-bond acceptors or NI functionalities for generating potent derivatives, which might be difficult at the N-terminus of the tubulin inhibitors.

As shown in figure 5.7, tubulysin M was also found to interact with the active site of tubulin protein via H-bond acceptor (HBA) and H-bond donor (HBD) types of H-bonding interactions simultaneously. The tubulin inhibitors **14a**–**l** interact with the active site of the tubulin protein mainly via Thr 223 B, Tyr 224, Gly 225 B amino acid residues through H-bond acceptor (HBA) interactions or Asn 329 C amino acid residues through both HBA and HBD interactions (Tables 5.4-5.5, Figures 5.8-5.19). This is because the amide side chain of Asn 329 C residue can interact through both side chain carbonyl and amino moieties, contributing to HBA and HBD interactions, respectively. Out of the 12 inhibitors, eight inhibitors (**14b, 14c**, **14d**, **14f**, **14g**, **14j**, **14k,** and **14l**) were found to have interactions with the amino acid residue Asn 329 C through either HBD or HBA or both. Further, in-depth analysis shows that the amino and carbonyl moieties of the isoleucine fragment of tubulysin derivatives interact through HBD and HBA, respectively. The isoleucine fragment of potent inhibitors **14b**, **14c**, and **14f** form both types of interactions (Figures 5.9, 5.10, and 5.13), while **14g** and **14j** interact through only HBD (Figures 5.14 and 5.17), and **14l** through HBA-type interactions (Figure 5.19). The HBD interactions were also identified in the active inhibitors **14d** and **14k**, but with the tertiary amino group of *N*-methylpipecolic acid and primary amino group of phenylalanine fragments, respectively (Figures 5.11 and 5.18). The less active inhibitors, **14h** and **14i**, did not show any interaction with the amino acid residue Asn 329 C due to their structural modifications with imidazole and cyclohexyl rings at the N-terminus (Figures 5.15 and 5.16). Therefore, it can be inferred that the HBD/HBA interactions of any tubulin inhibitor with the amino residue Asn 329 of the tubulin protein C-chain are critical for better binding affinity in the interface of α- and β-tubulins.

Apart from the ionic and H-bonding interactions, hydrophobic interactions shown in the structure-based pharmacophore of the inhibitors tubulysin M, **14a**–**l**, also play a critical role in the strong

binding of the inhibitors to the tubulin protein (Figures 5.20-5.32, Tables 5.4-5.5).

In the docking interaction studies of the inhibitors, the yellow sphere represents the hydrophobic pharmacophore of the inhibitor interacting with the hydrophobic region of the tubulin heterodimer active site. This region comprises hydrophobic amino acids like Leu 248 C, Val 353 C, Val 328 C, Ile 355 C, Ile 332 C, Val 177 B, Ala 247 C, and Thr 221 B. The aliphatic side chain of the inhibitor's isoleucine fragment interacts hydrophobically with different amino acid residues in the tubulin protein (Figures 5.21-5.31) except inhibitor **14l** (Figure 5.32). In the case of **14l**, the bulky bicyclic naphthyl ring fragment changes the structural orientation of the inhibitor in the active site to a pose where the isoleucine fragment is displaced to the hydrophilic region, leading to loss of hydrophobic interaction (Figure 5.32). Similar hydrophobic interactions were also observed with the valine fragment present in the inhibitors. In the docking poses of the inhibitors, the valine fragment interacts with the hydrophobic region present in the protein dimer. Thus, the presence of lipophilic fragments like isoleucine and valine in the middle portion of the inhibitors is very critical for hydrophobic interactions. Moreover, in all the inhibitors, a third fragment with a thiazole ring was also shown to interact with the hydrophobic region of the tubulin protein.

In the current study, 12 tubulin inhibitors were designed, synthesized, and *in vitro* cytotoxicity assays against human cancer cells were performed. The *in silico* studies were conducted to understand the effect of structural modifications on tubulin inhibitors for binding to the tubulin protein. According to our experimental and computational analysis, it was observed that the N-terminus of tubulin inhibitors is very sensitive towards any modifications, which may be due to the restricted pocket size in the protein. The replacement of the non-aromatic *N*-methylpipecolic acid moiety with electron-rich imidazole, cyclohexyl, phenyl, naphthyl, or amino functionalities was found to be detrimental for the anticancer activity of inhibitors. But any modifications at the C-

terminus of the tubulin inhibitors were found to be moderately tolerated due to the larger pocket size at the active binding site. The introduction of aromatic functionalities at the C-terminus, as in the case of **14f** and **14g,** slightly improves the binding affinity through hydrophobic interactions. The central lipophilic isoleucine, valine, and thiazole fragments strongly contribute to the binding affinity of the inhibitors through hydrophobic interactions with the tubulin protein. The computational analysis suggests the cationic N-terminus, hydrophobic central, and anionic C-terminus fragments are the most essential structural requirements for a better tubulin inhibitory effect.

Table 5.4. Comparison of inhibitors (**14a**–**g**) and type of interactions with the active site amino acid residues of the tubulin protein.

Amino acid residues	**Tubulysin M-native pose**	**Tubulysin M-Docked pose**	**14a**	**14b**	**14c**	**14d**	**14e**	**14f**	**14g**
Thr223 B	H/HBA	H	HBA	HBA	HBA	HBA	HBA		HBA/H
Tyr 224 B	H/HBA	H	H	H/HBA	H	H	H	HBA/H	H
Asn329 C	HBA/HBD	HBA/HBD		HBA/HBD	HBA/HBD	HBD		HBA/HBD	HBD
Asp179 B	PI	PI/HBD	PI/HBD	PI/HBD	PI/HBD	PI	PI/HBD	PI	PI/HBD
Leu248 C	H	H	H	H	H	H	H	H	H
Val 353 C	H	H	H	H	H	H		H	H
Val 328 C	H	H	H		H				H
Ile 355 C	H	H	H	H	H	H		H	H
Ile 332 C		H							
Val 177 B	H	H	H	H	H	HBD/H	H	H	H
Ala247 C		H				H	H	H	
Thr221 B			H			H	H		
Arg278 B	HBA/NI		HBA/NI	HBA/NI	HBA/NI	HBA/NI	HBA/NI		HBA/NI

Gly225 B	HBA		HBA	HBA		HBA			HBA
Leu227 B			H	H	H	H			
Val 250 C									
Tyr 210 B	H			H		H			
Gln 15 B									
Gln 11 B									
Lys176 B								HBD	
Thr 74 B									
Ala333 C									
Total no. of amino acid residue interactions	12	11	12	12	11	14	8	9	11

Table 5.5 Comparison of inhibitors (**14h**–**l**) and type of interactions with the active site amino acid residues of the tubulin protein.

Amino acid residues	**Tubulysin M- native pose**	**Tubulysin M-Docked pose**	**14h**	**14i**	**14k**	**14l**	**14j**
Thr223 B	H/HBA	H	H	H		HBA/H	H/HBA
Tyr 224 B	H/HBA	H	H	H/HBA	H	HBA	H/HBA
Asn329 C	HBA/HBD	HBA/HBD			HBD	HBA	HBD
Asp179 B	PI	PI/HBD	PI/HBD	PI	PI	HBD/PI	
Leu248 C	H	H	H	H	H	H	H
Val 353 C	H	H	H	H	H		H
Val 328 C	H	H	H		H		H
Ile 355 C	H	H	H	H	H		H
Ile 332 C		H			H		H
Val 177 B	H	H	H	H	H	H	H
Ala247 C		H					
Thr221 B							
Arg278 B	HBA/NI					HBA/NI	NI/HBA

Gly225 B	HBA			HBA			HBA
Leu227 B					H	H	
Val 250 C						H	
Tyr 210 B	H				H		
Gln 15 B				HBD			
Gln 11 B			HBA		HBD		
Lys176 B							
Thr 74 B					HBD		
Ala333 C					H		
Total no. of amino acid residue interactions	12	11	9	9	13	9	11

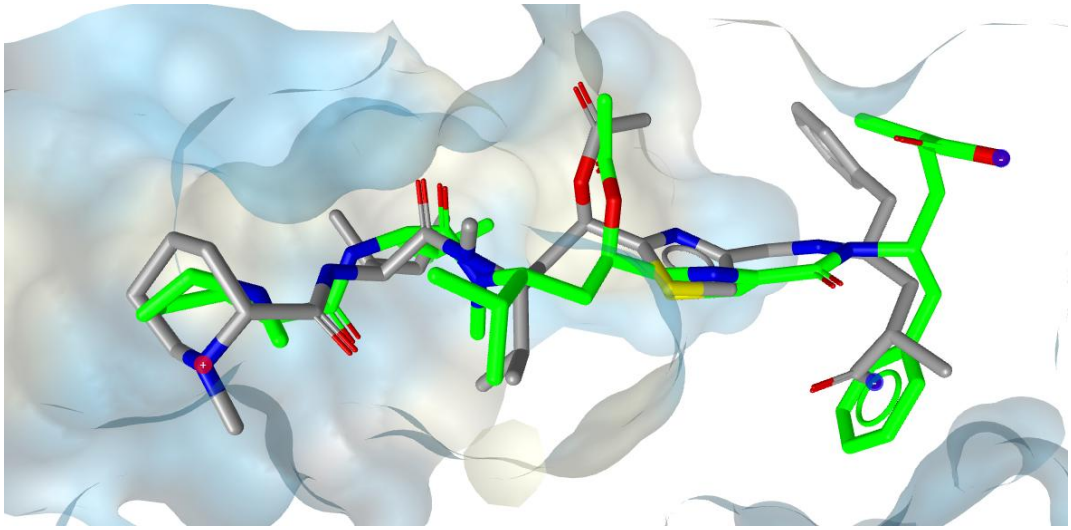

Figure 5.5 Superimposed orientation of native (green) and docked (grey) pose of co-crystallized inhibitor **55Q**.

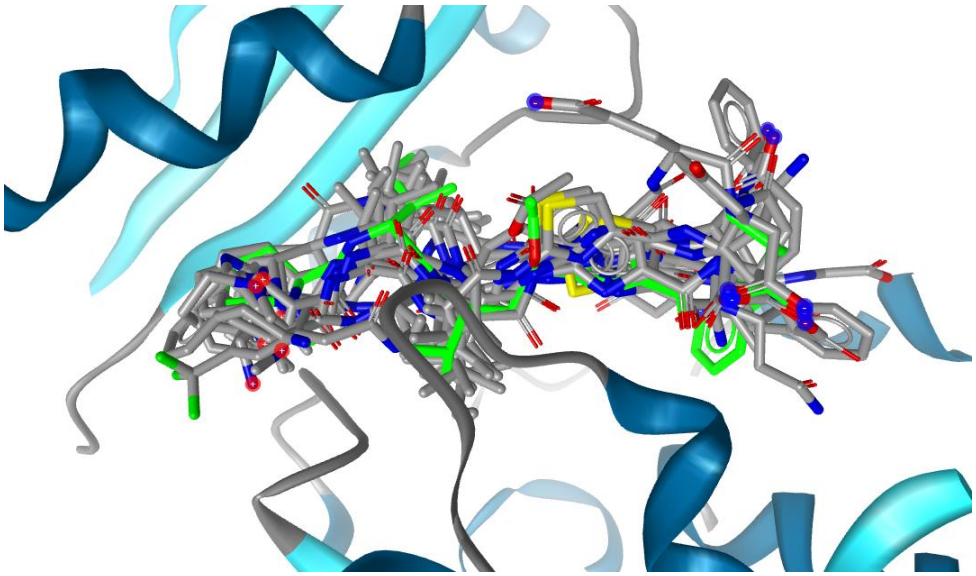

Figure 5.6 The post-docking superimposed orientation of all the inhibitors with co-crystallized inhibitor **55Q** at the active site of the tubulin protein.

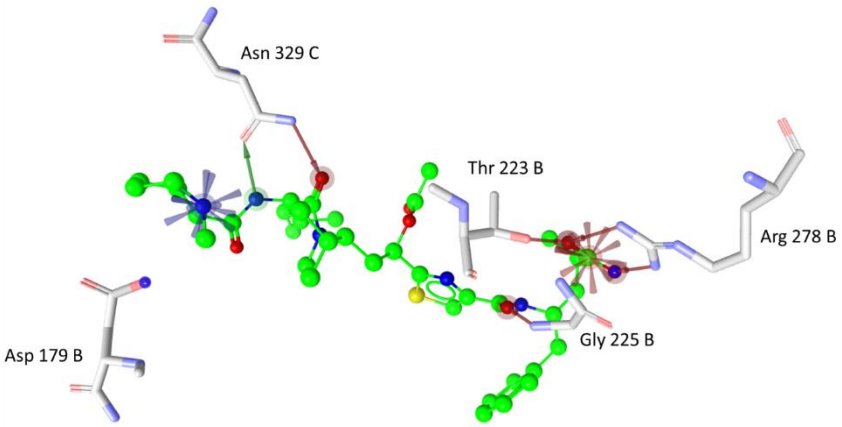

Figure 5.7 Interaction between tubulin active site amino acid residues (represented as stick rendering) and native pose of co-crystallized inhibitor **55Q** (represented as ball and stick rendering); Blue star, red star, green arrow, and red arrow represent positive ionizable, negative ionizable, H-bond donor, and H-bond acceptor interactions, respectively.

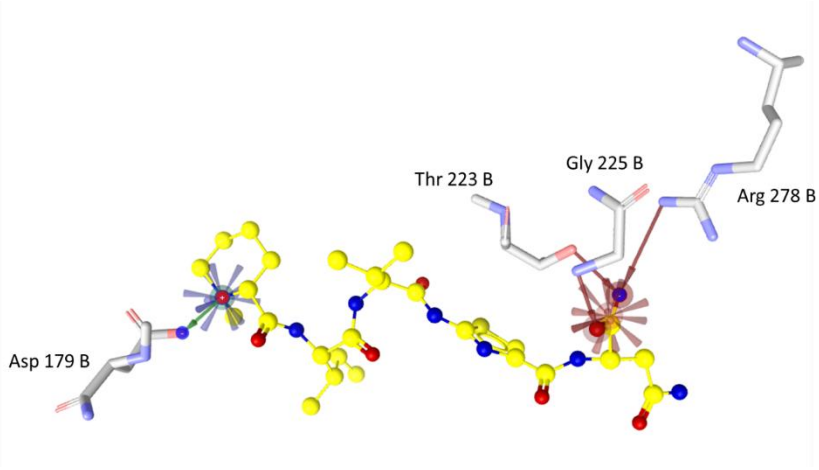

Figure 5.8 Interaction between tubulin active site amino acid residues (represented as stick rendering) and docked pose of **14a** (represented as ball and stick rendering); Blue star, red star, green arrow, and red arrow

represent positive ionizable, negative ionizable, H-bond donor, and H-bond acceptor interactions, respectively.

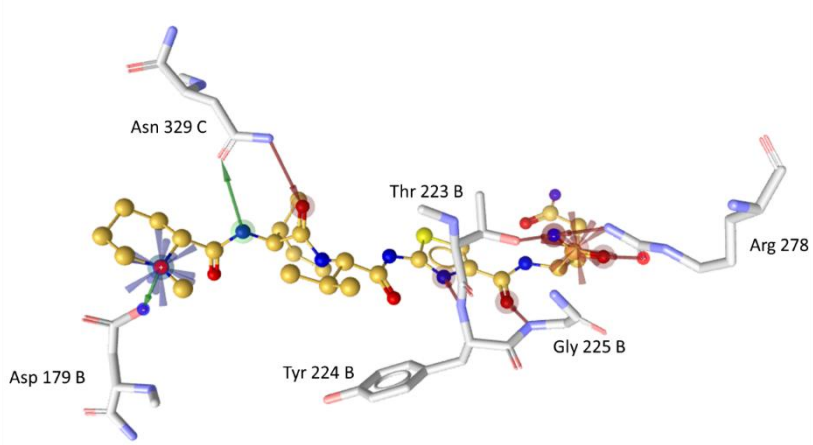

Figure 5.9 Interaction between tubulin active site amino acid residues (represented as stick rendering) and docked pose of **14b** (represented as ball and stick rendering); Blue star, red star, green arrow, and red arrow represent positive ionizable, negative ionizable, H-bond donor, and H-bond acceptor interactions, respectively.

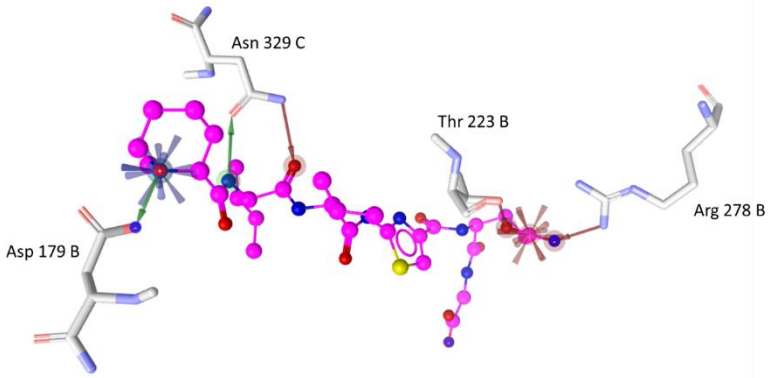

Figure 5.10 Interaction between tubulin active site amino acid residues (represented as stick rendering) and docked pose of **14c** (represented as ball and stick rendering); Blue star, red star, green arrow, and red arrow represent positive ionizable, negative ionizable, H-bond donor, and H-bond acceptor interactions, respectively.

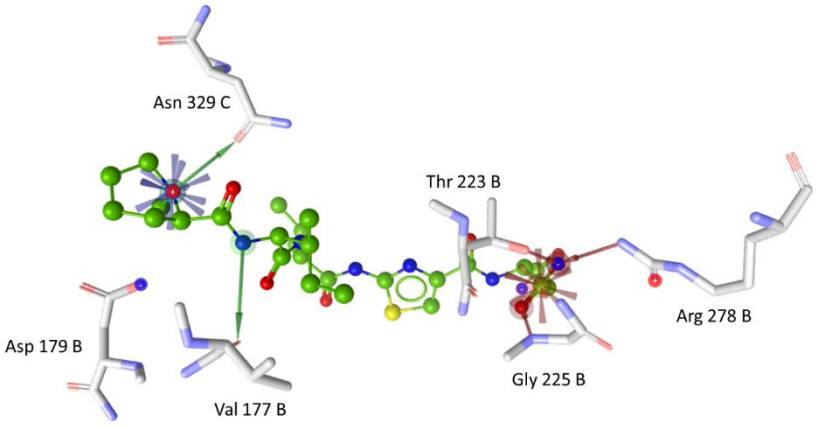

Figure 5.11 Interaction between tubulin active site amino acid residues (represented as stick rendering) and docked pose of **14d** (represented as ball and stick rendering); Blue star, red star, green arrow, and red arrow represent positive ionizable, negative ionizable, H-bond donor, and H-bond acceptor interactions, respectively.

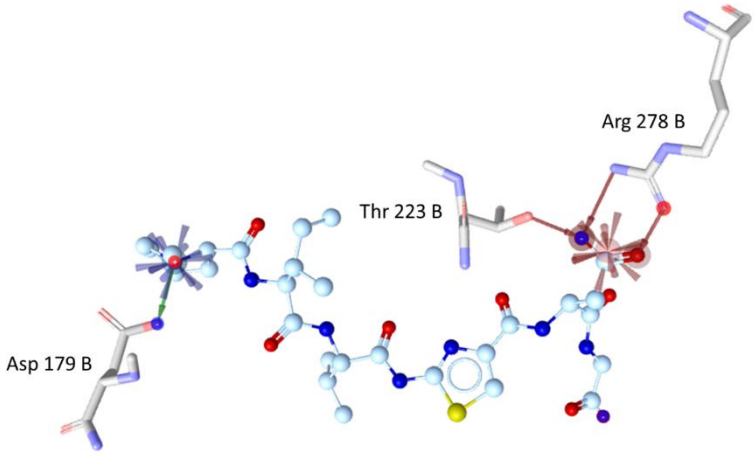

Figure 5.12 Interaction between tubulin active site amino acid residues (represented as stick rendering) and docked pose of **14e** (represented as ball and stick rendering); Blue star, red star, green arrow, and red arrow represent positive ionizable, negative ionizable, H-bond donor, and H-bond acceptor interactions, respectively.

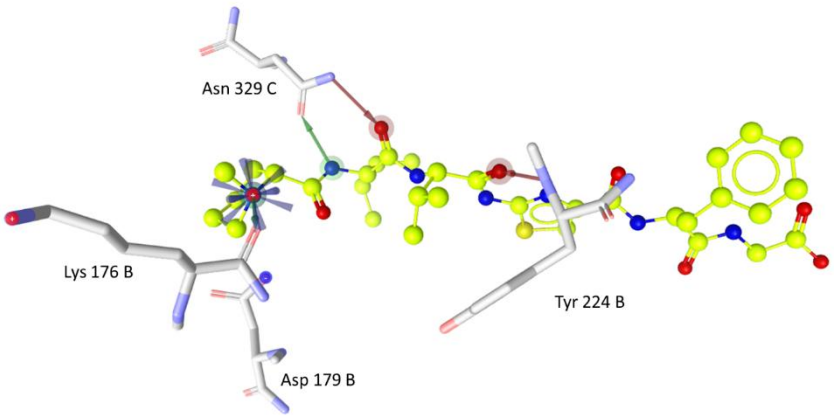

Figure 5.13 Interaction between tubulin active site amino acid residues (represented as stick rendering) and docked pose of **14f** (represented as ball and stick rendering); Blue star, green arrow, and red arrow represent positive ionizable, H-bond donor, and H-bond acceptor interactions, respectively.

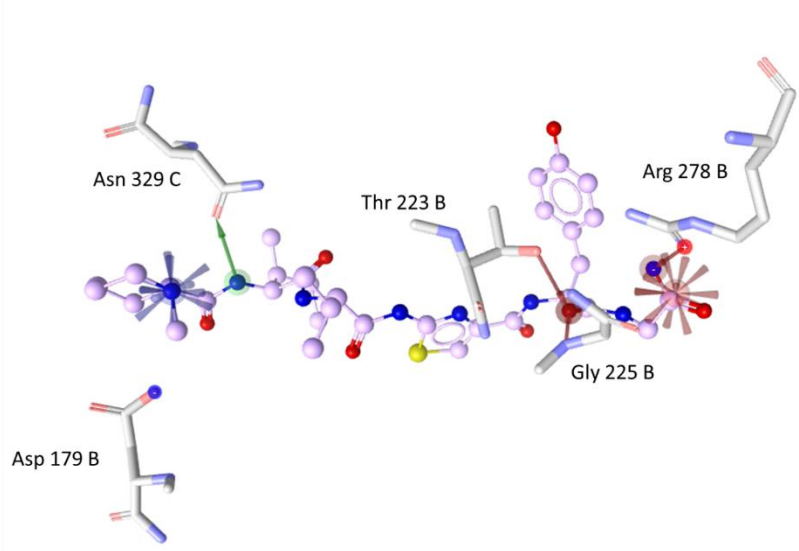

Figure 5.14 Interaction between tubulin active site amino acid residues (represented as stick rendering) and docked pose of **14g** (represented as ball and stick rendering); Blue star, red star, green arrow, and red arrow represent positive ionizable, negative ionizable, H-bond donor, and H-bond acceptor interactions, respectively.

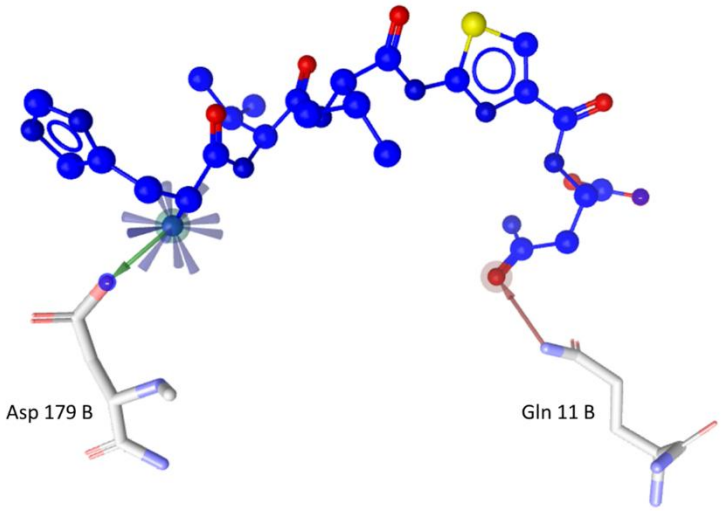

Figure 5.15 Interaction between tubulin active site amino acid residues (represented as stick rendering) and docked pose of **14h** (represented as ball and stick rendering); Blue star, green arrow, and red arrow represent positive ionizable, H-bond donor, and H-bond acceptor interactions, respectively.

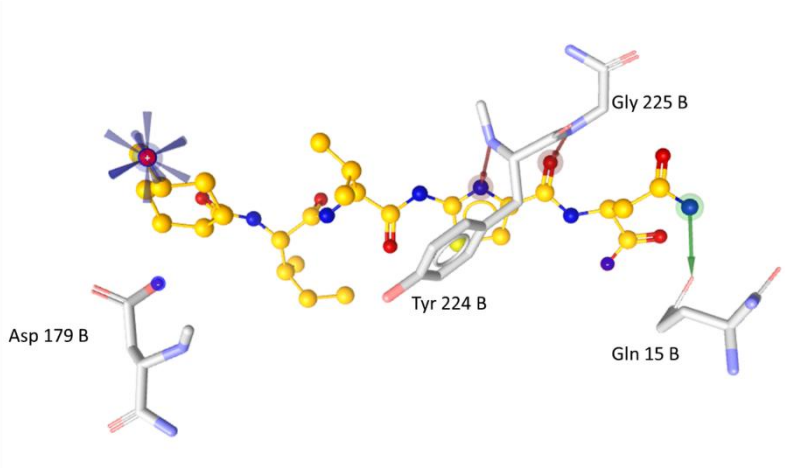

Figure 5.16 Interaction between tubulin active site amino acid residues (represented as stick rendering) and docked pose of **14i** (represented as ball and stick rendering); Blue star, green arrow, and red arrow represent positive ionizable, H-bond donor, and H-bond acceptor interactions, respectively.

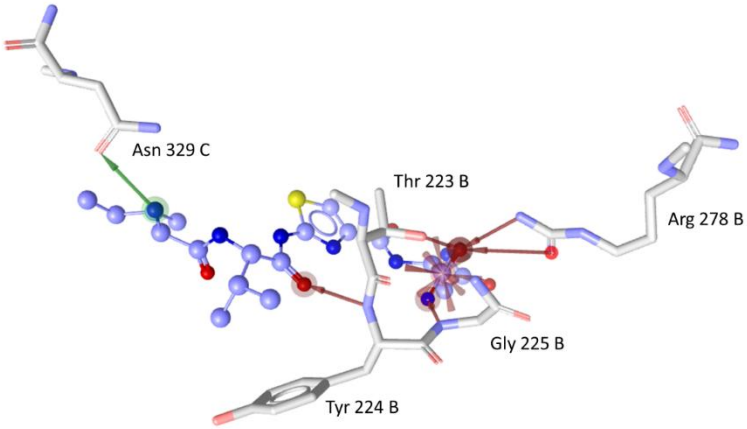

Figure 5.17 Interaction between tubulin active site amino acid residues (represented as stick rendering) and docked pose of **14j** (represented as ball and stick rendering); Red star, green arrow, and red arrow represent negative ionizable, H-bond donor, and H-bond acceptor interactions, respectively.

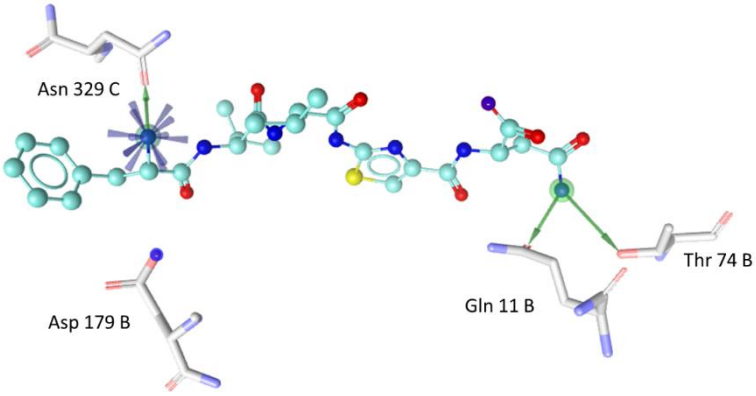

Figure 5.18 Interaction between tubulin active site amino acid residues (represented as stick rendering) and docked pose of **14k** (represented as ball and stick rendering); Blue star and green arrow represent positive ionizable and H-bond donor interactions, respectively.

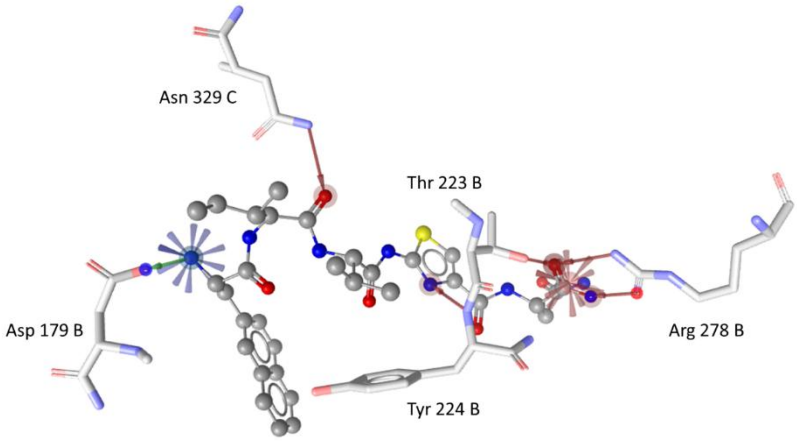

Figure 5.19 Interaction between tubulin active site amino acid residues (represented as stick rendering) and docked pose of **14l** (represented as ball and stick rendering)**;** Blue star, red star, green arrow, and red arrow represent positive ionizable, negative ionizable, H-bond donor, and H-bond acceptor interactions, respectively.

5.2.4 Structure-based pharmacophore hydrophobic interactions

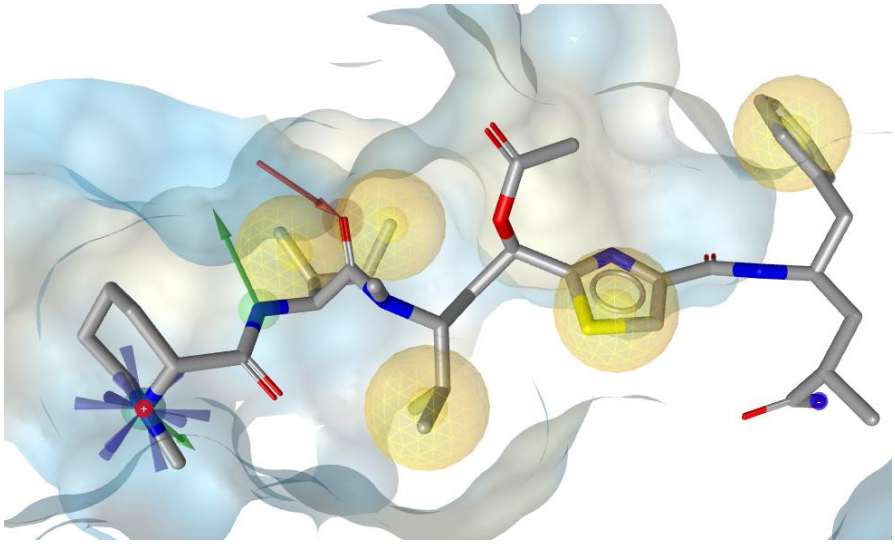

Figure 5.20 Post-docking structure-based pharmacophore of co-crystallized inhibitor **55Q**; Blue star, green arrow, red arrow, and yellow spheres represent positive ionizable, H-bond donor, H-bond acceptor, and hydrophobic pharmacophores, respectively.

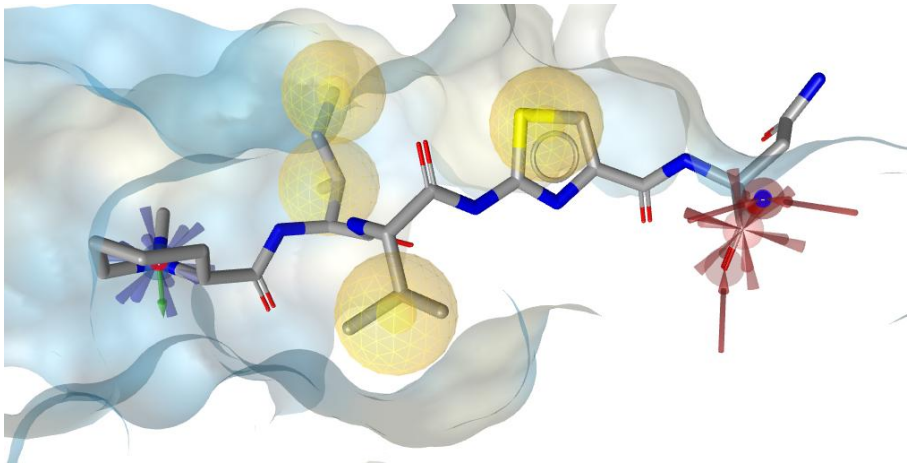

Figure 5.21 Post-docking structure-based pharmacophore of inhibitor **14a**; Blue star, red star, green arrow, red arrow, and yellow spheres represent positive ionizable, negative ionizable, H-bond donor, H-bond acceptor, and hydrophobic pharmacophores, respectively.

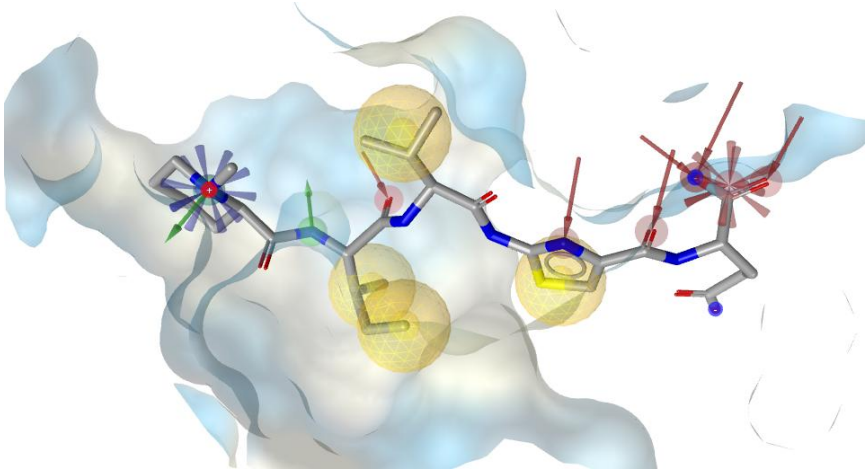

Figure 5.22 Post-docking structure-based pharmacophore of inhibitor **14b**; Blue star, red star, green arrow, red arrow, and yellow spheres represent positive ionizable, negative ionizable, H-bond donor, H-bond acceptor, and hydrophobic pharmacophores, respectively.

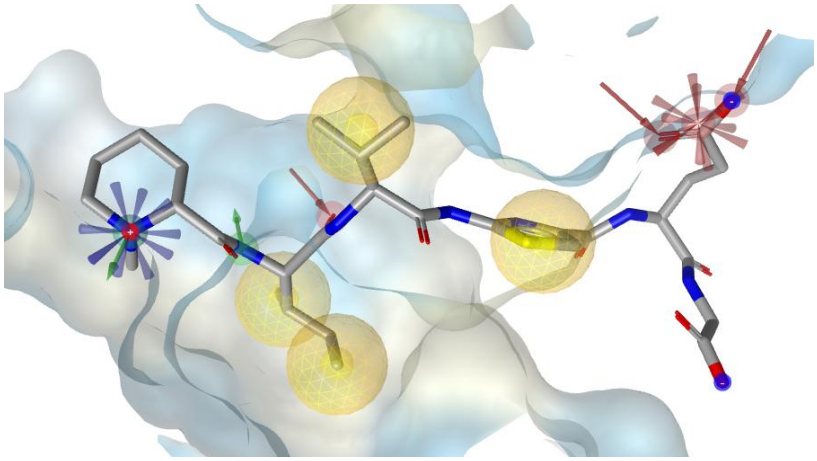

Figure 5.23 Post-docking structure-based pharmacophore of inhibitor **14c**; Blue star, red star, green arrow, red arrow, and yellow spheres represent positive ionizable, negative ionizable, H-bond donor, H-bond acceptor, and hydrophobic pharmacophores, respectively.

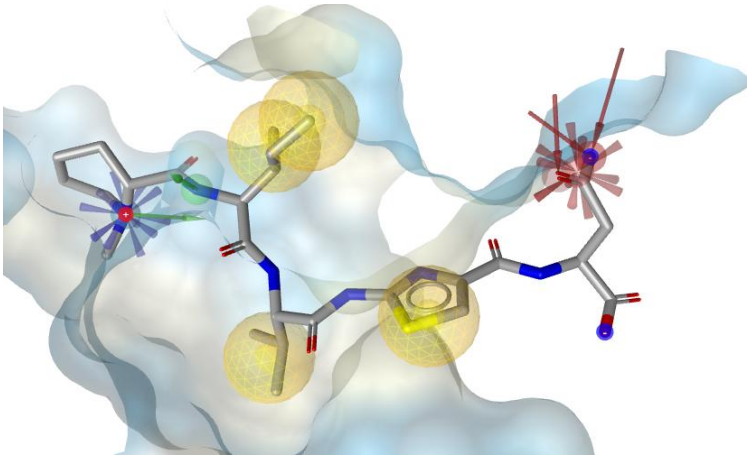

Figure 5.24 Post-docking structure-based pharmacophore of inhibitor **14d**; Blue star, red star, green arrow, red arrow, and yellow spheres represent positive ionizable, negative ionizable, H-bond donor, H-bond acceptor, and hydrophobic pharmacophores, respectively.

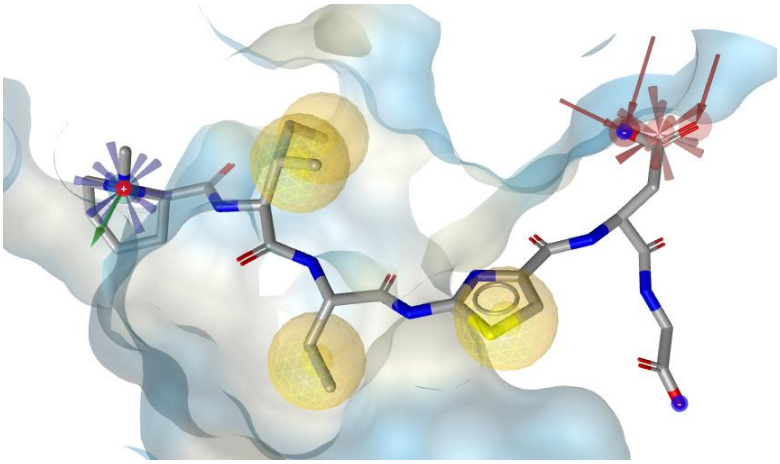

Figure 5.25 Post-docking structure-based pharmacophore of inhibitor **14e**; Blue star, red star, green arrow, red arrow, and yellow spheres represent positive ionizable, negative ionizable, H-bond donor, H-bond acceptor, and hydrophobic pharmacophores, respectively.

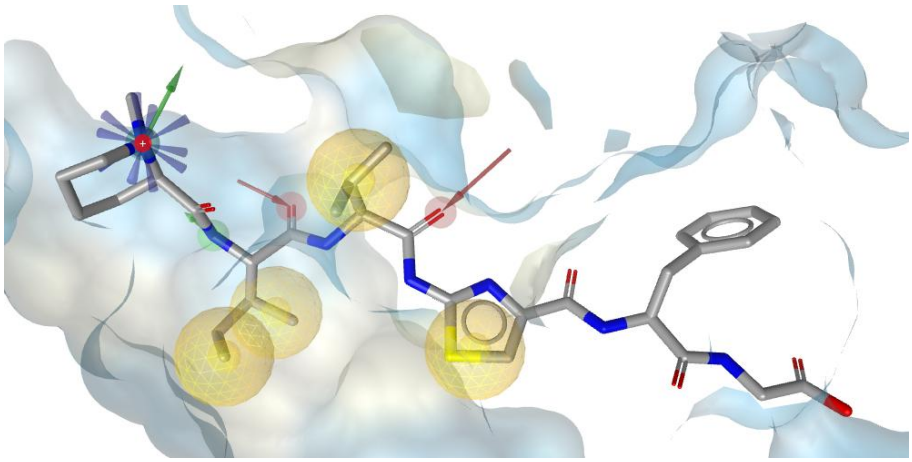

Figure 5.26 Post-docking structure-based pharmacophore of inhibitor **14f**; Blue star, green arrow, red arrow, and yellow spheres represent positive ionizable, H-bond donor, H-bond acceptor, and hydrophobic pharmacophores, respectively.

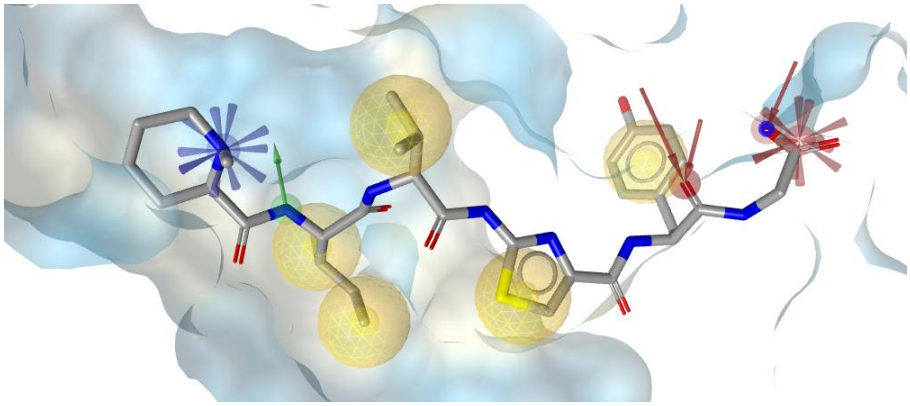

Figure 5.27 Post-docking structure-based pharmacophore of inhibitor **14g**; Blue star, red star, green arrow, red arrow, and yellow spheres represent positive ionizable, negative ionizable, H-bond donor, H-bond acceptor, and hydrophobic pharmacophores, respectively.

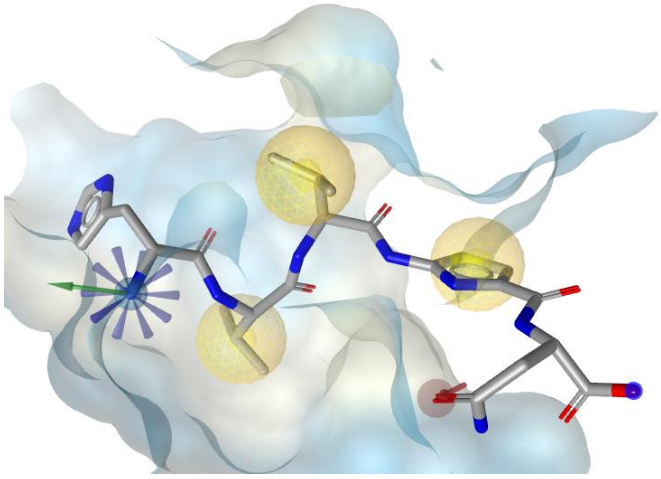

Figure 5.28 Post-docking structure-based pharmacophore of inhibitor **14h**; Blue star, green arrow, red arrow, and yellow spheres represent positive ionizable, H-bond donor, H-bond acceptor, and hydrophobic pharmacophores, respectively.

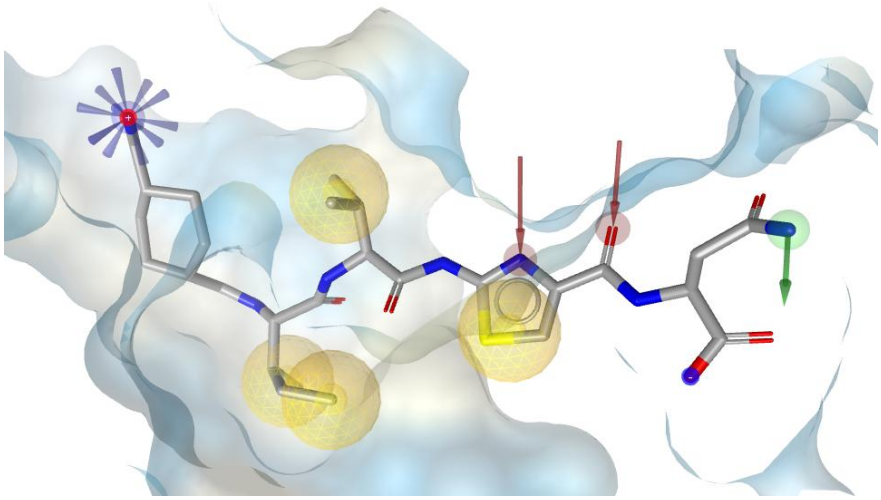

Figure 5.29 Post-docking structure-based pharmacophore of inhibitor **14i**; Blue star, green arrow, red arrow, and yellow spheres represent positive ionizable, H-bond donor, H-bond acceptor, and hydrophobic pharmacophores, respectively.

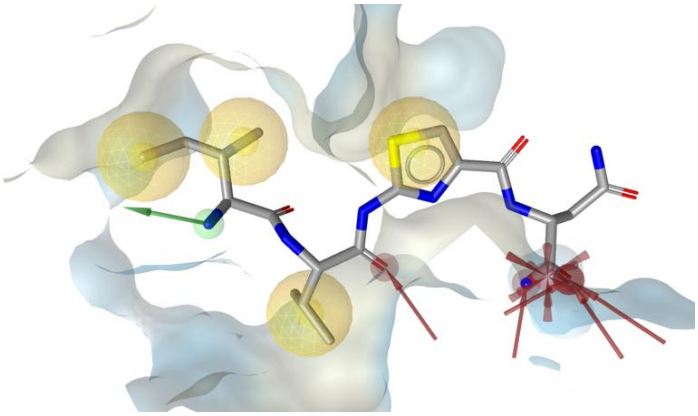

Figure 5.30 Post-docking structure-based pharmacophore of inhibitor **14j**; Blue star, red star, green arrow, red arrow, and yellow spheres represent positive ionizable, negative ionizable, H-bond donor, H-bond acceptor, and hydrophobic pharmacophores, respectively.

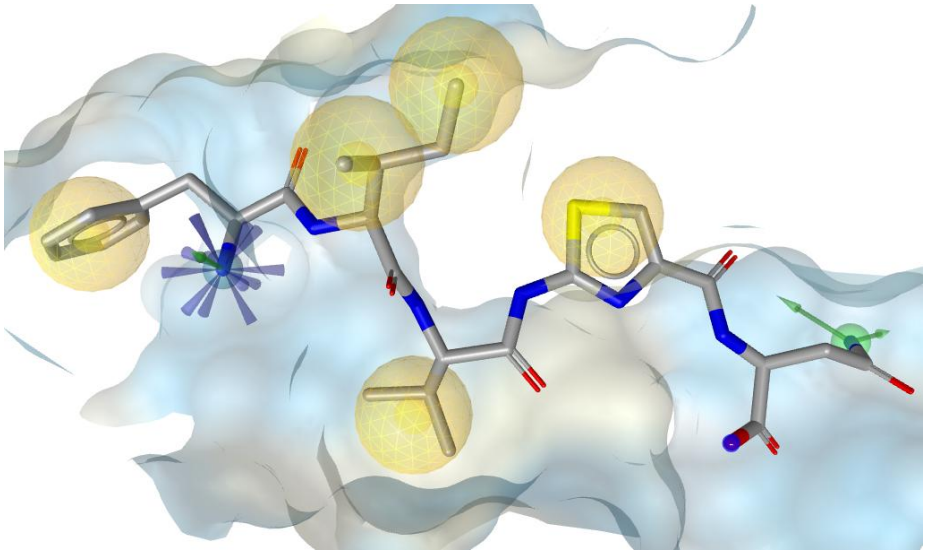

Figure 5.31 Post-docking structure-based pharmacophore of inhibitor **14k**; Blue star, red star, green arrow, and yellow spheres represent positive ionizable, negative ionizable, H-bond donor, and hydrophobic pharmacophores, respectively.

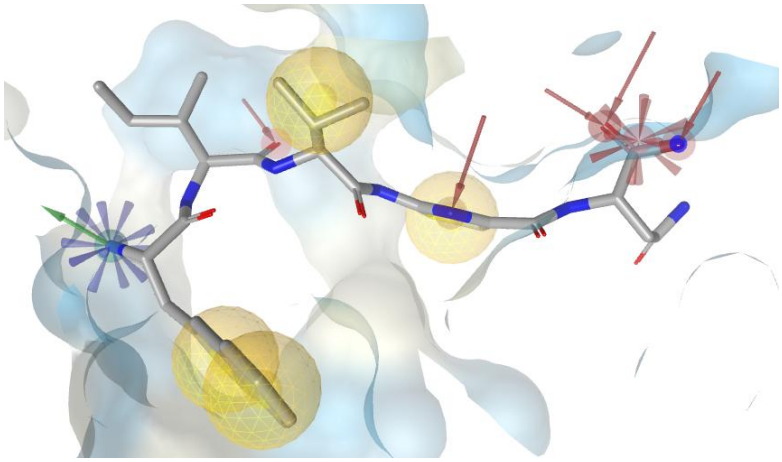

Figure 5.32 Post-docking structure-based pharmacophore of inhibitor **14l**; Blue star, red star, green arrow, red arrow, and yellow spheres represent positive ionizable, negative ionizable, H-bond donor, H-bond acceptor, and hydrophobic pharmacophores, respectively.

5.3 Conclusion

In summary, we report a hitherto unknown compact solid phase synthesis and biological evaluation of structurally simplified tubulysin derivatives whose design was based on extensive computational calculations and docking studies. Essential features of the structural

simplification are related to the amino acid units tubuvaline and tubuphenylalanine or tubutyrosine, which are usually only accessible by lengthy synthesis.

The new subclass of tubulysin derivatives is characterized by the fact that tubuphenylalanine can preferably be replaced by asparagine. At the same time, tubuvaline can be broken down into two smaller building blocks, namely (L)-valine and an aminothiazole-bearing carboxylic acid, which are linked together via a peptide bond and thus form a dipeptide unit. This simplification now allows access to new tubulysin derivatives by solid-phase synthesis for the first time. We have also shown that analogs derived by modification of either the C-terminus or the N-terminus can be prepared. As such, modifications may also include targeting ligands or imaging agents for diagnostic and therapeutic purposes. It is important to emphasize that lead structure **14a** showed excellent *in vitro* properties against various cancer cell lines with IC_{50} values in the nM range. The biological validation also reveals that the replacement of *N*-methylpipecolic acid with carboxylic acids containing other cycles leads to a drastic loss of activity. Remarkably, variations at the C-terminus with amino acids other than asparagine, including dipeptides with C-terminal glycine, predominantly retain the anticancer activity. As one of the most critical hurdles has been overcome, it can be assumed that tubulysin can be further developed for preclinical studies in the future.

5.4 Experimental section

5.4.1 General methods and materials

Chlorotrityl resins, Fmoc-protected amino acids, coupling reagents, chemicals, and solvents used for chemical synthesis of fragments and solid phase peptide synthesis (SPPS) were procured from Iris Biotech GmbH, Sigma Aldrich, Merck, Spectrochem, TCI, and Expressolv. Dry solvents were prepared by the use of suitable drying agents and standard procedures. All reactions were performed in oven-dried glasswares, the moisture-sensitive reactions were performed under a nitrogen atmosphere, and solutions were transferred via a glass syringe. The

progress of the reaction was monitored by thin-layer chromatography (TLC) using TLC plates (60 F254) and visualization under a UV chamber. The intermediates **4**, **6**, **7,** and **9** were then purified by column chromatography using 230–400 mesh size silica gel as the stationary phase with distilled hexane and ethyl acetate as eluents. Tubulin inhibitors **14a**–**l** were synthesized manually by using a peptide vessel (Chemglass) and following the standard peptide coupling procedures. The ^{1}H and ^{13}C NMR spectra were recorded using a Bruker AV 500 MHz NMR spectrometer with TMS as an internal standard. The ^{1}H NMR signals were reported in ppm with reference to residual $CDCl_3$ (7.26 ppm), DMSO-d_6 (2.50 ppm), MeOH-d_4 (3.31 ppm), and multiplicity was reported as s = singlet, d = doublet, t = triplet, q = quartet, m = multiplet or unresolved, and brs = broad singlet, with coupling constants in Hz. $CDCl_3$ and DMSO-d_6 were used as solvents for recording the NMR spectra. Tubulysin derivatives (**14a**, **14b**, **14c**, **14e**, **14f**, **14h**, **and 14l**) were obtained as the salt of TFA. Mass spectra were recorded on a Bruker Micro TOF-Q II instrument using positive mode electrospray ionization methods. The tubulysin derivatives (**14a**–**l**) were purified using an RP-PFP column (XSelect CSH Prep Fluorophenyl 5 μm OBD, 19 mm × 150 mm) in a Buchi Reveleris High Performance Preparative Chromatography instrument. The purity of tubulysin derivatives (**14a**–**l**) was analysed using a Dionex HPLC-Ultimate 3000 Analytical HPLC instrument.

5.4.2 Synthesis of 4-methoxybenzyl 2-aminothiazole-4-carboxylate (4)

In a single-neck round-bottom flask (25 mL), 2-aminothiazole-4-carboxylic acid (500 mg, 3.46 mmol) and sodium carbonate (735 mg, 6.93 mmol) were suspended in dry DMF (5 mL). 4-Methoxybenzyl chloride (0.93 mL, 6.93 mmol) was added dropwise at room temperature through a glass syringe (1 mL) over a period of 3 min, and the reaction was stirred for 16 h under an inert atmosphere. After the completion of the reaction, as monitored by TLC using EtOAc and hexane (1:1) as eluent, the reaction mixture was diluted with EtOAc (1 × 10 mL) and

quenched with chilled brine (1 × 10 mL). The aqueous layer was further extracted with EtOAc (3 × 10 mL). The organic layer was collected and dried over anhydrous Na_2SO_4, filtered, concentrated, and purified through silica gel (neutral 230–400 mesh) column chromatography using 40% EtOAc in hexane solvent mixture as eluent. Yield 56% (520 mg); Pale yellow solid; R_f = 0.36 (hexane/EtOAc 1:1); m.p. 202–204 ° C; ^{1}H NMR (500 MHz, DMSO-d_6) δ 7.88 (s, 2H), 7.70 (s, 1H), 7.33 (d, *J* = 8.6 Hz, 2H), 6.93 (d, *J* = 8.6 Hz, 2H), 5.14 (s, 2H), 3.75 (s, 3H), δ 173.6, 161.3, 159.2, 148.3, 129.9, 128.2, 114.3, 113.9, 65.4, 55.1; IR 2956–2919 (=C–H), 2849 (C–H), 1713 (C=O), 1515–1450 (C=C), 1255–1086 (C–O), 1019 (=C–H bend), 799 (C–N) cm^{-1}; HRMS (+ESI) m/z calcd. for $[C_{12}H_{12}N_2O_3S]$ $[M+Na]^+$, 287.0461, found, 287.0475.

5.4.3 Synthesis of 4-methoxybenzyl (*S*)-2-(2-((((9H-fluoren-9-yl)methoxy)carbonyl) amino)-3-methylbutanamido)thiazole-4-carboxylate (6)

In a single-neck round-bottom flask (25 mL), Fmoc-valine **(5)** (500 mg, 1.47 mmol) was dissolved in dry DCM (5 mL). EDC.HCl (563 mg, 2.94 mmol), HOBt (397 mg, 2.94 mmol), and 4-methoxybenzyl 2-aminothiazole-4-carboxylate **(4)** (465 mg, 1.76 mmol) were sequentially added to the solution at room temperature, and the reaction mixture was stirred for 6 h under an inert atmosphere. After the completion of the reaction, as monitored by TLC using hexane and EtOAc (8:2) as eluent, the reaction mixture was diluted with DCM (1 × 10 mL) and quenched with 1N HCl (1 × 10 mL). The aqueous layer was further extracted with DCM (3 × 10 mL). The organic layer was collected, washed with brine (1 × 5 mL), dried over anhydrous Na_2SO_4, filtered, concentrated, and the crude mixture was purified by silica gel (neutral, 230–400 mesh) column chromatography using 30% EtOAc in hexane as eluent. Yield 75% (860 mg); White solid upon standing; R_f = 0.36 (hexane/EtOAc 8:2); m.p. 321–323 °C; ^{1}H NMR (500 MHz, $CDCl_3$) δ 11.46 (s, 1H), 8.01 (s, 1H), 7.72 (d, *J* = 7.7 Hz, 2H), 7.55 (t, *J* = 6.9 Hz, 2H), 7.37–7.34 (m, 4H), 7.26 (t, *J* = 6.9 Hz, 2H), 6.89 (d, *J* = 7.7 Hz, 2H), 6.03–5.94 (m, 1H), 5.25 (s, 2H), 4.54–4.48 (m, 3H), 4.20 (t, *J* = 7.0 Hz, 1H), 3.80

(s, 3H), 2.18–2.10 (m, 1H), 0.97–0.94 (m, 6H); ^{13}C NMR (125 MHz, $CDCl_3$ δ 171.3, 162.3*, 162.0, 157.0, 144.6, 143.8, 143.7, 141.2*, 127.8, 127.1*, 125.1, 123.1, 120.0, 67.7, 60.4, 53.5, 52.3, 47.2, 31.6, 19.3, 18.3 (*higher intensity signals); IR 3299 (N–H), 2956-2872 (=C–H), 2465 (C–H), 1682 (C=O), 1536 (C=O), 1510 (C=O), 1243 (C–O), 1185 (=C–H bend), 737 (C–N) cm^{-1}; HRMS (+ESI) m/z calcd. for [$C_{32}H_{31}N_3O_6S$] [M+H]$^+$, 586.2006, found, 586.2006.

5.4.4 Synthesis of (*S*)-2-(2-((((9H-fluoren-9-yl)methoxy)carbonyl) amino)-3-methyl butanamido) thiazole-4-carboxylic acid (7)

In a single-neck round-bottom flask (25 mL), 4-methoxybenzyl (S)-2-(2-(((9H-fluoren-9-yl)methoxy)carbonyl)amino)-3-methylbutanamido) thiazole-4-carboxylate (**6**) (1 g, 1.70 mmol) was dissolved in DCM (2 mL). 20% TFA in DCM (10 mL) was added to the reaction mixture at room temperature, and the reaction was stirred for 1.5 h. After the completion of the reaction, as monitored by TLC using hexane and EtOAc (1:1) as eluent, TFA was evaporated under reduced pressure. The reaction mixture was then diluted with EtOAc (1 × 10 mL) and washed with Millipore water (1 × 10 mL). The aqueous layer was further extracted with EtOAc (3 × 10 mL). The organic layer was collected and dried over anhydrous Na_2SO_4, filtered, concentrated, and purified through silica gel (neutral 230–400 mesh) using 100% EtOAc. Yield 98% (785 mg); White solid upon standing; R_f = 0.23 (hexane/EtOAc 1:1); m.p 280–282 °C; ^{1}H NMR (500 MHz, DMSO-d_6) 12.67 (s, 1H), 8.07 (s, 1H), 7.87 (d, *J* = 7.6 Hz, 2H), 7.81 (d, *J* = 8.3 Hz, 1H), 7.73 (t, *J* = 7.8 Hz, 2H), 7.4 (t, *J* = 7.8 Hz, 2H), 7.33–7.29 (m, 2H), 4.31–4.20 (m, 3H), 4.16 (t, *J* = 7.9 Hz, 1H), 2.09–2.03 (m, 1H), 0.92 (d, *J* = 7.0 Hz, 3H), 0.89 (d, *J* = 7.0 Hz, 3H); ^{13}C NMR (125 MHz, DMSO-d_6) δ 171.7, 163.1, 161.6, 156.4, 144.7, 143.8, 140.8, 127.8, 127.20, 125.4, 123.1, 120.2, 65.9, 60.3, 46.7, 30.1, 19.1, 18.6; IR; 3334 (O–H) 3303 (N–H), 3081–2925 (=C–H), 2853 (C–H) 1668 (C=O), 1489 (C=C), 1206 (C–O), 1080 (=C–H bend), 1031 (C–N bend) cm^{-1}; HRMS (+ESI) m/z calcd. for [$C_{24}H_{23}N_3O_5S$] [M+H]$^+$, 466.1437, found, 466.1473.

5.4.5 Synthesis of (*R*)-1-methylpiperidine-2-carboxylic acid (9)

In a double-neck round-bottom flask (25 mL), a hydrogen gas-filled bladder was fitted to one neck of the round-bottom flask through a borosilicate glass heavy-wall glass stop cock adapter. Pipecolic acid (100 mg, 0.77 mmol) and formaldehyde (120 μL, 1.54 mmol%) were added to the round-bottom flask and dissolved in methanol (2 mL). 10% Pd/C (81.94 mg, 10 mol%) was added slowly to the mixture, and the reaction mixture was sealed using a rubber septum. The residual air in the reaction vessel was expunged through a syringe needle inserted through the rubber septum that is connected to a filtration pump through a silicone tube for 2 minutes or until the solution starts bubbling. The reaction mixture is now filled with hydrogen gas from the bladder via a stop cock and allowed to stir at room temperature for 24 h. After the completion of the reaction as monitored by TLC using MeOH and DCM (1:1) as eluent, the reaction mixture was diluted with MeOH (15 mL) and filtered through a celite powder filled sintered Buchner funnel with inner joint fitted to a round bottom flask (50 mL) to remove the palladium/charcoal with the help of a suction pump. The celite pad was washed with MeOH (3 × 3 mL), and the filtrate was concentrated under reduced pressure. Yield 99% (109 mg); White solid; R_f = 0.21 (MeOH/DCM) 1:1; m.p 101–103 °C; ^{1}H NMR (500 MHz, MeOH-d_4) δ 3.47–3.37 (m, 2H), 3.01 (t, *J* = 8.3 Hz, 1H), 2.88 (s, 3H), 2.23 (d, *J* = 13.4 Hz, 1H), 1.89–1.83 (m, 2H), 1.79–1.74 (m, 2H), 1.59–1.52 (m, 1H); ^{13}C NMR (125 MHz, MeOH-d_4) δ 173.5, 70.4, 55.3, 43.2, 29.5, 24.1, 22.6; IR 2936 (O–H), 2862 (C–H) 1606 (C=O), 1317 (C–C), 1173 (C–O), 1004 (C–N) cm^{-1}; HRMS (+ESI) m/z calcd. for $C_7H_{13}NO_2$ $[M+H]^+$, 144.1019, found, 144.1023.

5.4.6 General procedure of solid-phase peptide synthesis

5.4.6.1 Resin swelling

The resins used in solid phase synthesis were first swelled with DCM (5 mL) for 30 minutes by bubbling nitrogen gas through the beads in the peptide vessel. After draining DCM, the beads were again swelled with DMF (3 × 5 mL), repeating the process for 15 minutes.

5.4.6.2 General procedure for the Kaiser test

Kaiser test kit preparation reagents:

a) Dissolve 500 mg of ninhydrin in 10 mL of ethanol.

b) Dissolve 80 g of phenol in 20 mL of ethanol.

c) Dilute 2 mL of 0.001M solution of KCN to 100 mL with pyridine.

Add two drops of each of the above solutions to a few dried resin beads in a glass test tube and warm to 110 °C in a preheated sea sand bath for 2-3 minutes. The freshly prepared Kaiser test kit can be stored at room temperature for 6 months without decomposition. The appearance of dark blue colour signifies the presence of free amine groups in the resin beads, indicating the deprotection of the Fmoc group, while the colourless beads signify the absence of the amine group, indicating the completion of the coupling reaction. The test was performed after coupling of each amino acid, as well as after the deprotection of the Fmoc group at each step.

5.4.6.3 General procedure for Fmoc deprotection

The Fmoc group of the N-terminus of the growing peptide chain was deprotected using 20% piperidine in DMF (10 mL) by bubbling nitrogen gas through the resin beads for 10 minutes in each step of Fmoc deprotection. The procedure was repeated three times (1 × 4 mL; 2 × 3 mL) to ensure the complete deprotection of the Fmoc group.

5.4.6.4 General procedure for peptide cleavage from resin beads

The peptide was cleaved from the resin beads using 10 mL of cleavage cocktail (a mixture of 9.5 mL trifluoroacetic acid, 0.25 mL triisopropylsilane, and 0.25 mL water) by bubbling nitrogen gas through the resin. First, 5 mL of the cocktail was added to the resin, and nitrogen gas was bubbled for 30 minutes, followed by the addition of the cocktail solution (2 × 2.5 mL), with nitrogen bubbling for 5 minutes each time. The collected mother liquor after peptide cleavage was evaporated under reduced pressure, and the concentrated solution was precipitated in ice-

cold diethyl ether. The precipitate was then dried using nitrogen gas, and the obtained crude product was further purified using HPLC.

5.4.6.5 Procedure for solid-phase peptide synthesis of tubulysin derivatives 14a–l

H-Asn(Trt)-2-ClTrt resin (0.300 g, 0.168 mmol) was initially swelled in DCM (1 × 5 mL), followed by DMF (1 × 5 mL) for 15 min each. The solvent was drained using a filtration pump, and the beads were dried until freely flowing. Fmoc-Val-thiazole-OH **(7)** (0.156 g, 0.336 mmol), PyBOP (0.174 g, 0.336 mmol), and DIPEA (0.293 mL, 1.68 mmol) were dissolved in DMF (0.5 mL) in a 2 mL glass vial, mixed thoroughly using a Pasteur pipette, added to the peptide vessel containing resin beads and the coupling reaction was carried out for 6 h by bubbling a stream of nitrogen gas through the resin beads in the peptide vessel. The resin beads were then washed with DMF (3 × 5 mL), followed by isopropanol (3 × 5 mL) for 10 min each. The solvent was drained using a filtration pump, and the beads were dried until freely flowing by bubbling N_2 gas through the peptide vessel. The amide coupling was confirmed by performing the Kaiser test to obtain dipeptide **11**. Next, the FmocNH protecting group was cleaved by the addition of 20% piperidine in DMF (1 × 4 mL; 2 × 3 mL) for 10 min each to the resin beads. The resin beads were then washed with DMF (3 × 5 mL), followed by isopropanol (3 × 5 mL). The solvent was drained using a suction pump, and the beads were dried until freely flowing by bubbling N_2 gas through the resin beads in the peptide vessel. The Kaiser test was performed to confirm the deprotection of the Fmoc. The next amino acid, Fmoc-Ile-OH (0.118 g, 0.336 mmol), PyBOP (0.174 g, 0.336 mmol), and DIPEA (0.293 mL, 1.68 mmolwere dissolved in DMF (0.5 mL) in a 2 mL glass vial, mixed thoroughly using a Pasteur pipette, added to the peptide vessel containing resin beads and the coupling reaction was continued for 6h to afford tripeptide **12**. The FmocNH protecting group was cleaved by the addition of 20% piperidine in DMF. Finally, a mixture of 1-methylpiperidine-2-carboxylic acid **(9)** (0.048 g, 0.336 mmol), PyBOP (0.174 g, 0.336 mmol), and DIPEA (0.293 mL, 1.68 mmol) were

dissolved in DMF (0.5 mL) in a 2 mL glass vial and added to the peptide vessel containing tripeptide **12** to accomplish the amide coupling to obtain tetrapeptide **13**, followed by acid cleavage using a cocktail composed of TFA:TIPS:H_2O (9.5:0.25:0.25) (1 × 5 mL; 2 × 2.5 mL) as described earlier. The mother liquor was collected in a 25 mL round-bottom flask from the peptide vessel, then transferred to a 15 mL centrifuge tube and fitted with a septum. The crude peptide solution was concentrated under reduced pressure to evaporate TFA by inserting a 19-gauge stainless steel needle through the rubber septum. Ice-cold diethyl ether was added to precipitate the tubulysin derivative **14a** as a white solid, washed with ice-cold diethyl ether (3 × 5 mL), dried by passing a stream of nitrogen gas for 15 minutes, and purified by reverse-phase high-performance liquid chromatography (RP-HPLC). Using the same procedure, tubulysin derivatives **14b**–**l** with different Fmoc-protected amino acids derived from phenylalanine, tyrosine, glutamic acid, aspartic acid, naphthylalanine, histidine, or aminomethyl cyclohexane carboxylic acid and chlorotrityl resins capped with glutamic acid, glycine, or aspartic acid at the N-terminal were synthesized and purified by RP-HPLC.

Synthesis of (14b)

The synthesis of tetrapeptide **14b** was carried out by using H-Glu(O^{t}Bu)-2-ClTrt resin (0.300 g, 0.192 mmol) with free NH_2 group that was coupled with Fmoc-Val-thiazole-OH **(7)** (0.179 g, 0.384 mmol), Fmoc-Ile-OH (0.136 g, 0.384 mmol), and 1-methylpiperidine-2-carboxylic acid **(9)** (0.055 g, 0.384 mmol) sequentially as mentioned above, using PyBOP (0.200 g, 0.384 mmol) as a coupling agent. Further, the synthesized tetrapeptide **14b** was purified by reverse-phase high-performance liquid chromatography (RP-HPLC).

Synthesis of (14c)

The synthesis of tetrapeptide **14c** was carried out by using H-Gly-2-ClTrt resin (0.300 g, 0.132 mmol) with free NH_2 group that was coupled with Fmoc-Glu(O^{t}Bu)-OH (0.112 g, 0.264 mmol), Fmoc-Val-thiazole-OH **(7)** (0.123 g, 0.264 mmol), Fmoc-Ile-OH (0.093 g, 0.264 mmol),

and 1-methylpiperidine-2-carboxylic acid **(9)** (0.037 g, 0.264 mmol) sequentially as mentioned above, using PyBOP (0.137 g, 0.264 mmol) as a coupling agent. Further, the synthesized tetrapeptide **14c** was purified by reverse-phase high-performance liquid chromatography (RP-HPLC).

Synthesis of (14d)

The synthesis of tetrapeptide **14d** was carried out by using H-Asp(O^{t}Bu)-2-ClTrt resin (0.300 g, 0.144 mmol) with free NH_2 group that was coupled with Fmoc-Val-thiazole-OH **(7)** (0.134 g, 0.288 mmol), Fmoc-Ile-OH (0.101 g, 0.288 mmol), and 1-methylpiperidine-2-carboxylic acid **(9)** (0.041 g, 0.288 mmol) sequentially as mentioned above, using PyBOP (0.149 g, 0.288 mmol) as a coupling agent. Further, the synthesized tetrapeptide **14d** was purified by reverse-phase high-performance liquid chromatography (RP-HPLC).

Synthesis of (14e)

The synthesis of tetrapeptide **14e** was carried out by using H-Gly-2-ClTrt resin (0.300 g, 0.132 mmol) with free NH_2 group that was coupled with Fmoc-Asp(OtBu)-OH (0.108 g, 0.264 mmol), Fmoc-Val-thiazole-OH **(7)** (0.123 g, 0.264 mmol), Fmoc-Ile-OH (0.093 g, 0.264 mmol), and 1-methylpiperidine-2-carboxylic acid **(9)** (0.037 g, 0.264 mmol) sequentially as mentioned above, using PyBOP (0.137 g, 0.264 mmol) as a coupling agent. Further, the synthesized tetrapeptide **14e** was purified by reverse-phase high-performance liquid chromatography (RP-HPLC).

Synthesis of (14f)

The synthesis of pentapeptide **14f** was carried out by using H-Gly-2-ClTrt resin (0.300 g, 0.132 mmol) with free NH_2 group that was coupled with Fmoc-Phe-OH (0.102 g, 0.264 mmol), Fmoc-Val-thiazole-OH **(9)** (0.123 g, 0.264 mmol), Fmoc-Ile-OH (0.093 g, 0.264 mmol), and 1-methylpiperidine-2-carboxylic acid **(9)** (0.037 g, 0.264 mmol) sequentially as mentioned above, using PyBOP (0.137 g, 0.264 mmol) as a coupling agent. Further, the synthesized tetrapeptide **14f** was

purified by reverse-phase high-performance liquid chromatography (RP-HPLC).

Synthesis of (14g)

The synthesis of pentapeptide **14g** was carried out by using H-Gly-2-ClTrt resin (0.300 g, 0.132 mmol) with free NH_2 group that was coupled with Fmoc-Tyr-OH (0.121 g, 0.264 mmol), Fmoc-Val-thiazole-OH **(7)** (0.123 g, 0.264 mmol), Fmoc-Ile-OH (0.093 g, 0.264 mmol), and 1-methylpiperidine-2-carboxylic acid **(9)** (0.037 g, 0.264 mmol) sequentially as mentioned above, using PyBOP (0.137 g, 0.264 mmol) as a coupling agent. Further, the synthesized tetrapeptide **14g** was purified by reverse-phase high-performance liquid chromatography (RP-HPLC).

Synthesis of (14h)

The synthesis of tetrapeptide **14h** was carried out by using H-Asn(Trt)-2-ClTrt resin (0.300 g, 0.168 mmol) with a free NH_2 group that was coupled with Fmoc-Val-thiazole-OH (0.156 g, 0.336 mmol), Fmoc-Ile-OH (0.118 g, 0.336 mmol), and Fmoc-His(Trt)-OH (0.208 g, 0.336 mmol) sequentially as mentioned above, using PyBOP (0.174 g, 0.336 mmol) as a coupling agent. Further, the synthesized tetrapeptide **14h** was purified by reverse-phase high-performance liquid chromatography (RP-HPLC).

Synthesis of (14i)

The synthesis of tetrapeptide **14i** was carried out by using H-Asn(Trt)-2-ClTrt resin (0.300 g, 0.168 mmol) with a free NH_2 group that was coupled with Fmoc-Val-thiazole-OH **(7)** (0.156 g, 0.336 mmol), Fmoc-Ile-OH (0.124 g, 0.336 mmol), and trans-4-Fmoc-amino methylcyclohexanecarboxylic acid (0.127 g, 0.336 mmol) sequentially as mentioned above, using PyBOP (0.174 g, 0.336 mmol) as a coupling agent. Further, the synthesized tetrapeptide **14i** was purified by reverse-phase high-performance liquid chromatography (RP-HPLC).

Synthesis of (14j)

The synthesis of tripeptide **14j** was carried out by using H-Asn(Trt)-2-ClTrt resin (0.300 g, 0.168 mmol) with a free NH_2 group that was coupled with Fmoc-Val-thiazole-OH **(7)** (0.156 g, 0.336 mmol) and Fmoc-Ile-OH (0.124 g, 0.336 mmol) sequentially as mentioned above, using PyBOP (0.174 g, 0.336 mmol) as a coupling agent. Further, the synthesized tripeptide **14j** was purified by reverse-phase high-performance liquid chromatography (RP-HPLC).

Synthesis of (14k)

The synthesis of tetrapeptide **14k** was carried out by using H-Asn(Trt)-2-ClTrt resin (0.300 g, 0.168 mmol) with a free NH_2 group that was coupled with Fmoc-Val-thiazole-OH **(7)** (0.156 g, 0.336 mmol), Fmoc-Ile-OH (0.124 g, 0.336 mmol), and Fmoc-Phe-OH (0.130 g, 0.336 mmol) sequentially as mentioned above, using PyBOP (0.174 g, 0.336 mmol) as a coupling agent. Further, the synthesized tetrapeptide **14k** was purified by reverse-phase high-performance liquid chromatography (RP-HPLC).

Synthesis of (14l)

The synthesis of tetrapeptide **14l** was carried out by using H-Asn(Trt)-2-ClTrt resin (0.300 g, 0.168 mmol) with free NH_2 group that was coupled with Fmoc-Val-thiazole-OH **(7)** (0.156 g, 0.336 mmol), Fmoc-Ile-OH (0.124 g, 0.336 mmol), and Fmoc-2-Nal-OH (0.147 g, 0.336 mmol) sequentially as mentioned above, using PyBOP (0.174 g, 0.336 mmol) as a coupling agent. Further, the synthesized tetrapeptide **14l** was purified by reverse-phase high-performance liquid chromatography (RP-HPLC).

5.4.7 Preparative RP-HPLC method

The purification of tubulysin derivatives **14a**–**l** was performed using a Buchi Reveleris Prep RP-HPLC system. Crude tubulysin derivatives **14a**–**l** (40 mg) were dissolved in a mixture of CH_3CN:H_2O (1:1, 1 mL) and injected into the sample injector for elution using RP-PFP (Reverse Phase PentafluoroPhenyl) preparative column (XSelect CSH Prep

Fluorophenyl 5 μm; 19 × 150 mm). A flow rate of 10 mL/min (mobile phase, A = 0.1% trifluoroacetic acid in H_2O and B = acetonitrile) is maintained throughout the run, and the mobile phase gradient was gradually changed from 1% B (v/v) to 50% B (v/v) over 25 min. The gradient of mobile phase was further increased to 90% B (v/v) in another 10 min. The chromatograms were recorded at λ = 210, 240, and 280 nm with retention times of tR = 12.7, 13.9, 11.3, 11.8, 10.2, 18.0, 14.6, 8.2, 19.7, 15.0, 20.8, 14.1, for tubulysin derivatives **14a**–**l**, respectively. Pure fractions of tubulysin derivatives **14a**–**l** were collected using an automatic fraction collector, the organic solvent was evaporated under reduced pressure using a rotary evaporator, and the aqueous solution was lyophilized for 48 h to yield tubulysin derivatives **14a**–**l**.

5.4.8 Characterization data of tubulysin derivatives 14a–l

14a: White solid, yield 52% (53 mg), ^{1}H NMR (500 MHz, DMSO-d_6) δ 12.50 (s, 1H), 9.65 (s, 1H), 8.77 (d, *J* = 7.5 Hz, 1H), 8.71 (d, *J* = 7.9 Hz, 1H), 8.36 (d, *J* = 7.8 Hz, 1H), 8.11 (s, 1H), 7.40 (s, 1H), 6.93 (s, 1H), 4.67 (q, *J* = 7.9 Hz, 1H), 4.42 (t, *J* = 7.5 Hz, 1H), 4.32 (t, *J* = 7.8 Hz, 1H), 3.35 (d, *J* = 12.2 Hz, 1H), 3.07–3.01 (m, 1H), 2.69–2.64 (m, 4H), 2.57–2.53 (m, 1H), 2.11–2.02 (m, 2H), 1.79–1.74 (m, 3H), 1.71–1.55 (m, 2H), 1.43–1.36 (m, 2H), 1.14–1.07 (m, 1H), 0.91 (d, *J* = 6.7 Hz, 3H), 0.88 (d, *J* = 6.7 Hz, 3H), 0.84 (d, *J* = 6.7 Hz, 3H), 0.8 (t, *J* = 7.3 Hz, 3H); ^{13}C NMR (125 MHz, DMSO-d_6) δ 172.8, 171.2, 171.1, 170.6, 167.7, 160.5, 160.1, 139.9, 127.3, 66.0, 58.0, 57.0, 54.4, 49.4, 41.4, 36.6, 36.5, 30.1, 28.4, 24.2, 22.3, 21.0, 18.9, 18.3, 15.3, 10.8; HRMS (+ESI) (m/z) calcd. for $[C_{26}H_{41}N_7O_7S]$, $[M+H]^+$ 596.2861; found, 596.2863.

14b: White solid, yield 56% (66 mg), ^{1}H NMR (500 MHz, DMSO-d_6) δ 12.51 (s, 1H), 9.64 (s, 1H), 8.74 (d, *J* = 8.2 Hz, 1H), 8.64 (d, *J* = 7.8 Hz, 1H), 8.36 (d, *J* = 7.8 Hz, 1H), 8.17 (s, 1H), 4.42 (t, *J* = 7.8 Hz, 1H), 4.37–4.31 (m, 2H), 3.78 (t, *J* = 11.7 Hz, 1H), 3.07–3.01 (m, 1H), 2.66 (s, 3H), 2.34 (t, *J* = 7.6, 2H), 2.11–2.02 (m, 3H), 1.94–1.86 (m, 1H), 1.79–1.75 (m, 3H), 1.69–1.55 (m, 2H), 1.43–1.36 (m, 2H), 1.12–1.06 (m, 1H), 0.91 (d, *J* = 6.8 Hz, 3H), 0.88 (d, *J* = 6.8 Hz, 3H), 0.84 (d, *J* =

6.7 Hz, 3H), 0.81 (t, *J* = 7.3 Hz, 3H); ^{13}C NMR (125 MHz, DMSO-d_6) δ 173.8, 173.2, 170.9, 170.6, 167.7, 160.9, 160.2, 140.0, 127.2, 65.9, 58.0, 56.9, 54.3, 51.6, 41.4, 36.5, 30.3, 30.1, 28.4, 26.0, 24.2, 22.3, 21.0, 18.9, 18.2, 15.2, 10.8; HRMS (+ESI) (m/z) calcd. for [$C_{27}H_{42}N_6O_8S$], $[M+H]^+$ 611.2858; found, 611.2858.

14c: White solid, yield 61% (55 mg), ^{1}H NMR (500 MHz, DMSO-d_6) δ 12.55 (s, 1H), 9.67 (s, 1H), 8.79 (d, *J* = 8.3 Hz, 1H), 8.59 (t, *J* = 6.0 Hz, 1H), 8.32 (d, *J* = 7.8 Hz, 1H), 7.87 (d, *J* = 8.3 Hz, 1H), 7.83 (s, 1H), 4.58–4.54 (m, 2H), 4.38 (t, *J* = 8.3 Hz, 1H), 4.31 (t, *J* = 7.8 Hz, 1H), 3.85–3.73 (m, 3H), 3.34 (d, *J* = 12.9 Hz, 1H), 3.02 (t, *J* = 12.9 Hz, 1H), 2.66 (s, 3H), 2.27 (t, *J* = 7.8 Hz, 2H), 2.10–2.00 (m, 3H), 1.93–1.85 (m, 1H), 1.80–1.74 (m, 3H), 1.68–1.55 (m, 2H), 1.44–1.35 (m, 2H), 1.14–1.05 (m, 1H), 0.91 (d, *J* = 6.7 Hz, 3H), 0.88 (d, *J* = 6.7 Hz, 3H), 0.84 (d, *J* = 6.9 Hz, 3H), 0.80 (t, *J* = 7.4 Hz, 3H); ^{13}C NMR (125 MHz, DMSO) δ 174.0, 171.2, 171.0*, 170.9, 167.8, 160.1, 157.6, 144.0, 118.2, 66.0, 58.3, 57.2, 54.5, 51.5, 41.5, 40.8, 36.5, 30.2, 29.8, 28.5, 28.3, 24.3, 22.4, 21.1, 19.0, 18.4, 15.3, 10.9, , (*higher intensity signal); HRMS (+ESI) (m/z) calcd. for [$C_{29}H_{45}N_7O_9S$], $[M+H]^+$ 668.3072; found, 668.3074.

14d: White solid, yield 54% (47 mg), ^{1}H (500 MHz, DMSO-d_6) δ 12.54 (s, 1H), 9.67 (s, 1H), 8.79–8.76 (m, 1H), 8.31 (d, *J* = 7.8 Hz, 1H), 8.09 (d, *J* = 8.0 Hz, 1H), 7.85 (s, 1H), 4.77–4.73 (m, 1H), 4.41 (t, *J* = 7.8 Hz, 1H), 4.32 (t, *J* = 8.0 Hz, 1H), 3.81–3.78 (m, 1H), 3.36–3.33 (m, 1H), 3.06–3.01 (m, 1H), 2.90 (dd, *J* = 17.1 Hz, 5.4 Hz, 1H), 2.80 (dd, *J* = 17.1 Hz, 5.4 Hz, 1H), 2.69–2.66 (m, 3H), 2.12–1.99 (m, 2H), 1.80–1.74 (m, 3H), 1.71–1.55 (m, 2H), 1.44–1.35 (m, 2H), 1.14–1.05 (m, 1H), 0.92–0.87 (m, 6H), 0.84 (d, *J* = 6.9 Hz, 3H), 0.81 (t, *J* = 7.2 Hz, 3H); ^{13}C NMR (125 MHz, DMSO–d_6) δ 172.2, 172.1, 170.9, 170.8, 167.7, 160.0, 157.6, 143.8, 118.3, 64.0, 58.1, 57.1, 54.4, 48.2, 41.4, 36.5, 36.0, 30.2, 28.5, 24.2, 22.3, 21.0, 19.0, 18.3, 15.3, 10.8; HRMS (+ESI) (m/z) calcd. for [$C_{26}H_{40}N_6O_8S$], $[M+H]^+$ 597.2701; found, 597.2701.

14e: White solid, yield 50% (49 mg), ^{1}H NMR (500 MHz, DMSO-d_6) δ 12.50 (brs, 1H), 9.68(s, 1H), 8.79 (d, *J* = 8.0 Hz, 1H), 8.73 (d, *J* = 7.9

Hz, 1H), 8.35 (d, *J* = 7.7 Hz, 1H), 8.22 (t, *J* = 6.0 Hz, 1H), 8.13 (s, 1H), 4.81–4.77 (m, 1H), 4.41 (t, *J* = 8.0 Hz, 1H), 4.30 (t, *J* = 7.9 Hz, 1H), 3.79–3.68 (m, 4H), 3.35 (d, *J* = 12.2 Hz, 1H), 3.05–2.98 (m, 1H), 2.79 (dd, *J* = 4.9 Hz, 16.7 Hz, 1H), 2.66 (s, 3H), 2.63–2.59 (m, 1H), 2.10–2.01 (m, 2H), 1.79–1.40 (m, 3H), 1.70–1.55 (m, 2H), 1.43–1.35 (m, 2H), 1.16–1.05 (m, 1H), 0.91 (t, *J* = 6.6 Hz, 3H), 0.87 (t, *J* = 6.6 Hz, 3H), 0.84 (t, *J* = 6.7 Hz, 3H), 0.79 (t, *J* = 7.3 Hz, 3H); ^{13}C NMR (125 MHz, DMSO-d_6) δ 171.8, 171.12, 171.10, 171.08, 170.8, 167.8, 160.8, 160.2, 140.3, 127.4, 66.1, 58.2, 57.2, 54.5, 49.9, 41.5, 41.0, 36.5, 36.2, 30.2, 28.5, 24.3, 22.4, 21.1, 19.0, 18.4, 15.3, 10.9; HRMS (+ESI) (m/z) calcd. for $[C_{28}H_{43}N_7O_9S]$, $[M+H]^+$ 654.2916; found, 654.2915.

14f: White solid, yield 63% (58 mg), ^{1}H NMR (500 MHz, DMSO-d_6) δ 12.47 (s, 1H), 9.64 (s, 1H), 8.75 (d, *J* = 8.1 Hz, 1H), 8.70 (d, *J* = 8.6 Hz, 1H), 8.47 (t, *J* = 7.4 Hz, 1H), 8.34 (d, *J* = 7.7 Hz, 1H), 8.13 (s, 1H), 7.32 (d, *J* = 7.5 Hz, 2H), 7.23 (t, *J* = 7.9 Hz, 2H), 7.15 (t, *J* = 7.9 Hz, 1H), 4.69 (t, *J* = 7.7 Hz, 1H), 4.39 (t, *J* = 8.1 Hz, 1H), 4.29 (t, *J* = 8.6 Hz, 1H), 3.83–3.76 (m, 4H), 3.13 (d, *J* = 13.3 Hz, 1H), 3.02 (t, *J* = 13.1 Hz, 1H), 2.91(t, *J* = 12.4 Hz, 1H), 2.64 (s, 3H), 2.07–2.01 (m, 2H), 1.78–1.75 (m, 3H), 1.67–1.54 (m, 2H), 1.43–1.36 (m, 2H), 1.11–1.05 (m, 1H), 0.90 (d, *J* = 6.7 Hz, 3H), 0.86 (d, *J* = 6.7 Hz, 3H), 0.82 (d, *J* = 6.9 Hz, 3H), 1`0.79 (t, *J* = 6.8 Hz, 3H); ^{13}C NMR (125 MHz, DMSO-d_6) δ 171.9, 171.3, 171.2, 170.8, 167.9, 160.8, 160.3, 140.1, 138.4, 129.3, 128.3, 127.5, 126.5, 66.2, 58.3, 57.3, 54.6*, 41.6, 41.0, 37.4, 36.5, 30.27, 28.6, 24.3, 22.5, 21.1, 19.1, 18.4, 15.4, 11.0 (*higher intensity signals); HRMS (+ESI) (m/z) calcd. for $[C_{33}H_{47}N_7O_7S]$, $[M+H]^+$ 686.3330; found, 686.3343.

14g: White solid, yield 67% (62 mg), ^{1}H NMR (500 MHz, DMSO-d_6) δ 12.48 (s, 1H), 9.63 (s, 1H), 8.75 (d, *J* = 8.8 Hz, 1H), 8.62 (d, *J* = 8.9 Hz, 1H), 8.42 (s, 1H), 8.33 (d, *J* = 9.0 Hz, 1H), 8.12 (s, 1H), 7.10 (d, *J* = 8.0 Hz, 2H), 6.61 (d, *J* = 8.0 Hz, 2H), 4.58 (t, *J* = 9.0 Hz, 1H), 4.38 (t, *J* = 8.8 Hz, 1H), 4.26 (t, *J* = 8.9 Hz, 1H), 3.79–3.76 (m, 4H), 3.33 (d, *J* = 13.0 Hz, 2H), 3.02–2.99 (m, 2H), 2.79 (t, *J* = 12.5 Hz, 1H), 2.64 (s, 3H), 2.07–2.00 (m, 2H), 1.77–1.75 (m, 3H), 1.69–1.54 (m, 2H), 1.44–1.38

(m, 2H), 1.13–1.03 (m, 1H), 0.89 (d, *J* = 7 Hz, 3H), 0.86 (d, *J* = 7.0 Hz, 3H), 0.82 (d, *J* = 7.0 Hz, 3H), 0.78 (t, *J* = 7.0 Hz, 3H); ^{13}C NMR (125 MHz, DMSO-d_6) δ 172.1, 171.3, 171.3, 170.9, 168.1, 160.8, 160.3, 155.9, 140.1, 130.3, 128.5, 127.6, 115.1, 66.2, 58.3, 57.4, 55.1, 54.7, 41.6, 4, 36.7, 36.5, 30.3, 28.6, 24.4, 22.5, 21.1, 19.1, 18.5, 15.4, 11.0;; HRMS (+ESI) (m/z) calcd. for [$C_{33}H_{47}N_7O_8S$], $[M+H]^+$ 702.3280; found, 702.3273.

14h: White solid, yield 48% (49 mg), ^{1}H NMR (500 MHz, DMSO-d_6) δ 12.57 (s, 1H), 8.96 (s, 1H), 8.49 (d, *J* = 7.5 Hz, 1H), 8.45 (d, *J* = 7.8 Hz, 1H), 8.34 (brs, 2H), 8.16 (d, *J* = 8.6 Hz, 1H), 7.84 (s, 1H), 7.50 (s, 1H), 7.41 (s, 1H), 6.94 (s, 1H), 4.71–4.67 (m, 1H), 4.40 (t, *J* = 7.5 Hz, 1H), 4.31 (t, *J* = 7.8 Hz, 1H), 4.22 (t, *J* = 6.6 Hz, 1H), 3.15 (d, *J* = 6.6 Hz, 2H), 2.82 (dd, *J* = 16.3 Hz, 5.0 Hz, 1H), 2.61 (dd, *J* = 16.3 Hz, 5 Hz, 1H), 2.12–2.05 (m, 1H), 1.79–1.72 (m, 1H), 1.50–1.42 (m, 1H), 1.17–1.07 (m, 1H), 0.92–0.87 (m, 9H), 0.83 (t, *J* = 7.3 Hz, 3H); ^{13}C NMR (125 MHz, DMSO-d_6) δ 172.4, 171.8*, 171.5, 170.6, 167.3 159.9, 157.6, 143.9, 134.4, 118.3, 117.9, 58.2, 57.4, 51.0, 48.2, 36.5, 36.3, 30.2, 26.6, 24.2, 19.0, 18.3, 15.2, 11.0 (*higher intensity signals); HRMS (+ESI) (m/z) calcd. for [$C_{25}H_{37}N_9O_7S$], $[M+H]^+$ 608.2615; found, 608.2660.

14i: White solid, yield 45% (47 mg), ^{1}H NMR (500 MHz, DMSO-d_6) δ 12.54 (s, 1H), 8.16 (d, *J* = 7.5 Hz, 1H), 7.84 (d, *J* = 7.9 Hz, 1H), 7.83 (s, 1H), 7.78 (d, *J* = 8.5 Hz, 1H), 7.74 (s, 2H), 7.49 (s, 1H), 6.94 (s, 1H), 4.71–4.67 (m, 1H), 4.38 (t, *J* = 7.5 Hz, 1H), 4.22 (t, *J* = 8.5 Hz, 1H), 2.82 (dd, *J* = 5.1 Hz, 16.2 Hz, 1H), 2.66 (t, *J* = 6.2 Hz, 2H), 2.62 (dd, *J* = 5.1 Hz, 16.2 Hz, 1H), 2.54 (s, 2H), 2.23–2.18 (m, 1H), 2.09–2.02 (m, 1H), 1.79–1.71 (m, 5H), 1.53–1.45 (m, 1H), 1.42–1.36 (m, 1H), 1.34–1.27 (m, 2H), 1.10–1.03 (m, 1H), 0.89–0.87 (m, 6H), 0.82–0.77 (m, 6H); ^{13}C NMR (125 MHz, DMSO-d_6) δ 174.9, 172.5, 171.8, 171.8, 170.9, 160.0, 157.6, 143.9, 118.2, 57.9, 56.4, 48.2, 44.4, 43.2, 36.4, 36.2, 35.1, 30.3, 29.0, 28.9, 28.7, 28.2, 24.4, 19.0, 18.3, 15.4, 10.9 HRMS (+ESI) (m/z) calcd. for [$C_{27}H_{43}N_7O_7S$], $[M+H]^+$ 609.3017; found, 610.2974.

14j: White solid, yield 65% (52 mg), ^{1}H NMR (500 MHz, DMSO-d_6) δ 12.65 (s, 1H), 8.14 (d, *J* = 5.4, 2H), 8.61 (d, *J* = 7.3 Hz, 1H), 8.17 (t, *J* = 8.7 Hz, 1H), 7.83 (s, 1H), 7.50 (s, 1H), 6.94 (s, 1H), 4.71–4.67 (m, 1H), 4.44 (t, *J* = 8.7 Hz, 1H), 3.77 (t, *J* = 5.4 Hz, 1H), 2.82 (dd, *J* = 5.1 Hz, 16.2 Hz, 1H), 2.60 (dd, *J* = 5.1 Hz, 16.2 Hz, 1H), 2.54 (s, 1H), 2.13–2.06 (m, 1H), 1.85–1.77 (m, 1H), 1.51–1.43 (m, 1H), 1.15–1.05 (m, 1H), 0.95–0.93 (m, 6H), 0.90 (d, *J* = 7.0 Hz, 3H), 0.83 (t, *J* = 7.0 Hz, 3H); ^{13}C NMR (125 MHz, DMSO-d_6) δ 172.5, 171.9, 170.5, 168.5, 160.0, 157.6, 144.0, 118.3, 58.4, 56.3, 48.3, 40.4, 36.3, 30.1, 23.8, 19.0, 18.4, 14.6, 11.0; HRMS (+ESI) (m/z) calcd. for [$C_{19}H_{30}N_6O_6S$], $[M+H]^+$ 471.2026; found, 471.2069.

14k: White solid, yield 59% (61 mg), ^{1}H NMR (500 MHz, DMSO-d_6) δ 12.58 (s, 1H), 8.57 (d, *J* = 8.7 Hz, 1H), 8.34 (d, *J* = 7.5 Hz, 1H), 8.23–8.02 (brs, 2H) 8.17 (d , J = 8.7 Hz, 1H), 7.82 (s, 1H), 7.50 (s, 1H), 7.31–7.22 (m, 5H), 6.94 (s, 1H), 4.71–4.67 (m, 1H), 4.41 (t, *J* = 7.5 Hz , 1H), 4.34 (t, *J* = 8.7 Hz, 1H), 4.13 (t, *J* = 6.2 Hz, 1H), 3.08 (dd, *J* = 14.3 Hz, 7.2 Hz, 1H), 2.95 (dd, *J* = 14.3 Hz, 7.2 Hz, 1H), 2.82 (dd, *J* = 5.1 Hz, 16.4 Hz, 1H), 2.61 (dd, *J* = 5.1 Hz, 16.4 Hz, 1H), 2.11–2.05 (m, 1H), 1.75–1.67 (m, 1H), 1.52–1.45 (m, 1H), 1.13–1.04 (m, 1H), 0.94 (d, *J* = 6.7 Hz , 3H), 0.91 (d, *J* = 6.7 Hz, 3H), 0.85 (d, *J* = 6.7 Hz, 3H), 0.83 (t, *J* = 7.4 Hz, 3H); ^{13}C NMR (125 MHz, DMSO-d_6) δ 172.5, 171.8, 171.1, 170.9, 167.7, 156.0, 157.6, 143.9, 134.7, 129.7, 128.5, 127.1, 118.2, 58.2, 56.7, 53.0, 48.3, 36.9, 36.8, 36.4, 30.0, 24.4, 19.0, 18.5, 15.2, 11.0; HRMS (+ESI) (m/z) calcd. for [$C_{28}H_{39}N_7O_7S$], $[M+H]^+$ 618.2704; found, 617.2727.

14l: White solid, yield 61% (68 mg), ^{1}H NMR (500 MHz, DMSO-d_6) δ 12.61 (s, 1H), 8.77 (d, *J* = 8.5 Hz, 1H), 8.71 (d, *J* = 7.7 Hz, 1H), 8.18–8.14 (m, 4H), 7.90–7.83 (m, 3H), 7.65 (s, 1H), 7.53–7.49 (m, 3H), 7.40 (dd, *J* = 8.4 Hz, 1.6 Hz, 1H), 6.94 (s, 1H), 4.72–4.68 (m, 1H), 4.46 (t, *J* = 7.7 Hz, 1H), 4.38 (t, *J* = 8.5 Hz, 1H), 4.29–4.21 (m, 1H), 3.27 (dd, *J* = 7.7 Hz, 14.3 Hz, 1H), 3.12 (dd, *J* = 7.7 Hz, 14.3 Hz, 1H), 2.82 (dd, *J* = 5.1 Hz, 16.4 Hz, 1H), 2.61 (dd, *J* = 5.1 Hz, 16.4 Hz, 1H), 2.11–2.04 (m, 1H), 1.80–1.72 (m, 1H), 1.54–1.47 (m, 1H), 1.15–1.07 (m, 1H), 0.92–

0.90 (m, 6H), 0.88 (d, J = 6.7 Hz, 3H), 0.84 (t, J = 7.3 Hz, 3H); ^{13}C NMR (125 MHz, DMSO-d_6) δ 172.5, 171.8, 171.1, 170.9, 167.7, 159.9, 157.6, 143.9, 133.0, 132.31, 132.26, 128.5, 128.0, 127.71, 127.67, 127.5, 126.1, 125.9, 118.2, 58.2, 56.8, 53.0, 48.2, 37.0, 36.8, 36.4, 30.0, 24.4, 19.0, 18.4, 15.2, 11.0; HRMS (+ESI) (m/z) calcd. for [$C_{32}H_{41}N_7O_7S$], $[M+H]^+$ 668.2866; found, 668.2866.

5.4.9 Culture of cancer cell lines

Henrietta Lacks (HeLa), Michigan Cancer Foundation-7 (MCF7), Adenocarcinomic human alveolar basal epithelial cells (A549), human melanoma cell line (A375), human epidermoid carcinoma cell line (A431), and Lymph Node Carcinoma of the Prostate (LNCaP) cancer cell lines were procured from National Centre for Cell Sciences (NCCS), Pune, India. The cell lines were grown in T-75 Flask (Tarson, 950040) containing sterile filtered RPMI 1640 medium (Thermo Fisher, 11875093) supplemented with fetal bovine serum (Thermo Fisher, 1027016), 100 mM of sodium pyruvate (Thermo Fisher, 11360070), non-essential amino acid (Thermo Fisher, 11140050), and 1% penicillin streptomycin (Thermo Fisher, 15140122) under 37 °C and 5% CO_2 to form a monolayer until 60% confluency. The cells were then trypsinized using 0.25% trypsin-EDA (Thermo Fisher, 15050065), collected, and centrifuged at 800 rpm for 5 min. The obtained cell pellet was resuspended in fresh medium and then used for cytotoxicity assay.

5.4.10 *In vitro* cytotoxicity assay of tubulysin derivatives 14a–l

HeLa, MCF7, A549, A375, A431, and LNCaP 5000 cells/well were seeded in a 96-well plate and allowed to form a monolayer of 60% confluency over a period of 48 h. The spent medium was then discarded, and cells were washed with 1X PBS (1 × 200 µL). 200 µL of fresh medium containing tubulysin derivatives **14a–l** with various concentrations (10 pM, 50 pM, 100 pM, 500 pM, 1 nM, 5 nM, 10 nM, 50 nM, 100 nM, 500 nM, 1 µM, 5 µM, 10 µM, 50 µM, 100 µM) was then added into the well in triplicate. The cells were then incubated for 48 h or 24 h. After incubation, the spent medium was discarded, and the

cells were washed carefully with 1X DPBS (2 × 200 µL). 50 µL of MTT solution (5 mg/mL) was added to each well, plates were then carefully wrapped with aluminium foil and incubated at 37 °C and 5% CO_2 for 4 h. After incubation, MTT solution was carefully aspirated using a pipette, and 200 µL of DMSO per well was added to dissolve the formazan crystals. The absorbance from each well corresponding to live cells was measured using a Synergy H4 multiplate reader at a wavelength of 570 nm. Dose vs response curves were obtained from a plot of log[concentration] vs % cell viability, and IC_{50} values were calculated using GraphPad Prism 7.04.

5.4.11 Computational docking studies

In the current work, the molecular docking studies were performed to correlate the observed experimental cytotoxicity against human cancer IC_{50} values (Cell line LNCaP with 48 h incubation) with the structural features of synthesised tubulysin derivatives. For the docking study, the tubulin protein PDB 4ZOL was downloaded from the protein data bank, which is co-crystallized with tubulysin M, a potent tubulin polymerization inhibitor.

5.4.11.1 Protein and ligand preparation and molecular docking

Tubulin protein PDB ID 4ZOL was prepared using the structural preparation module of MOE 2022.02 software. Structural correction and protonation of the 3D protein were performed by the default setting using MMFF94x as the force field. For ligand preparation, all the 3D structures of the synthesised inhibitor and tubulysin M were loaded into the same software as a database. Using the "QuickPrep module" with default settings, all the structures were prepared and minimised, and charges were assigned. The Amber force field was applied for ligand preparation. All the inhibitors were saved as .sdf files. Under the "Compute" button, the "Dock" tab was clicked for the molecular docking study. Prepared 4ZOL protein was loaded as the receptor, and the co-crystallized inhibitor tubulysin M (55Q) was selected as the docking site. Under the "Ligand" button, the prepared .sdf file of

inhibitors with 55Q was entered. The method for refinement of docking poses was performed using the induced fit method, and the scoring function applied was Generalized-Born Volume Integral / Weighted Surface Area dG (GBVI/WSA dG). The rest of the options were kept as the default. After completion of molecular docking, the result was saved as a ".sdf" file, including "S" as the docking score.

5.4.12 Pharmacophore analysis

For docking result analysis and pharmacophore generation, LigandScout 4.0 was used. Under the Structure-Based analysis tab, the prepared protein file was uploaded, and all docked poses of inhibitors were uploaded as an .sdf file. After visual inspection, the best docking pose for all inhibitors was selected by comparing the co-crystallized pose as a standard. For selected poses, structure-based pharmacophores were generated. Pharmacophores are the structural features of inhibitors that represent the type of protein-ligand interactions. It may be classified as Hydrogen bond donors (HBD), Hydrogen bond acceptors (HBA), Hydrophobic (H), Aromatic pharmacophores, and Positive/negative ionizable pharmacophores.

5.4.13 Copies of ^{1}H, ^{13}C NMR, and HRMS spectra

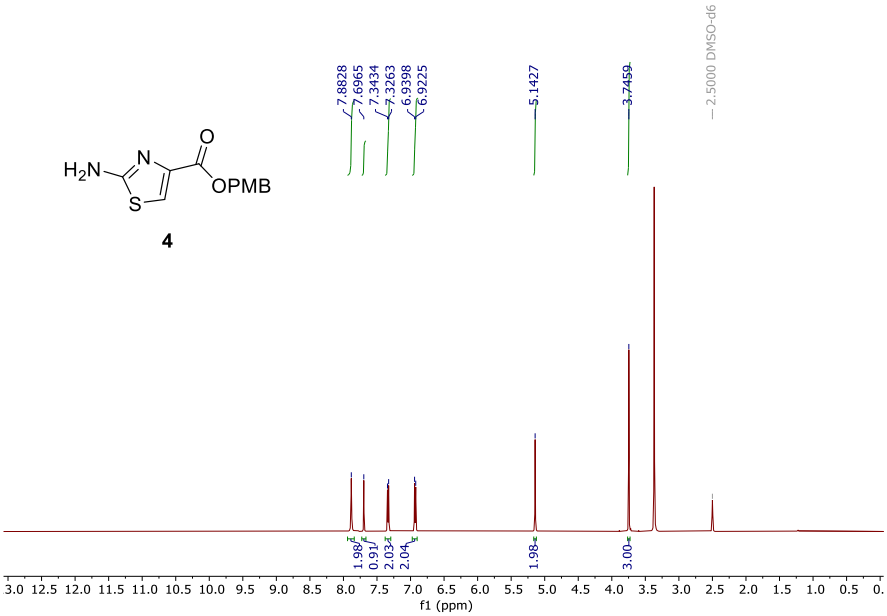

Figure 5.33 ^{1}H NMR spectrum (500 MHz, DMSO-d_6) of **4**.

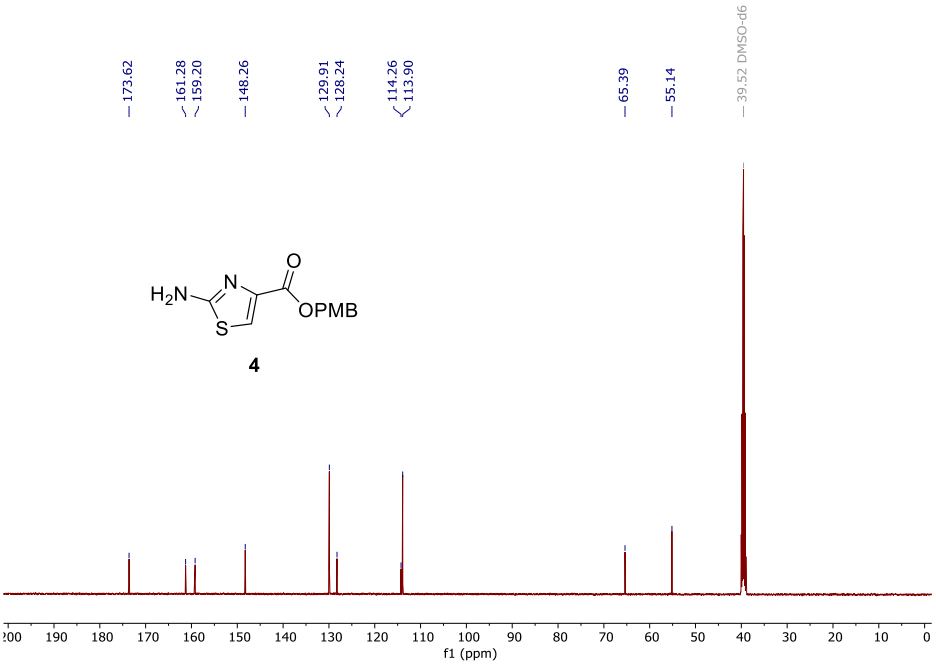

Figure 5.34 ^{13}C NMR spectrum (125 MHz, DMSO-d_6) of **4**.

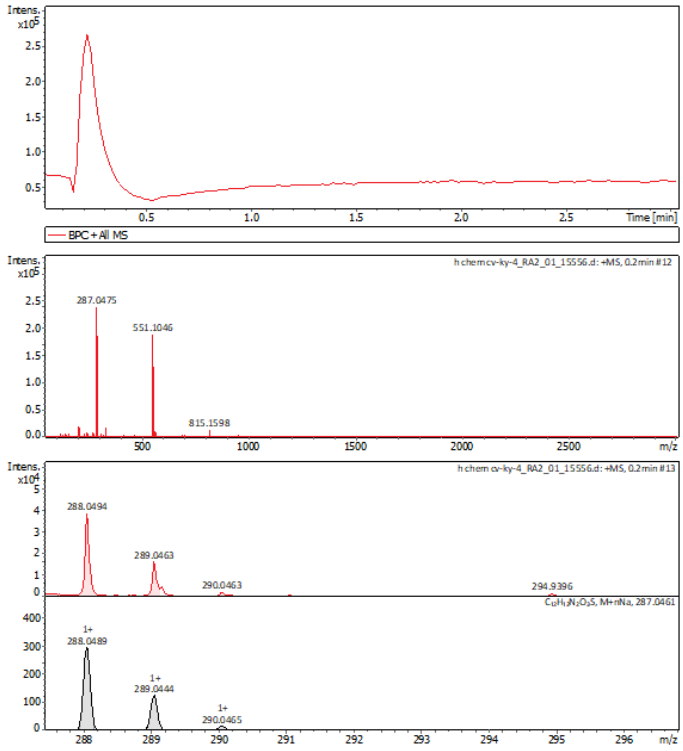

Figure 5.35 HRMS of **4**.

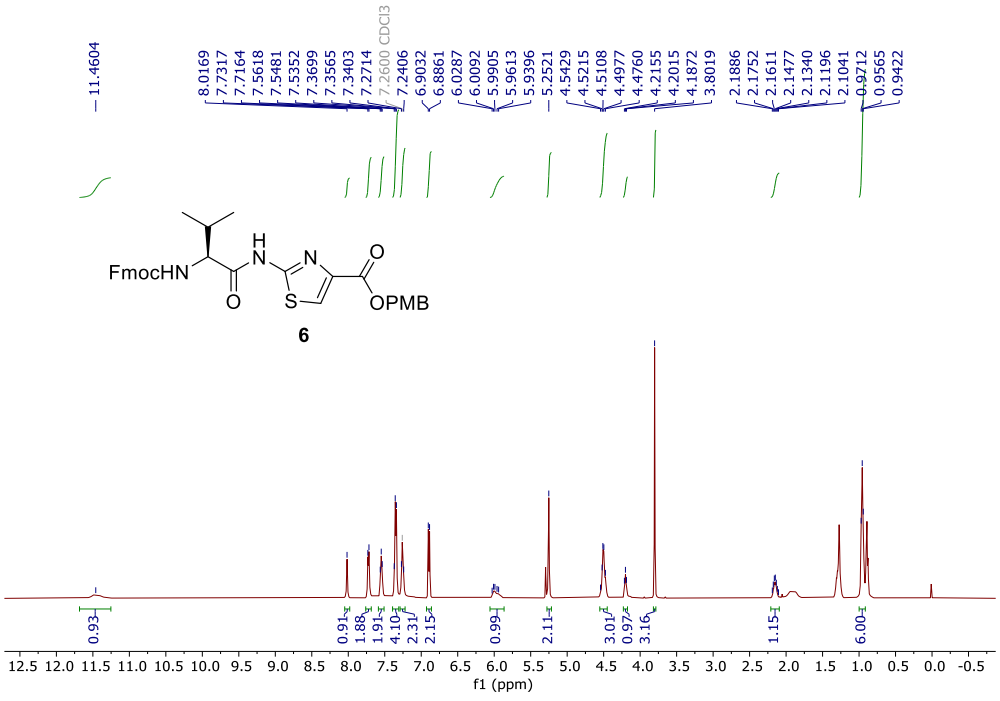

Figure 5.36 ^{1}H NMR spectrum (500 MHz, DMSO-d_6) of **6**.

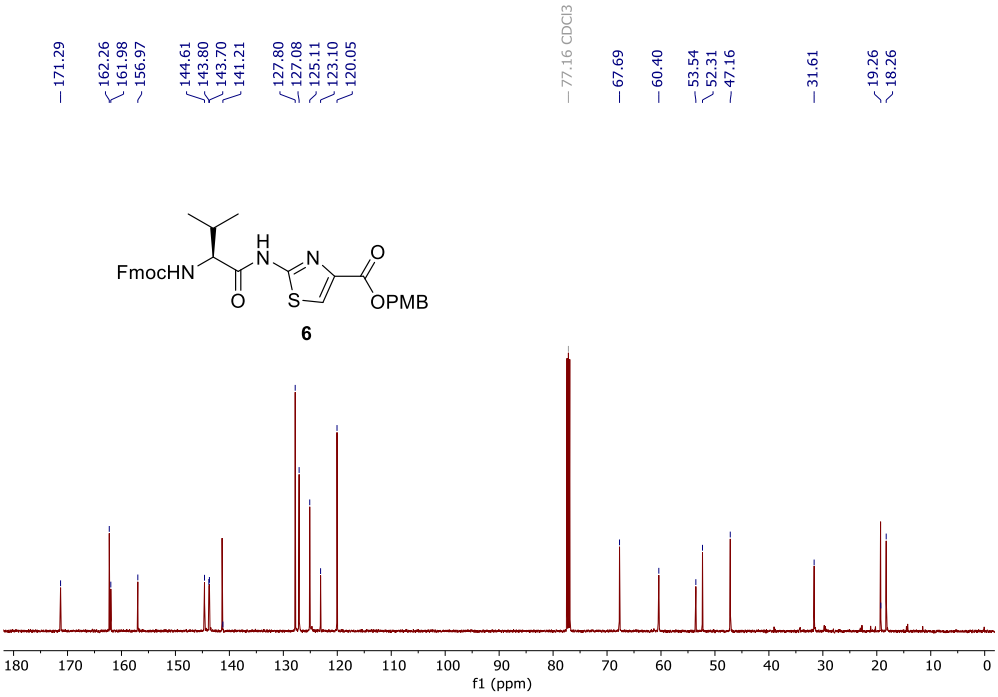

Figure 5.37 ^{13}C NMR spectrum (125 MHz, DMSO-d_6) of **6**.

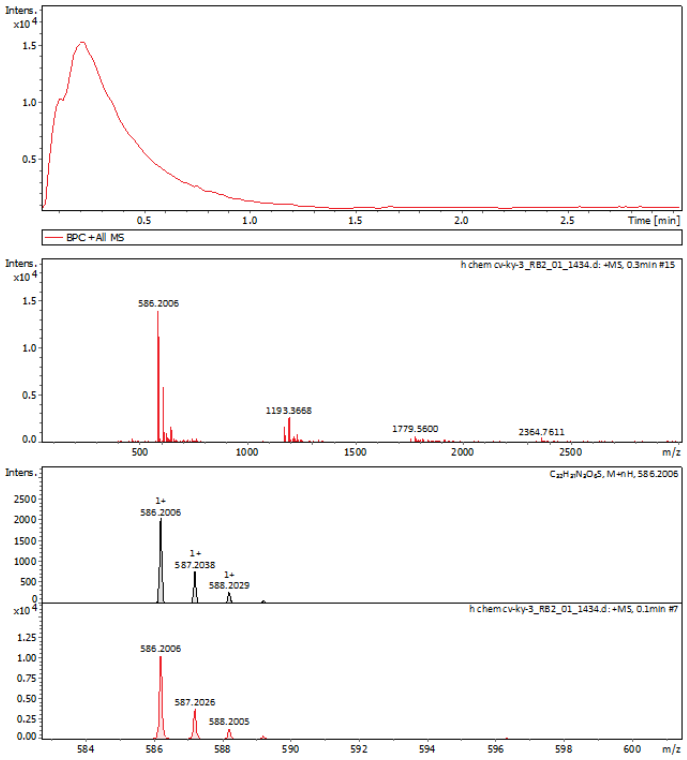

Figure 5.38 HRMS of **6**.

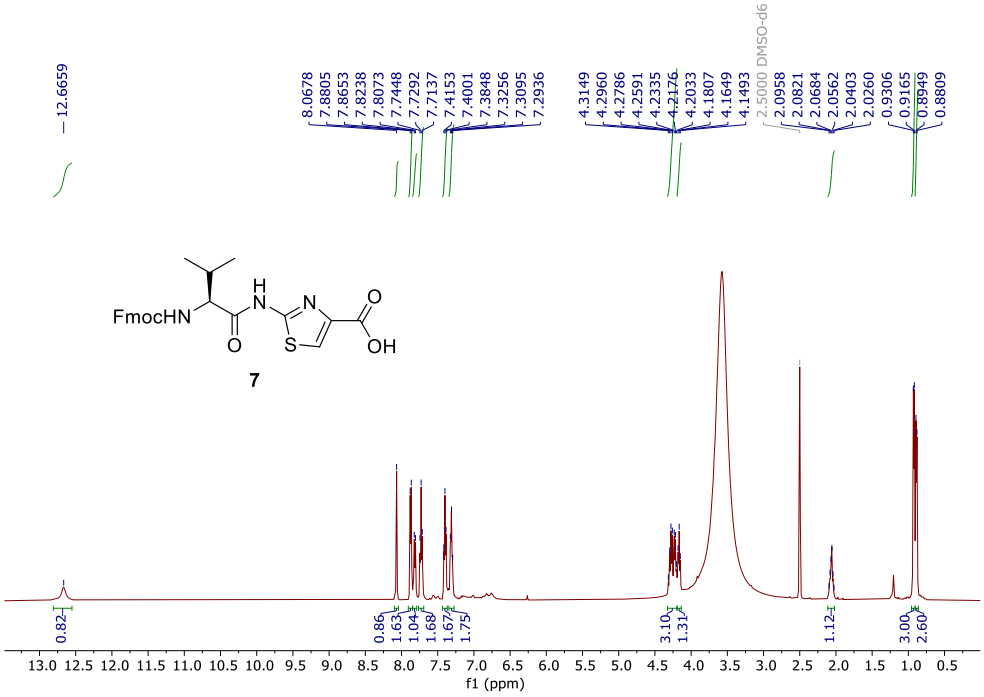

Figure 5.39 ^{1}H NMR spectrum (500 MHz, DMSO-d_6) of **7**.

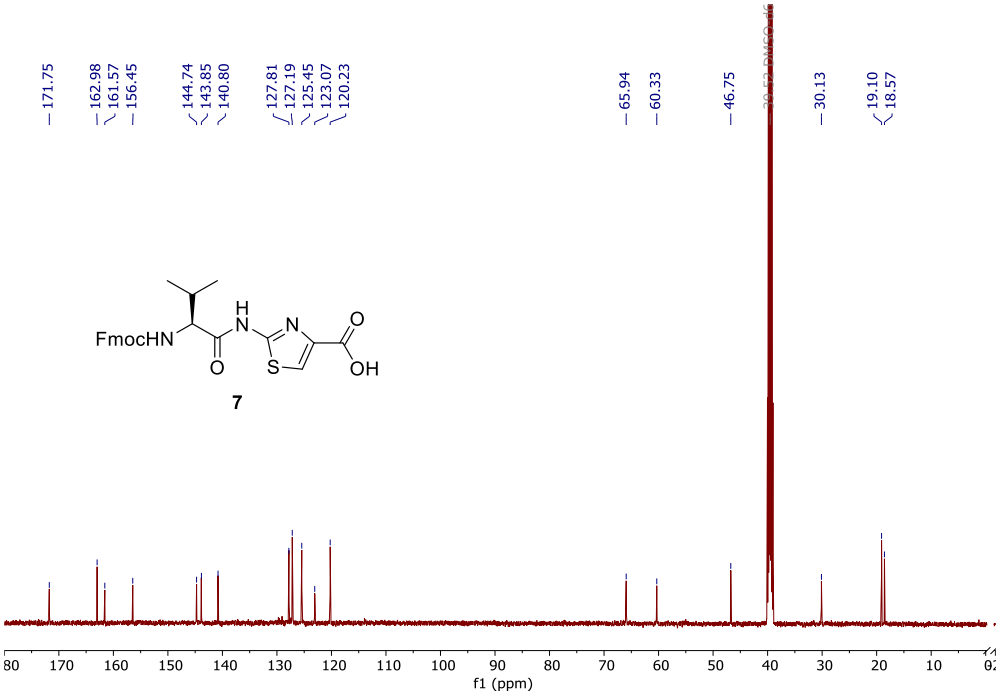

Figure 5.40 ^{13}C NMR spectrum (125 MHz, DMSO-d_6) of **7**.

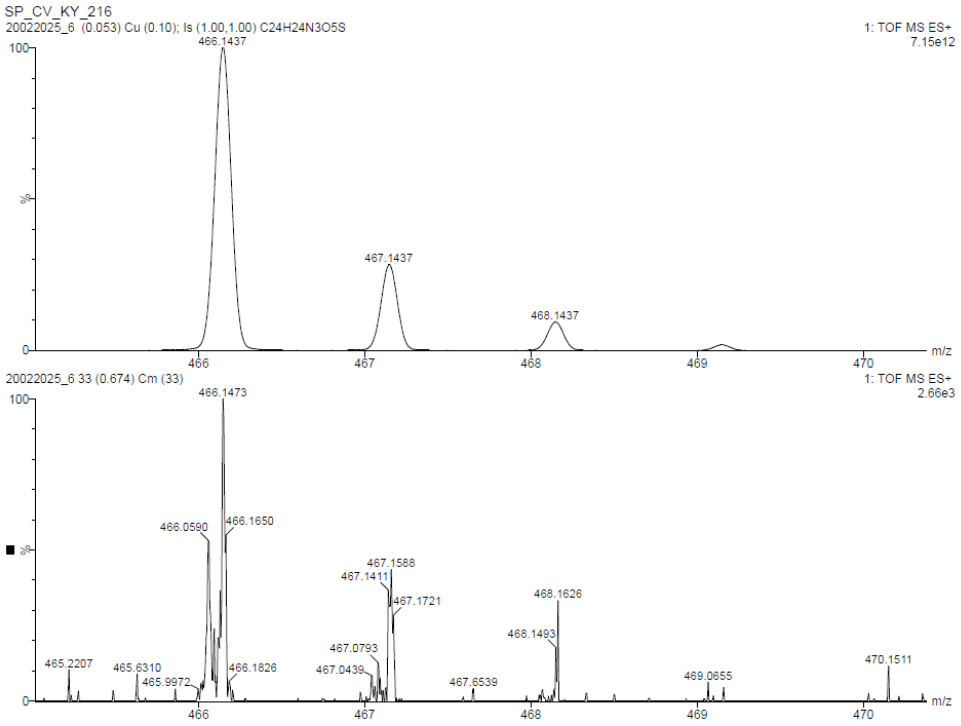

Figure 5.41 HRMS of **7**.

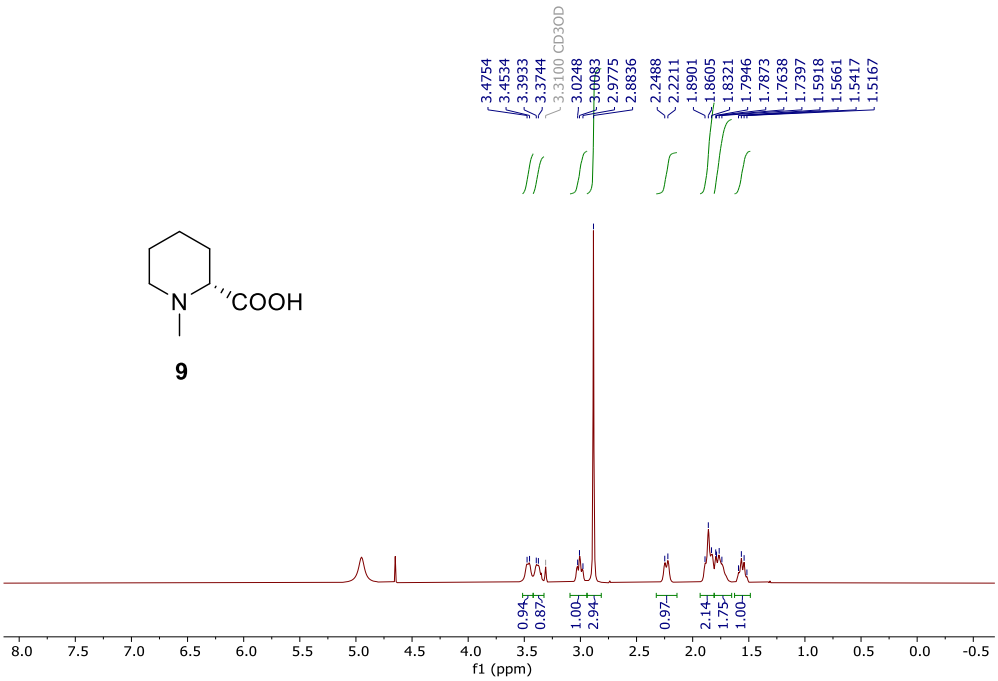

Figure 5.42 ^{1}H NMR spectrum (500 MHz, DMSO-d_6) of **9**.

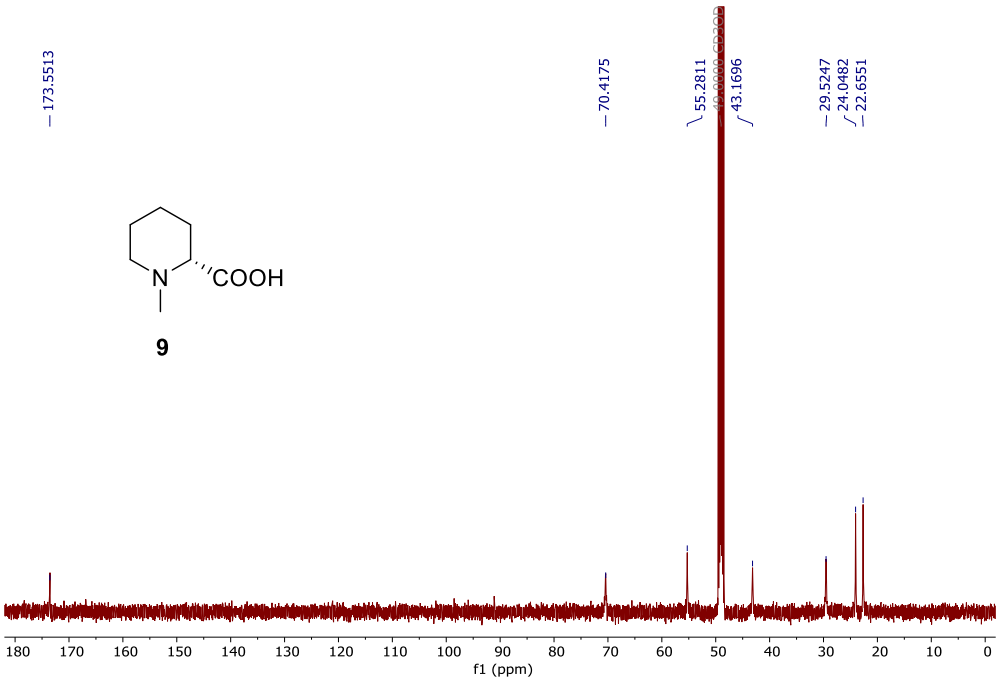

Figure 5.43 ^{13}C NMR spectrum (125 MHz, DMSO-d_6) of **9**.

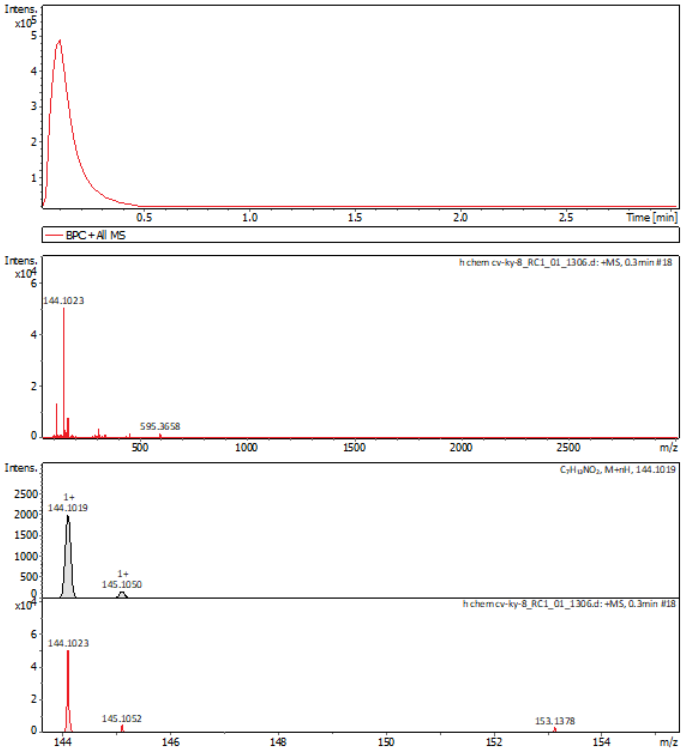

Figure 5.44 HRMS of **9**.

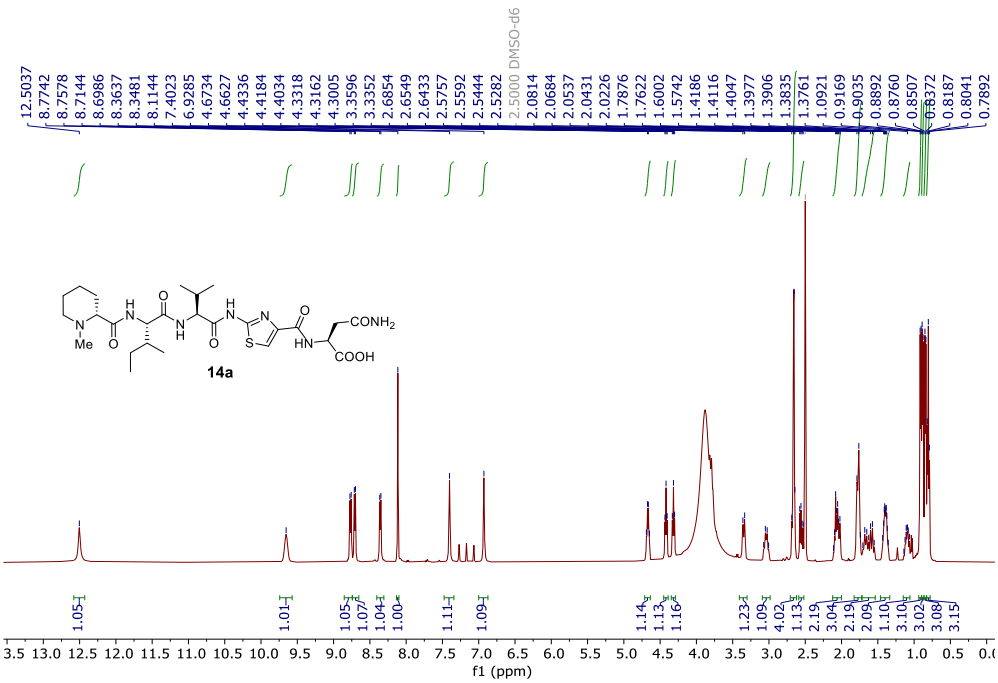

Figure 5.45 ^{1}H NMR spectrum (500 MHz, DMSO-d_6) of **14a**.

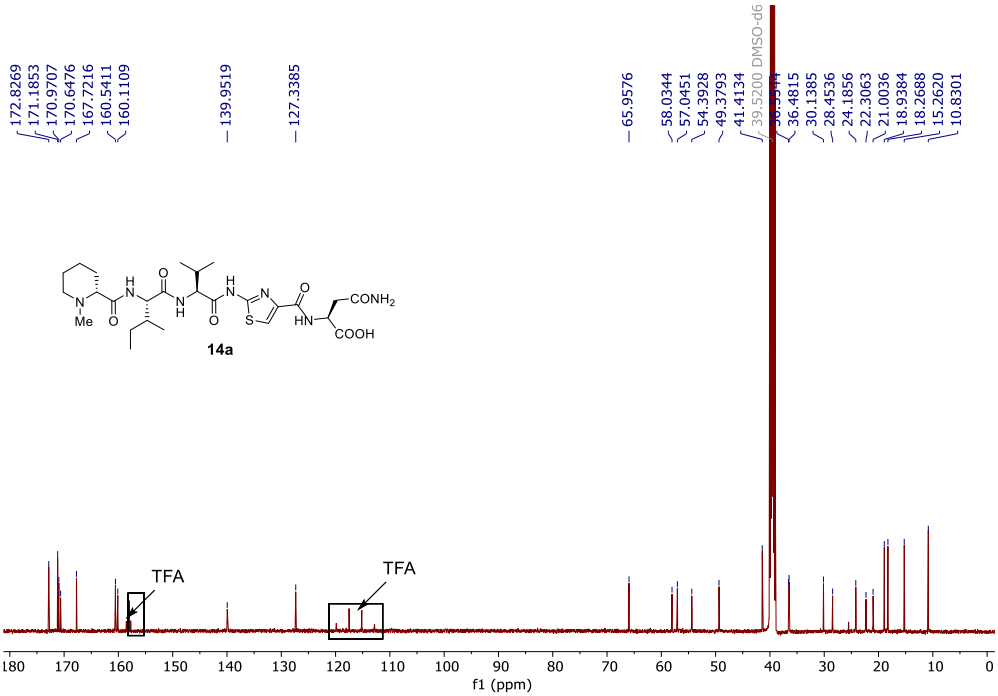

Figure 5.46 ^{13}C NMR spectrum (125 MHz, DMSO-d_6) of **14a**.

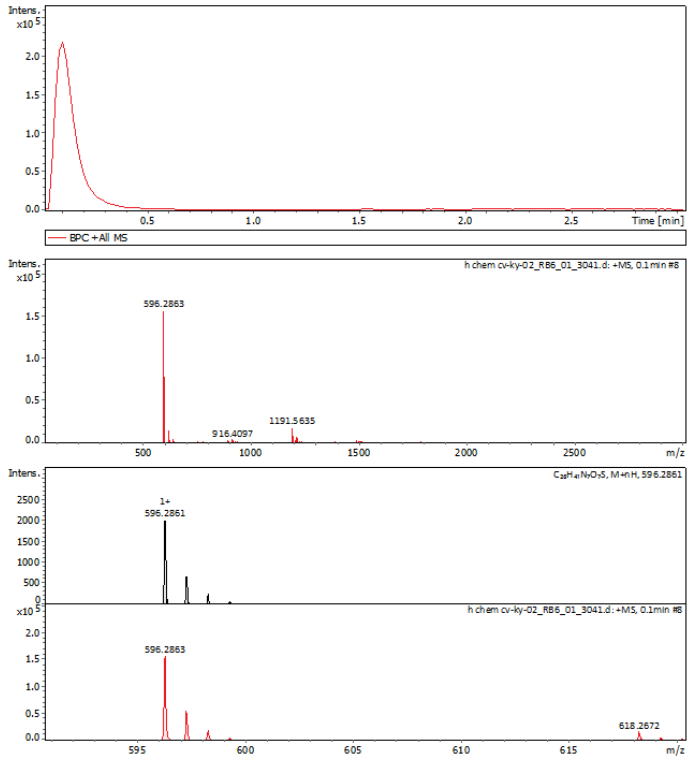

Figure 5.47 HRMS of **14b**.

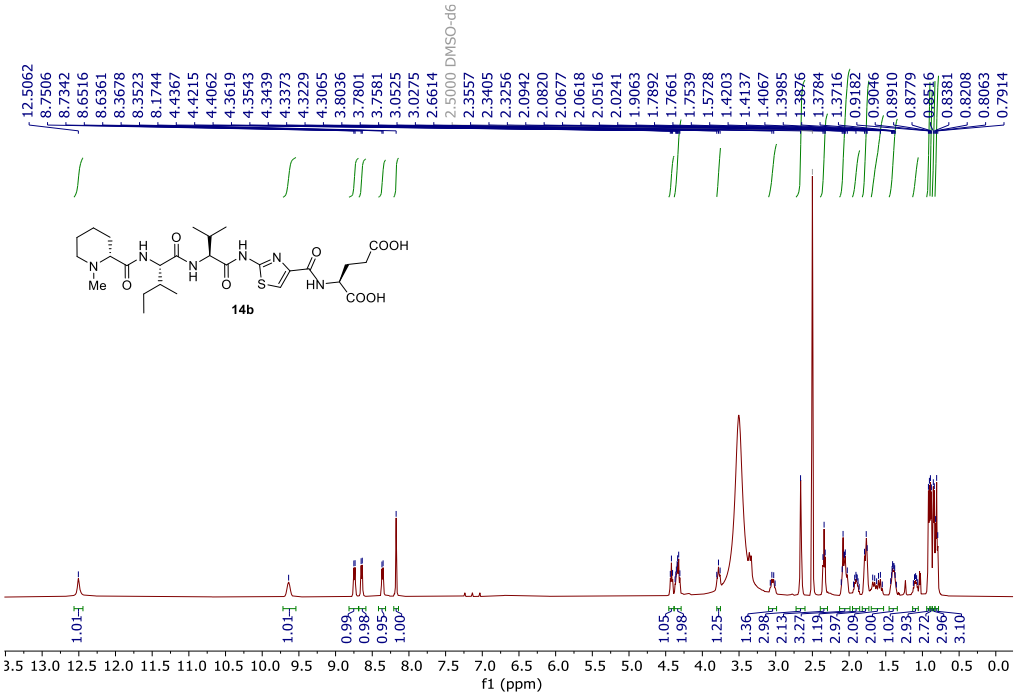

Figure 5.48 ^{1}H NMR spectrum (500 MHz, DMSO-d_6) of **14b**.

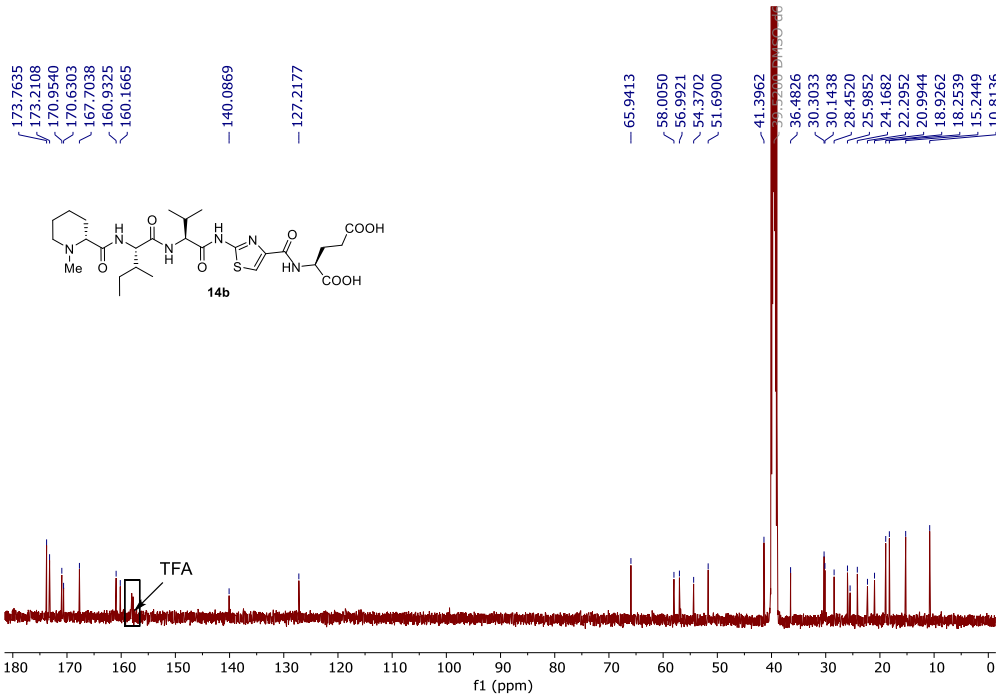

Figure 5.49 ^{13}C NMR spectrum (125 MHz, DMSO-d_6) of **14b**.

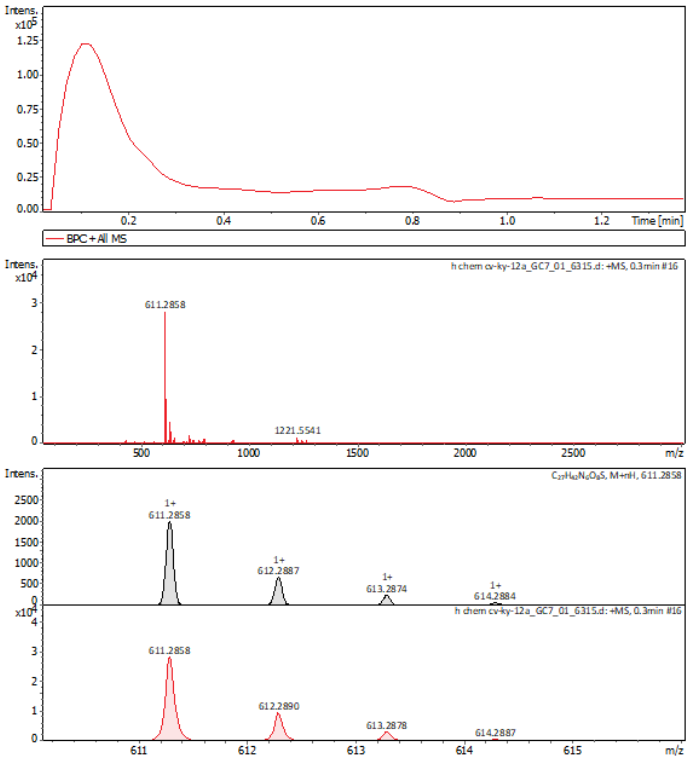

Figure 5.50 HRMS of **14b**.

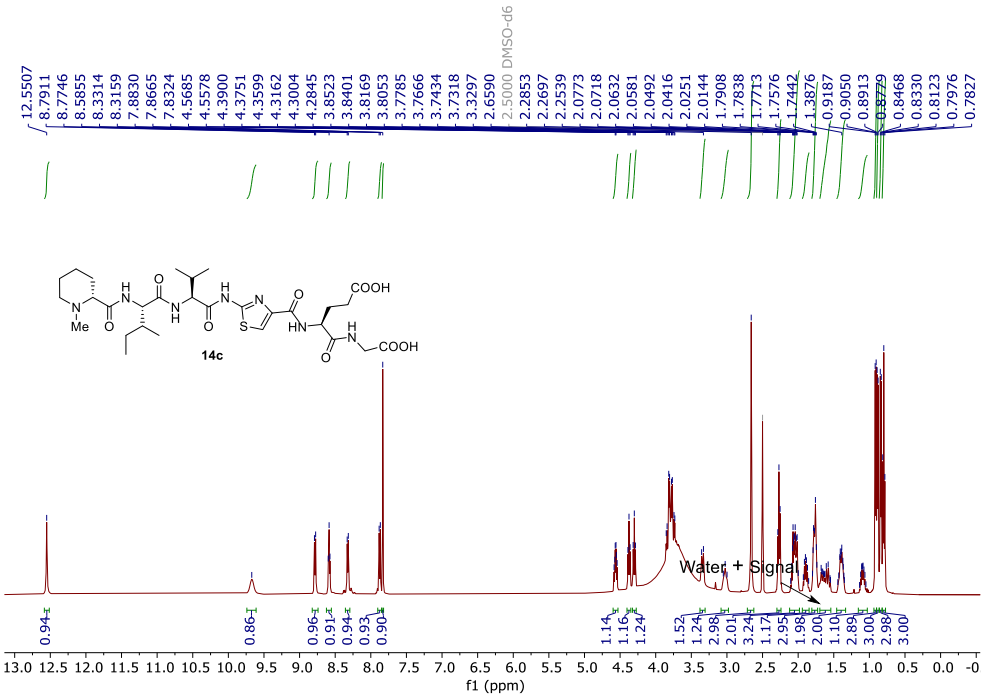

Figure 5.51 ^{1}H NMR spectrum (500 MHz, DMSO-d_6) of **14c**.

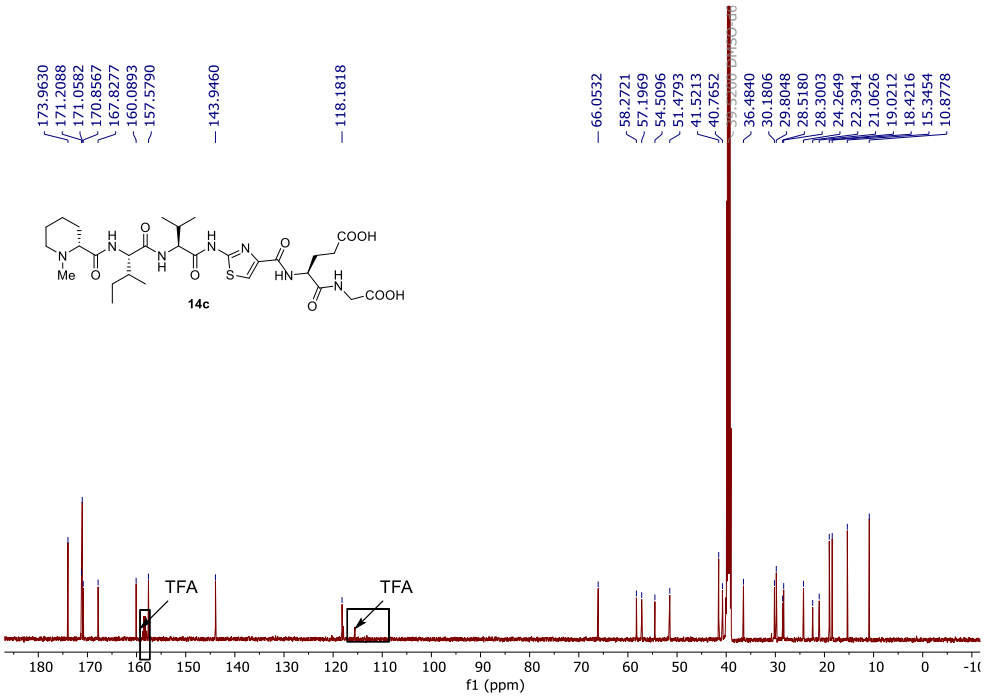

Figure 5.52 ^{13}C NMR spectrum (125 MHz, DMSO-d_6) of **14c**.

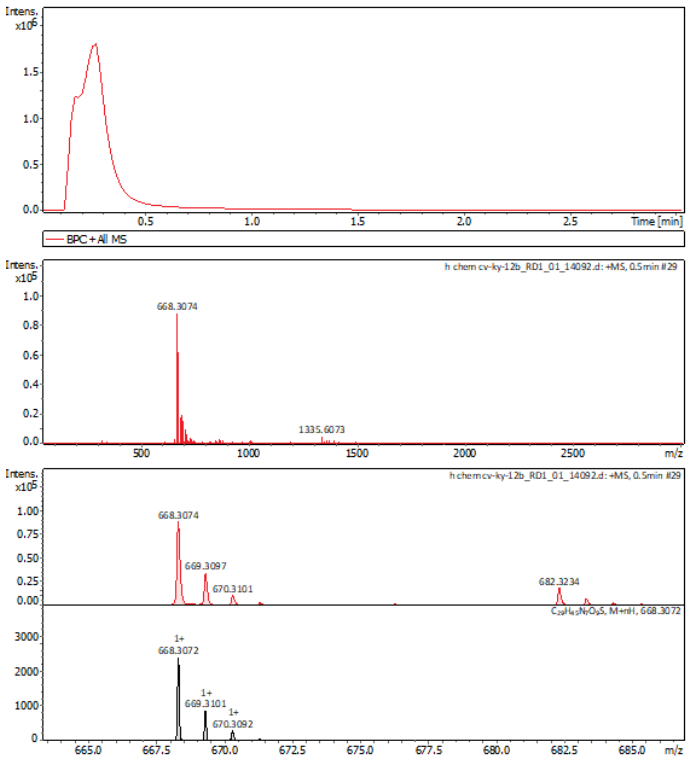

Figure 5.53 HRMS of **14c**.

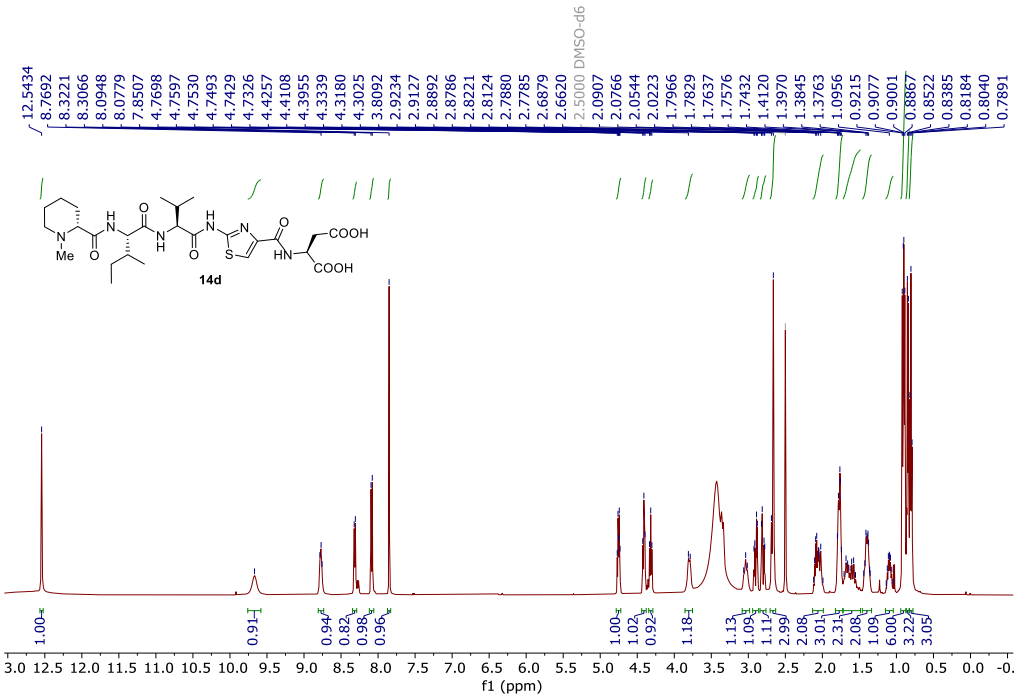

Figure 5.54 ^{1}H NMR spectrum (500 MHz, DMSO-d_6) of **14d**.

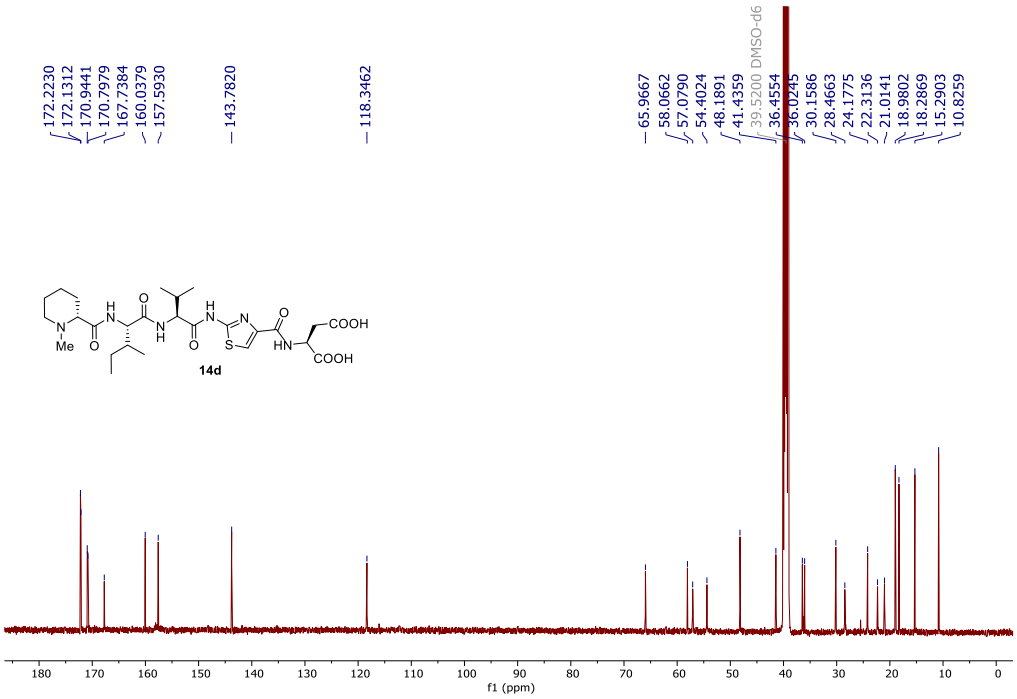

Figure 5.55 ^{13}C NMR spectrum (125 MHz, DMSO-d_6) of **14d**.

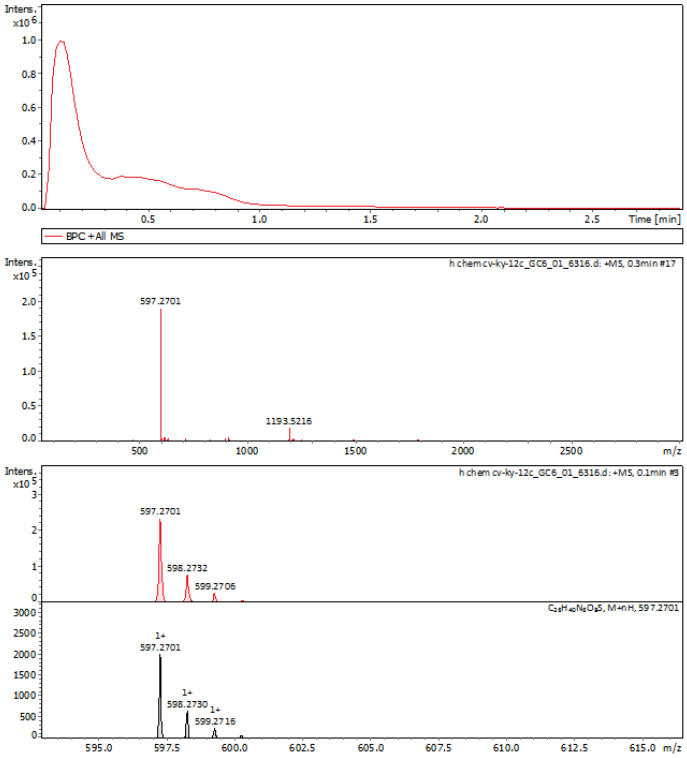

Figure 5.56 HRMS of **14d**.

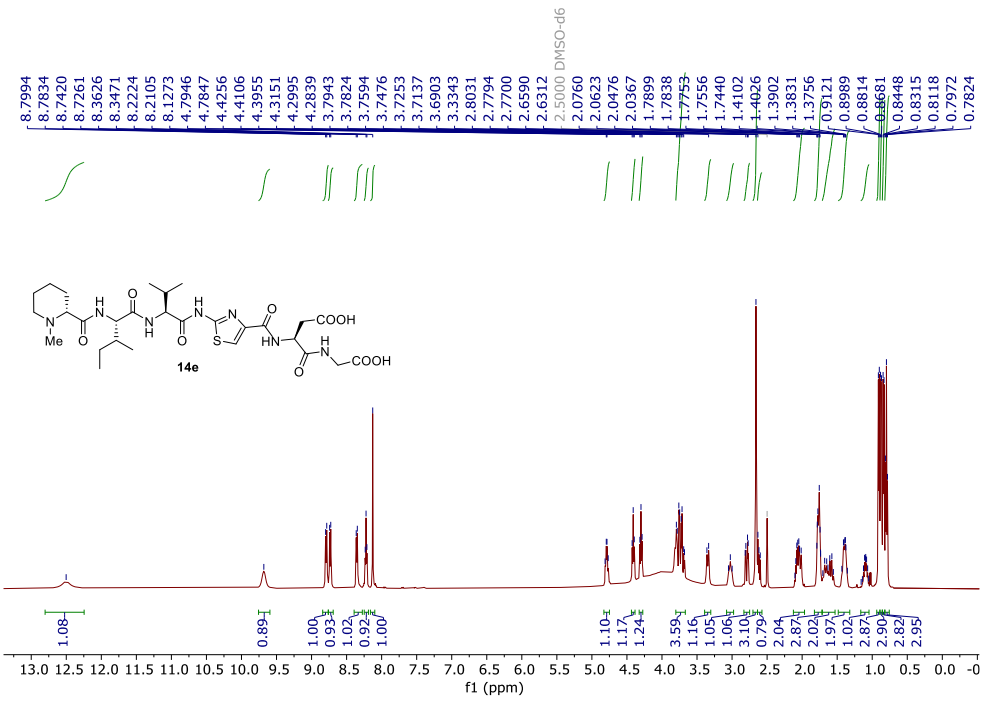

Figure 5.57 ^{1}H NMR spectrum (500 MHz, DMSO-d_6) of **14e**.

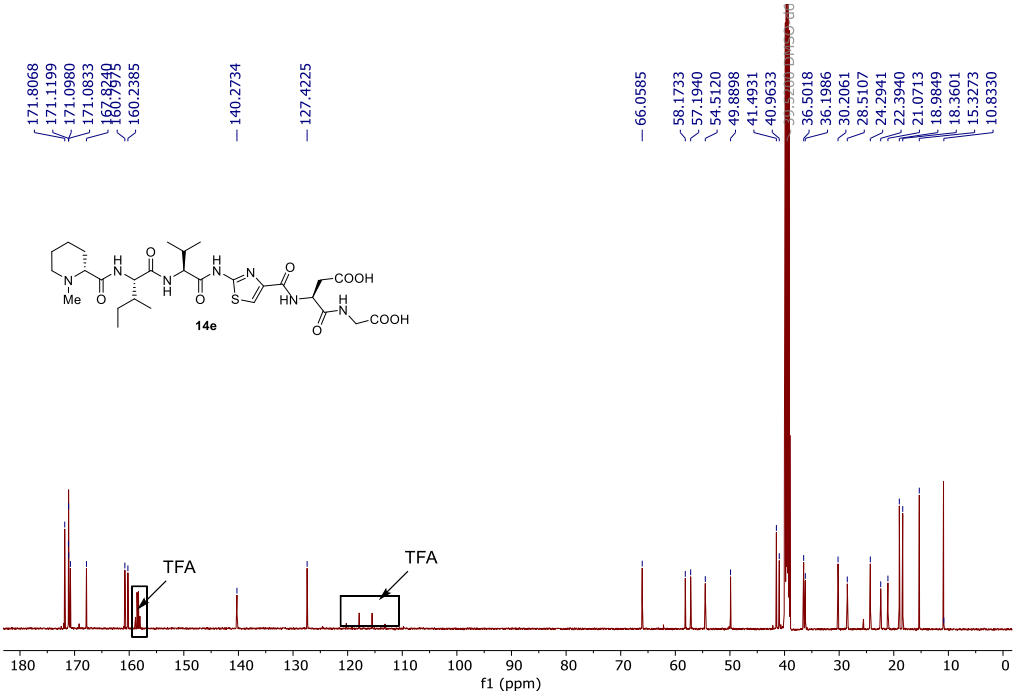

Figure 5.58 ^{13}C NMR spectrum (125 MHz, DMSO-d_6) of **14e.**

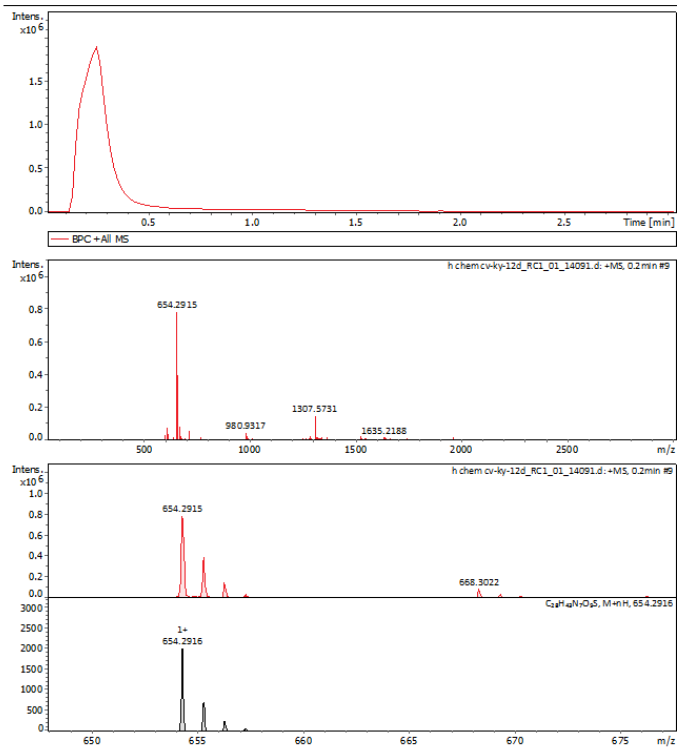

Figure 5.59 HRMS of **14e.**

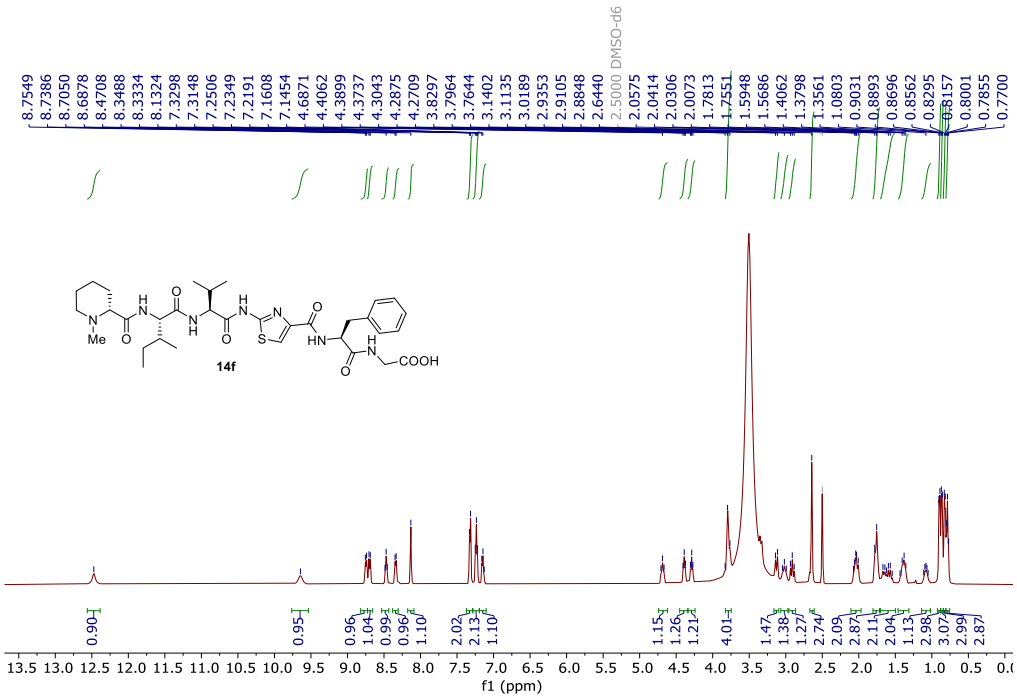

Figure 5.60 ^{1}H NMR spectrum (500 MHz, DMSO-d_6) of **14f**.

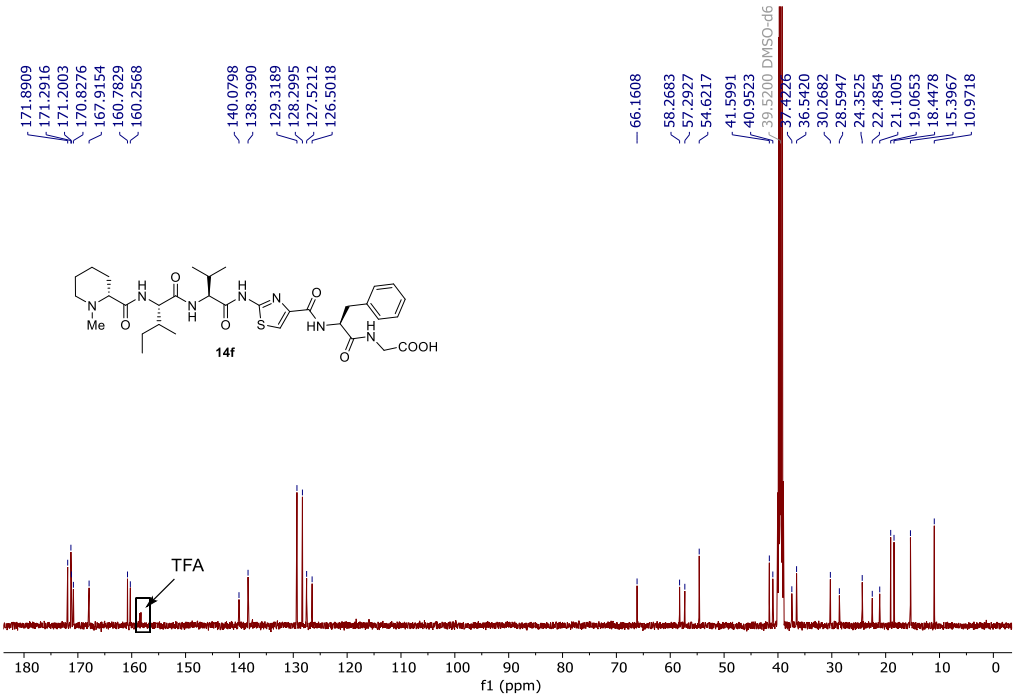

Figure 5.61 ^{13}C NMR spectrum (125 MHz, DMSO-d_6) of **14f**.

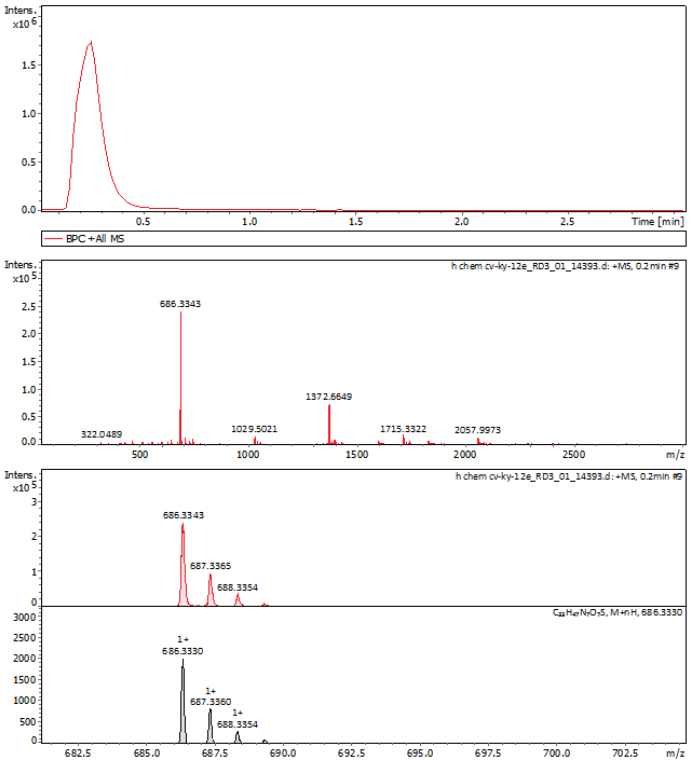

Figure 5.62 HRMS of **14f**.

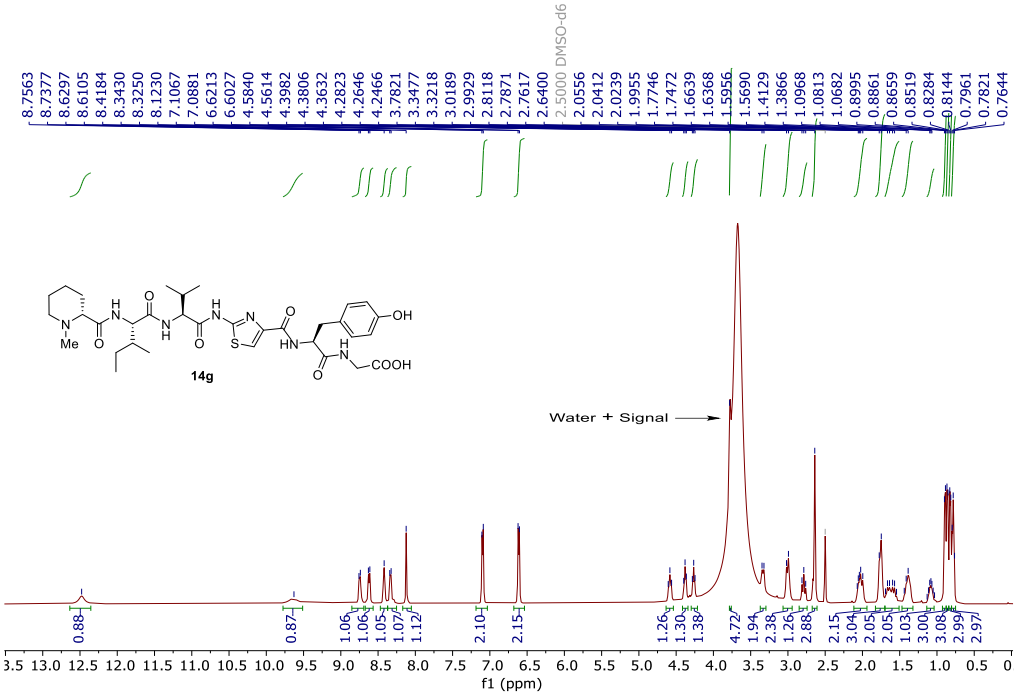

Figure 5.63 ^{1}H NMR spectrum (500 MHz, DMSO-d$_6$) of **14g**.

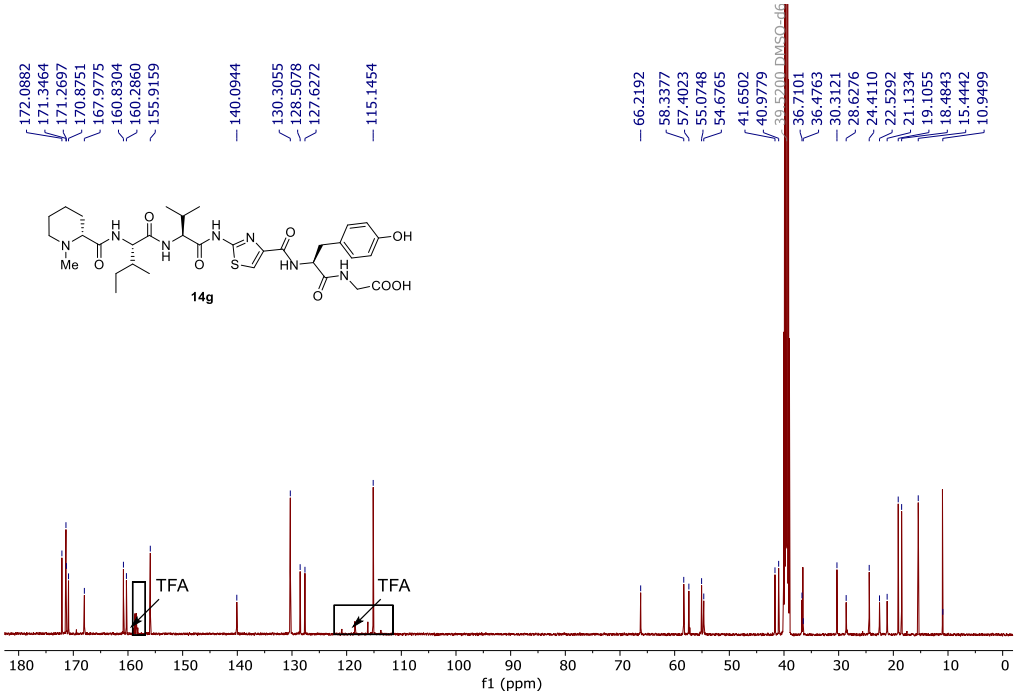

Figure 5.64 ^{13}C NMR spectrum (125 MHz, DMSO-d$_6$) of **14g**.

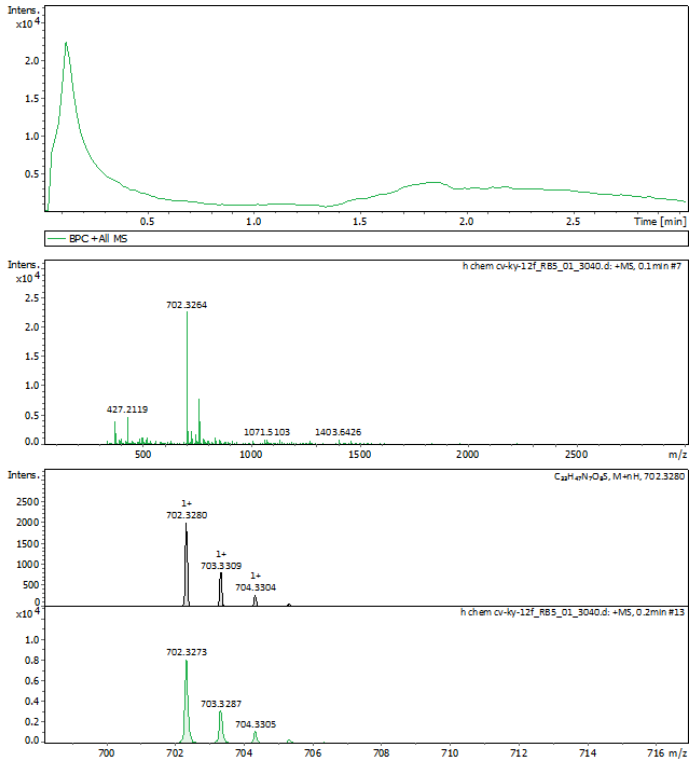

Figure 5.65 HRMS of **14g**.

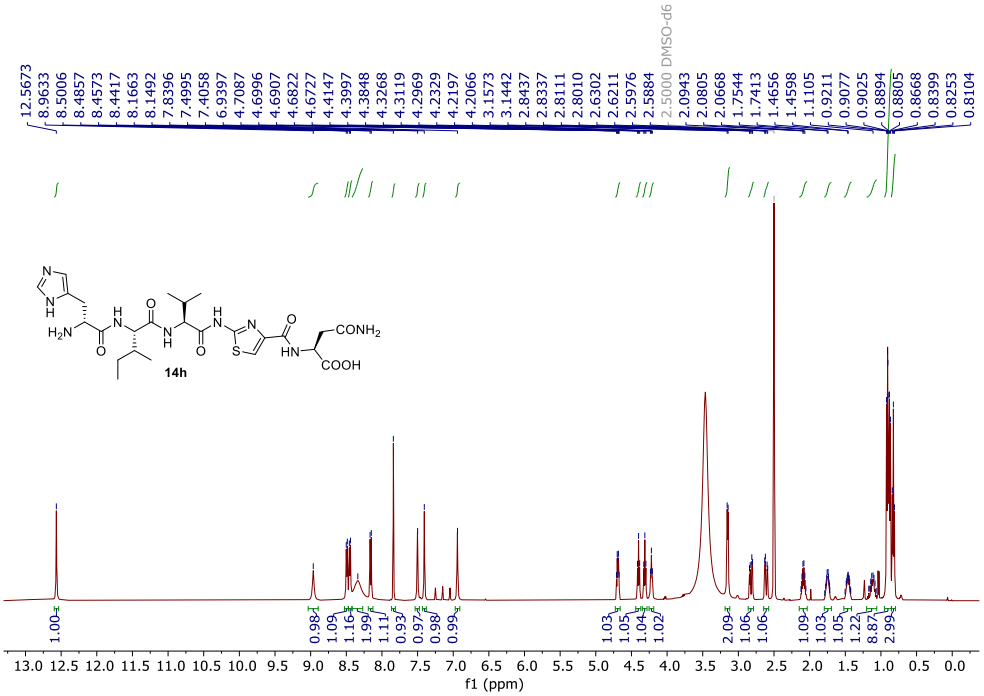

Figure 5.66 ^{1}H NMR spectrum (500 MHz, DMSO-d_6) of **14h**.

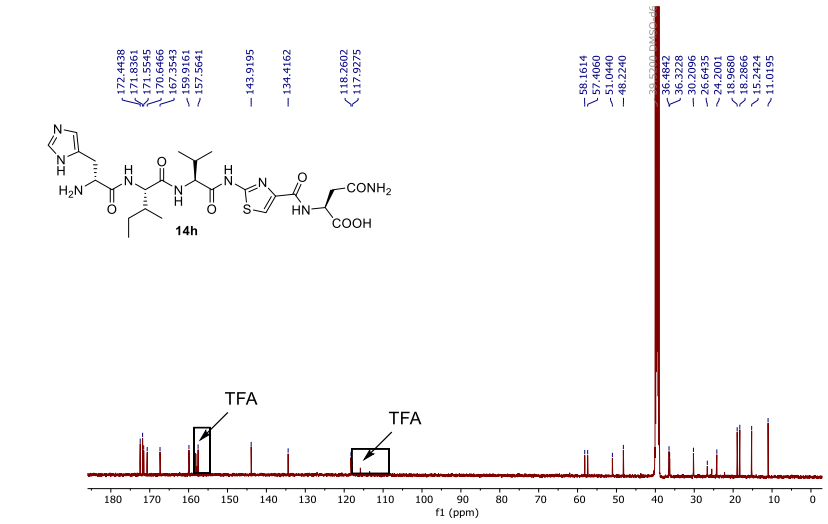

Figure 5.67 ^{13}C NMR spectrum (125 MHz, DMSO-d_6) of **14h**.

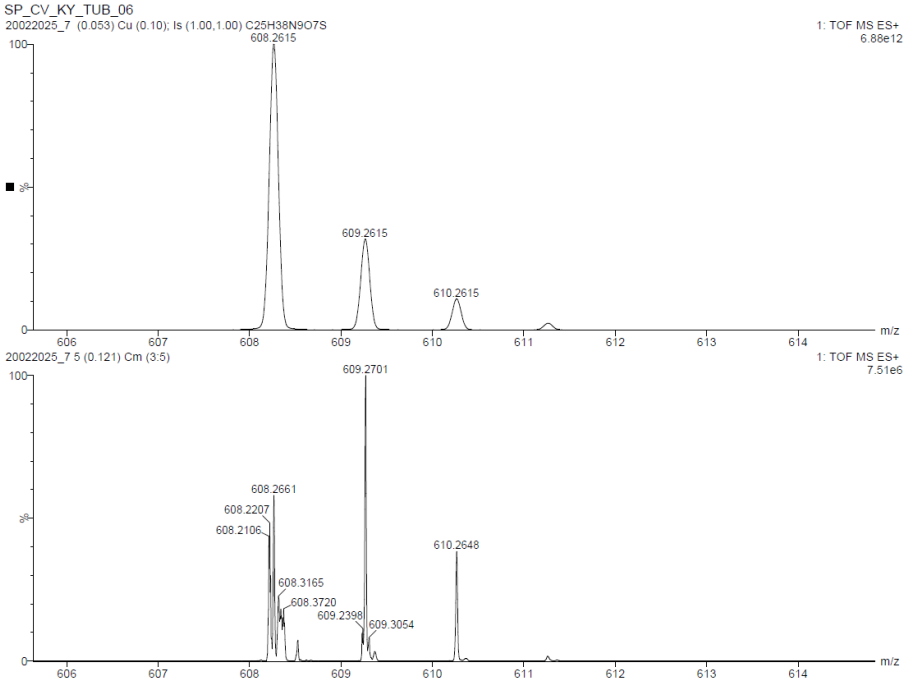

Figure 5.68 HRMS of **14h**.

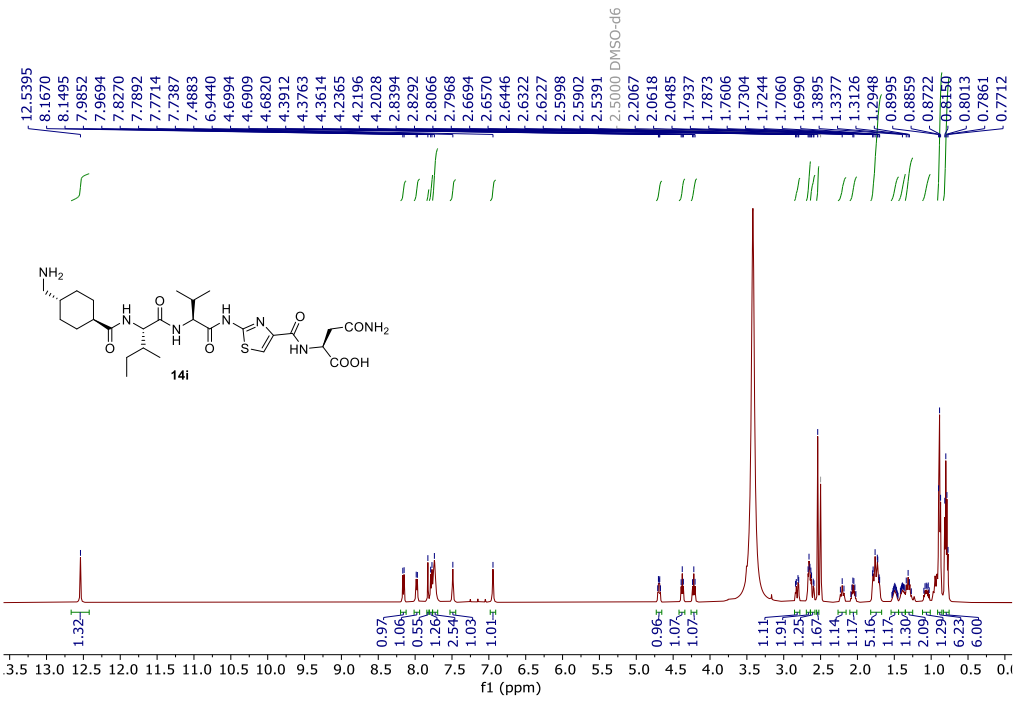

Figure 5.69 ^{1}H NMR spectrum (500 MHz, DMSO-d_6) of **14i**.

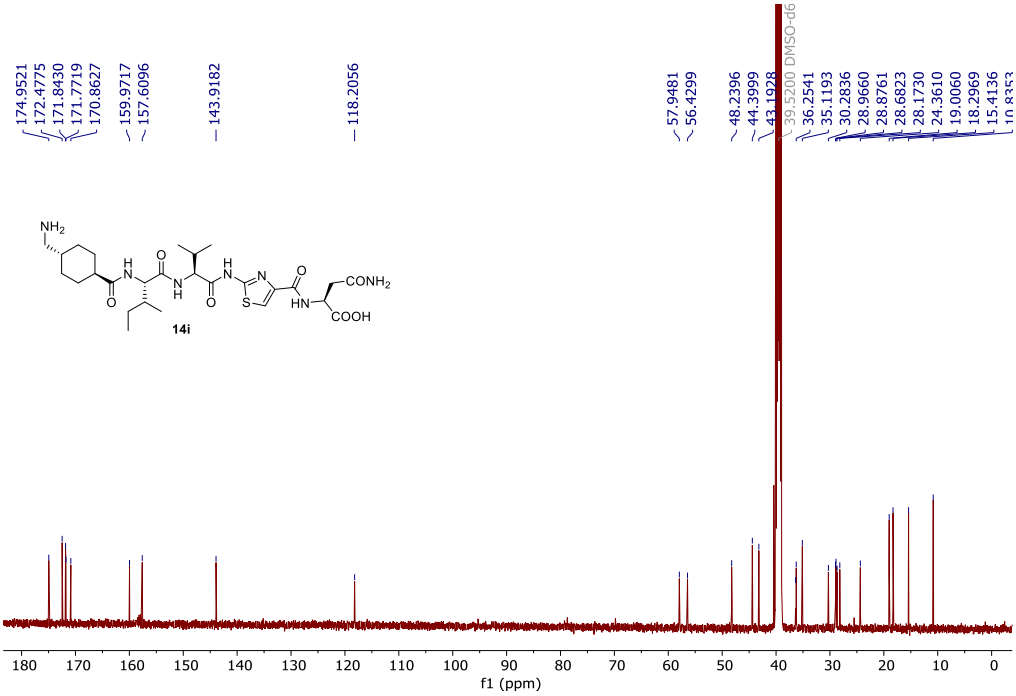

Figure 5.70 ^{13}C NMR spectrum (125 MHz, DMSO-d_6) of **14i**.

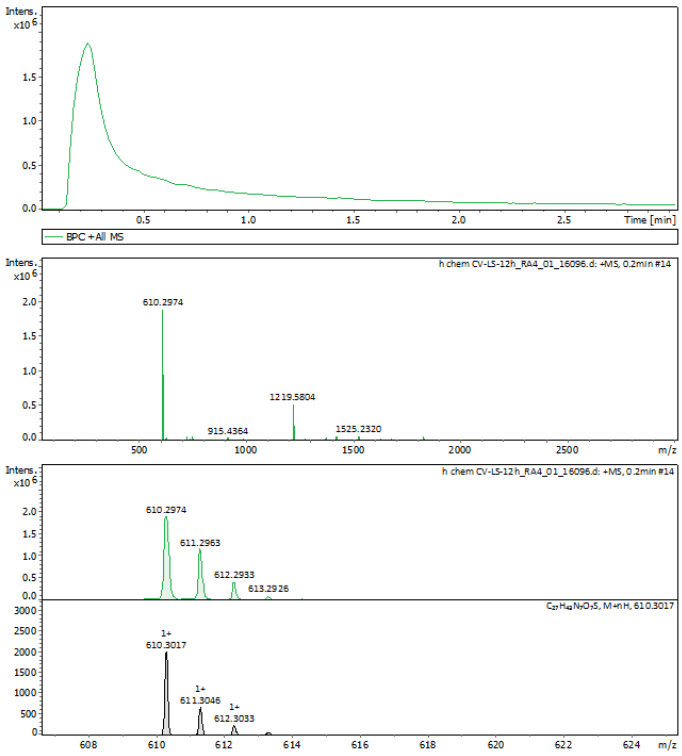

Figure 5.71 HRMS of **14i**.

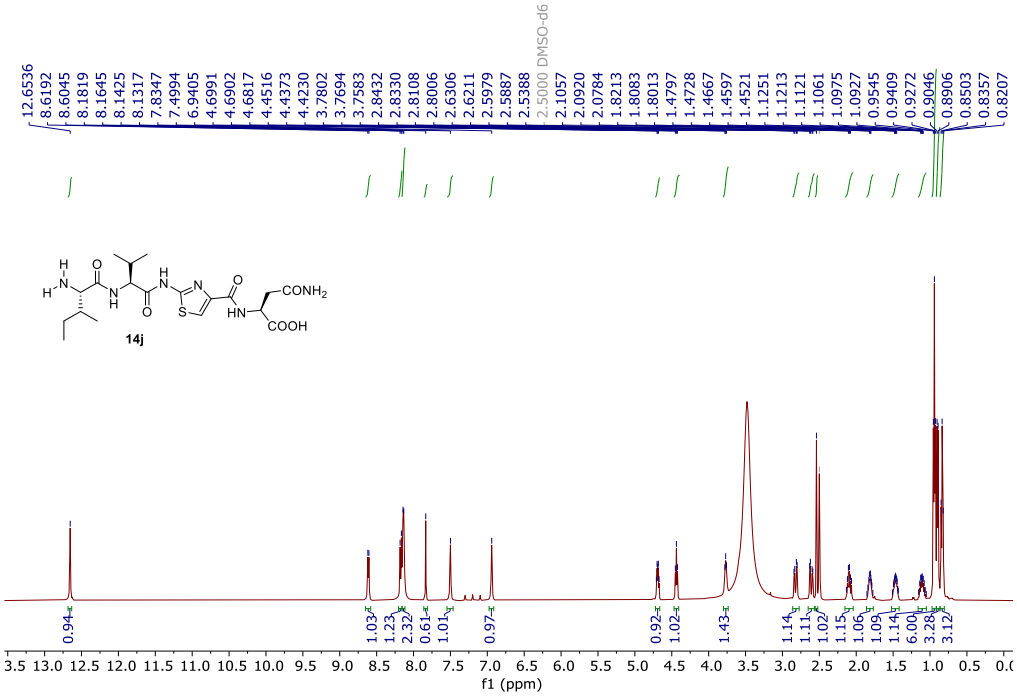

Figure 5.72 ^{1}H NMR spectrum (500 MHz, DMSO-d_6) of **14j**.

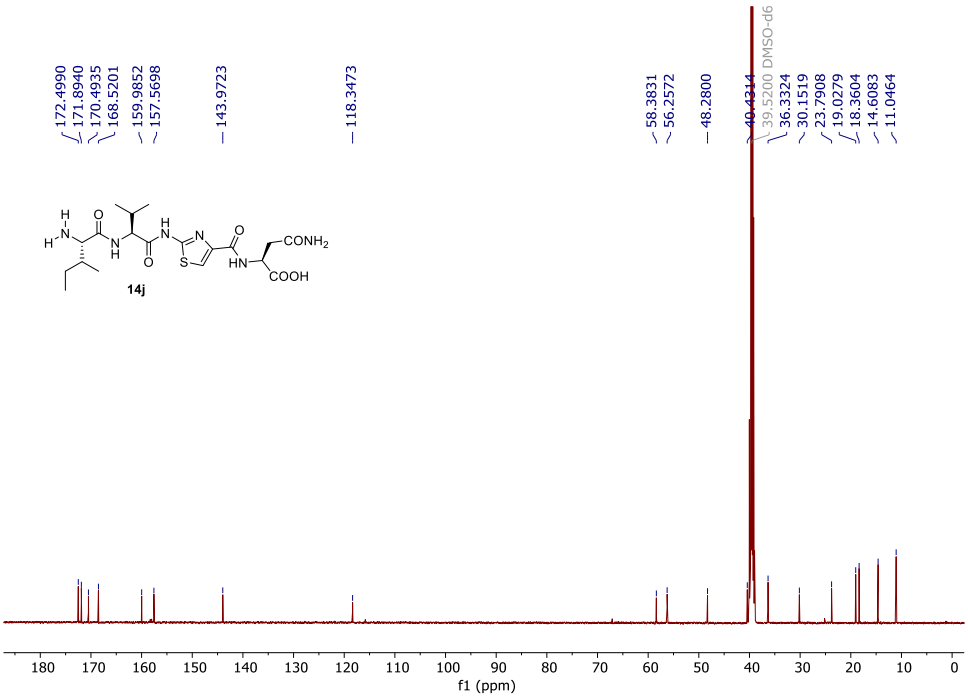

Figure 5.73 ^{13}C NMR spectrum (125 MHz, DMSO-d_6) of **14j**.

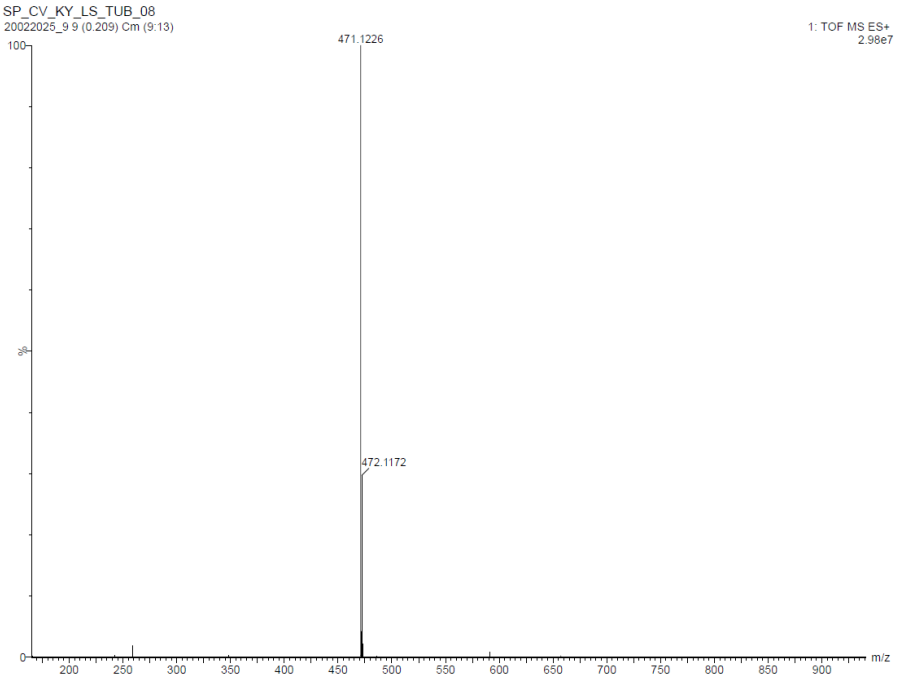

Figure 5.74 HRMS of **14j**.

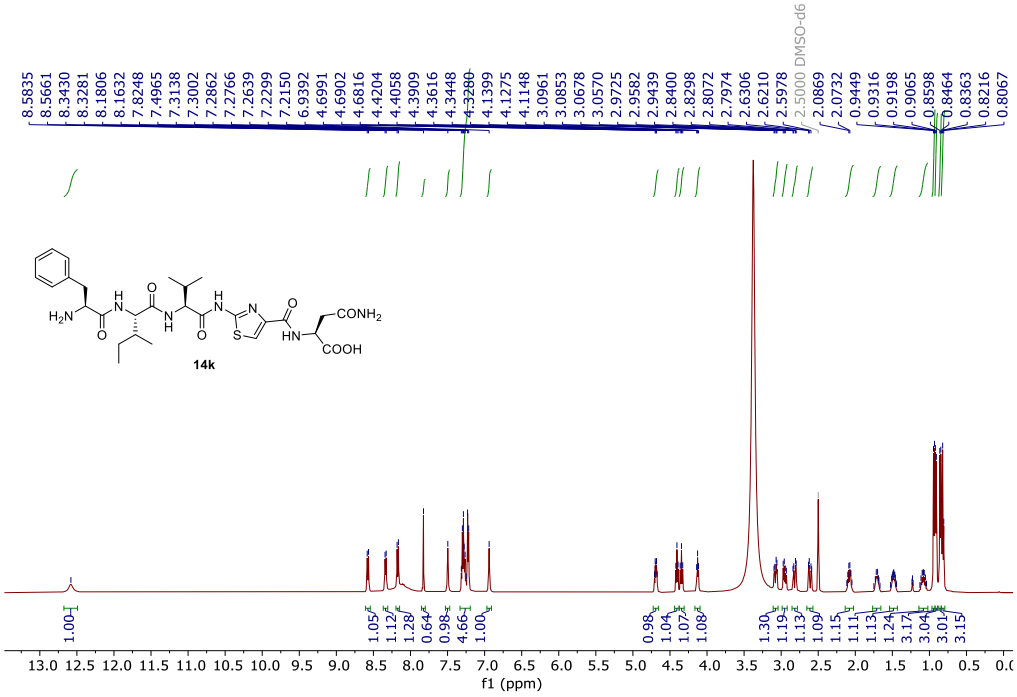

Figure 5.75 ^{1}H NMR spectrum (500 MHz, DMSO-d$_6$) of **14k**.

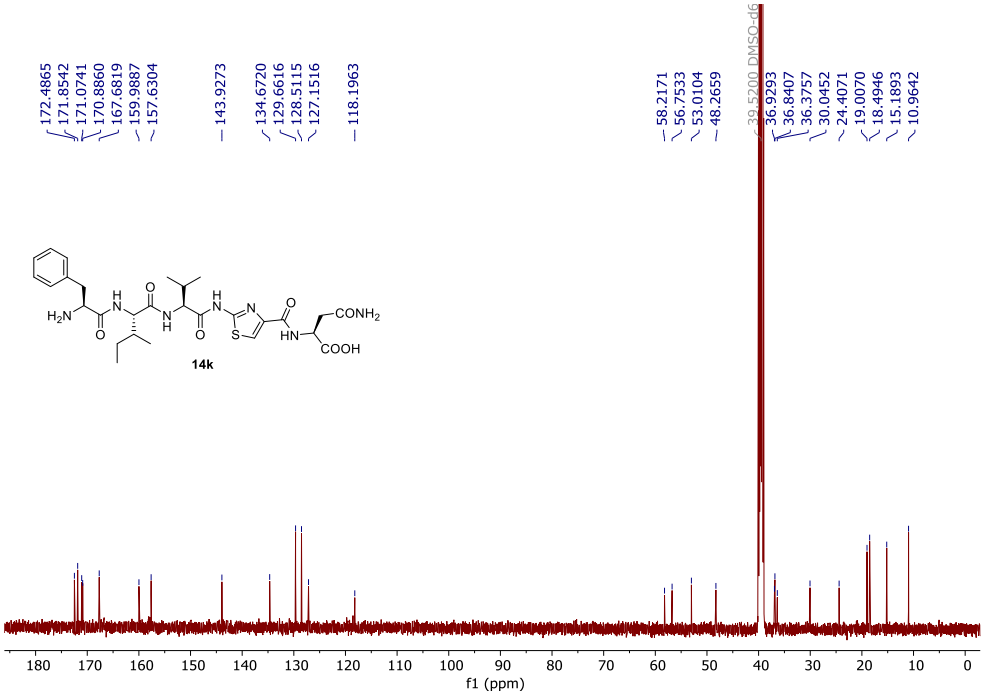

Figure 5.76 ^{13}C NMR spectrum (125 MHz, DMSO-d$_6$) of **14k**.

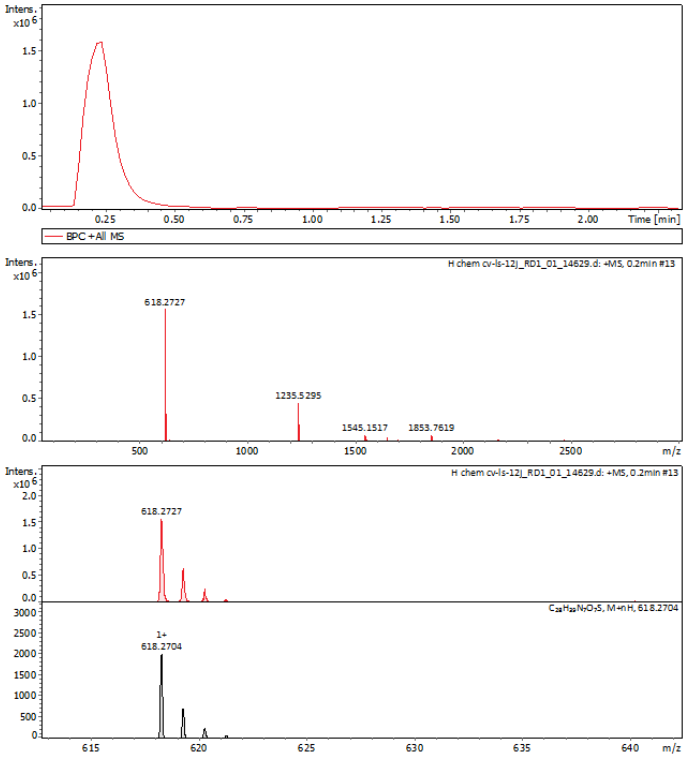

Figure 5.77 HRMS of **14k**.

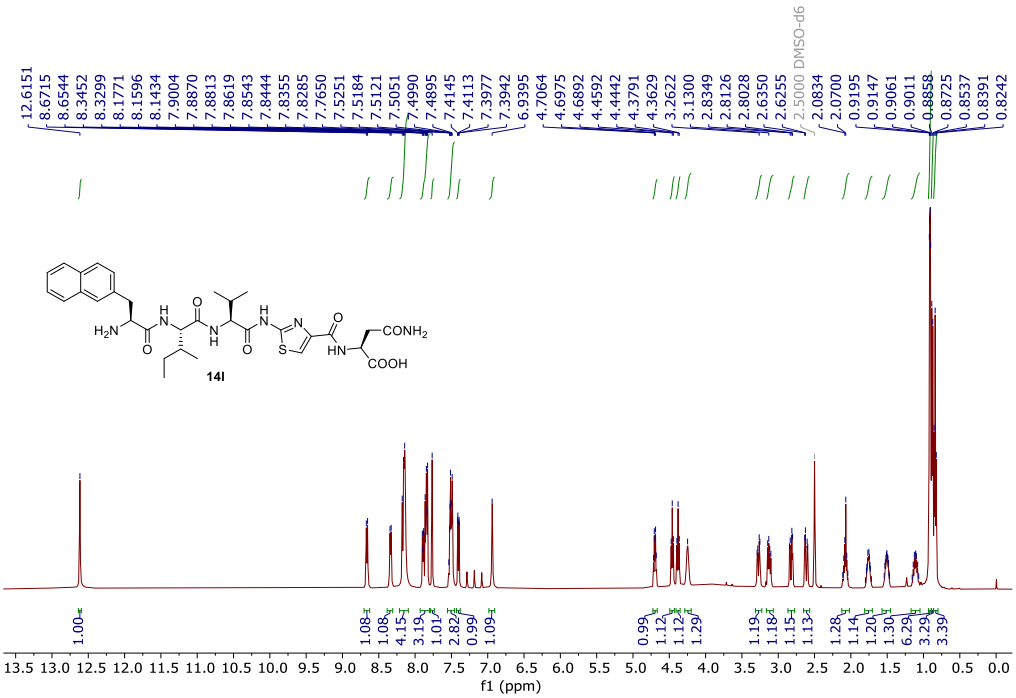

Figure 5.78 ^{1}H NMR spectrum (500 MHz, DMSO-d_6) of **14l**.

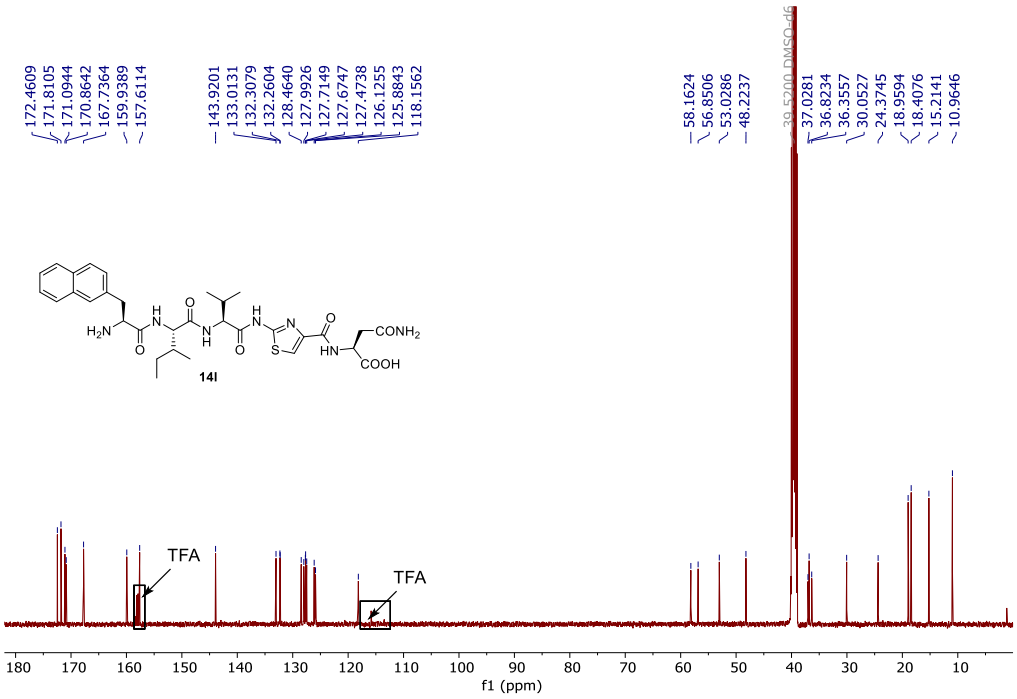

Figure 5.79 ^{13}C NMR spectrum (125 MHz, DMSO-d_6) of **14l**.

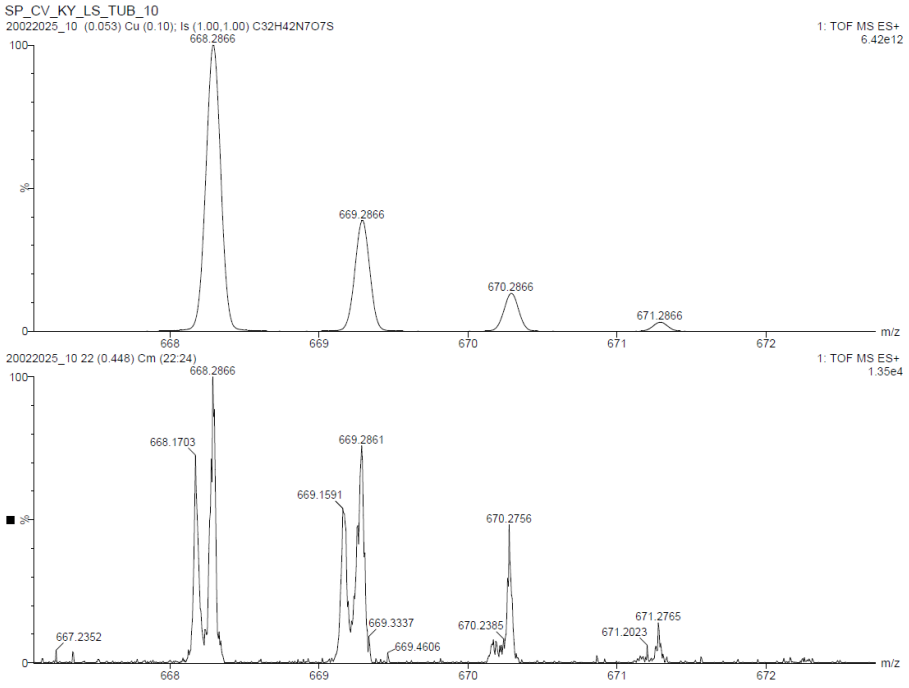

Figure 5.80 HRMS of **14l**.

5.5 References

1. Bray F, Laversanne M, Sung H, et al. Global cancer statistics 2022: GLOBOCAN estimates of incidence and mortality worldwide for 36 cancers in 185 countries. *CA Cancer J Clin*. 2024, 74, 229–263. doi:10.3322/caac.21834.
2. Hanahan D, Weinberg RA. Hallmarks of cancer: The next generation. *Cell*. 2011, 144, 646–674. doi:10.1016/j.cell.2011.02.013.
3. Paier CRK, Maranhão SS, Carneiro TR, et al. Natural products as new antimitotic compounds for anticancer drug development. *Clinics*. 2018, 73, 1–11. doi:10.6061/clinics/2018/E813S.
4. Chen H, Lin Z, Arnst KE, Miller DD, Li W. Tubulin inhibitor-based antibody-drug conjugates for cancer therapy. *Molecules*. 2017, 22, 1281–1309. doi:10.3390/molecules22081281.
5. Zhang L, Wang Z, Liu K, et al. Targets of tumor microenvironment for potential drug development. *Med Comm - Oncol*. 2024, 3, 67–82. doi:10.1002/mog2.68.
6. Muroyama A, Lechler T. Microtubule organization, dynamics and functions in differentiated cells. *Dev*. 2017, 144, 3012–3021. doi:10.1242/dev.153171.
7. Rogalska A, Szula E, Gajek A, Marczak A, Jóźwiak Z. Activation of apoptotic pathway in normal, cancer ovarian cells by epothilone B. *Environ Toxicol Pharmacol*. 2013, 36, 600–610. doi:10.1016/j.etap.2013.06.003.
8. Čermák V, Dostál V, Jelínek M, et al. Microtubule-targeting agents and their impact on cancer treatment. *Eur J Cell Biol*. 2020, 99, 151075–151089. doi:10.1016/j.ejcb.2020.151075.
9. Martino E, Casamassima G, Castiglione S, et al. Vinca alkaloids and analogues as anti-cancer agents: Looking back, peering ahead. *Bioorganic Med Chem Lett*. 2018, 28, 2816–2826. doi:10.1016/j.bmcl.2018.06.044.
10. Kaur G, Hollingshead M, Holbeck S, et al. Biological evaluation of tubulysin A: A potential anticancer and antiangiogenic natural product. *Biochem J*. 2006, 396, 235–242.

doi:10.1042/BJ20051735.

11. Sasse F, Steinmetz H, Heil J, Hofle G, Reichenbach H. Tubulysins, new cytostatic peptides from myxobacteria acting on microtubuli. production, isolation, physico-chemical and biological properties. *J Antibiot (Tokyo)*. 2000, 53, 879–885. doi:10.7164/antibiotics.53.879.
12. Shankar SP, Jagodzinska M, Malpezzi L, et al. Synthesis and structure-activity relationship studies of novel tubulysin U analogues-effect on cytotoxicity of structural variations in the tubuvaline fragment. *Org Biomol Chem*. 2013, 11, 2273–2287. doi:10.1039/c3ob27111k.
13. Höfle G, Glaser N, Leibold T, Karama U, Sasse F, Steinmetz H. Semisynthesis and degradation of the tubulin inhibitors epothilone and tubulysin. *Pure Appl Chem*. 2003, 75, 167–178. doi:10.1351/pac200375020167.
14. Wipf P, Takada T, Rishel MJ. Synthesis of the tubuvaline-tubuphenylalanine (Tuv-Tup) fragment of tubulysin. *Org Lett*. 2004, 6, 4057–4060. doi:10.1021/ol048252i.
15. Peltier HM, McMahon JP, Patterson AW, Ellman JA. The total synthesis of tubulysin D. *J Am Chem Soc*. 2006, 128, 16018–16019. doi:10.1021/ja067177z.
16. Wipf P, Wang Z. Total Synthesis of N^{14}-Desacetoxytubulysin H. *ChemInform*. 2007, 38, 7–9. doi:10.1002/chin.200735186.
17. Nicolaou KC, Yin J, Mandal D, et al. Total synthesis and biological evaluation of natural and designed tubulysins. *J Am Chem Soc*. 2016, 138, 1698–1708. doi:10.1021/jacs.5b12557.
18. Reddy RB, Dudhe P, Chauhan P, Sengupta S, Chelvam V. Synthesis of tubuphenylalanine and epi-tubuphenylalanine via regioselective aziridine ring opening with carbon nucleophiles followed by hydroboration-oxidation of 1,1-substituted amino alkenes. *Tetrahedron*. 2018, 74, 6946–6953. doi:10.1016/j.tet.2018.10.024.
19. Reddy RB, M V, Krishnan MA, Chelvam V. Synthesis of tubuvaline (Tuv) fragment of tubulysin via diastereoselective

dihydroxylation of homoallylamine. *Synth Commun*. 2021, 51, 797–809. doi:10.1080/00397911.2020.1855355.

20. Pandit A, Yadav K, Reddy RB, Sengupta S, Sharma R, Chelvam V. Structure activity relationships (SAR) study to design and synthesize new tubulin inhibitors with enhanced anti-tubulin activity: In silico and in vitro analysis. *J Mol Struct*. 2021, 1223, 129204–129216. doi:10.1016/j.molstruc.2020.129204.

Chapter 6

3D Spheroid model development for *in vitro* cytotoxicity evaluation of tubulin inhibitor: An approach to enhance biomimetic accuracy for clinical research

6.1 Introduction

Tubulysins, a class of natural products initially isolated from myxobacteria cultures, have gained significant attention due to their potent cytotoxic activity, primarily mediated by binding to β-tubulin, causing destabilization of microtubules, resulting in apoptosis induction.[1,2] Among the fourteen naturally occurring tubulysin family of natural products, tubulysin M is one of the most promising anticancer peptides with an IC_{50} of 0.02 nM.[3] The structural elucidation revealed that tubulysin M is a tetrapeptide with *N*-methyl-D-pipecolic acid (D-Mep) at the N terminus, followed by isoleucine (L-IIe), tubuvaline (Tuv), and tubuphenylalanine (Tup).[4] However, the availability of the molecule is limited due to natural scarcity, chemically complex structure with multiple chiral centres, robust synthesis, poor yield, and biological instability.[5] For the feasible and scalable synthesis of Tubulysin M, initial studies from our lab reported the convenient synthesis of tubuvaline (Tuv) and tubuphenylalanine fragments (Tup).[6,7] However, the robust multistep chemical synthesis remains the major challenge. A systematic modification of the tubulysin fragments was carried out to address this problem, and a novel third-generation tubulysin derivative, Tub_01, was developed, without tubuvaline and tubuphenylalanine fragments.[8]

Despite promising *in vitro* results, many drug candidates fail in preclinical studies due to a primary reliance on the traditional 2D monolayer cell culture system, which does not adequately mimic the complex and heterogeneous tumor microenvironment (TME).[9] The 2D model fails to replicate the *in vivo*-like tumor architecture, including

compact cell-cell and cell-extracellular matrix (ECM) interactions, critical signalling pathways, hypoxic conditions, and vasculature, leading to inaccurate and false positive results that cause significant loss of time, money, and resources during drug development.[10] The 3D spheroid model has emerged as a more biologically relevant system to address these limitations and is capable of accurately mimicking the tumor microenvironment.[11] Drug discovery programs have created an urgency to develop new advanced *in vitro* 3D platforms that offer more predictive and physiologically relevant information.[12] Statistics have shown that incorporating 3D models reduces early false positive results during *in vitro* screening, lowering drug attrition rates and bridging the gap between 2D and preclinical studies.[13] Various techniques have been developed for synthesizing 3D tumor models, such as liquid overlay, hanging drop, forced floating, spinner, gel embedding, and microfluidic-based culture.[14,15,16] However, the spheroids generated using these methods have faced several limitations, including low throughput, high cost, time consumption, low reproducibility, distorted spheroid geometry, and non-homogeneous spheroid generation. In our laboratory, to overcome these limitations, we have developed a scaffold-based agarose 3D microsphere platform to produce homogeneous, compact spheroids of desired size by varying the diameter of the microspheres generated on the agarose platform.[17] Using this system, we evaluated a simplified, highly potent tubulysin derivative with an optimized synthetic framework that allows feasibility for large-scale production and therapeutic development. The tubulysin derivative was initially validated in the 2D model and subsequently in the 3D spheroid model to assess its efficacy in a physiologically relevant context before proceeding to *in vivo* studies.

6.2 Results and discussion

Several reports have mentioned that a structurally simplified tubulysin natural product with various alterations in tubuvaline and tubuphenylalanine fragments resulted in a substantial loss of activity. The naturally occurring tubulysin M, which exhibits activity in the sub-

nanomolar range (0.02 nM), was synthetically challenging due to its robust, multistep synthesis and purification, resulting in poor yield. In our laboratory, we designed and retrosynthetically dissected the tubulysin derivative **15** into four building blocks suited for solid-phase peptide synthesis, such as *N*-methyl-D-pipecolic acid **8**, Fmoc-protected (L)-isoleucine **9**, dipeptide **6**, and (L)-asparagine **10**, from N- to C-termini (Scheme 6.1).

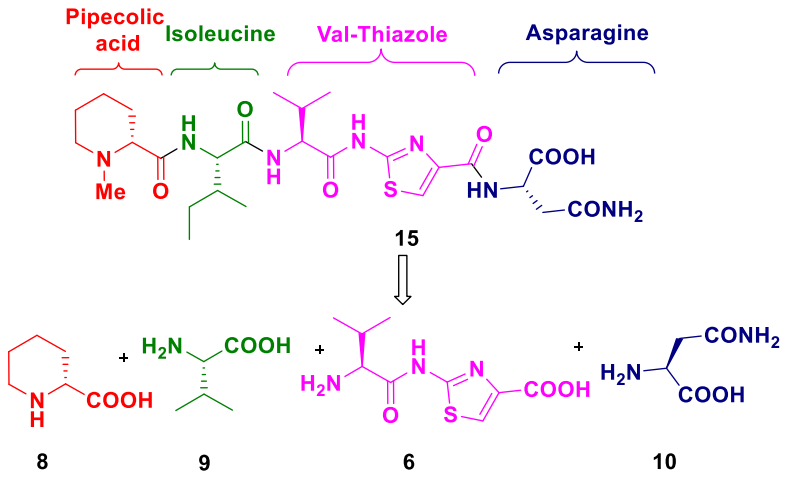

Scheme 6.1 Retrosynthetically dissected fragments of tubulysin derivative **15**.

The synthesis of Fmoc valine thiazole dipeptide **6** begins with the *para*-methoxybenzyl (PMB) protection of 2-aminothiazole-4-carboxylic acid **1** to afford 4-methoxybenzyl 2-aminothiazole-4-carboxylate **3** in 56% yield, which was then coupled with Fmoc-protected valine **4** using EDC.HCl as amide coupling to afford PMB-protected Fmoc valine thiazole dipeptide **5** in 75% yield. The acid-labile PMB group was then deprotected using 10% trifluoroacetic acid (TFA) in DCM, as shown in scheme 6.2, to afford dipeptide **6** in 98% yield. The *N*-methyl-D-pipecolic acid **8** was chemically synthesized by reaction of pipecolic acid with formaldehyde in the presence of Pd/C as a catalyst under H_2 atmosphere (Scheme 6.3). The solid-phase peptide synthesis (SPPS) of the tetrapeptide **15** was carried out by incorporation of the two synthesized fragments, and Fmoc valine thiazole dipeptide **6** and *N*-methyl-D-pipecolic acid **8**, as shown in scheme 6.4. The chlorotrityl resin **11** was used as a polymeric support that was already capped with

asparagine amino acid. The free NH_2 group of the resin was initially coupled with valine thiazole fragment **6** to obtain dipeptide **12**, followed by coupling with isoleucine to yield tripeptide **13**. Finally, the N-terminal amino acid, *N*-methyl-D-pipecolic acid fragment was coupled to the free NH_2 group of the growing peptide chain and the final tetrapeptide **14** was cleaved from the resin using a cleavage cocktail solution of a mixture of TFA:TIPS:H_2O (9.5:0.25:0.25), precipitation in ice cold diethyl ether to obtain tetrapeptide, purification using Reverse-Phase High-Performance Liquid Chromatography (RP-HPLC) to obtain pure tubulysin derivative **15** in 63% yield which was used for 2D and 3D *in vitro* studies.

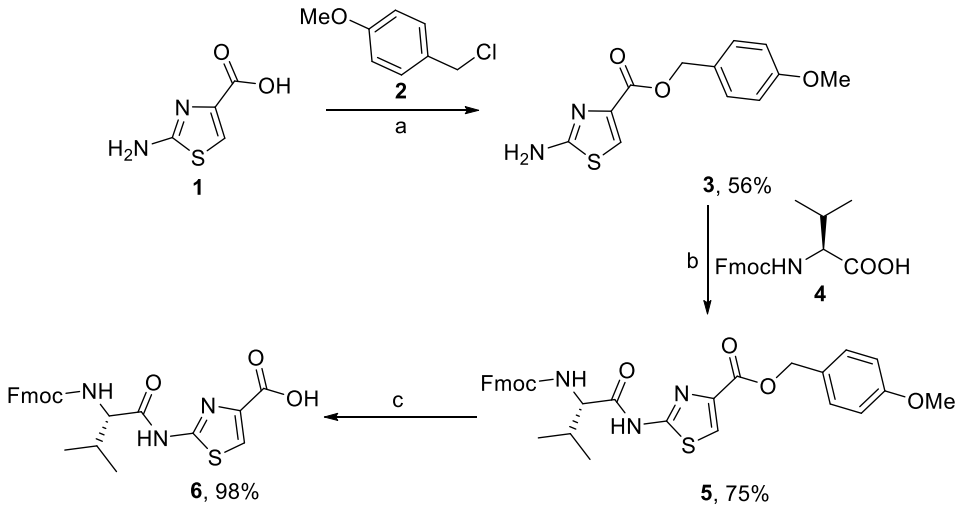

Scheme 6.2 Synthesis of Fmoc valine thiazole fragment **6**. Reagents and conditions:(a) Na_2CO_3, DMF, rt, 16 h; (b) EDC.HCl, HOBt, DCM, rt, 16 h; (c) 10% TFA in DCM, rt, 1.5 h.

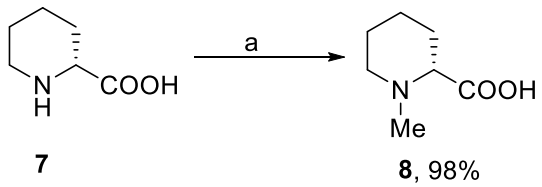

Scheme 6.3 Synthesis of *N*-methyl-D-pipecolic acid **8**. Reagents and conditions: (a) Formaldehyde (37% in water), 10 mol% Pd/C, H_2 (1 atm), MeOH, rt, 24 h.

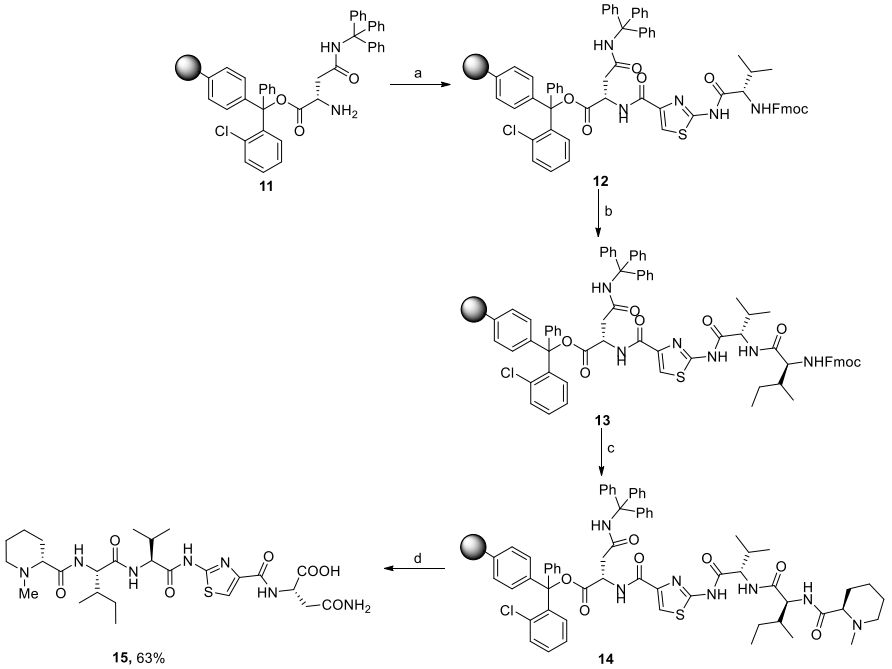

Scheme 6.4 Synthesis of tubulysin derivative **15**. Reagents and conditions: (a) Fmoc-Val-thiazole-OH, PyBOP, DIPEA, DMF, 6 h; (b) (i) 20% Piperidine in DMF, rt, 30 min; (ii) Fmoc-Ile-OH, PyBOP, DIPEA, DMF, 6 h; (c) (i) 20% Piperidine in DMF, rt, 30 min; (ii) *N*-methyl-D-pipecolic acid, PyBOP, DIPEA, DMF, 6 h; (d) (i) TFA/TIPS/H_2O (9.5:0.25:0.25) (1 × 5 mL, 30 min; 2 × 5 mL, 5 min); (ii) Evaporate TFA; (iii) Precipitation in ice-cold diethyl ether.

6.2.1 Cytotoxicity study of tubulysin derivative 15 in a PC3 2D monolayer model

The *in vitro* cytotoxicity study of tubulysin derivative **15** was initially performed in a 2D monolayer model of PC3 (Prostate Cancer) cell line for an incubation period of 48 h, with concentrations ranging from 10 µM to 0.5 nM, along with a standard tubulin inhibitor, colchicine. Tubulysin derivative **15** demonstrates potent cytotoxicity, with an IC_{50} of 21.99 nM, significantly higher than that of colchicine (IC_{50} = 277.10 nM) (Figure 6.1). The replacement of the Tuv fragment with a simple thiazole ring system retained cytotoxicity activity and resulted in greater potency compared to the standard tubulin inhibitor, colchicine.

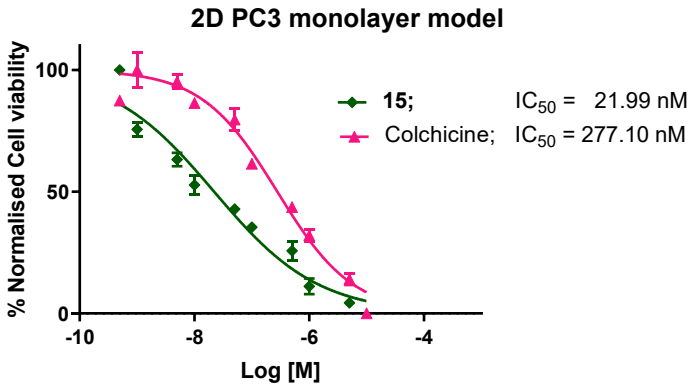

Figure 6.1 IC_{50} study of tubulysin derivative **15** in 2D PC3 monolayer culture model for an incubation period of 48 h, along with a standard tubulin inhibitor, colchicine. Data are expressed as mean ±S.D. (n=3).

6.2.2 Development and viability study of PC3 3D spheroid model developed using μ sphere platform: Superior alternative within 24 h.

The 3D model simulates a biologically relevant tumour microenvironment by considering cell-cell and cell-extracellular matrix (ECM) compact interactions, facilitating nutrient and oxygen gradients in tumour cells, thereby affecting drug penetration abilities. Homogeneous spheroids were generated using an agarose-based microsphere platform developed in our laboratory, as shown in figure 6.2. The agarose-based microwells were generated using a high-grade heat-resistant wooden brush with spherical bristles immersed in the molten agarose, upon solidification, results in regularly sized spherical compartments for the generation of PC3 spheroids using 2×10^5 cells/microwell within 24 h. The generated spheroids with a diameter of 1010 μm were evaluated for their viability using confocal laser microscopy (CLSM) by staining with fluorescein diacetate (FDA) and propidium iodide (PI) dyes. The results indicate that the PC3 cells remain highly viable even at the core, with a mean fluorescent intensity of 184 A.U. for live cells (FDA) and 8 A.U. for dead cells (PI) (Figure 6.3). The cell viability was comparable to that of 2D monolayer cell cultures. The highly viable spheroids were used for *in vitro* cytotoxicity evaluation with tubulysin derivative **15**.

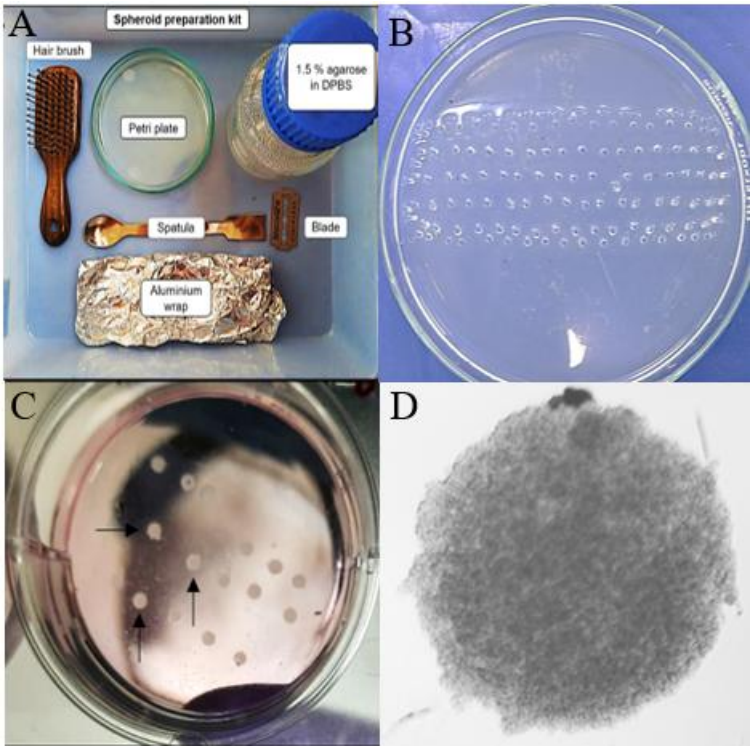

Figure 6.2 (A) Image of spheroid generation kit for sterilization using autoclave; (B) Impressions of microwells in agarose platform created using a hairbrush; (C) Image of 2.5 × 10^5 PC3 cells seeded into microwells; (D) PC3 spheroid formation within 24 h of incubation.

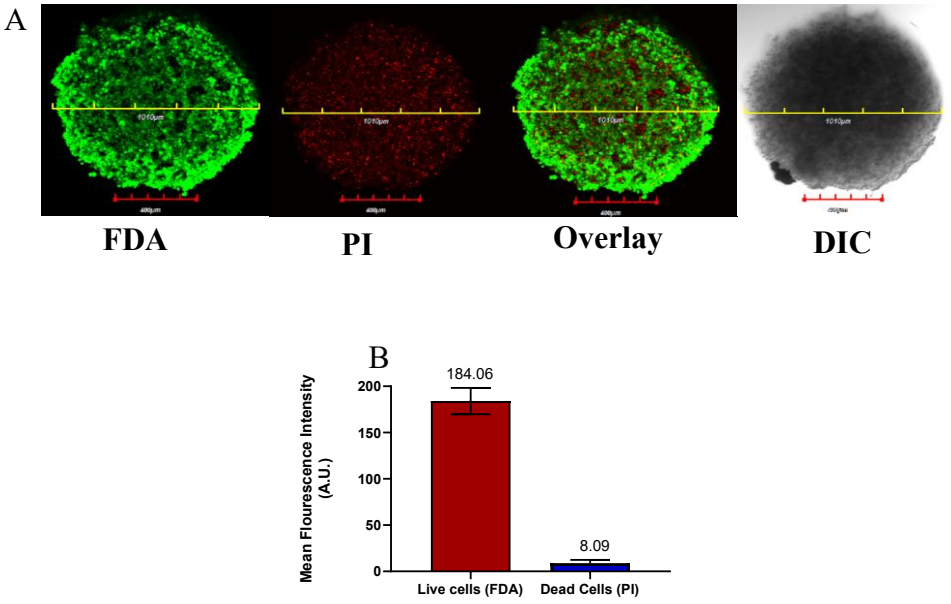

Figure 6.3 (A) Confocal images of PC3 spheroid stained with FDA and PI, scale = 300 µm, spheroid diameter = 1010 µm; (B) Bar graph

quantifying dead and live cells in PC3 spheroid is shown in (A). Error bars indicate S.D. (n=3).

6.2.3 Cytotoxicity study of tubulysin derivative 15 in a PC3 3D spheroid model

The initial cytotoxicity assessment of tubulysin derivative **15** in 2D monolayer cell culture, with an IC_{50} of 21 nM, prompted us to evaluate the potency in the PC3 3D spheroid model. The uniform and homogenous PC3 spheroids with a diameter of 900 µm were generated using the µsphere platform, as described above. The spheroids were treated with tubulysin derivative **15** and a standard tubulin inhibitor, colchicine for 48 h, and cytotoxicity was evaluated based on two parameters: (1) IC_{50} value, which was obtained using the MTT assay to determine cell viability, and (2) spheroid diameter, indicating the morphological and structural integrity of the spheroid as shown in figure 6.4. The IC_{50} values obtained after treatment indicate the cytotoxic potential of tubulin inhibitor **15** in a 3D model, with an IC_{50} of 20.43 nM, which is found to be more potent than the tubulin standard inhibitor colchicine, showing an IC_{50} of 0.84 µM, suggesting the potency of tubulysin derivative **15** even in a structurally complex 3D model (Figure 6.5). The structural and morphological analysis, based on spheroid diameter measurements, revealed a concentration-dependent reduction in spheroid size. In contrast, the untreated spheroid retained its structural compactness with well-defined boundaries.

Treatment of 3D spheroids with different concentrations of tubulysin derivative **15** demonstrated a significant morphological difference, with a reduction in diameter from 836 µm to 0 µm. At a 5 nM concentration, the spheroid treated with tubulysin derivative **15** shows a loss of structural compactness and uneven boundaries. At a higher concentration of 1 µM, the spheroids were disintegrated entirely. In contrast, treatment with colchicine reduced the spheroid diameter from 827 µm to 191 µm, with loss of compactness visible at 500 nM, and no disintegration of the spheroid was observed. The tubulysin derivative **15** has retained its biological activity in the 3D spheroid model, whereas

the standard tubulin inhibitor, colchicine, has reduced biological activity to 0.84 µM.

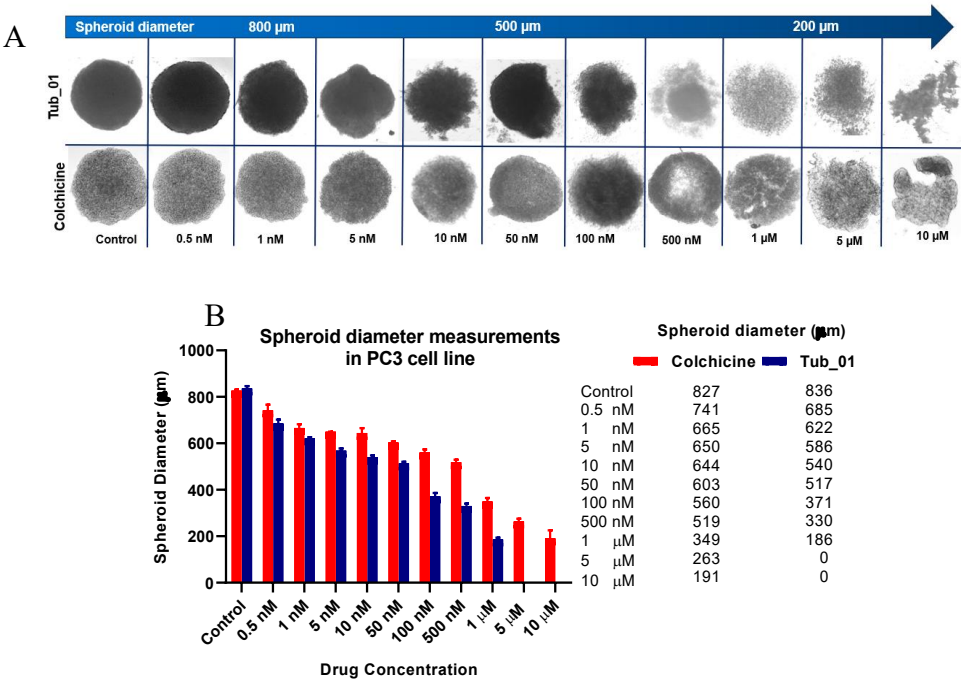

Figure 6.4 (A) Schematic illustration of morphological alteration in PC3 3D spheroids treated with various concentrations of colchicine and tubulysin derivative **15**; (B) Bar graph shows the decrease in spheroid diameter on treatment with various concentrations of colchicine and tubulysin derivative **15**. Data are expressed as mean ±S.D. (n=3).

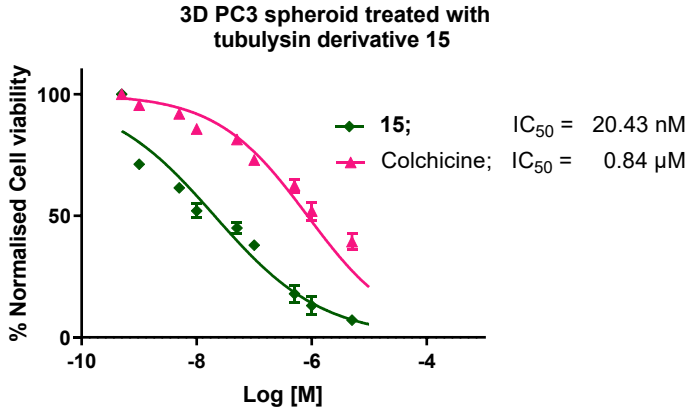

Figure 6.5 *In vitro* cytotoxicity study of tubulysin derivative **15** in a 3D PC3 spheroid model for an incubation period of 48 h, along with a standard microtubule inhibitor, colchicine. Data are expressed as mean ±S.D. (n=3).

6.2.4 Live cell and dead cell analysis of tubulysin derivative 15 in the PC3 3D spheroid model

After 48 h of incubation, spheroids treated with tubulysin derivative **15** and a standard microtubule inhibitor, colchicine, at concentrations of 1 µM, 100 nM, and 10 nM and analyzed for cell viability by staining with FDA and PI dye using two-photon confocal laser scanning microscopy (Figure 6.6). Morphological and structural alterations were evident for tubulysin derivative **15** at 10 nM, as indicated by red fluorescence in the necrotic core region, representing dead cells. At 1 µM of **15**, the spheroid lost its compactness, and most cells were non-viable as indicated by PI dye. In contrast, at 1 µM, colchicine retained its structural compactness with only 50% of the dead cell population. These data were then quantified by measuring mean fluorescence intensity, and the values obtained show an increase in MFI of PI dye from 14 A.U. to 206 A.U. for tubulysin derivative **15** compared with colchicine, which shows an increase of MFI from 14 A.U. to 87 A.U.

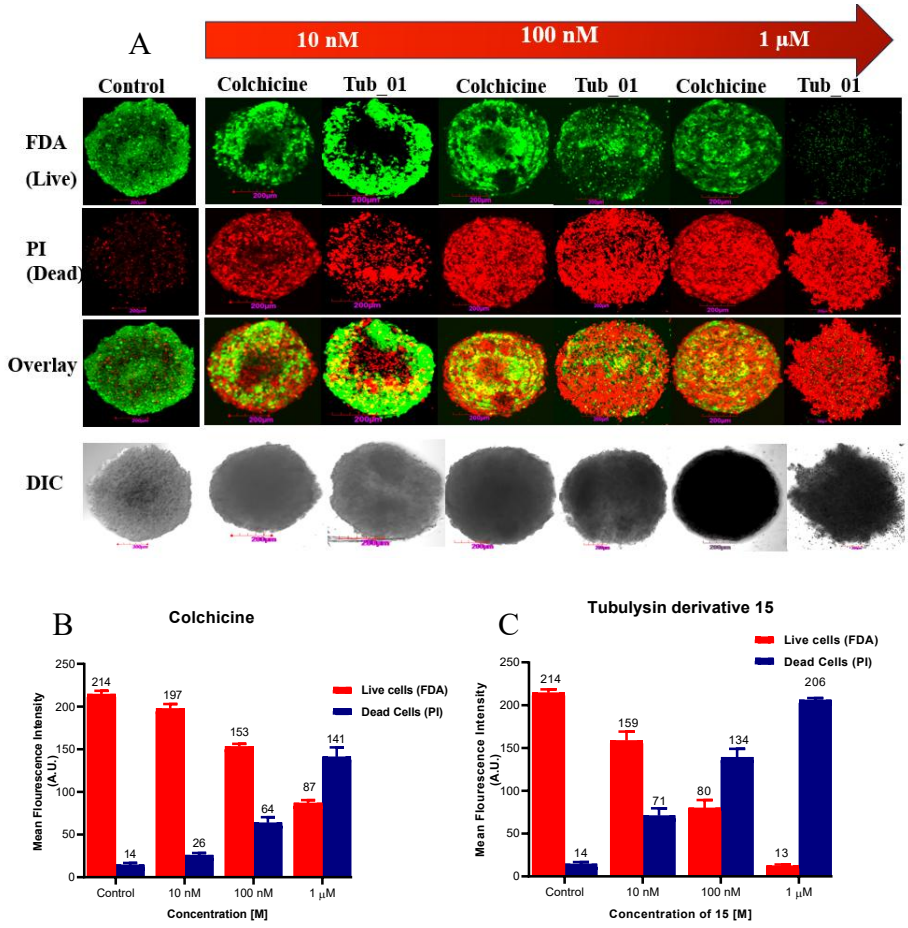

Figure 6.6 (A) A schematic illustration of cell death in PC3 3D spheroids treated with various concentrations of colchicine and tubulysin derivative **15**, as visualized through FDA and PI dyes; (B) Bar graph quantifying dead and live cells in the PC3 spheroids model treated with colchicine for 48 h, shown in (A). Error bars indicate S.D. (n=3); (C) Bar graph quantifying dead and live cells in the PC3 spheroids model treated with tubulysin derivative **15** for 48 h, as shown in (A). Error bars indicate S.D. (n=3).

6.3 Conclusion

In conclusion, we have evaluated the cytotoxic potential of novel tubulysin derivative **15** in both the conventional 2D monolayer cell culture and advanced 3D spheroid models. The transition of drug candidates from 2D analysis to 3D analysis is crucial, as 3D models more accurately mimic the tumor microenvironment by forming compact cell-cell interactions, creating nutrients and oxygen gradients, which affect drug diffusion across the tumor tissue. The reliability of 3D models in drug discovery programs has proven to significantly enhance the success rate by reducing late-stage preclinical failure of drug candidates.

The tubulysin derivative **15** has proven effective in a 2D monolayer cell culture model with an IC_{50} of 22 nM, and retained its potency in a complex 3D spheroid model with an IC_{50} of 20 nM. Suggesting its ability to penetrate the tumour architecture while retaining its ability to inhibit tubulin polymerization even in cells located at the hypoxic core of the spheroid. In contrast, the standard microtubule tubulin inhibitor, colchicine, shows a marked reduction in cytotoxic activity, with its IC_{50} increasing from 277 nM in the 2D model to 0.84 μM in the 3D model, indicating poor penetration and limited tubulin inhibition. Furthermore, post-treatment structural analysis of spheroids with tubulysin derivative **15** revealed a decrease in the spheroid diameter and loss of structural compactness, ultimately disrupting spheroid architecture. The tubulin inhibitor **15** has retained the cytotoxic activity in the 3D model,

highlighting its potential as a promising candidate for *in vivo* validation and clinical translation.

6.4 Experimental section

6.4.1 General methods and materials

Chlorotrityl resins, Fmoc-protected amino acids, coupling reagents, chemicals, and solvents used for chemical synthesis of fragments and solid phase peptide synthesis (SPPS) were procured from Iris Biotech GmbH, Sigma Aldrich, Merck, Spectrochem, TCI, and Expressolv. Dry solvents were prepared using suitable drying agents and standard procedures. All reactions were performed in oven-dried glasswares, and the moisture-sensitive reactions were performed under a nitrogen atmosphere. Solutions were transferred using a glass syringe. The progress of the reaction was monitored by thin-layer chromatography (TLC) using silica gel 60 F254 TLC plates and visualized under a UV chamber. The compounds **3**, **5**, and **6** were purified by column chromatography using 230–400 mesh silica gel as the stationary phase with distilled hexane and ethyl acetate as eluents. Tubulysin derivative **15** was synthesized manually using a peptide vessel (Chemglass) and following the standard peptide coupling procedures. The ^{1}H and ^{13}C NMR spectra were recorded using a Bruker AV 500 MHz NMR spectrometer with TMS as an internal standard. The ^{1}H NMR signals were reported in ppm with reference to residual $CDCl_3$ (7.26 ppm), DMSO-d_6 (2.50 ppm), MeOH-d_4 (3.31 ppm), and multiplicities were reported as s = singlet, d = doublet, t = triplet, q = quartet, m = multiplet or unresolved, and brs = broad singlet, with coupling constants in Hz. $CDCl_3$ and DMSO-d_6 were used as solvents for recording the NMR spectra. Tubulysin derivative **15** was obtained as a salt of TFA. Mass spectra were recorded on a Bruker Micro TOF-Q II instrument using positive mode electrospray ionization methods. The tubulysin derivative **15** was purified using a RP-PFP column (XSelect CSH Prep Fluorophenyl 5 μm OBD, 19 mm × 150 mm) in a Buchi Reveleris High Performance Preparative Chromatography instrument. The purity of

tubulysin derivative **15** was analysed using a Dionex HPLC-Ultimate 3000 Analytical HPLC instrument.

6.4.2 Synthesis of 4-methoxybenzyl 2-aminothiazole-4-carboxylate (3)

In a single-neck round-bottom flask (25 mL), 2-aminothiazole-4-carboxylic acid **1** (500 mg, 3.46 mmol) and sodium carbonate (735 mg, 6.93 mmol) were suspended in dry DMF (5 mL). 4-Methoxybenzyl chloride **2** (0.93 mL, 6.93 mmol) was then added dropwise at room temperature using a glass syringe (1 mL) over a period of 3 min. The reaction was continued to stir for 16 h under an inert atmosphere. After the completion of the reaction, as monitored by TLC using EtOAc and hexane (1:1) as eluent, the reaction mixture was diluted with EtOAc (1 × 10 mL) and quenched with chilled brine (1 × 10 mL). The aqueous layer was further extracted with EtOAc (3 × 10 mL). The organic layer was collected and dried over anhydrous Na_2SO_4, filtered, concentrated, and purified through silica gel (neutral 230–400 mesh) column chromatography using 40% EtOAc in hexane solvent mixture as eluent. Yield 56% (520 mg); Pale yellow solid; R_f = 0.36 (hexane/EtOAc 1:1); m.p. 202–204 °C; ^{1}H NMR (500 MHz, DMSO-d_6) δ 7.88 (s, 2H), 7.70 (s, 1H), 7.33 (d, *J* = 8.6 Hz, 2H), 6.93 (d, *J* = 8.6 Hz, 2H), 5.14 (s, 2H), 3.75 (s, 3H); ^{13}C NMR (125 MHz, DMSO-d_6) δ 173.62, 161.28, 159.20, 148.26, 129.91, 128.24, 114.26, 113.90, 65.39, 55.14; IR 2956–2919 (=C–H), 2849 (C–H), 1713 (C=O), 1515–1450 (C=C), 1255–1086 (C–O), 1019 (=C–H bend), 799 (C–N) cm^{-1}; HRMS (+ESI) m/z calcd. for [$C_{12}H_{12}N_2O_3S$] $[M+Na]^+$, 287.0461, found, 287.0475.

6.4.3 Synthesis of 4-methoxybenzyl (S)-2-(2-((((9H-fluoren-9-yl)methoxy)carbonyl) amino)-3-methylbutanamido)thiazole-4-carboxylate (5)

In a single-neck round-bottom flask (25 mL), Fmoc-valine **(4)** (500 mg, 1.47 mmol) was dissolved in dry DCM (5 mL). EDC.HCl (563 mg, 2.94 mmol), HOBt (397 mg, 2.94 mmol), and 4-methoxybenzyl 2-aminothiazole-4-carboxylate **(3)** (465 mg, 1.76 mmol) were sequentially

added to the suspension at room temperature. The reaction mixture was further stirred for 16 h at room temperature under an inert atmosphere. After the completion of the reaction, as monitored by TLC using hexane and EtOAc (8:2) as eluent, the reaction mixture was diluted with DCM (1 × 10 mL) and quenched with 1N HCl (1 × 10 mL). The aqueous layer was further extracted with DCM (3 × 10 mL). The organic layer was collected, washed with brine (1 × 5 mL), dried over anhydrous Na_2SO_4, filtered, concentrated, and purified by silica gel (neutral, 230–400 mesh) column chromatography using 30% EtOAc in hexane as eluent. Yield 75% (860 mg), White solid upon standing; R_f = 0.36 (hexane/EtOAc 8:2); m.p. 321–323 °C; ^{1}H NMR (500 MHz, $CDCl_3$) δ 11.46 (s, 1H), 8.01 (s, 1H), 7.72 (d, *J* = 7.7 Hz, 2H), 7.55 (t, *J* = 6.9 Hz, 2H), 7.37–7.34 (m, 4H), 7.26 (t, *J* = 6.9 Hz, 2H), 6.89 (d, *J* = 7.7 Hz, 2H), 6.03–5.94 (m, 1H), 5.25 (s, 2H), 4.54–4.48 (m, 3H), 4.20 (t, *J* = 7.0 Hz, 1H), 3.80 (s, 3H), 2.18–2.10 (m, 1H), 0.97–0.94 (m, 6H); ^{13}C NMR (125 MHz, $CDCl_3$) δ 171.29, 162.26*, 161.98, 156.97, 144.61, 143.80, 143.70, 141.21*, 127.80, 127.08*, 125.11, 123.10, 120.05, 67.69, 60.40, 53.54, 52.31, 47.16, 31.61, 19.26, 18.26 (*higher intensity signals); IR 3299 (N–H), 2956-2872 (=C–H), 2465 (C–H), 1682 (C=O), 1536 (C=O), 1510 (C=O), 1243 (C–O), 1185 (=C–H bend), 737 (C–N) cm^{-1}; HRMS (+ESI) m/z calcd. for $[C_{32}H_{31}N_3O_6S]$ $[M+H]^+$, 586.2006, found, 586.2006.

6.4.4 Synthesis of (*S*)-2-(2-((((9H-fluoren-9-yl)methoxy)carbonyl) amino)-3-methyl butanamido) thiazole-4-carboxylic acid (6)

In a single-neck round bottom flask (25 mL), 4-methoxybenzyl (S)-2-(2-(((9H-fluoren-9-yl)methoxy)carbonyl)amino)-3-methylbutanamido) thiazole-4-carboxylate **(5)** (1 g, 1.70 mmol) was dissolved in DCM (2 mL), followed by addition of 20% TFA in DCM (10 mL) to the reaction mixture at room temperature, and the reaction was stirred for 1.5 h. After the completion of the reaction, as monitored by TLC using hexane and EtOAc (1:1) as eluent, TFA was evaporated under reduced pressure. The reaction mixture was then diluted with EtOAc (1 × 10 mL) and washed with Millipore water (1 × 10 mL). The aqueous layer was further

extracted with EtOAc (3 × 10 mL). The organic layer was collected and dried over anhydrous Na_2SO_4, filtered, concentrated, and purified through silica gel (neutral 230–400 mesh) using 100% EtOAc. Yield 98% (785 mg); White solid upon standing; R_f = 0.23 (hexane/EtOAc 1:1); m.p 280–282 °C; ^{1}H NMR (500 MHz, DMSO-d_6) 12.67 (s, 1H), 8.07 (s, 1H), 7.87 (d, *J* = 7.6 Hz, 2H), 7.81 (d, *J* = 8.3 Hz, 1H), 7.73 (t, *J* = 7.8 Hz, 2H), 7.4 (t, *J* = 7.8 Hz, 2H), 7.33–7.29 (m, 2H), 4.31–4.20 (m, 3H), 4.16 (t, *J* = 7.9 Hz, 1H), 2.09–2.03 (m, 1H), 0.92 (d, *J* = 7.0 Hz, 3H), 0.89 (d, *J* = 7.0 Hz, 3H); ^{13}C NMR (125 MHz, DMSO-d_6) δ 171.75, 162.98, 161.57, 156.45, 144.74, 143.85, 140.80, 127.81, 127.19, 125.45, 123.07, 120.23, 65.94, 60.33, 46.75, 30.13, 19.10, 18.57; IR 3334 (O–H) 3303 (N–H), 3081–2925 (=C–H), 2853 (C–H) 1668 (C=O), 1489 (C=C), 1206 (C–O), 1080 (=C–H bend), 1031 (C–N bend) cm^{-1}; HRMS (+ESI) m/z calcd. for $[C_{24}H_{23}N_3O_5S]$ $[M+H]^+$, 466.1437, found, 466.1473.

6.4.5 Synthesis of (*R*)-1-methylpiperidine-2-carboxylic acid (8)

In a double-neck round-bottom flask (25 mL), a hydrogen-filled bladder was fitted to one neck of the round-bottom flask through a borosilicate glass heavy-wall glass stop cock adapter. Pipecolic acid **7** (100 mg, 0.77 mmol) and formaldehyde (120 µL, 1.54 mmol%) were added to the round-bottom flask and dissolved in methanol (2 mL). 10% Pd/C (81.94 mg, 10 mol%) was added slowly to the mixture, and the reaction mixture was sealed using a rubber septum. The residual air in the reaction vessel was expunged through a syringe needle inserted through the rubber septum that is connected to a filtration pump through a silicone tube for 2 minutes or until the solution starts bubbling. The reaction mixture is now filled with hydrogen gas from the bladder via a stop cock and allowed to stir at room temperature for 24 h. After the completion of the reaction as monitored by TLC using MeOH and DCM (1:1) as eluent, the reaction mixture was diluted with MeOH (15 mL) and filtered through a celite powder filled sintered Buchner funnel with inner joint fitted to a round bottom flask (50 mL) to remove the palladium/charcoal with the help of a suction pump. The celite pad was washed with MeOH

(3 × 3 mL), and the filtrate was concentrated under reduced pressure. Yield 99% (109 mg); White solid; R_f = 0.21 (MeOH/DCM 1:1); m.p 101–103 °C; ^{1}H NMR (500 MHz, MeOH-d_4) δ 3.47–3.37 (m, 2H), 3.01 (t, *J* = 8.3 Hz, 1H), 2.88 (s, 3H), 2.23 (d, *J* = 13.4 Hz, 1H), 1.89–1.83 (m, 2H), 1.79–1.74 (m, 2H), 1.59–1.52 (m, 1H); ^{13}C NMR (125 MHz, MeOH-d_4) δ 173.55, 70.42, 55.28, 43.17, 29.52, 24.05, 22.66; IR 2936 (O–H), 2862 (C–H) 1606 (C=O), 1317 (C–C), 1173 (C–O), 1004 (C–N) cm^{-1}; HRMS (+ESI) m/z calcd. for $C_7H_{13}NO_2$ $[M+H]^+$, 144.1019, found, 144.1023.

6.4.6 General procedure of solid-phase peptide synthesis

6.4.6.1 Resin swelling

The resins used in solid phase synthesis were first swollen with DCM (5 mL) for 30 minutes by bubbling nitrogen gas through the beads in the peptide vessel. After draining DCM, the beads were swollen with DMF (3 × 5 mL), repeating the process for 15 minutes.

6.4.6.2 General procedure for the Kaiser test

Kaiser test kit preparation reagents

a) Dissolve 500 mg of ninhydrin in 10 mL of ethanol

b) Dissolve 80 g of phenol in 20 mL of ethanol

c) Dilute 2 mL of 0.001M solution of KCN to 100 mL with pyridine

Add two drops each of the above solutions to a few dried resin beads in a glass test tube and heat at 110 °C in a sea sand bath for 2-3 minutes. The freshly prepared Kaiser test kit can be stored at room temperature for 6 months without decomposition. The appearance of dark blue indicates the presence of free amine groups in the resin beads, indicating the deprotection of the Fmoc group, while the colourless beads signify the absence of the amine group, indicating the completion of the coupling reaction. The test was performed after coupling each amino acid, as well as after the deprotection of the Fmoc group at each step.

6.4.6.3 General procedure for Fmoc deprotection

The Fmoc group of the N-terminus of the growing peptide chain was deprotected using 20% piperidine in DMF (10 mL) by bubbling nitrogen

gas through the resin beads for 10 minutes in each step of Fmoc deprotection. The procedure was repeated three times (1 × 4 mL; 2 × 3 mL) to ensure the complete deprotection of the Fmoc group.

6.4.6.4 General procedure for peptide cleavage from resin beads

The peptide was cleaved from the resin beads using 10 mL of cleavage cocktail (a mixture of 9.5 mL trifluoroacetic acid, 0.25 mL triisopropylsilane, and 0.25 mL water) by bubbling nitrogen gas through the resin. First, 5 mL of the cocktail was added to the resin, and nitrogen gas was bubbled for 30 minutes, followed by the addition of the cocktail solution (2 × 2.5 mL), with nitrogen bubbling for 5 minutes each time. The collected mother liquor after peptide cleavage was evaporated under reduced pressure, and the concentrated solution was precipitated in ice-cold diethyl ether. The precipitate was then dried using nitrogen gas, and the obtained crude product was further purified using HPLC.

6.4.6.5 Procedure for solid phase peptide synthesis of tubulysin derivative 15

H-Asn(Trt)-2-ClTrt resin **11** (0.300 g, 0.168 mmol) was initially swollen in DCM (1 × 5 mL), followed by DMF (1 × 5 mL) for 15 min each. The solvent was drained using a filtration pump, and the beads were dried until free-flow. Fmoc-Val-thiazole-OH **6** (0.156 g, 0.336 mmol), PyBOP (0.174 g, 0.336 mmol), and DIPEA (0.293 mL, 1.68 mmol) were dissolved in DMF (0.5 mL) in a 2 mL glass vial, mixed thoroughly using a Pasteur pipette, transferred to the peptide vessel containing resin beads and the coupling reaction was carried out for 6 h by bubbling a stream of nitrogen gas through the resin beads in the peptide vessel. The resin beads were then washed with DMF (3 × 5 mL) followed by isopropanol (3 × 5 mL) for 10 min each. The solvent was drained using a filtration pump, and the beads were dried until free-flow by bubbling N_2 gas through the peptide vessel. The amide coupling was confirmed by performing the Kaiser test to obtain dipeptide **12**. Next, the FmocNH protecting group was cleaved by addition of 20% piperidine in DMF (1 × 4 mL; 2 × 3 mL) for 10 min each to the resin beads. The resin beads

were washed with DMF (3 × 5 mL) and isopropanol (3 × 5 mL). The solvent was drained using a suction pump, and the beads were dried until freely flowing by bubbling N_2 gas through the resin beads in the peptide vessel. The Kaiser test was performed to confirm the deprotection of the Fmoc group. The next amino acid Fmoc-Ile-OH **9** (0.118 g, 0.336 mmol), PyBOP (0.174 g, 0.336 mmol), and DIPEA (0.293 mL, 1.68 mmol) were dissolved in DMF (0.5 mL) in a 2 mL glass vial, mixed thoroughly using a Pasteur pipette, transferred to the peptide vessel containing resin beads and the coupling reaction was continued for 6 h to obtain tripeptide **13**. As mentioned earlier, the FmocNH protecting group was cleaved by addition of 20% piperidine in DMF. Finally, 1-methylpiperidine-2-carboxylic acid **8** (0.048 g, 0.336 mmol), PyBOP (0.174 g, 0.336 mmol), and DIPEA (0.293 mL, 1.68 mmol) dissolved in DMF (0.5 mL) in a 2 mL glass vial was added to the tripeptide **13** to accomplish the amide coupling, followed by resin cleavage using a cocktail solution of TFA:TIPS:H_2O (9.5:0.25:0.25) (1 × 5 mL; 2 × 2.5 mL) as described earlier. The mother liquor was collected in a 25 mL round-bottom flask from the peptide vessel, transferred to a 15 mL centrifuge tube, and fitted with a septum. The crude peptide solution was concentrated under reduced pressure to evaporate TFA by inserting a 19-gauge stainless steel needle through the rubber septum. Ice-cold diethyl ether was added to precipitate the tubulysin derivative **15** as a white solid, washed with ice-cold diethyl ether (3 × 5 mL), dried by passing a stream of nitrogen gas for 15 minutes, and purified using reverse-phase high-performance liquid chromatography (RP-HPLC).

6.4.7 Preparative RP-HPLC method

Tubulysin derivative **15** was purified using a Buchi Reveleris Prep RP-HPLC system. Crude tubulysin derivative **15** (40 mg) was dissolved in a mixture of CH_3CN:H_2O (1 mL, 1:1) and injected into the sample injector for elution using RP-PFP (Reverse Phase PentafluoroPhenyl) preparative column (XSelect CSH Prep Fluorophenyl 5 µm; 19 × 150 mm). A flow rate of 10 mL/min (mobile phase, A = 0.1% trifluoroacetic acid in H_2O and B = acetonitrile) is maintained throughout the run, and

the mobile phase gradient was gradually increased from 1% B (v/v) to 50% B (v/v) over a period of 25 min. The mobile phase gradient was further increased to 90% B (v/v) in another 10 min, and the chromatograms were recorded at λ = 210, 240, and 280 nm with a retention time of t_R = 12.7 for tubulysin derivative **15**. Pure fractions of tubulysin derivative **15** were collected using an automatic fraction collector, the organic solvent was evaporated under reduced pressure using a rotary evaporator, and the aqueous solution was lyophilized for 48 h to yield tubulysin derivative **15**. yield 52% (53 mg); White solid; ^{1}H NMR (500 MHz, DMSO-d_6) δ 12.50 (s, 1H), 9.65 (s, 1H), 8.77 (d, *J* = 7.5 Hz, 1H), 8.71 (d, *J* = 7.9 Hz, 1H), 8.36 (d, *J* = 7.8 Hz, 1H), 8.11 (s, 1H), 7.40 (s, 1H), 6.93 (s, 1H), 4.67 (q, *J* = 7.9 Hz, 1H), 4.42 (t, *J* = 7.5 Hz, 1H), 4.32 (t, *J* = 7.8 Hz, 1H), 3.35 (d, *J* = 12.2 Hz, 1H), 3.07–3.01 (m, 1H), 2.69–2.64 (m, 4H), 2.57–2.53 (m, 1H), 2.11–2.02 (m, 2H), 1.79–1.74 (m, 3H), 1.71–1.55 (m, 2H), 1.43–1.36 (m, 2H), 1.14–1.07 (m, 1H), 0.91 (d, *J* = 6.7 Hz, 3H), 0.88 (d, *J* = 6.7 Hz, 3H), 0.84 (d, *J* = 6.7 Hz, 3H), 0.8 (t, *J* = 7.3 Hz, 3H); ^{13}C NMR (125 MHz, DMSO-d_6) δ 172.83, 171.19, 170.97, 170.65, 167.72, 160.54, 160.11, 139.95, 127.34, 65.96, 58.03, 57.05, 54.39, 49.38, 41.41, 36.55, 36.48, 30.14, 28.45, 24.19, 22.31, 21.00, 18.94, 18.27, 15.26, 10.83; HRMS (+ESI) (m/z) calcd. for $[C_{26}H_{41}N_7O_7S]$, $[M+H]^+$ 596.2861; found, 596.2863.

6.4.8 Culture of cancer cell lines

PC3 cancer cell line was procured from the National Centre for Cell Sciences (NCCS), Pune, India. The cell line was grown in T-75 Flask (Tarson, 950040) containing sterile filtered RPMI 1640 medium (Thermo Fisher, 11875093) supplemented with fetal bovine serum (Thermo Fisher, 1027016), 100 mM of sodium pyruvate (Thermo Fisher, 11360070), non-essential amino acid (Thermo Fisher, 11140050), and 1% penicillin streptomycin (Thermo Fisher, 15140122) under 37 °C and 5% CO_2 to form a monolayer until 60% confluency. The cells were trypsinized using 0.25% trypsin-EDTA (Thermo Fisher, 15050065), collected, and centrifuged at 800 rpm for 5 min. The

obtained cell pellet was resuspended in fresh medium and used for cytotoxicity assay and spheroid generation.

6.4.9 *In vitro* cytotoxicity assay of tubulysin derivative 15

PC3 5000 cells/well were seeded in a 96-well plate and allowed to form a monolayer of 60% confluency over a period of 48 h. The spent medium was discarded, and cells were washed with 1X PBS (1 × 200 µL). Fresh medium (200 µL) containing tubulysin derivative **15** at various concentrations (0.5 nM, 1 nM, 5 nM, 10 nM, 50 nM, 100 nM, 500 nM, 1 µM, 5 µM, 10 µM 0.5 nM) along with colchicine as a standard, were added into the wells in triplicate. The cells were further incubated for 48 h in a CO_2 incubator. After 48 h incubation, the spent medium was discarded, and the cells were washed carefully with 1X DPBS (2 × 200 µL). 50 µL of MTT solution (5 mg/mL) was added to each well, plates were then carefully wrapped with aluminium foil and incubated at 37 °C and 5% CO_2 for 4 h. After incubation, the MTT solution was carefully aspirated using a pipette, and DMSO (200 µL) was added to each well to dissolve the formazan crystals. The absorbance from each well corresponding to live cells was measured using a Synergy H4 multiplate reader at a wavelength of 570 nm. Dose vs response curves were obtained from a plot of log[concentration] vs % cell viability, and IC_{50} values were calculated using GraphPad Prism 8.01.

6.4.10 Generation and characterization of PC3 3D spheroid model

Agarose (1.5 g, low EEO) was weighed on a weighing balance and transferred to a 250 mL reagent bottle containing 100 mL 1X DPBS buffer pH 7.4. Agarose solution, a wooden hairbrush (bristle diameter 2000 µm), a stainless-steel spatula, a blade, and a petri plate were wrapped in aluminium foil and sterilised using an autoclave. The molten agarose was immediately poured into a glass Petri dish, and a wooden brush was immersed in the molten agarose, allowing 3/4th of the spherical tips to be immersed. The setup was left undisturbed for 20 min. The comb was then gently removed, and rows of distantly placed microwells, with a diameter of 1800 µm, were generated. The agarose

μsphere platform was then cut into sections, each containing 15–20 microwells. These sections were then carefully transferred into a 6-well plate and subjected to sterilisation under UV for 45 min. After sterilisation, RPMI 1640 media (3 mL) was added to each well for fabrication. The spent media was removed using a 200 μL micropipette from each microwell. The PC3 cells grown in a T-75 flask were trypsinized using 0.25% trypsin-EDTA, collected, and centrifuged at 800 rpm for 5 min. The cell pellet was resuspended in a fresh medium (100 μL-500 μL) depending on the total number of spheroids required for an experiment. 25,000 cells in 5 μL media were added to each microwell carefully. After the addition of cells to each microwell, medium (3 mL) was added to immerse the agarose chip with seeded cells, and the chip was carefully relocated to a CO_2 incubator at 37 °C and 5% CO_2 for 24 h to allow spheroid formation. After the formation of spheroids, the spheroids were harvested using 1 mL cut microtips and transferred to a 1.5 mL Eppendorf. The spheroids (n = 5) were immersed in a fresh medium (500 μL) containing fluorescein diacetate (FDA, 5mg/mL) and propidium iodide (PI, 2 mg/mL) without FBS and stored under dark conditions inside a CO_2 incubator at 37 °C and 5% CO_2 for 15 min. After 15 min, the spheroids were rinsed with PBS (3 × 1 mL) and transferred into Nunc™ Lab-Tek™ II Chambered Coverglass for imaging using confocal laser scanning microscopy. The imaging parameters were set as follows: FDA, λex 488 nm, and emission collection range 500–560 nm, and for PI, λex 559 nm, emission collection range 575–675 nm. Z-Scan imaging parameter: Z-dimension is 4266.18–4370.78 μm, 9.51 μm per slice. Images were processed using Olympus Fluoview ver.4.2.

6.4.11 Cytotoxicity study of tubulysin derivative 15 in PC3 3D spheroid model

The PC3 spheroids generated using the aforementioned procedure were transferred into a 24-well plate with one spheroid per well. Fresh medium (1 mL) containing tubulysin derivative **15** at various concentrations (0.5 nM, 1 nM, 5 nM, 10 nM, 50 nM, 100 nM, 500 nM,

1 μM, 5 μM, 10 μM), along with a standard inhibitor, colchicine, were added to the wells in triplicate. The cells were further incubated for 48 h. After 48 h incubation, the spent medium was discarded, and the spheroids were washed carefully with 1X DPBS (2 × 200 μL) followed by the addition of MTT solution (200 μL, 5 mg/mL). The plates were carefully wrapped with aluminium foil and incubated at 37 °C and 5% CO_2 for 4 h. After incubation, MTT solution was carefully aspirated using a pipette, and DMSO (500 μL) was added to each well to dissolve the formazan crystals. The absorbance from each well corresponding to live cells was measured using a Synergy H4 multiplate reader at a wavelength of 570 nm. Dose vs response curves were obtained from a plot of log[concentration] vs % cell viability, and IC_{50} values were calculated using GraphPad Prism 7.04. The morphological structural analysis was carried out by imaging the spheroid under an inverted microscope at 5X, and the corresponding diameter of the treated spheroids was determined using MagCam 5 software, and a graph was plotted using GraphPad Prism 7.04.

5.4.12 Live cell and dead cell analysis of tubulysin derivative 15 in PC3 3D spheroid model

After the treatment of spheroids (n = 3) with tubulysin derivative **15** and colchicine at various concentrations, such as 10 nM, 100 nM, and 1 μM for 48 h, the treated spheroids were analyzed for cell viability. The treated spheroids were immersed in a fresh medium (500 μL) containing fluorescein diacetate (FDA, 5mg/mL) and propidium iodide (PI, 2 mg/mL) without FBS and stored under dark conditions inside a CO_2 incubator at 37 °C and 5% CO_2 for 15 min. After 15 min, the spheroids were rinsed with PBS (3 × 1 mL) and transferred into Nunc™ Lab-Tek™ II Chambered Coverglass for imaging using confocal laser scanning microscopy. The imaging parameters were set as follows: FDA, λex 488 nm and emission collection range 500–560 nm, and for PI, λex 559 nm, emission collection range 575–675 nm. Z-Scan imaging parameter: Z-dimension is 5378.06–5488.66 μm, 7.65 μm per slice. Images were analysed using Olympus Fluoview ver.4.2. The mean

fluorescent intensity was determined using Image J software, and a graph was plotted using GraphPad Prism 7.04. "Z Dimension".

6.4.13 Copies of ^{1}H, ^{13}C NMR, and HRMS spectra

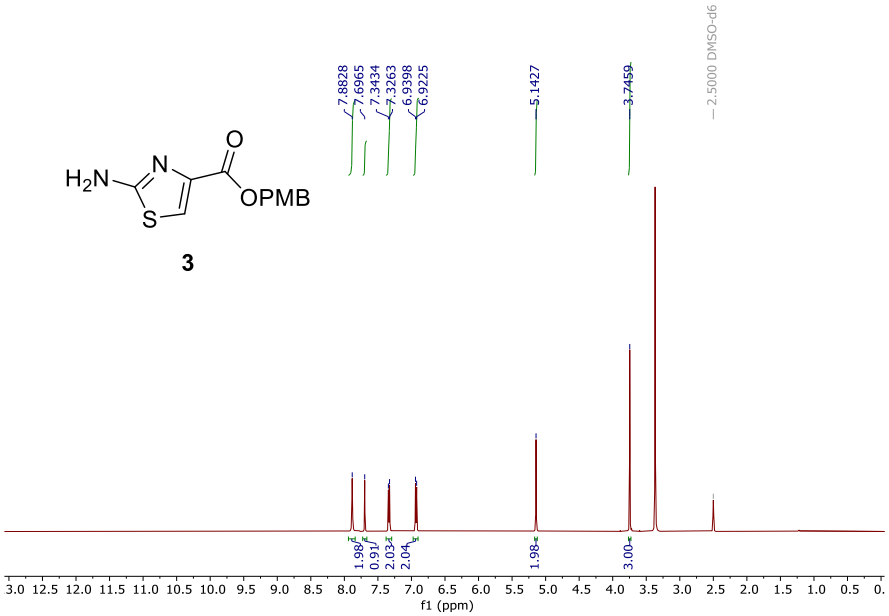

Figure 6.7 ^{1}H NMR spectrum (500 MHz, DMSO-d_6) of **3**.

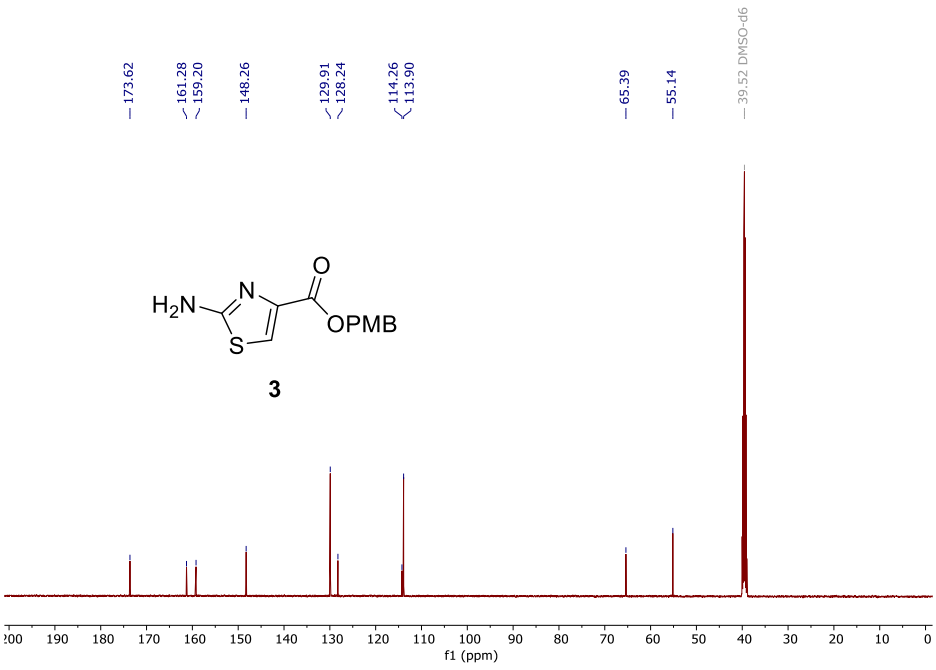

Figure 6.8 ^{13}C NMR spectrum (125 MHz, DMSO-d_6) of **3**.

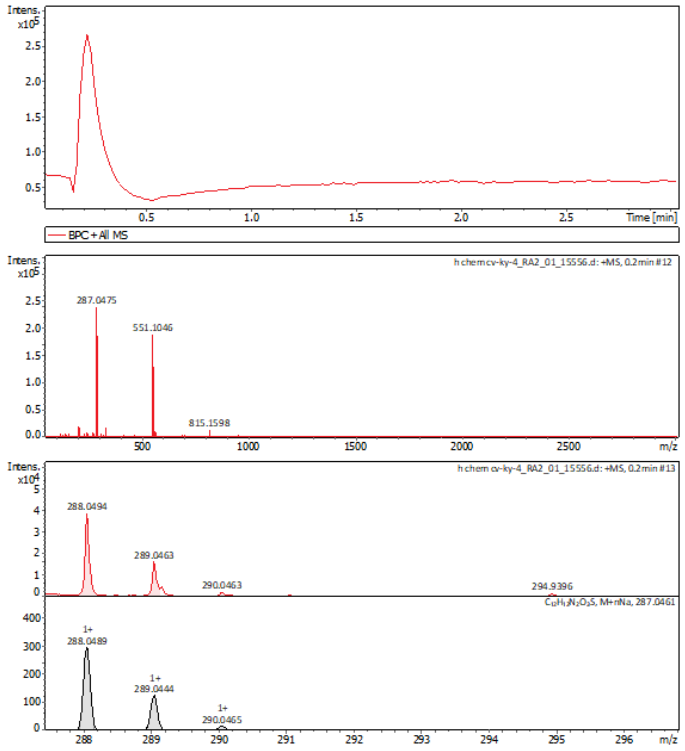

Figure 6.9 HRMS of **3**.

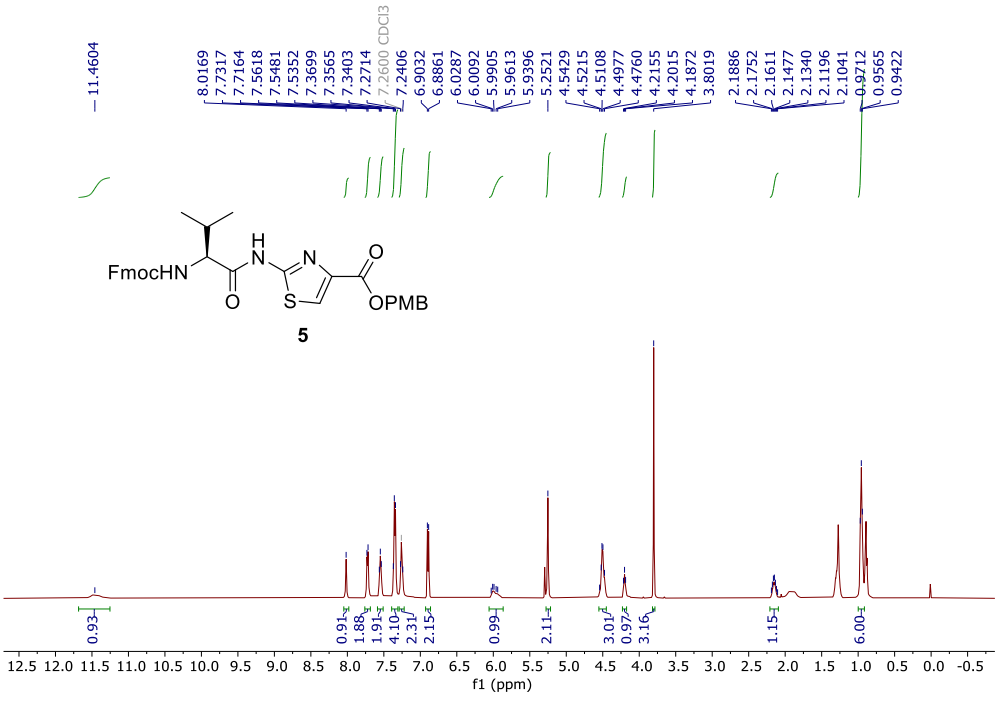

Figure 6.10 ^{1}H NMR spectrum (500 MHz, DMSO-d_6) of **5**.

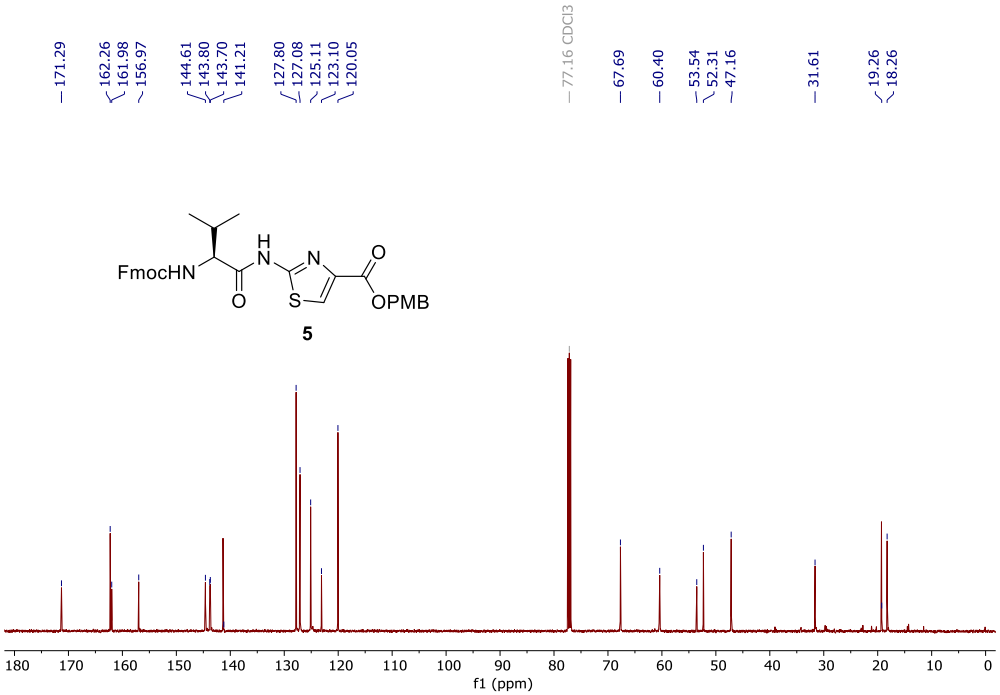

Figure 6.11 ^{13}C NMR spectrum (125 MHz, DMSO-d$_6$) of **5**.

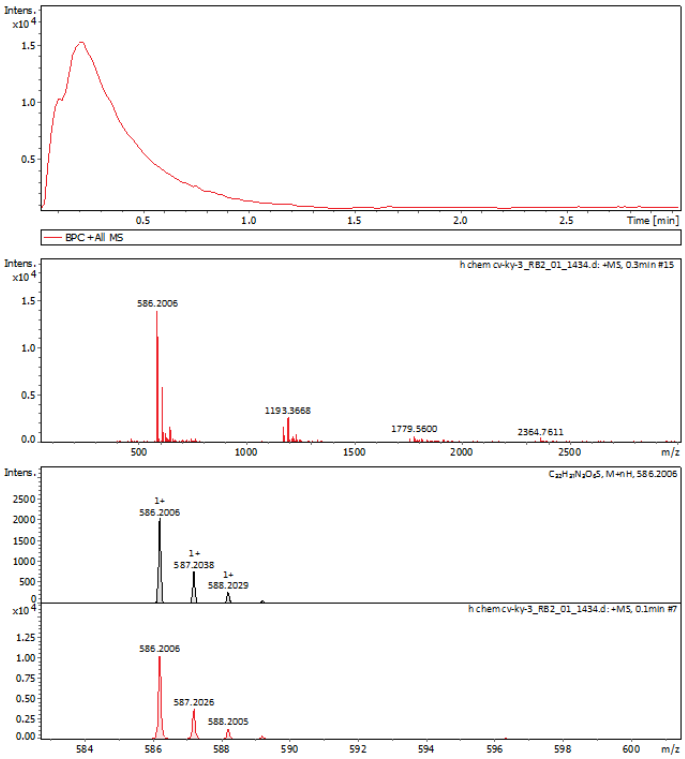

Figure 6.12 HRMS of **5**.

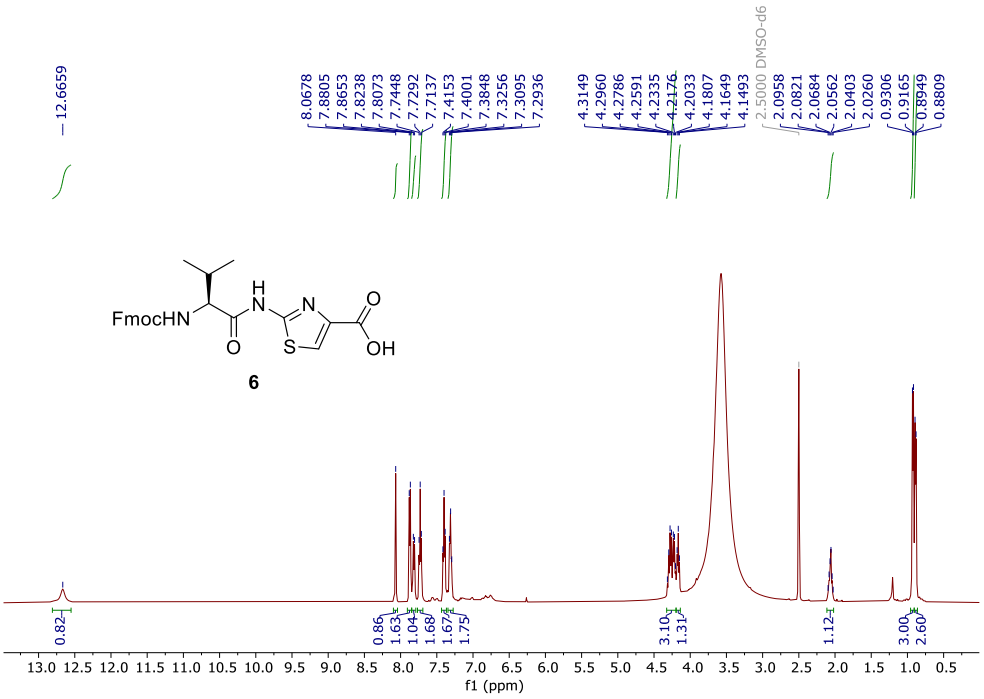

Figure 6.13 ^{1}H NMR spectrum (500 MHz, DMSO-d_6) of **6**.

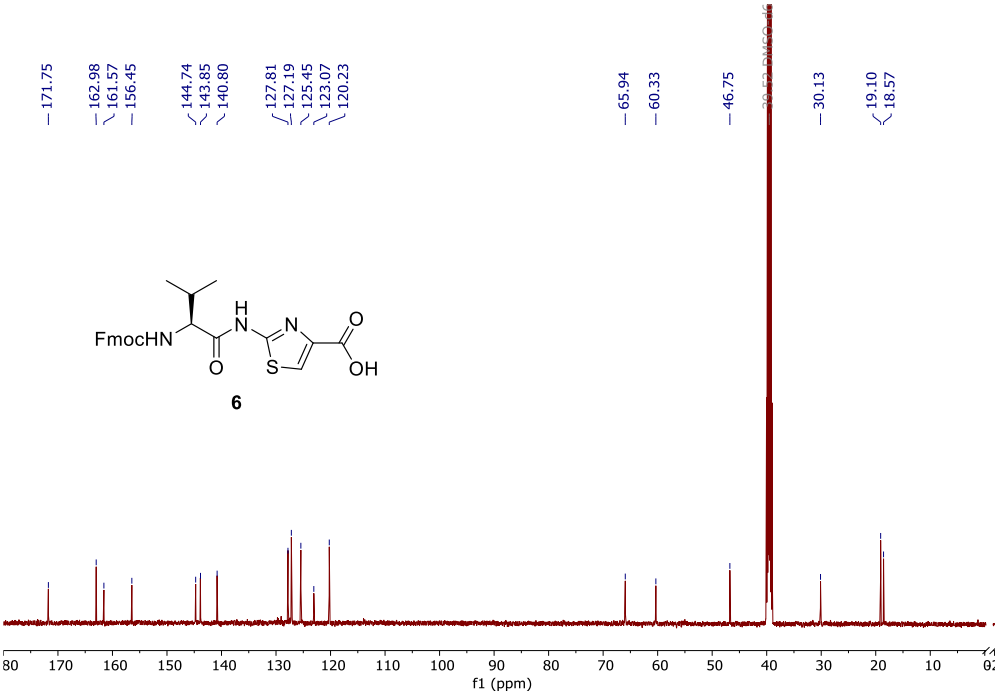

Figure 6.14 ^{13}C NMR spectrum (125 MHz, DMSO-d_6) of **6**.

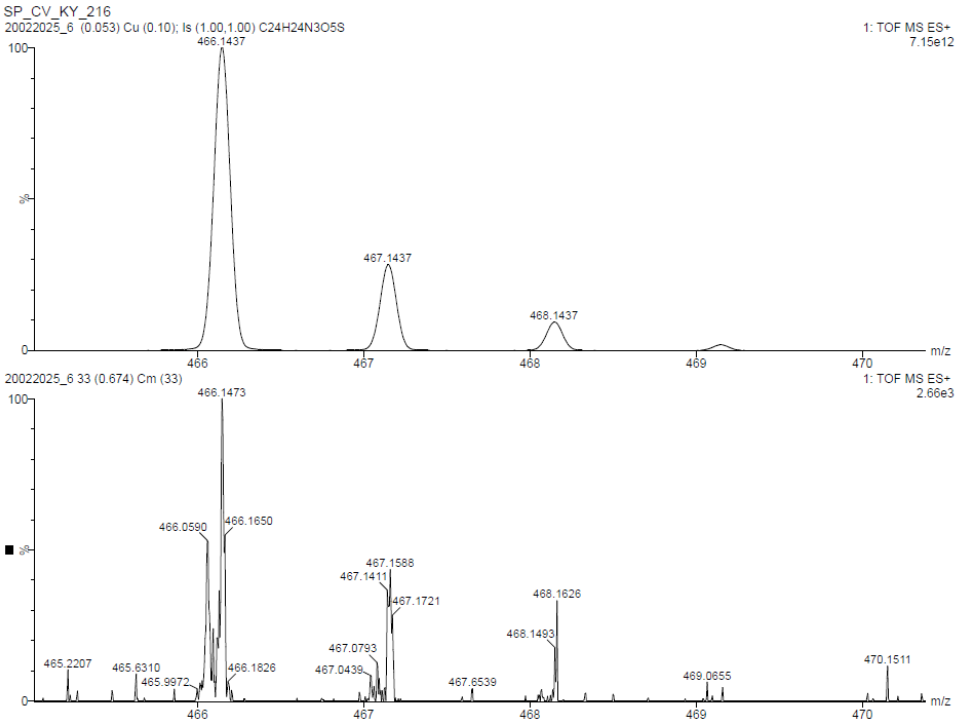

Figure 6.15 HRMS of **6**.

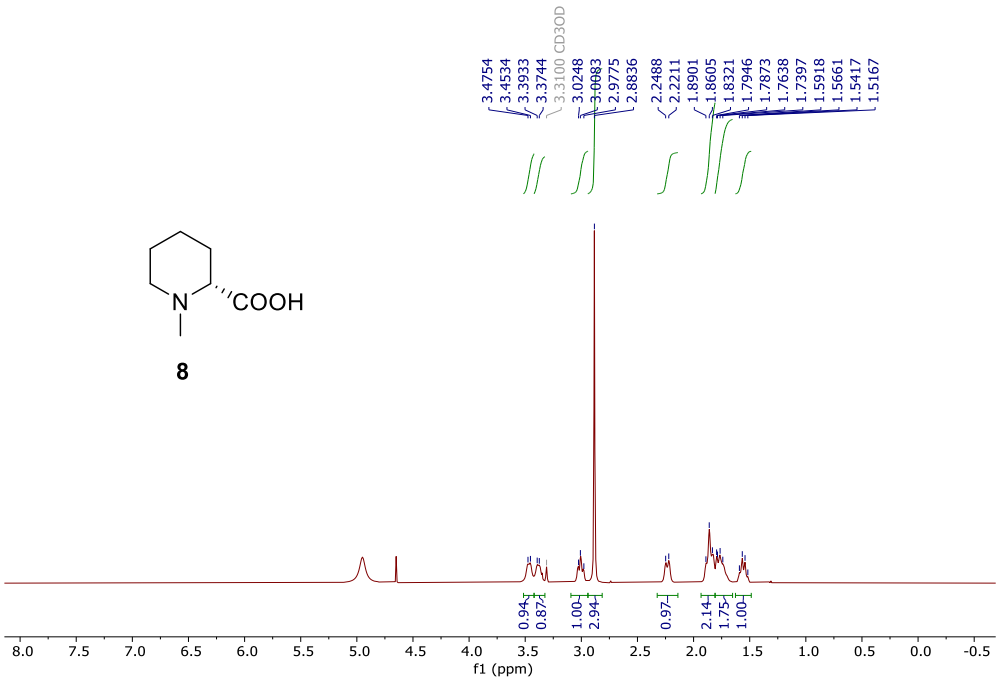

Figure 6.16 ^{1}H NMR spectrum (500 MHz, DMSO-d_6) of **8**.

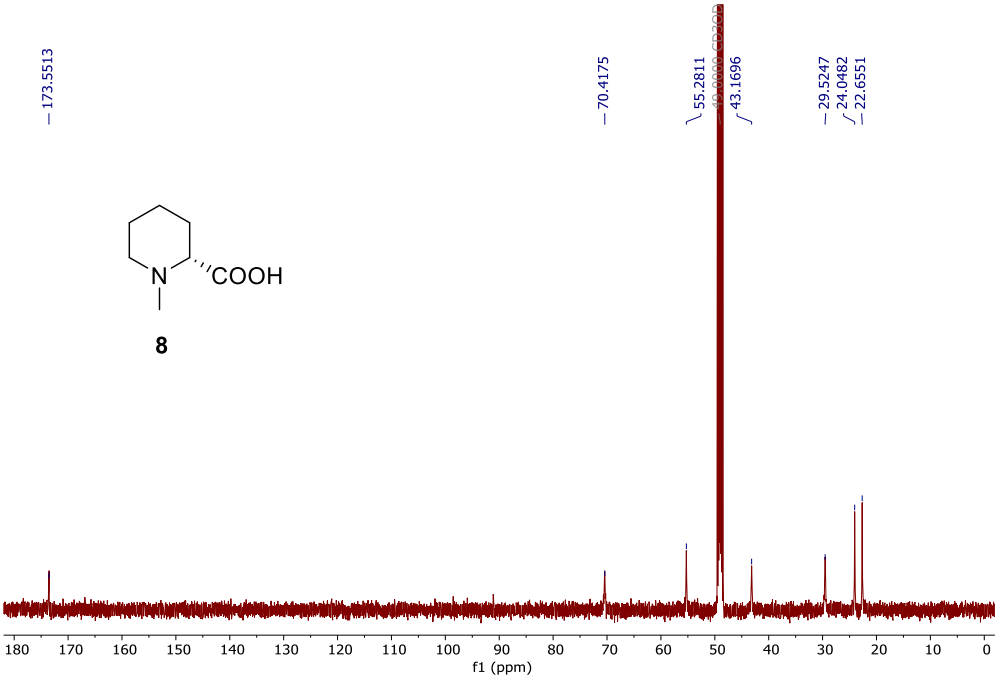

Figure 6.17 ^{13}C NMR spectrum (125 MHz, DMSO-d_6) of **8**.

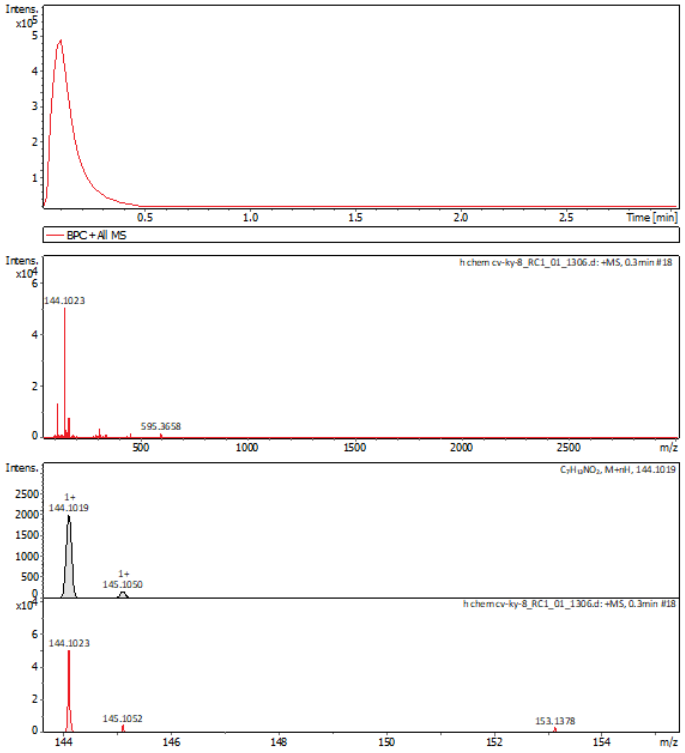

Figure 6.18 HRMS of **8**.

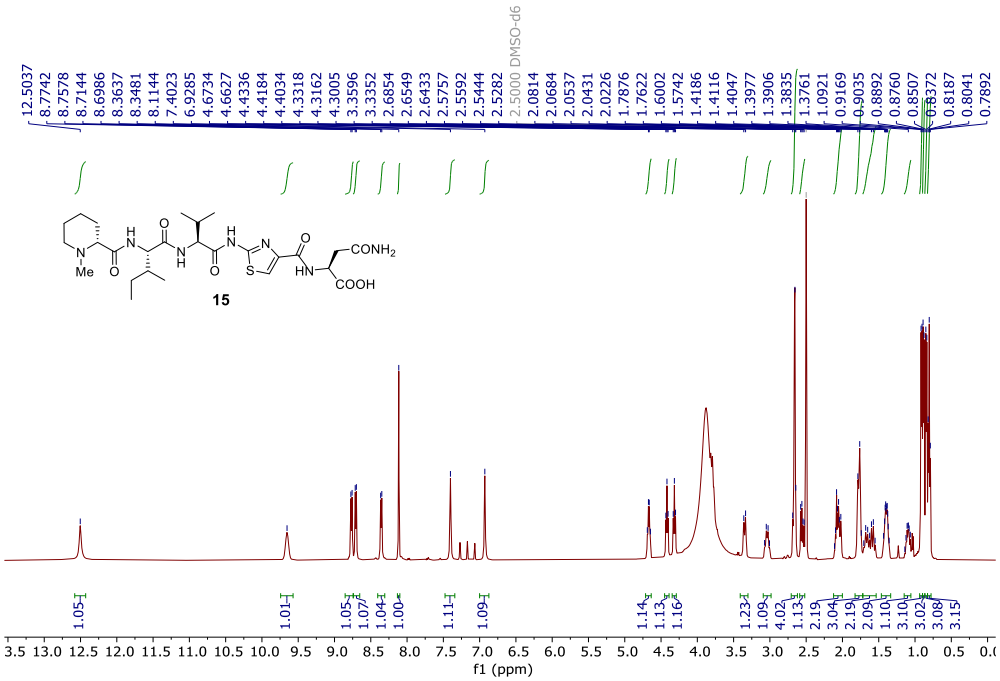

Figure 6.19 ^{1}H NMR (500 MHz, DMSO-d_6) spectrum of **15**.

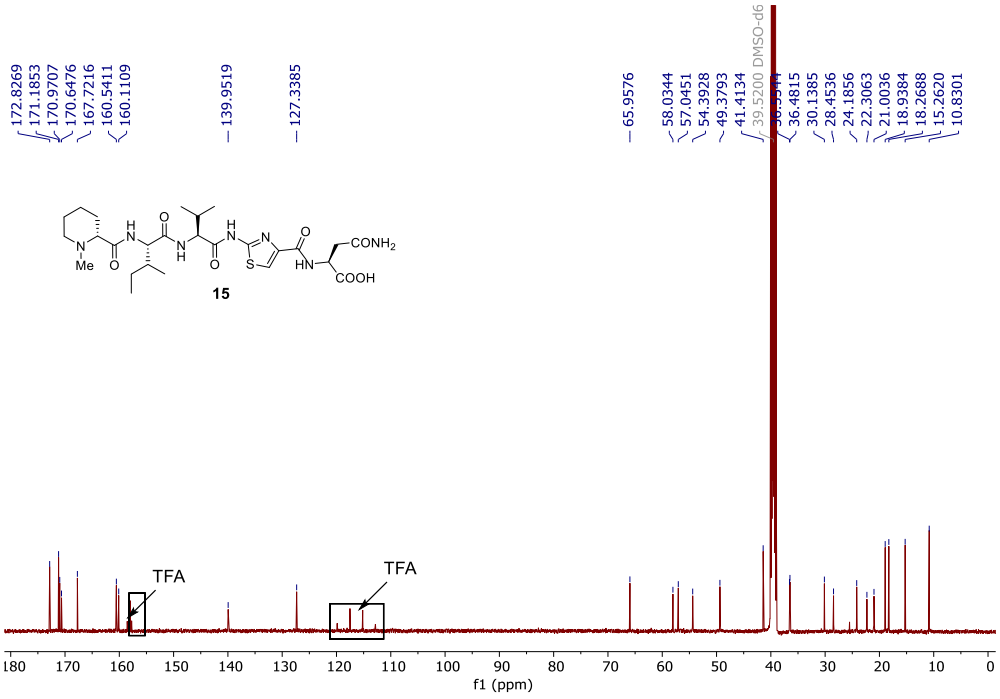

Figure 6.20 ^{13}C NMR (125 MHz, DMSO-d_6) spectrum of **15**.

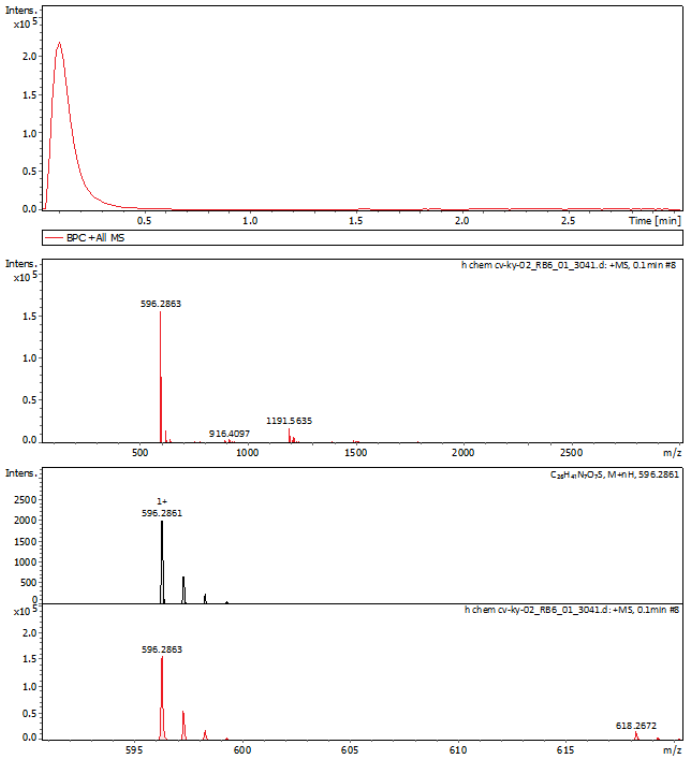

Figure 6.21 HRMS data of **15**.

6.5 References

1. Sasse F, Steinmetz H, Heil J, Hofle G, Reichenbach H. Tubulysins, new cytostatic peptides from myxobacteria acting on microtubuli. Production, isolation, physico-chemical and biological properties. *J Antibiot (Tokyo)*. 2000, 53, 879–885. doi:10.7164/antibiotics.53.879.

2. Shankar SP, Jagodzinska M, Malpezzi L, et al. Synthesis and structure-activity relationship studies of novel tubulysin U analogues-effect on cytotoxicity of structural variations in the tubuvaline fragment. *Org Biomol Chem*. 2013, 11, 2273–2287. doi:10.1039/c3ob27111k.

3. Nicolaou KC, Yin J, Mandal D, et al. Total synthesis and biological evaluation of natural and designed tubulysins. *J Am Chem Soc*. 2016, 138, 1698–1708. doi:10.1021/jacs.5b12557.

4. Wipf P, Wang Z. Total synthesis of N_{14}-desacetoxytubulysin H. *ChemInform*. 2007, 38, 7–9. doi:10.1002/chin.200735186.

5. Murray BC, Peterson MT, Fecik RA. Chemistry and biology of tubulysins: Antimitotic tetrapeptides with activity against drug-resistant cancers. *Nat Prod Rep*. 2015, 32, 654–662. doi:10.1039/c4np00036f.

6. Reddy RB, M V, Krishnan MA, Chelvam V. Synthesis of tubuvaline (Tuv) fragment of tubulysin via diastereoselective dihydroxylation of homoallylamine. *Synth Commun*. 2021, 51, 797–809. doi:10.1080/00397911.2020.1855355.

7. Reddy RB, Dudhe P, Chauhan P, Sengupta S, Chelvam V. Synthesis of tubuphenylalanine and epi-tubuphenylalanine via regioselective aziridine ring opening with carbon nucleophiles followed by hydroboration-oxidation of 1,1-substituted amino alkenes. *Tetrahedron*. 2018, 74, 6946–6953. doi:10.1016/j.tet.2018.10.024.

8. Pandit A, Yadav K, Reddy RB, Sengupta S, Sharma R, Chelvam V. Structure activity relationships (SAR) study to design and synthesize new tubulin inhibitors with enhanced anti-tubulin activity: In silico and in vitro analysis. *J Mol Struct*. 2021, 1223, 129204–129216. doi:10.1016/j.molstruc.2020.129204.

9. Kunnumakkara AB, Bordoloi D, Sailo BL, et al. Cancer drug development: The missing links. *Exp Biol Med*. 2019, 244, 663–689. doi:10.1177/1535370219839163.

10. Saglam-Metiner P, Gulce-Iz S, Biray-Avci C. Bioengineering-inspired three-dimensional culture systems: Organoids to create tumor microenvironment. *Gene*. 2019, 686, 203–212. doi:10.1016/j.gene.2018.11.058.

11. Fang Y, Eglen RM. Three-dimensional cell cultures in drug discovery and development. *SLAS Discov*. 2017, 22, 456–472. doi:10.1177/1087057117696795.

12. Hoarau-Véchot J, Rafii A, Touboul C, Pasquier J. Halfway between 2D and animal models: Are 3D cultures the ideal tool to study cancer-microenvironment interactions? *Int J Mol Sci*. 2018, 19, 181–190. doi:10.3390/ijms19010181.

13. Li J, Zhou Y, Chen W, et al. A novel 3D in vitro tumor model based on silk fibroin/chitosan scaffolds to mimic the tumor microenvironment. *ACS Appl Mater Interfaces*. 2018, 10, 36641–36651. doi:10.1021/acsami.8b10679.

14. Costa EC, Moreira AF, de Melo-Diogo D, Gaspar VM, Carvalho MP, Correia IJ. 3D tumor spheroids: An overview on the tools and techniques used for their analysis. *Biotechnol Adv*. 2016, 34, 1427–1441. doi:10.1016/j.biotechadv.2016.11.002.

15. Amaral RLF, Miranda M, Marcato PD, Swiech K. Comparative analysis of 3D bladder tumor spheroids obtained by forced floating and hanging drop methods for drug screening. *Front Physiol*. 2017, 8, 605–612. doi:10.3389/fphys.2017.00605.

16. Gupta N, Liu JR, Patel B, Solomon DE, Vaidya B, Gupta V. Microfluidics-based 3D cell culture models: Utility in novel drug discovery and delivery research. *Bioeng Transl Med*. 2016, 1, 63–81. doi:10.1002/btm2.10013.

17. Krishnan MA., Chelvam V. Developing μsphereplatform using a commercial hairbrush: An agarose 3D culture platform for deep. *ACS Appl Bio Mater.* 2021, 4, 4254–4270. doi:10.1021/acsabm.1c00086.

Chapter 7

Conclusion and scope of future work

7.1 Conclusion

Current cancer treatment strategies use a targeted approach involving targeting ligands that recognize specific biomarkers expressed on cancer cells, allowing for precise delivery of diagnostic and therapeutic cargos for imaging and treatment of cancer. Conventional chemotherapeutic drugs targeting microtubule dynamics have shown limitations such as multidrug resistance, poor solubility requiring higher doses, poor therapeutic index, and dose-limited toxicity. This thesis focuses on the design, synthesis, and development of small-molecule targeted bioconjugates and inhibitors for the diagnosis and therapy of cancer. We have successfully designed and developed a novel class of amino acetamide ligands targeting the PSMA receptor, conjugated with ^{99m}Tc via a hydrophobic spacer, and the role of the hydrophobic pocket in the PSMA receptor was investigated. A series of bioconjugates was prepared by varying the aromatic amino acid residues with aliphatic amino acids. Additionally, we designed and synthesized a series of novel third-generation tubulin inhibitors composed of four distinct fragments using a simplified solid-phase peptide synthesis method developed in our laboratory. These derivatives were evaluated for cytotoxic activity in various human cancer cell lines, and the most active tubulin inhibitor was then assessed for its cytotoxic potential in a 3D spheroid model.

Chapter 1 provides general information about cancer and its statistics, along with prostate cancer, which is the second most diagnosed cancer in men, conventional fluorescent imaging techniques, and their drawbacks. This chapter gives detailed insights into prostate-specific membrane antigen and various radioactive isotopes used for the early diagnosis of prostate cancer. It also provides a literature review on various microtubule-targeting agents, and synthetic strategies developed for the synthesis of biologically active tubulysin natural products, their derivatives, and drawbacks. In addition, various literature methods for

creating 3D spheroid models are discussed in detail, along with their clinical relevance compared to the 2D cell culture model.

Chapter 2 provides a literature review covering the development of various PSMA-targeting ligands and their clinical applications. It also details the chemical synthetic approach developed for the synthesis of tubulysins, natural products. Additionally, it covers the current methods for generating 3D spheroids and their limitations.

Chapter 3 describes the design and development of novel and effective small-molecule PSMA-targeting ligands and PSMA-targeted radioactive bioconjugates for the early diagnosis of prostate cancer. The radioactive bioconjugate exhibited high binding affinity in the low nM range with an excellent specificity for the PSMA receptor, as indicated by the *in vitro* binding affinity study in comparison to 2-PMPA, a standard high-affinity inhibitor of PSMA. The *in vivo* studies of the radiopharmaceutical have also been performed to determine the selectivity and specificity of the ^{99m}Tc-bioconjugate. These results showed the highest uptake in tumor tissue with minimal uptake in excretory organs such as the kidneys and bladder.

Chapter 4 explores the role of the hydrophobic pocket in the PSMA protein by introducing various modifications in the radioactive bioconjugates. Six radioactive bioconjugates were prepared by varying the peptidic spacer with aromatic and aliphatic amino acids. The binding affinity of the synthesized radioactive bioconjugates was evaluated *in vitro* against PSMA$^+$ LNCaP cell lines to study the effect of aromatic moiety modifications in the peptidic spacer. The results concluded that aromatic amino acids increase the targeting ligand binding affinity, as their replacement with aliphatic amino acids such as glycine results in a drastic loss of binding affinity.

Chapter 5 describes the design, synthesis, and development of several new tubulysin derivatives, with N-terminal and C-terminal modifications. A simple synthesis of valine thiazole and N-methyl pipecolic acid fragments was carried out, and the chemically synthesized

fragments were coupled using solid-phase peptide synthesis (SPPS). The desired tubulysin derivatives, obtained in high yields, were evaluated for their cytotoxic potential against various cancer cell lines for 24 h and 48 h incubation periods. The results showed that the tubulin inhibitors **14a**–**c** exhibit IC_{50} in the low nM range, and the modification at the N-terminal led to a substantial decrease in potency from nM to μM. In contrast, aliphatic amino acids had a minimal impact on the inhibitor's efficacy at the C-terminal, whereas the activities were moderately affected by replacing aromatic amino acids.

Chapter 6 explores the cytotoxic potential of a potent tubulin inhibitor in 3D spheroid models. Highly viable spheroids, generated using μSpherePlatform, were used to evaluate the tubulin inhibitor's cytotoxic potential based on two parameters: (1) IC_{50} value and (2) spheroid diameter. The results showed that the tubulin inhibitor retains its inhibitory activity with an IC_{50} obtained in nM compared to colchicine, which loses its cytotoxic potential in the 3D spheroid model, with an IC_{50} obtained in μM.

7.2 Scope of future work

This thesis focuses on the design, synthesis, and development of small-molecule targeted bioconjugates and inhibitors for the diagnosis and therapy of cancer. The targeted radiopharmaceuticals can be used for early diagnosis and treatment of prostate cancers that are resistant to hormone therapy, including metastatic castration-resistant prostate cancers (mCRPC). These bioconjugates show immense potential for becoming commercial products following successful clinical evaluations.

The potent tubulin inhibitor, showing promising results in both 2D and 3D *in vitro* models, can be encapsulated in nanovehicles/liposomes or directly attached with a targeting moiety that targets specific biomarkers (eg, folate receptor or PSMA) overexpressed during cancer for targeted delivery of the tubulin inhibitor in cancer cells. This targeted inhibitor can be further evaluated in preclinical trials, making it a promising clinical candidate.